Nanoantennas for Solar Energy Harvesting

Ahmed M A Sabaawi

Newcastle University

Newcastle upon Tyne, UK.

A thesis submitted for the degree of

Doctor of Philosophy

June 2015

TO

my beloved wife, **Nadia**

AND

my loving sons, **Omar** , **Mohammed**, **Yousif** and **Ibrahim**.

Acknowledgements

After the end of my four-year journey in PhD study, I must begin my acknowledgement with thanking the almighty Allah for giving me the strength and the courage to be what I am now.

I am using this opportunity to express my sincere gratitude to many kind people around me who supported me throughout my PhD study. It would not have been possible to write this thesis without their help and support, to whom I would like to give particular mention here.

First and foremost I wish to thank my first supervisor, Dr Charalampos Tsimenidis, for his aspiring guidance and constructive criticism which paved my way during my study. From him, I received unlimited help and support and from him I learnt how to think positively and how to be a successful researcher. I would also like to show my greatest appreciation to my second supervisor, Prof Bayan Sharif, for his invaluable friendly advices on both academic and personal level, for which I am extremely grateful. I am sincerely grateful to both of my supervisors for being supportive and helpful since the days I began working on my project.

I express my warm thanks to my fellow postgraduate students at the school of Electrical and Electronics Engineering: Ibrahim, Sabah, Abdulrahman, Mohamad, Emad, Muayad, Salah, Sedki, Sangar and Oras for their endless support and for sharing their truthful and illuminating views on a number of issues related to the project. They provided me with a great academic and social atmosphere, which motivated me to do my best and to be as successful as they are.

I would like to acknowledge the financial, academic and technical support of the Higher Committee of Education Development (HCED) in Iraq, particularly in the award of a fully-sponsored scholarship that provided the necessary financial support for this research. I would like to show my deepest appreciation to the Ministry of Higher Education in Iraq and the University of Mosul

for providing me with a study leave to get the degree of PhD from Newcastle University. I also thank the School of Electrical and Electronic Engineering for their assistance and support since my first day in the school, especially the kind Postgraduate Research Coordinator, Gillian Webber and the lovely Receptionist, Deborah Alexander.

I owe a very important debt to my parents, brothers and sisters who have given me their endless love and support throughout. Without their encouragement, this thesis would not have been written.

Last but not least, my heartfelt appreciation goes to my wife, Nadia, and my sons, Omar, Mohammed, Yousif and Ibrahim for their personal support and great patience at all times. From them I stole great moments and special days for the sake of study. They offered me all these sacrifices without showing any grievance. My lovely family has been a constant source of love, motivation and energy ever since, for which my mere expression of thanks likewise does not suffice.

Abstract

Recent years have witnessed an enormous interest in developing solar cells by utilising different materials to increase their efficiency. This interest was motivated by the rapid world demand on cheap and clean energy sources, where the main source of world's power is the fossil fuels. The current photovoltaics technology can not meet the solar power market due to the very low efficiency provided. The philosophy of this thesis is to find an efficient alternative by designing an efficient nanoantenna for receiving the solar radiation and coupling it to an integrated rectifier for AC to DC conversion. This thesis presents the design and optimisation of different types of nanoantennas with a performance comparison to find the optimum solution for this application. The figure of merit in choosing the best design was the captured electric field in the feed gap of the nanoantenna and the area under curve, which is essential in calculating the harvested energy. In addition, this thesis investigates the use of nanoarray instead of single elements. The aims is to increase the captured electric field at the gap of the array where all the elements will contribute in increasing the field in one common gap. Feeding lines will be employed to drive the captured fields from the centre of each single element towards the common gap. Another reason behind using nanoarrays is to reduce the number of rectifiers by using one rectifier per array instead of one rectifier per single element, and hence increase the total efficiency. Futhermore, a simple analysis on dipole nanoantenna using method of moments (MoM) is presented in this thesis. The results obtained from this method is compared with those found from finite element method (FEM) simulations and an acceptable agreement is achieved. To calculate the total conversion efficiency of solar rectennas, it is important to compute the rectification efficiency of the metal/insulator/metal (MIM) diode along with the coupling efficiency between the antenna and the diode. To this end, quantum mechanics was used to calculate the characteristics of the MIM diode. The results show that bowtie nanoantennas are the best candidate for this application in either the single and array form since they have wider bandwidth and larger

area under curve. Additionally, the analysis using MoM gives the designer better understanding on how the system works and exhibits lower complexity and reduced computational requirements.

Contents

List of Figures

List of Tables

Nomenclature

Acronyms

AF Array Factor

AUC Area Under Curve

BEM Boundary Element Method

E_i Incident Electric Field

E_s Scattered Electric Field

E_t Tangent Electric Field

$FDTD$ Finite Difference Time Domain

FEM Finite Element Method

FIT Finite Integration Technique

IR Infra-red

LPF Low Pass Filter

$LSPR$ Localised Surface Plasmon Resonance

MIM Metal/Insulator/Metal

MoM Method of Moments

$NEGF$ Non-equilibrium Green's Function

PDM Polarisation Division Multiplexing

PEC Perfect Electric Conductor

PML Perfectly Matched Layer

PV Photovoltaics

$QTBM$ Quantum Transmitting Boundary Method

RF Radio Frequency

THz Tera-Hertz

TMM Transfer-Matrix Method

$UPML$ Uni-axial Perfectly Matched Layer

UV Ultra Violet

WPT Wireless Power Transmission

Chapter 1

Introduction

1.1 Introduction

The world has witnessed an increasing demand on energy sources during the last decades, where the main source of the world's power is the fossil fuels. This worldwide demand for energy, in addition to the environmental effects of the existed hydrocarbon-based power sources, has led to significant need for alternative clean and renewable energy sources. One of the alternative candidates is solar cells, which are utilised to collect and convert the solar energy into electricity.

Solar energy, which represents the largest energy flow that enters the atmosphere, reaches the earth in both visible and infrared regions. Part of this energy is absorbed by atmospheric gases and re-radiated to the earth's surface in the mid-infrared and far-infrared regions. Other parts of this energy is absorbed by the surface or organic life and re-radiated [1]. The power density of the solar radiation that reach the Earth's atmosphere is approximately 1370 W/m^2 over a wide spectrum. This spectrum can be classified into three main bands: ultraviolet (UV) radiation $(\lambda < 400$ nm$)$ of which the content is less than 9%; visible light $(400$ nm $< \lambda < 700$ nm$)$ where the content is approximately 39%; and the remaining 52% consisting of infrared (IR) [2]. Not all solar radiation reaches the earth but the radiation which penetrates the atmosphere [ultraviolet (0.29 to 0.40 μm), visible (0.40 to 0.76 μm), and infrared rays (0.76 to 1000 μm] have a large energy content. This energy is converted to heat when it is absorbed by any object on earth.

This solar energy represents a renewable energy resource that is used by humans and has opened a new era on exploiting the solar radiation for the production of electricity. Since the creation of the first photovoltaic (PV) cell in the early 1950s, the development of photovoltaic is increasing rapidly. However, this development still can not cover the market demand on solar panels because of their low efficiency. Thus, the PV industry will need cheaper and higher efficiency technologies to meet these requirements of the solar power market. Nanoantennas have been suggested to replace the solar cells by embedding an appropriate rectifier in the feed gap of the antenna forming a **rec**tifying-an**tenna** (rectenna) using the wave nature of light, where they exhibit higher efficiency (theoretically 100%) compared to the current solar cells.

The use of optical antennas for solar energy harvesting has received a significant interest as they represent a pragmatic and efficient alternative to the traditional energy harvesting technologies, such as solar panels, exploiting the rapid advancement in nanotechnology and optical materials . Additionally, nanoantennas have found many applications

in the visible and infrared regimes due to their ability to enhance the interaction of light or infrared waves with nanoscale matter and confine a highly localized field in their feed gap [3].

This chapter highlights the history of optical and infrared antennas for solar rectennas and mentions the important contributions made in this field. Moreover, it demonstrates the versatility of solar rectennas over the traditional solar cells. The structure and the operation theory of the solar rectennas have also been presented in this chapter. In this thesis, the design and optimisation of nanoantennas for the use in the solar energy harvesting systems is presented.

1.2 Historical Overview

The story begun during the early years of the last century when researchers began to investigate the transfer of electrical power without wires coining the term wireless power transmission (WPT). Early works on this approach goes back to the work of Hertz and Tesla, when the latter carried out his early experiments by utilising a giant coil and a 3-ft-diameter copper ball to transport the low frequency electromagnetic wave from one point to another. This work has inspired other researchers later to develop the idea of power transmission after significant advancements in microwave technology [4]. In 1963, Raytheon Co. invented the first rectenna, which was composed of 28 half-wave dipole antennas. Each dipole terminated with a bridge rectifier, where 40% efficiency was achieved. The rectenna developed by Raytheon Co. was used to power a microwave-powered helicopter. It is worth to mention that all the rectenna systems conceived at that time were working at microwave frequencies with efficiencies exceeding 80% at a single frequency. However, the idea of converting the solar power to an electricity by using rectennas was firstly proposed by Bailey in 1972 [5]. He suggested a pair of pyramids or cones as modified dipole similar to rod antennas, each pair connected to a diode (half-wave rectifier) and then to a load.

In 1984, Marks presented the use of arrays of crossed dipoles as shown in Fig. 1.1 on an insulating sheet with fast full-wave rectification [6]. This is different from Bailey's proposal, as Marks proposed to use a conventional broadside array antenna with the output signal from several dipoles feeding into a transmission line that transfer the signals to a rectifier. This requires the combined signals to add in-phase. Lin et al. in 1996 reported the first experimental work on light absorption by fabricated metallic resonant nanostruc-

tures and rectification at light frequency [7]. The device used a parallel dipole antenna array on a silicon substrate and a p-n diode as a half-wave rectifier.

Berland in 2003 has designed infrared rectenna structures with Metal-Insulator-Metal (MIM) diodes between dipoles for operation at 10 μm wavelength, however the efficiency of his system was very low (less than 1%) [8].

Kotter et al. in 2010 have designed and fabricated a spiral nanoantenna for solar energy collection at mid-infrared region [1]. They demonstrated progress in addressing significant technological barriers including: development of frequency-dependent modelling square spiral antenna, selection of materials with proper THz properties, and development of manufacturing methods that could lead to large-scale manufacturing.

Midrio et al. in 2011 designed a monopole antenna made of nickel for the reception of thermal radiation. The antenna is overlapping with the ground plane; the overlapping area is supposed to host an MIM (nickel-nickel oxide-nickel) diode for conversion of terahertz fields into electrical current. The effect of geometrical parameters on the antenna performance was investigated [9].

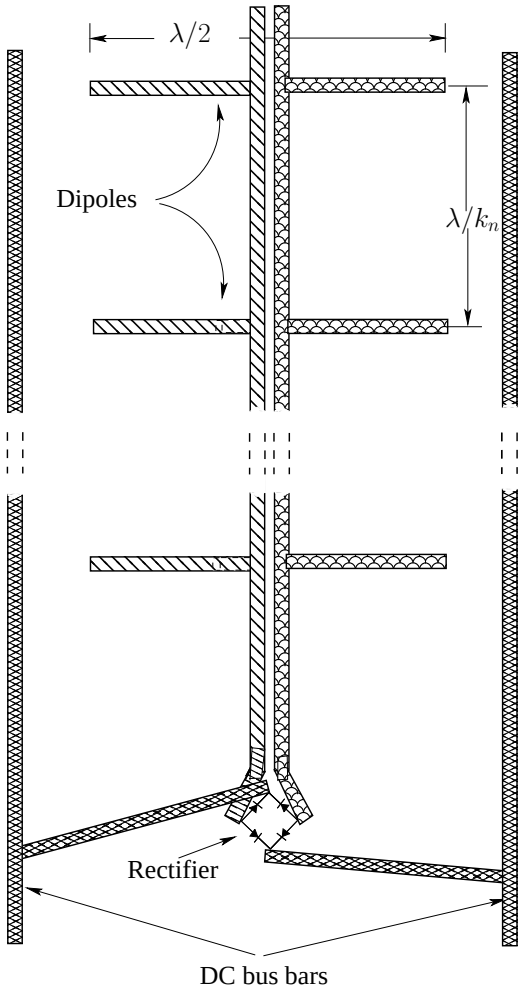

Figure 1.1: Marks' dipolar light/electricity converter.

1.3 Why Solar Rectennas?

The first photovoltaic cell was created in the early 1950s, and thereafter, the development of photovoltaics has been increasing rapidly. However, photovoltaics have many disadvantages that led scientists and researchers to find alternative technologies that can overcome theses disadvantages. The main drawbacks of photovoltaic based technologies are their low conversion efficiency and their strong dependence on daylight, which in turn makes them sensitive to the weather conditions. Furthermore, they require a mechanical sun-tracking system to optimise conversion.

With PV, the efficiency is a function of, and limited by, the bandgap; and each photon above the bandgap produces an electron-hole pair regardless its energy. Photons that have an energy matched to the bandgap will generate the same energy delivered from high energy photons. This limits the upper efficiency to $\sim 30\%$ for single-junction cells, and the theoretical efficiency to around 55% for complex multi-junction cells [10].

Currently, significant efforts are being made towards improving the performance of PV by implementing complex, multi-junction designs. However, these designs are still not considered as a cost-effective solution to overcoming the efficiency limitations [1]. In contrast, solar nano-rectennas demonstrate versatility over PV devices by exceeding efficiency during the day. In addition, solar nanoantennas show wider angular reception characteristics than traditional solar cells as such and importantly, they do not require a sun tracking system.

1.4 Solar Rectenna Structure and Theory of Operation

Like traditional RF antennas, nanoantennas respond to the incident electromagnetic wave (visible light or infrared) by inducing an AC current onto the antenna surface such that it oscillates at the same frequency of that wave. A high electric field (hot spot) is typically concentrated at the feeding gap of the antenna. This enhanced field in the antenna's gap is exploited in the application of solar power collection to produce DC power by rectifying the oscillated AC current with the aid of a proper diode-based rectifier.

According to theory of boundary conditions, the tangential electric field vanishes, i.e. $\mathbf{E}^t = 0$, at the surface of the antenna. This is true for the conventional antennas at RF frequencies, where the metals are considered to be perfect electric conductors, so that the $\mathbf{E}^s = -\mathbf{E}^i$, where $\mathbf{E}^s$ is the scattered electric field and $\mathbf{E}^i$ is the incident electric field.

However, in the case of nano-scale antennas operating at the optical and IR regimes, metals are no longer considered to be perfect conductors, as they exhibit lower conductivity. Consequently, the term $\mathbf{E}^t$ has to be taken into consideration, which can be represented by the surface impedance multiplied by the surface current for the case of an antenna placed on the z-axis.

The block diagram of a typical solar rectenna is shown in Fig. 1.2 [11], where the optical antenna is responsible for receiving the electromagnetic wave within a specific frequency band and delivering it to the low-pass filter (LPF).

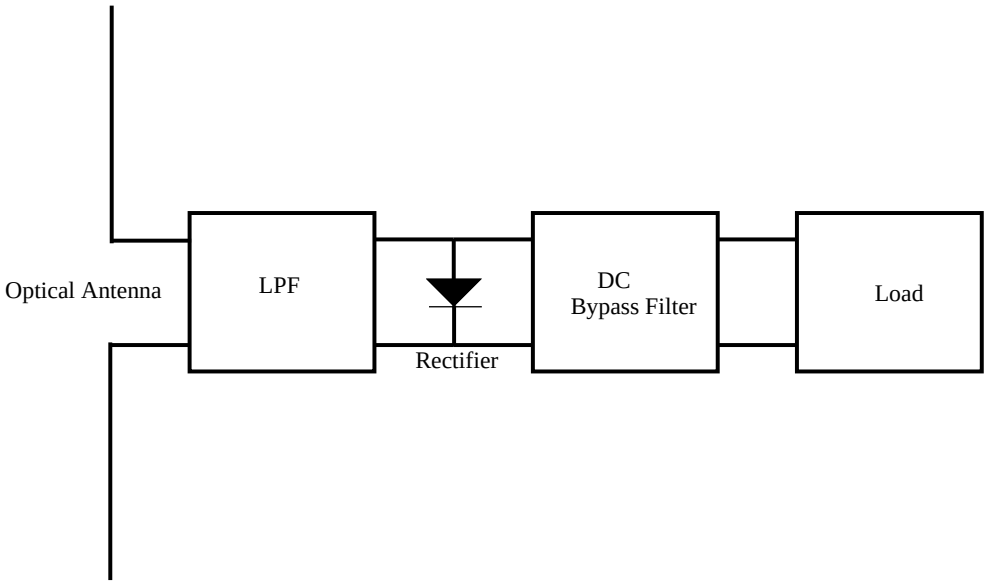

Figure 1.2: Block diagram of a solar rectenna.

The low pass filter between the antenna and the rectifier (diode) prevents the re-radiation of higher harmonics generated from rectification process by the non-linear diode, where its re-radiation could result in power losses. In addition, this filter matches the impedance between the antenna and the subsequent circuitry. The DC LPF is necessary to smooth the rectified signal to DC and pass it to the load. The most popular rectifier in solar rectennas is the MIM diode. The rectification occurs based on the electron tunnelling process through the insulator layer.

1.5 Contribution

The aim of this research is to design efficient non-expensive nanoantennas for the use in solar energy harvesting applications. In addition, the aim is to introduce a simple analysis for these types of antennas by providing their circuit model and calculating their parame-

ters. As mentioned earlier in this chapter, solar rectennas are considered as an alternative to conventional solar cells, which work only within the visible region of electromagnetic spectrum. Thus, it is important to exploit the unused part of the electromagnetic spectrum (i.e infrared region) and to overcome the efficiency limits in solar cells. From the foregoing, the contribution of this thesis can be outlined in the following points.

- Different types of antennas have been designed and a comparison between their performance, based on the captured electric field, has been presented to find the optimum geometry.
- All these nanoantenns have been designed to work within the infrared region to exploit the unused part of solar radiation and the thermal radiation from objects.
- Combine more than two elements in an array form to increase the captured electric field and enhance the performance.
- Introduce the concept of using feed lines to connect the array elements and to drive the captured fields from the feed gap of antennas towards common feed gap for the entire array. In this case, only one diode is required per single array, and hence, the thermal losses in the rectifier will be reduced and the efficiency will be increased.
- Geometrical parametric study is carried out to improve the array performance and increase the system efficiency.
- In order to fully understand the principles and concepts of solar rectennas, an efficient analysis has been presented, which gives a physical insight into how solar rectennas work.
- Quantum-mechanics analysis have been applied to calculate the rectification efficiency of metal/insulator/metal (MIM) diodes, which is essential in computing the overall system efficiency.

1.6 Publications Arising From This Research

- Book Chapters

1. **A. M. A. Sabaawi**, C. C. Tsimenidis and B. S. Sharif, "Overview of Nanoantennas for Solar Rectennas," *Rectenna Solar Cells*, Springer New York, 231-256. ISBN 978-1-4614-3715-4, October 2013.

- Journal Papers

1. **A. M. A. Sabaawi**, C. C. Tsimenidis and B. S. Sharif, "Analysis and Modeling of Infra-red Solar Rectennas," *IEEE Journal of Selected Topics in Quantum Electronics*, Volume 19, Issue 3, 2013.

2. **A. M. A. Sabaawi**, C. C. Tsimenidis and B. S. Sharif, "Planar Bowtie Nanoarray for THz Energy Detection," *IEEE Transactions on Terahertz Science and Technology*, Volume 3, Issue 5, 2013.

3. **A. M. A. Sabaawi**, C. C. Tsimenidis and B. S. Sharif "Characterization of Conversion Efficiency in Solar Rectennas" Submitted, 2014.

- Conference Papers

1. **A. M. A. Sabaawi**, C. C. Tsimenidis and B. S. Sharif, "Infra-red nano-antennas for solar energy collection," *Loughborough Antennas and Propagation Conference (LAPC)*, pp.1-4, 14-15 Nov. 2011.

2. **A. M. A. Sabaawi**, C. C. Tsimenidis and B. S. Sharif, "'Bow-Tie Nano-Array Rectenna: Design and Optimization," *The 6th European Conference on Antennas and Propagation (EuCAP 2012)*, Prague, Czech Republic, 26-30 March 2012.

3. **A. M. A. Sabaawi**, C. C. Tsimenidis and B. S. Sharif, "Infra-red Spiral nano-antennas," in *Loughborough Antennas and Propagation Conference (LAPC)*, Loughborough, UK, pp.1-4, 12-13 Nov. 2012.

4. **A. M. A. Sabaawi**, C. C. Tsimenidis and B. S. Sharif, "Characterization of Coupling and Quantum Efficiencies in Solar Rectennas," *Loughborough Antennas and Propagation Conference (LAPC)*, 11-12 Nov. 2013.

5. **A. M. A. Sabaawi**, C. C. Tsimenidis and B. S. Sharif, "Auxiliary Ring Resonator for Local Field Enhancement in Solar Rectennas," *Loughborough Antennas and Propagation Conference (LAPC)*, 10-11 Nov. 2014.

1.7 Thesis Outline

The thesis is organised as follows:

Chapter 2 presents a background on the electromagnetic theory with brief discussions on Maxwell's equation and the boundary conditions. It also introduces the history and concept of nanoantennas and outlines the main differences between nanoantennas and the conventional RF antennas. Moreover, it provides details on the physical properties of nanoantennas and discusses their relevant theories.

Chapter 3 gives brief introduction on the numerical methods used to solve various electromagetic problems with the aid of Maxwell's equations. The chapter is divided into two parts. The first part provides general information on the key methodologies behind computational methods, where some of the popular basis function that have been used in computational methods are discussed. The second part highlights the most commonly used methods such as method of moments (MoM), finite element method (FEM), finite difference time domain (FDTD).

Chapter 4 provides in depth details on the simulation and optimisation of nanoantennas for the use in solar energy collection. The criteria of selecting the appropriate material and geometry will be presented in this chapter. Furthermore, three types of nanoantennas will be simulated and discussed.

Chapter 5 focuses on the design of bowtie nanoarrays at infrared wavelengths for utilisation in solar energy collection. The chapter presents a detailed parametric study to optimise the designed array by varying different geometrical parameters.

Chapter 6 introduces a simple and efficient numerical analysis of nanoantennas to find their electrical properties and to calculate the nanoantenna efficiency. Additionally, the chapter demonstrates the use of quantum mechanics techniques to find the characteristics of MIM diodes, and hence, to calculate the conversion efficiency of solar rectennas.

Finally, conclusions and future work are outlined in Chapter 7.

Chapter 2

Background

In this chapter, a theoretical background on electromagnetics and antennas is presented. The chapter is divided into three main sections. The first section introduces the electromagnetic theory with brief discussions on Maxwell's equations, boundary conditions and other relevant theories. The second section presents the classical antenna theory and the radiation mechanism. Finally, the last section introduces the history and concept of nanoantennas, highlighting the main differences between nanoantennas and the conventional RF antennas. In addition, the section presents the physical properties of nanoantennas and discusses the surface plasmon resonance, which is a unique feature in optical nanoantennas. These three sections cover the background theory needed to understand the work presented in this thesis.

2.1 Electromagnetic Theory

The basic principles of modern electromagnetic theory have been introduced by J C Maxwell in 1873. He described the mathematical expressions that explain different phenomena such as propagation, scattering and reflection. This mathematical formulation was very complex until it was simplified by Oliver Heaviside in 1887, however the theory was only a hypothesis. In 1891, Heinrich Hertz validated Maxwell's theory experimentally and paved the way for the emergence of many technologies such as radio, television, radar, antennas, wireless communication and many others. Electromagnetic theory is valid from low frequencies to optical regimes.

2.1.1 Maxwell's equations

Maxwell's equations describe the relation between the electric and magnetic fields with the charge and current densities at any point in space. These fields have magnitude and direction and they are vector quantities. In this chapter, the differential form of Maxwell's equations will be presented, which can be written as [13]

$$\nabla \times \mathbf{E} = -\frac{\partial \mathbf{B}}{\partial t}, \tag{2.1}$$

$$\nabla \times \mathbf{H} = \frac{\partial \mathbf{D}}{\partial t} + \mathbf{J}, \tag{2.2}$$

$$\nabla \cdot \mathbf{D} = \rho, \tag{2.3}$$

$$\nabla \cdot \mathbf{E} = 0, \tag{2.4}$$

$$\nabla \cdot \mathbf{J} = -\frac{\partial \rho}{\partial t}, \tag{2.5}$$

where $\nabla\times$ is the curl of a vector and $\nabla\cdot$ its divergence. Using the constitutive relations for linear medium

$$\mathbf{D} = \epsilon\mathbf{E}, \tag{2.6}$$

$$\mathbf{B} = \mu\mathbf{H}, \tag{2.7}$$

$$\mathbf{J} = \sigma\mathbf{E}, \tag{2.8}$$

where

$\mathbf{E}$ is the electric field intensity in $(\frac{V}{m})$;

$\mathbf{H}$ is the magnetic field intensity in $(\frac{A}{m})$;

$\mathbf{D}$ is the electric flux density in $(\frac{C}{m^2})$;

$\mathbf{B}$ is the magnetic flux density in $(\frac{Wb}{m^2})$;

$\mathbf{J}$ is the surface current density in $(\frac{A}{m^2})$;

ρ is the electric charge density in $(\frac{C}{m^3})$;

ϵ is the permittivity of the medium and μ and σ are its permeability and conductivity, respectively.

2.1.2 Boundary conditions

The constitutive parameters ε, μ and σ play a key role in characterising the medium. The medium is *linear*, *homogeneous* and *isotropic* if its constitutive parameters are independent of field strength, position and direction, respectively. The constitutive parameters along with Maxwell's equations can be used to find a unique solution for the electromagnetic problem by enforcing the appropriate boundary conditions related to this problem.

The boundary conditions at the interface of two media (shown in Fig. 2.1) can be derived directly from the integral form of Maxwell's equations as follows [13]

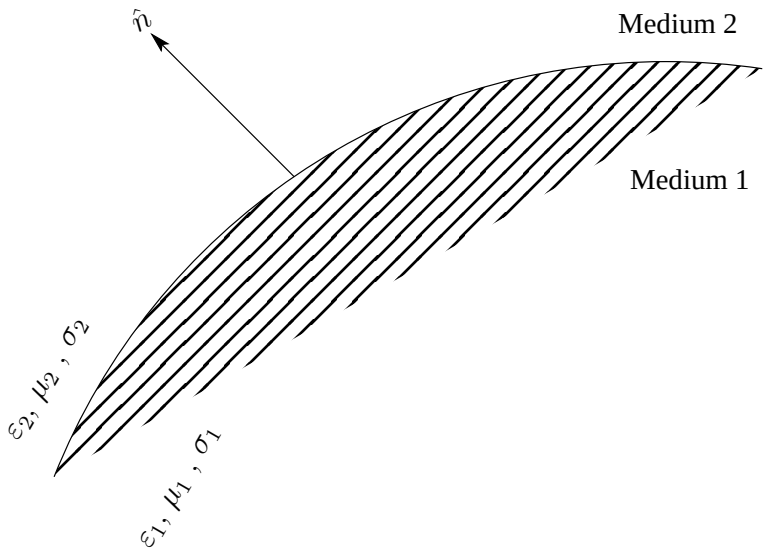

Figure 2.1: Boundary conditions between two media.

$$(\mathbf{E}_1 - \mathbf{E}_2) \times \hat{n} = 0, \tag{2.9}$$

$$(\mathbf{D}_1 - \mathbf{D}_2) \cdot \hat{n} = 0, \tag{2.10}$$

$$(\mathbf{H}_1 - \mathbf{H}_2) \times \hat{n} = 0, \tag{2.11}$$

$$(\mathbf{B}_1 - \mathbf{B}_2) \cdot \hat{n} = 0, \tag{2.12}$$

where $\hat{n}$ is a unit vector normal to the interface between the two media, and the subscripts 1 and 2 indicate medium 1 and medium 2, respectively.

Note that in (2.10) and (2.11) it is assumed that the medium is source-free (i.e $\rho_s = 0$ and $\mathbf{J}_s = 0$), otherwise, they must be written as

$$(\mathbf{D}_1 - \mathbf{D}_2) \cdot \hat{n} = \rho_s, \tag{2.13}$$

$$(\mathbf{H}_1 - \mathbf{H}_2) \times \hat{n} = \mathbf{J}_s, \tag{2.14}$$

When medium 1 or medium 2 is a perfect electric conductor, (2.9) and (2.12) reduce to

$$\mathbf{E} \times \hat{n} = 0, \tag{2.15}$$

$$\mathbf{B} \cdot \hat{n} = 0, \tag{2.16}$$

In this case, the boundary can uphold a surface charge and a surface current.

If one of the media is an imperfectly conducting surface, **E** and **H** at this surface will be related by

$$\hat{n} \times \mathbf{H} = \frac{1}{\hat{\eta}} \left[\mathbf{E} - (\hat{n} \cdot \mathbf{E})\hat{n}\right], \tag{2.17}$$

or

$$\hat{n} \times \mathbf{E} = \hat{\eta} \left[\mathbf{H} - (\hat{n} \cdot \mathbf{H})\hat{n}\right]. \tag{2.18}$$

where $\hat{\eta} = \eta\eta_0$, $\eta = \sqrt{\frac{\mu_r}{\varepsilon_r}}$ is the normalised intrinsic impedance of the medium and $\eta_0 = \sqrt{\frac{\mu_0}{\varepsilon_0}}$ is the free-space intrinsic impedance. Equations (2.17) and (2.18) are called the *impedance boundary condition*.

2.1.3 Wave equations

Maxwell's equations are coupled first-order differential equations, which are very difficult to solve in boundary-value problems. In coupled differential equations, each equation contains both the unknown electrical and magnetic fields in the same equation. Hence, these equations need to be decoupled and represented by only one unknown, however, this will increase the order. The result will be the *wave equation*, which is a second-order differential equation that will facilitate the problem [12].

The wave equation for a linear, homogeneous and isotropic medium can be obtained from the first two of Maxwell's equations

$$\nabla \times \mathbf{E} = -\frac{\partial \mathbf{B}}{\partial t}, \tag{2.19}$$

$$\nabla \times \mathbf{H} = \frac{\partial \mathbf{D}}{\partial t} + \mathbf{J}. \tag{2.20}$$

We need to obtain an equation with either the electric or the magnetic field as an unknown. This can be achieved by taking curl of both sides of (2.19). This yields

$$\nabla \times \nabla \times \mathbf{E} = -\frac{\partial}{\partial t}(\nabla \times \mathbf{B}). \tag{2.21}$$

Applying $\mathbf{J} = 0$ in (2.20) and $\mathbf{B} = \mu\mathbf{H}$ in (2.21) then substituting (2.20) in (2.21) results in

$$\nabla \times \nabla \times \mathbf{E} = -\mu\varepsilon\frac{\partial^2 \mathbf{E}}{\partial t^2}. \tag{2.22}$$

Using the vector identity

$$\nabla \times \nabla \times \mathbf{F} = \nabla(\nabla \cdot \mathbf{F}) - \nabla^2\mathbf{F}, \tag{2.23}$$

into (2.22) leads to

$$\nabla(\nabla \cdot \mathbf{E}) - \nabla^2\mathbf{E} = -\mu\varepsilon\frac{\partial^2 \mathbf{E}}{\partial t^2}. \tag{2.24}$$

By applying $\nabla \cdot \mathbf{E} = 0$, (2.24) will be simplified to

$$\nabla^2\mathbf{E} - \mu\varepsilon\frac{\partial^2 \mathbf{E}}{\partial t^2} = 0. \tag{2.25}$$

The last equation is the time-dependent wave equation or what so called *Helmholtz equation*. Similarly, the wave equation for $\mathbf{H}$ can be obtained if we start the derivation from (2.20), which can be written as

$$\nabla^2\mathbf{H} - \mu\varepsilon\frac{\partial^2 \mathbf{H}}{\partial t^2} = 0. \tag{2.26}$$

2.2 Classical Antenna Theory

An antenna is a means for transmitting or receiving radio wave, as defined by IEEE [13]. It is the transitional device between the free-space and the transmission line. The antenna works in receiving mode if it transports the electromagnetic energy from the transmitting source to the receiver. On the other hand, if the antenna radiates the energy to free-space, it can be said that it is working in transmitting mode. It should be mentioned that antennas

are reciprocal devices, which means that their properties do not depend on the working mode. In other words, they can transmit and receive in the same way, thus, an efficient transmitting antenna can be used as a receiving antenna efficiently.

The principle of operation for antennas depends on the conduction electrons on the surface of a piece of metal. When an *ac* voltage is applied or an electromagnetic waves hits the surface, the distribution of charges will be changed with time and they will start to oscillate. This will change the electric field at any distance from the source. The frequency of harmonic oscillation will be as follows [3]

$$f_0 = \frac{1}{2\pi\sqrt{LC}}, \tag{2.27}$$

where L and C are the inductance and the capacitance of the antenna system. The antenna can be tuned to resonate at a specific frequency by adjusting L and C. In order to bring the resonance into the infrared regime, L and C must be very small. This can be achieved by reducing the dimensions of the antenna with respect to the wavelength.

2.2.1 Antenna radiation

For a system made of two parallel thin wires with an open end, the current distribution will be sinusoidal due to the standing waves as shown in Fig. 2.2. The system will start radiating electromagnetic waves when the terminals are bent at a distance of $\frac{L}{2}$ from both sides. The strongest radiation occurs when the bending angle is 90^o. The current distribution on the the surface of the bent arms can be described by

$$I(z) = I_0 \sin[k(\frac{L}{2} - |z|)]. \tag{2.28}$$

Bending the terminals of the wire will construct a simple dipole antenna with an impedance, Z_a, that differs form the characteristic impedance of the guiding line, Z_o. Due to the mismatch between Z_a and Z_o, we would expect a standing wave pattern. Thus, the antenna impedance can be given as the ratio of the voltage across the antenna feed gap and the current, which has the complex form of $Z_a = R_a + iX_a$.

The real part of the antenna impedance, R_a, determines the amount of the power dissipated as heat in antenna and the radiated power, where it can be written as

$$R_a = R_r + R_l, \tag{2.29}$$

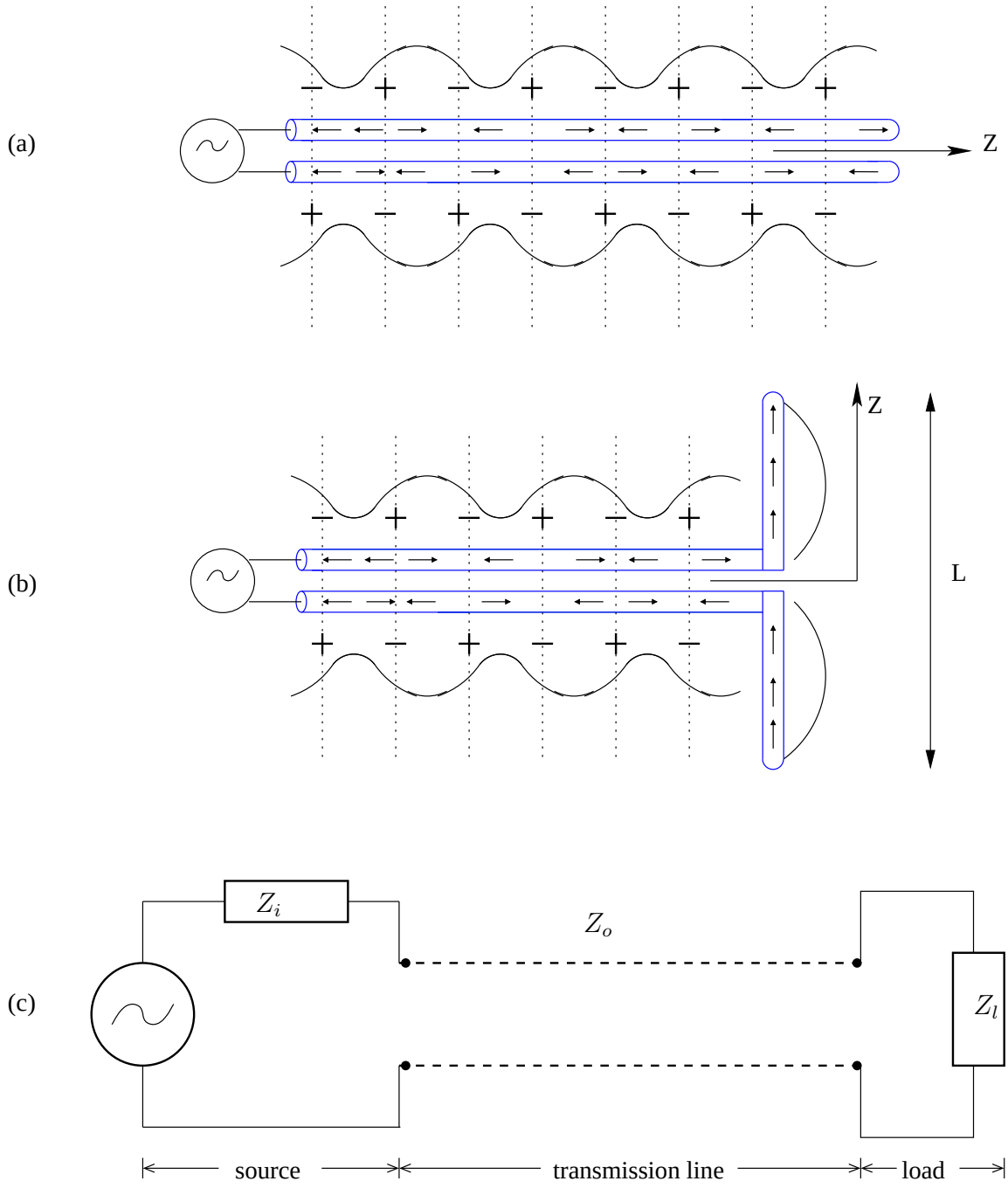

Figure 2.2: Radiation mechanism of a transmitting antenna.

where R_r is the radiation resistance and R_l is the resistance that is responsible for Ohmic losses inside the antenna. The radiated power can be calculated as

$$P_r = \frac{R_r}{2} I^2. \tag{2.30}$$

The radiation efficiency,η_r, will therefore be defined as

$$\eta_r = \frac{R_r}{R_r + R_l}. \tag{2.31}$$

Matching the antenna to the source or the guiding line is very important to achieve maximum power transfer. In some cases, the antenna receives the electromagnetic wave efficiently, however, only a trivial amount of power reaches the receiver due to the poor matching between the antenna and the subsequent circuitry. Maximum power transfer happens when the complex conjugate matching is achieved by making $Z_o = Z_a^*$.

2.2.2 Reciprocity theorem

Antennas are devices used to either transmit or collect electromagnetic waves in many applications. There is a question that may arise here about the relation between the ability of antennas to transmit and their ability to receive electromagnetic waves. The answer can be found in the reciprocity theorem, which states the connection between the emitting and the collecting properties of antennas. The Lorentz reciprocity theorem shows that the radiation properties of an antenna are the same regardless whether it is used in transmitting or receiving mode. Assume that the sources $\mathbf{J}_1$ and $\mathbf{M}_1$ are producing the fields $\mathbf{E}_1$ and $\mathbf{H}_1$ and the sources $\mathbf{J}_2$ and $\mathbf{M}_2$ are producing the fields $\mathbf{E}_2$ and $\mathbf{H}_2$ as shown in Fig. 2.3 [14]. For an isotropic medium, the Lorentz reciprocity theorem states that

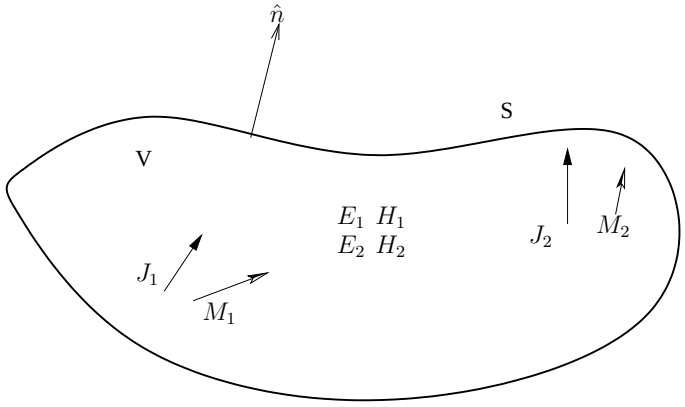

Figure 2.3: Sketch of Lorentz reciprocity theorem explaining the sources and their corresponding fields in two different media, s and v.

$$\iiint_{V_1} (\mathbf{E}_2 \cdot \mathbf{J}_1 - \mathbf{H}_2 \cdot \mathbf{M}_1)\, dV = \iiint_{V_2} (\mathbf{E}_1 \cdot \mathbf{J}_2 - \mathbf{H}_1 \cdot \mathbf{M}_2)\, dV \tag{2.32}$$

If the sources 1 and 2 are antennas excited with only current generators (i.e no magnetic sources), (2.32) will be reduced to

$$\iiint_{V_1} \mathbf{E}_2 \cdot \mathbf{J}_1 \quad dV = \iiint_{V_2} \mathbf{E}_1 \cdot \mathbf{J}_2 \quad dV \tag{2.33}$$

Equation (2.33) shows the interaction between the sources 1 and 2.

2.2.3 Near- and far-fields

In some applications we need to measure the electromagnetic fields in close proximity to the antenna such as in sensing and imaging applications. In contrast, there are applications that need the value of the fields far away from the antenna such as scattering and radar cross section applications. Thus, this subsection will focus on the electromagnetic radiation of antennas in near- and far-fields.

Let's begin with Fig. 2.4 (a), where the observation point is close to the radiating antenna. The magnetic field generated by an electric current can be given from the equation of the magnetic vector potential as follows [12]

$$\mathbf{H}(\mathbf{r}) = \frac{1}{\mu}\nabla \times \mathbf{A}(\mathbf{r}) = \nabla \times \iiint_V \mathbf{J}(\mathbf{r}')\frac{e^{-jkr}}{4\pi r} \quad d\mathbf{r}', \tag{2.34}$$

where $r = |\mathbf{r} - \mathbf{r}'|$.

Using the vector identity and some simplifying steps, (2.34) can be written as [15]

$$\mathbf{H}(\mathbf{r}) = -\iiint_V [(\mathbf{r} - \mathbf{r}') \times \mathbf{J}(\mathbf{r}')]\frac{1 + jkr}{4\pi r^3} \quad d\mathbf{r}'. \tag{2.35}$$

The above can be expanded into the rectangular components as follows

$$H_x(\mathbf{r}) = \iiint_V [(z - z')J_y - (y - y')J_z]\frac{1 + jkr}{4\pi r^3} \quad dx'\,dy'\,dz', \tag{2.36}$$

$$H_y(\mathbf{r}) = \iiint_V [(x - x')J_z - (z - z')J_x]\frac{1 + jkr}{4\pi r^3} \quad dx'\,dy'\,dz', \tag{2.37}$$

$$H_z(\mathbf{r}) = \iiint_V [(y - y')J_x - (x - x')J_y]\frac{1 + jkr}{4\pi r^3} \quad dx'\,dy'\,dz'. \tag{2.38}$$

Using Maxwell's equations, the electric field components can be given as

$$E_x(\mathbf{r}) = \iiint_V [C_1 J_x - C_2(x - x')C_3]e^{-jkr} \quad dx'\,dy'\,dz', \tag{2.39}$$

$$E_y(\mathbf{r}) = \iiint_V [C_1 J_y - C_2(y - y')C_3]e^{-jkr} \quad dx'\,dy'\,dz', \tag{2.40}$$

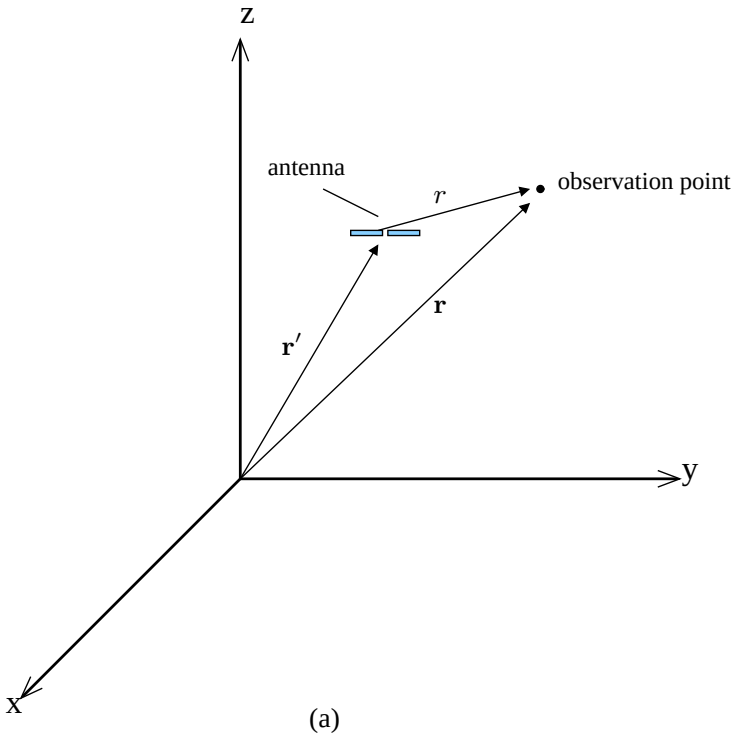

(a)

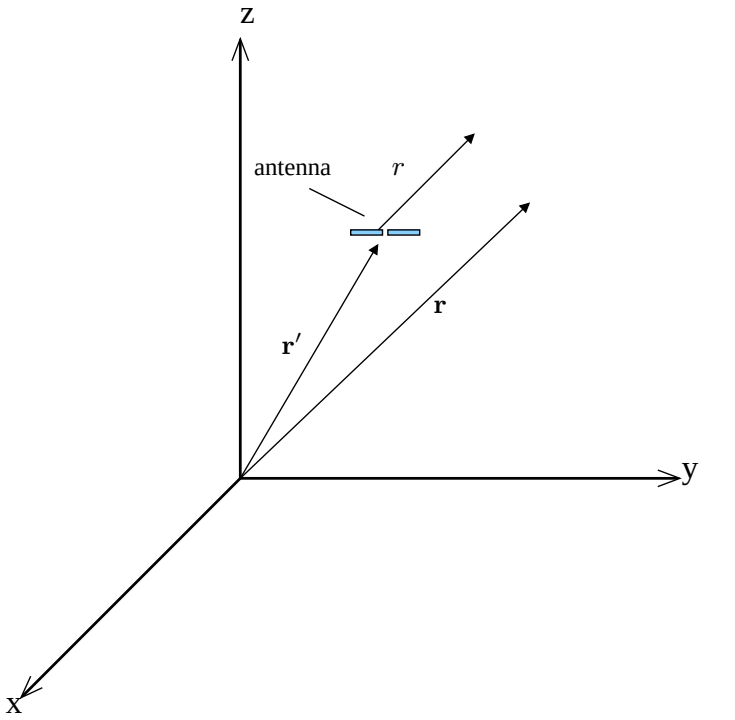

(b)

Figure 2.4: Antenna zones: (a) near-field zone, (b) far-field zone.

$$E_z(\mathbf{r}) = \iiint_V [C_1 J_z - C_2(z - z')C_3]e^{-jkr} \quad dx'\, dy'\, dz', \tag{2.41}$$

where

$$C_1 = \frac{-1 - jkr + k^2r^2}{4\pi r^3}, \tag{2.42}$$

and

$$C_2 = (x - x')J_x + (y - y')J_y + (z - z')J_z, \tag{2.43}$$

and

$$C_3 = \frac{3 + 3jkr - k^2r^2}{4\pi r^5}. \tag{2.44}$$

Equations (2.36)-(2.41) are used to calculate the electromagnetic fields at any point close to a radiating antenna. For an observation point far away from the radiating antenna, the vectors $\mathbf{r}$ and $\mathbf{r} - \mathbf{r}'$ will be approximately parallel as shown in Fig. 2.4 (b). The electric field at the far-field zone for this case can be written as

$$\mathbf{E}(\mathbf{r}) = -j\frac{e^{-jkr}\omega\mu}{4\pi r} \iiint_V \mathbf{J}(\mathbf{r}')e^{-jk\mathbf{r}'.\hat{\mathbf{r}}} \quad d\mathbf{r}'. \tag{2.45}$$

2.3 Nanoantennas: From RF to Optical Frequencies

The propagation of light is usually controlled using mirrors, lenses or diffraction elements. However, these techniques are not able to confine the light in an area smaller than half-wavelength due to diffraction limit. For visible light, the wavelength lies between about 390 to 700 nm, which makes the diffraction limit roughly between 180 to 350 nm. This scale is too far from the interest of current nanotechnologies. In contrast, RF antennas can control the electromagnetic waves in sub-wavelength scale efficiently. The need for localising and confining the light beyond the diffraction limit and to control optical fields at nanometre scale has led to the emergence of nanoantennas. The advances in nanotechnology and nanoscience provided a great opportunity to fabricate and develop nanoantennas in the scale below 100 nm using nanofabrication tools such as E-beam lithography and focused ion beam milling [16] [17]. In order for nanoantennas to interact efficiently with light, their dimensions need to be in the order of the wavelength of incident light wave.

The interaction of light with matter has found many applications in optical regime as demonstrated in Fig. 2.5. In photovoltaics, the energy of incident photons separates the electron-hole pair producing charges in the material. An opposite process occurs in light emitting elements, in which the electrons and holes pair together to emit photons.

Nanoantennas play a key role in both cases by transferring the energy between the external fields and the feed gap. In spectroscopy, when the incident light hits the material of interest, it will be polarised and will emit a radiation with a different wavelength. The material will therefore be chemically identified based on the generated wavelength. These examples have been presented to introduce the concept of nanoantennas in optical application, however, many other applications can be linked to nanoantennas in the optical regime such as microscopy, THz radiation detection, biological sensing and many others.

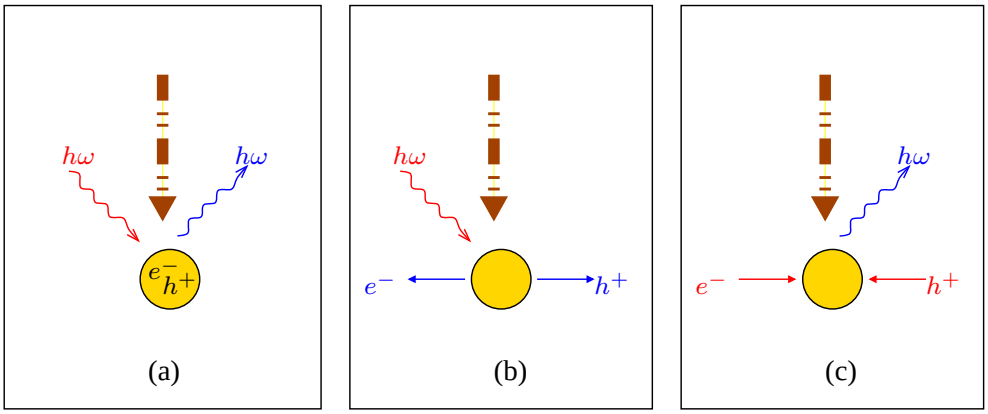

Figure 2.5: Applications of the light-matter interaction: (a) spectroscopy, (b) photovoltaics, (c) light emitting.

The advances of modern scanning probe microscopy have encouraged the invention of nanoantennas, where a nanoantenna is used as an alternative to conventional lens for focusing laser beam into a nanometre scale area effectively. However, the idea of using nanoantennas as a light source in microscopy is dated back to 1928 when Edward Hutchinson Synge and Albert Einstein exchanged letters about using the scattered field from a tiny particle as a light source [18]. In 1985, John Wessel mentioned that a particle can receive and radiate electromagnetic waves, which made him the first to link the behaviour of nano-particles to classical antenna performance [19]. After a few years, in 1989 in particular, Ulrich Fischer and Dieter Pohl carried out Synge's idea experimentally, where they used gold-coated particle to produce light [20]. Since then, research on nanoantennas has been increased dramatically in developing the nanoantenna applications, modelling and simulating the surface plasmon effect in nanoantennas and nanoantenna fabrication.

The invention of point-contact diodes has also contributed to the development of nanoantenna especially in the field of THz detection and mixing [21]. Fig. 2.6 illustrates several examples of fabricated nanoantennas.

Having presented a brief introduction of nanoantennas, we can summarise that a

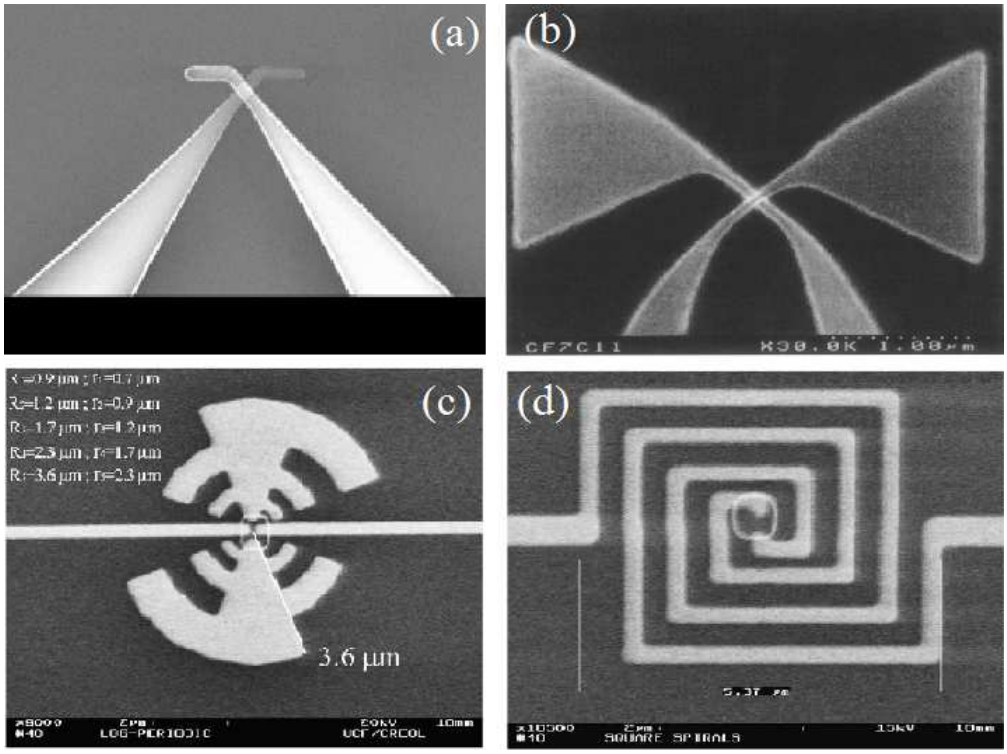

Figure 2.6: Fabricated IR nanoantennas: (a) dipole nanoantenna, (b) bowtie nanoantenna, (c) log-periodic nanoantenna and (d) spiral nanoantenna.

nanoantenna is ”a device designed to efficiently convert free-propagating optical radiation to localized energy, and vice versa.” as defined by Bharadwaj *et al* [16].

2.3.1 Physical properties of nanonatennas

RF engineers can choose different shapes of antennas for a single application due to the high radiation efficiency of RF antennas. The reason behind this high efficiency is the fact that metals are considered as perfect conductors (i.e lossless) at these frequencies. The designers will have no concerns about the radiation efficiency while their focus will be on the radiation pattern, size, bandwidth ,.. etc. The difference will appear when we move up to THz frequencies (shorter wavelengths), where the losses will increase, thus affecting the radiation efficiency. In RF antennas, the losses in matching networks are trivial. Hence, the radiation efficiency with and without the matching network is almost the same. However, the matching techniques will be a real problem at optical frequencies, where matching circuits and stubs will be accompanied with higher losses that reduce the overall efficiency of the antenna system. The performance of nanoantennas depends strongly on the material and the shape. They can take unusual shapes that do not exist in conventional RF antennas, where the tips and the particles play a critical role in shaping

the properties of nanoantennas due to the surface plasmon resonances. All these issues need to be paid more attention when designing nanoantennas since metals are no longer perfect conductors at these short wavelengths.

The behaviour of metals at optical frequencies is fully controlled by their frequency-dependent dielectric properties, $\varepsilon(\omega) = \varepsilon'(\omega) + i\varepsilon''(\omega)$. The imaginary part, $\varepsilon''(\omega)$, is responsible for the Ohmic losses, hence, this part needs to be as small as possible in order to achieve acceptable performance. Alternatively, we can keep Ohmic losses low by choosing a metal with negative and large real part (i.e $\varepsilon'(\omega)$).

2.3.2 Skin depth and dimension scaling

Skin depth is the distance that the fields can penetrate into the skin of metals. Its value is negligible compared to the dimensions of antennas at radio frequencies due to the high conductivity of metals at these frequencies. However, at THz frequencies (i.e optical frequencies) an ultrafast response is needed by electrons, which is not achievable. This makes the skin depth of the order of tens of nanometres, which is high compared to the dimension of nanoantenna (typically larger than the antenna diameter). The design parameters in conventional RF antennas depend heavily on the wavelength, λ, of incident wave. Hence, the length of dipole in Yagi-Uda antenna can be easily set to $\lambda/2$ while the other distances between its elements will be proportional to λ. In addition, the antenna can be easily scaled from one frequency to another due to the dependence of dimensions on λ. However, this is no longer valid in optical regime due to the effect of skin depth, which is larger in optical frequencies, where the electrons in metal respond to the effective wavelength, λ_{eff}, instead of λ. The effective wavelength can be simply calculated as [22]

$$\lambda_{eff} = n_1 + \frac{n_2 \lambda}{\lambda_p}, \tag{2.46}$$

where n_1 and n_2 are constants related to antenna geometry, and λ_p is the palsma wavelength of metal. According to (2.46), the length of a half-wave nanoantenna will be $\lambda_{eff}/2$ instead of $\lambda/2$ which is shorter, as the difference between λ and λ_{eff} is within 2-5 for most metals.

So far, we realised two facts that describe the difference between nanoantennas and RF antennas, which are (i) nanoantennas are characterised by large Ohmic losses and significant skin depth and (ii) the wavelength in the metal of nanoantenna is shorter than that of free-space.

2.3.3 Surface plasmon resonance

There are various differences in radiation mechanism between nanoantennas and conventional RF antennas. One of them is the ability of nanoantennas to confine the fields in the feed gap, tips and around the structure, and furthermore, these fields decay when we move away from the structure. The strength of these confined fields depends on the shape, material and dielectric background of nanoantenna. The concentration of local fields in nanoantennas occurs due to the surface plasmon resonance or what so called localised surface plasmon resonance (LSPR). Surface plasmons are highly confined fields made by electrons oscillation at the metal/dielectric interface in nanoantennas. When a metallic nano-particle is illuminated by light (non-propagating excitation), surface plasmons will be coupled with the photons of incident light. This coupling results in charge oscillation in the visible and infrared regimes depending on the metal used. For noble metals, surface plasmon resonance occurs in visible or ultraviolet regions of electromagnetic spectrum. The field confinement leads to a strong near field enhancement, which is very important and can be exploited in many optical applications. Fig. 2.7(a) illustrates a nano-particle under excitation by EM wave, where the electrons are moving with respect to the positive background [23]. The incident light will shift the free conduction electrons and make them resonate in phase with the applied external field, which can be modelled as a dipole moment. At time t_1, the positive and negative charges will be moved collectively to both sides of the particle. While at time t_2, the charges will accumulate at the opposite direction. This behaviour may be approximated by the mass-and-spring model for simplicity as shown in Fig. 2.7(b).

2.3.4 Input impedance, matching and loading of nanoantennas

In the previous subsection we discussed theoretical concepts of nanoantennas such as the skin depth and the plasmonic resonance to show the difference between nanoantennas and RF antennas. The goal of this section is to demonstrate the important considerations in designing nanoantennas. The current density at the gap of a nano-dipole can be written as

$$\mathbf{J}_{dip} = j\omega\varepsilon\mathbf{E}_g, \tag{2.47}$$

where $\mathbf{E}_g$ is the confined field at the feed gap. A current, $I_{dip} = |\mathbf{J}_{dip}|S$, will flow towards the gap, where S is the cross-section area of the dipole [24]. The voltage across the

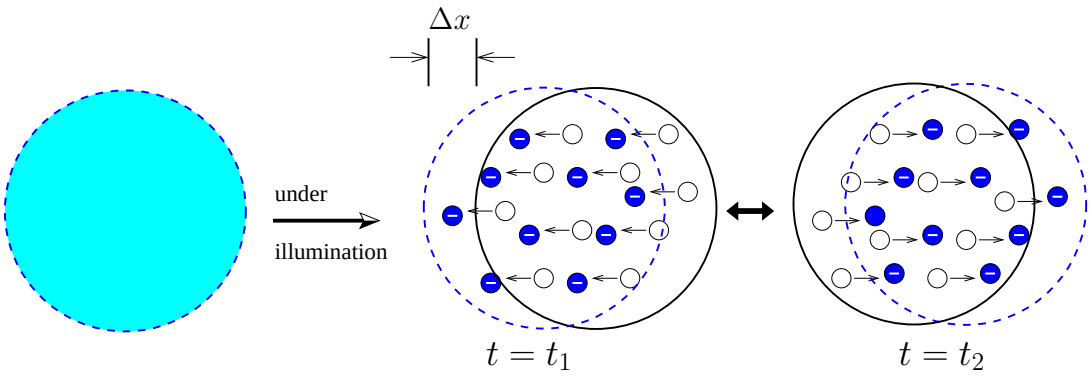

(a)

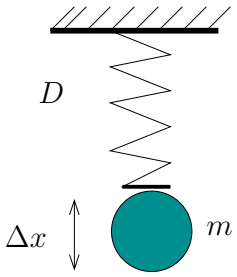

(b)

Figure 2.7: Surface plasmon in a nano-particle. (a) the electrons are moving with respect to the positive background, (b)The oscillation can be modelled using the mass-and-spring model, where D is the effective spring constant and m is the effective mass of the electrons.

gap is proportional to the gap size, g, and can be calculated using the magnitude of the concentrated electric field, where

$$V_g = |\mathbf{E}_g| * g. \tag{2.48}$$

Regardless the antenna operating mode, the nanoantenna input impedance, Z_{in}, can be defined as

$$Z_{in} = \frac{V_g}{I_{dip}}. \tag{2.49}$$

It can be seen that this approach in calculating the input impedance of nanoantennas is similar to RF antennas, where a voltage source can be applied in the gap and the induced current can be calculated numerically.

It is worth mentioning that the size of the feed gap in nanoantennas plays an important

role in determining the total input impedance. The gap is non-negligible as the case of RF antennas and can be represented by a capacitance, C_g, which can be given as

$$C_g = \varepsilon_0 \frac{r^2}{g}\pi, \tag{2.50}$$

where r is the radius of the antenna arms.

It is generally accepted that perfect matching between the antenna and the transmission line or source is required to ensure maximum power transfer and to exploit the large field enhancement provided in the feed gap. For complex impedances, a complex conjugated matching is needed for this purpose. If a nano-device or particle is inserted in the feed gap of a nanoantenna the input impedance will be changed, and hence, the resonant frequency will be tuned. For an antenna of input impedance Z_a and a load of impedance Z_l, a perfect matching can be obtained when $Z_l = Z_a^*$. The effect of load impedance on the input impedance and the resonant frequency is studied and discussed in Chapter 6 of this thesis.

In some cases the nanoantenna is loaded with a non-linear load such as the case of rectennas. This non-linearity should be taken into account as the load impedance, Z_l, varies with the magnitude of incident field, E_{inc}. The non-linear impedance of a nanodisk with radius, r, placed in the feed gap of a nanoantenna can be given by [25]

$$Z_l = \frac{t}{j\omega\pi r^2 \varepsilon_l |E_{inc}|}, \tag{2.51}$$

where t is the thickness of the disk, ε_l is the dielectric constant of the load and $|E_{inc}|$ is the amplitude of the field at the feed gap.

2.4 Chapter Summary

This chapter discussed the theoretical concepts related to electromagetics and classical antennas. The aim of this chapter was to cover and provide the necessary background information in order to understand the work in this thesis. The first part of this chapter has been dedicated to the theories of boundary conditions and wave equations and their derivation from Maxwell's equations. In the second part, the classical antenna theory was presented with a brief explanation of the radiation mechanism, reciprocity theorem and near- and far-field zones around the antenna. The main part of this chapter is the third part, where it highlights the major differences between RF antennas and nanoantennas

and describes the changes that take effect when we go up in frequencies. Furthermore, the chapter includes a historical overview on nanoantennas and their types and applications. Finally, a detailed description on surface plasmon resonance and the design considerations have also been presented.

Chapter 3

Numerical Electromagnetics

This chapter focuses on different numerical methods used to solve various electromagnetic problems starting with Maxwell's equations. The first part of the chapter provides a general introduction into the key methodologies behind numerical methods. These include the key steps in solving any boundary-value problem. Some of the popular basis function that have been used in computational methods are discussed in this chapter. Additionally, a formula is presented to test the convergence of the numerical solution. Furthermore, the chapter highlights the sources of error that affect the solution stability and accuracy. The second half includes a brief description on the most commonly used numerical methods such as method of moments (MoM), finite element method (FEM), finite difference time domain (FDTD) which are provided by textbooks.

Nowadays, there have been numerous commercial full-wave software packages used to simulate the properties of nanoantennas in the THz range. These may include COMSOL Multiphysics based on FEM [26] [27] , XFDTD or MODE based on FDTD, and CST Microwave Studio based on finite integration technique (FIT) [28] [29]. In some cases, the nanoantenna designer prefers to write his own code implementing one of the numerical methods to solve different problems related to nanoantennas. For example, MoM has been used to calculate the efficiency of nanoantennas for different metals [30]; whereas the boundary element method (BEM) is used to simulate the interaction of the incident electromagnetic wave with silver circular nanostructures [31]. Another example is the use of FDTD to simulate plasmonic wire antennas for optical microscopy [32].

3.1 Introduction to Numerical Methods in Electromagnetics

It is important to analyse the design theoretically before the fabrication process. This analysis will reduce the cost of fabricating multiple prototypes before achieving the desired characteristics. In addition, the theoretical analysis provides the designer a close physical insight on the operating principle of the design and helps in optimising it by implementing parametric studies.

The theoretical analysis can be classified into the following methods [33]:

- **Analytical methods:** this may include the method of variables separation, Green's function, Fourier transform and Perturbation methods. These methods depend on closed-form equations, which make them accurate, however, the disadvantage of

these methods is the fact that their use is restricted to regular geometries and homogeneous media.

- **Model methods:** such as the widely used transmission line and cavity models. These methods provide in-depth understanding on how the system works by simplifying the problem using district assumptions.

- **Numerical (computational) methods:** These include MoM, FEM, and FDTD numerical methods. They represent the most popular solution for complex electromagnetic problems. The availability of commercial software based on these numerical techniques made them easer and versatile. These methods are accurate but expensive due to the high computational resources required (i.e high computational complexity).

- **Computational intelligence methods:** these methods can be used for optimisation based on data from computational methods, and include the Neural Network and the Fuzzy techniques.

Most of the theoretical analysis techniques use different approaches to solve Maxwell's equation by adopting either the integral or differential forms, which are called *governing equations*. The aim of solving the governing equation is to find the unknown fields, the current distribution or the charge density on the surface of a given structure at a specific frequency range. This is accomplished by imposing appropriate boundary conditions. In the early stage of the electromagnetic theory, the analytical methods were used to solve most of the problems by hand without the use of computers. However, one needs to have a basic understanding and knowledge of vectors, orthogonal functions, image theory, and reciprocity in order to be able to solve very basic problems. With the development and the rapid advances in computers, a new tendency has emerged towards the use of the numerical methods, which need basic knowledge of computer programming. Classical analytical methods fail to solve the problems if [34]:

- the structure to be simulated is complex,

- the boundary conditions are time-varying,

- the solution region is anisotropic or inhomogeneous,

- the differential equations are not linear.

Numerical solutions need to be employed when one of the problems above exists. The main approach in numerical methods is to expand the unknown function into a series of basis functions, which is accomplished by dividing the structure into segments or elements referred to as *discretisation* (meshing) process. With the discretisation process, the governing equation will be solved at each element of the device individually. This will overcome the problem of dielectric inhomogeneity and will help the solution method to be applied to arbitrary shapes.

The solution of boundary value problems is based on solving the operator equation

$$F(g) = h, \tag{3.1}$$

where F is an operator (integral, differential, integro-differential), g represents the unknown function and h is the known excitation. The aim is to find the unknown function g when F and h are known. This can be achieved by subdividing the structure and expanding g into series of basis functions. This leads to expressing equation (3.1) in the form of matrix equation as follows

$$[Z][I] = [V], \tag{3.2}$$

where $[Z]$ is a matrix corresponds to F, and $[I]$ and $[V]$ are vectors correspond to the unknown coefficients and the excitation function, respectively.

The values of the unknown coefficients of $[I]$ depend on several factors, such as the geometrical shape, dielectric, boundary conditions, and operating frequency. The differences between various numerical methods of analysis come from the choice of the basis functions and the methods of finding the coefficients.

3.2 Key Elements of Numerical Analysis

There are several factors that should be taken into account when using any numerical analysis for solving different electromagnetic problems. These include the governing equation, meshing and the matrix solver. All numerical methods that are used for solving electromagnetic or microwave problems begin with Maxwell's equations to reach the governing equation. The form of finite difference in space and time is used to express Maxwell's equations in the FDTD method, whereas the wave equation is employed in the FEM method. In MoM method, the integral form of the wave equation is employed.

Meshing or discretisation of the structure is the key difference between the analytical

solutions and numerical analysis. This process enables the user to analyse arbitrary shapes and overcomes the problem of dielectric inhomogeneity, where the governing equation can be solved at every single element or cell individually. The whole simulation domain is divided into a large number of small non-overlapped elements such that the material is homogeneous within the element. The elements shape could be triangular, rectangular or quadrilateral, or a combination of all these types in one structure taking into consideration the position of the element (such as the edges between metal and dielectric). Fig. 3.1 illustrates different element shapes used in the discretisation of a U-shaped geometry. The accuracy of the solution depends primarily on the number of elements (mesh size), where it is generally accepted that the finer the meshing , the better the accuracy achieved [35]. In case of simulating nanoantennas, when computing the localised field in the feed gap, a finer mesh is required in this area to obtain an accurate solution.

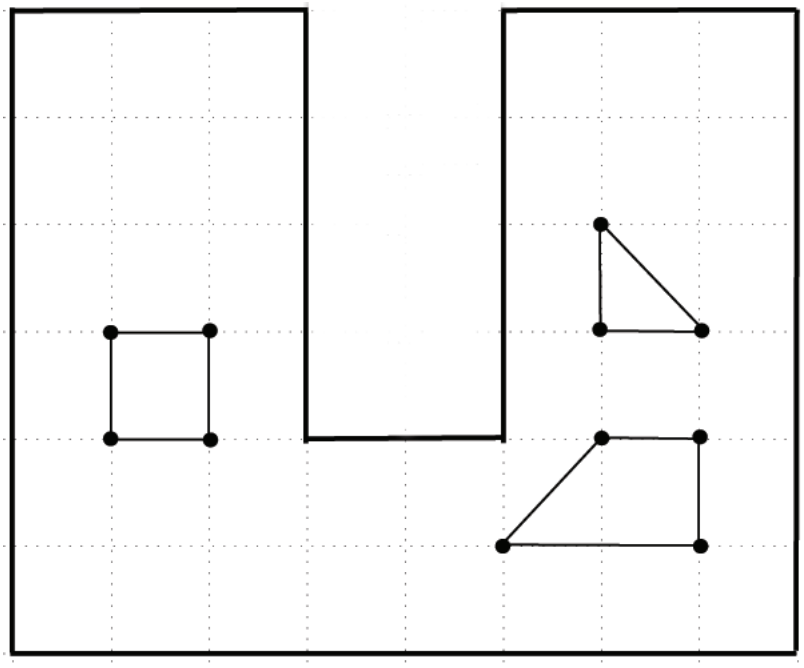

Figure 3.1: Meshing a U-shaped geometry into a number of elements with different shapes.

After subdividing the geometry, a system of linear equations will be generated in the matrix form as described in (3.2). The size of the matrix $[Z]$ is $N \times N$, where N is the number of the unknown coefficients. Due to the large number of elements produced by meshing, efficient algorithms are required to solve the matrices such as the L-U factorisation or using iterative solvers to reduce the processing time. Postprocessing the data resulted from solving the matrices represents the final step in simulating any electromagnetic problem. The solution of the system matrix can be processed to find the other char-

acteristics of the device such as the S-parameters, surface current distribution, impedance and far-fields.

3.3 Basis Functions

The choice of the appropriate basis functions is one important step in solving any electromagnetic problem numerically. The choice should be based on the ability of the basis functions to represent the unknown distribution accurately. There are a large variety of basis functions used in numerical analysis which can be classified into the subdomain basis functions and the entire domain basis functions.

The subdomain functions have a non-zero value over only a limited part of the domain. On the other hand, the entire domain functions are defined over the whole domain of the unknown function. In this work, the focus will be on the first class (i.e the subdomain basis functions) as they are widely used in computational electromagnetics.

The subdomain basis functions exist over subinterval in one or two elements of the simulation domain and their value is zero elsewhere. In following subsections, we will discuss three types of subdomain basis functions in details.

3.3.1 Pulse function

Pulse functions are the most popular choice among the other types of basis functions due to their simplicity as they are constant over the entire subinterval. For better understanding of this type, let us assume a piece of wire of length L is divided into N segments each of width $D_x = \frac{L}{N}$ as shown in Fig. 3.2. The unknown function g in (3.1) will therefore be expanded into a series of N terms as follows

$$g(x') = \sum_{n=1}^{N} a_n G_n(x'), \qquad n = 1, 2, \cdots, N \tag{3.3}$$

where $G_n(x')$ is piecewise constant function that can be defined as

$$G_n(x') = \begin{cases} 1 & \text{if} \quad x_{n-1} \leq x' \leq x_n \\ \\ 0 & \text{elsewhere} \end{cases} \tag{3.4}$$

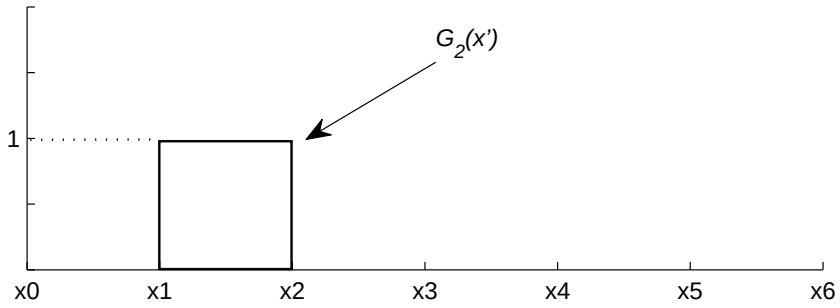

(a)

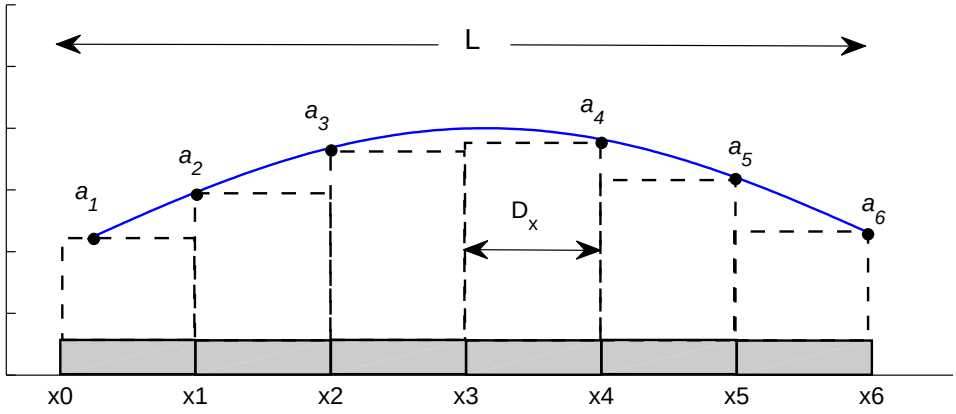

(b)

Figure 3.2: The pulse basis function: (a) Single; (b) Representing the unknown function by pulse function.

3.3.2 Triangular function

The triangular function is another basis set commonly used in numerical analysis. This function can be defined as

$$G_n(x') = \begin{cases} \frac{x'-x_{n-1}}{D_x} & \text{if} \quad x_{n-1} \leq x' \leq x_n \\ \frac{x_{n+1}-x'}{D_x} & \text{if} \quad x_n \leq x' \leq x_{n+1} \\ 0 & \text{elsewhere} \end{cases} \tag{3.5}$$

Fig. 3.3 shows the representation of unknown distribution by a set of triangular functions. It can be seen that the triangular function covers two cells of the discretised structure and overlaps with adjacent function, which results in smoother representation compared with the pulse function. However, the computational complexity will be increased with this type of functions.

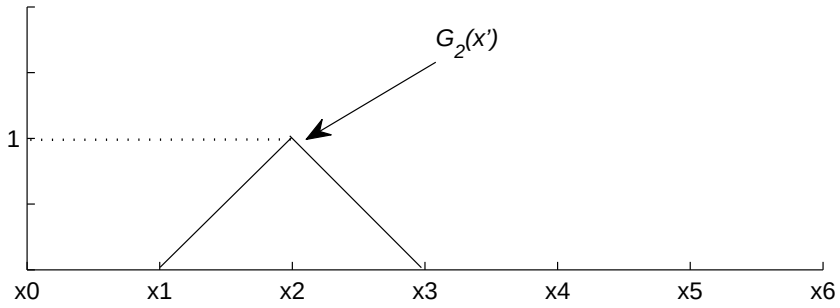

(a)

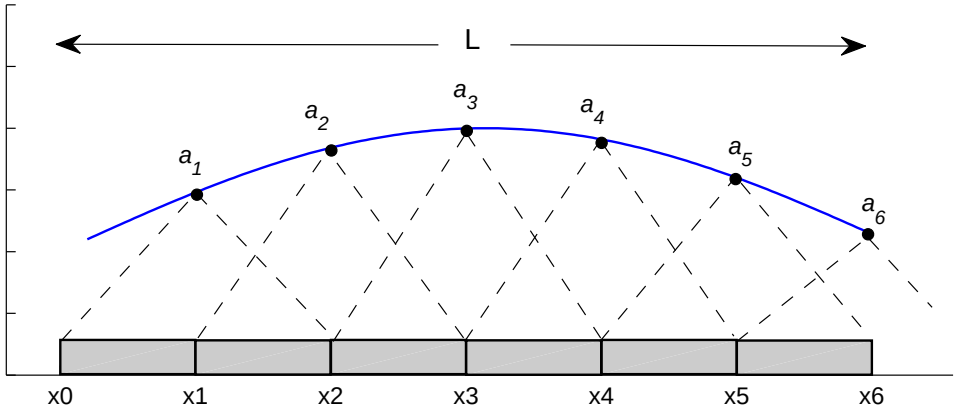

(b)

Figure 3.3: The triangular basis function: (a) Single; (b) Representing the unknown function by triangular function.

3.3.3 Sinusoidal function

Often, the integrands of the integral operations are multiplied by $\sin(\beta x')$ or $\cos(\beta x')$. In such cases, the integrations can be evaluated without numerical integrations, where sinusoidal functions may be used to represent the unknown function [12]. This will reduce the errors and the computational time. The sinusoidal basis function is shown in Fig. 3.4 and can be defined as

$$G_n(x') = \begin{cases} \frac{\sin[\beta(x'-x_{n-1})]}{\sin[\beta(x_n-x_{n-1})]} & \text{if} \quad x_{n-1} \leq x' \leq x_n \\ \frac{\sin[\beta(x_{n+1}-x')]}{\sin[\beta(x_{n+1}-x_n)]} & \text{if} \quad x_n \leq x' \leq x_{n+1} \\ 0 & \text{elsewhere} \end{cases} \tag{3.6}$$

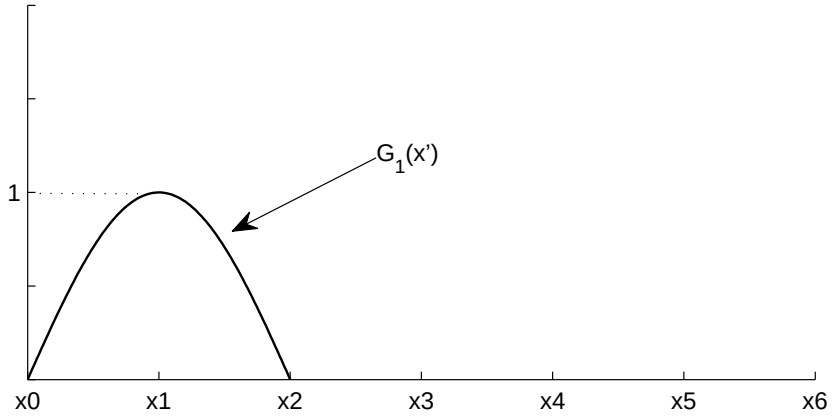

(a)

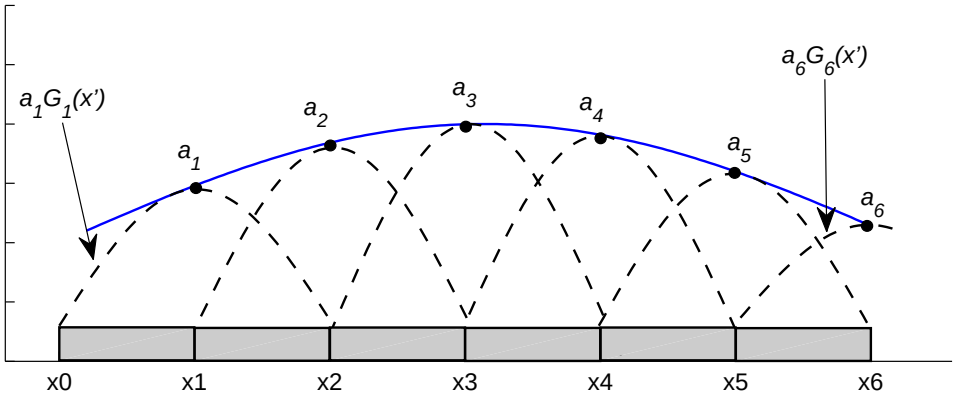

(b)

Figure 3.4: The sinusoidal basis function: (a) Single; (b) Representing the unknown function.

3.4 Convergence, Stability and Accuracy of Numerical Solutions

The user of numerical analysis methods should be aware of several issues related to the problem solution such as convergence, stability, and accuracy of the solution. The error in the solution can be easily found by comparing with the exact solution. However, in particular cases the distribution of the function is unknown, thus, the only way is to check the *convergence* of the approximate solution. The convergence is the difference between the computed and the exact values of a particular problem. It is evident that the convergence decreases when increasing the number of elements by meshing [33] [36].

The use of computational methods for solving an electromagnetic problem is similar

to the integration methods as they both discretise the unknown distribution. In some cases the integrand is singular, such as in the case of current distribution at the edges of a conductor. Thus, the solution might not converge in these cases. An efficient way to test the convergence is by using Richardson extrapolation [37].

Consider an unknown function $g(x)$ which has values of g_1, g_2 and g_3 corresponding to the divisions number of N_1, N_2 and N_3, respectively. The ratio, $\Re$, can be calculated to test the convergence behaviour of the solution as follows

$$\Re = \frac{c_2 g_2 - c_1 g_1}{c_3 g_3}, \tag{3.7}$$

where $c_1 = N_1^2(N_3^2 - N_2^2)$, $c_2 = N_2^2(N_3^2 - N_1^2)$ and $c_3 = N_3^2(N_2^2 - N_1^2)$.

For a converged solution, $\Re$ should be close to unity. It should be mentioned here that the solution convergence depends heavily on the nature of the function.

The second issue is the *stability* of numerical solutions. The stability can be defined as the unexpected divergence instead of convergence in the numerical solution when a finer mesh is made; or in other words it is the increase in error when the mesh size is decreased. The growth factor, Υ, of the error, e_{rr}, in the numerical solution gives an indication about the solution stability as follows

$$e_{rr}^{N+1} = \Upsilon e_{rr}^{N}, \tag{3.8}$$

where e_{rr}^{N} is the error corresponds to a mesh size of N and e_{rr}^{N+1} is the error associated with a smaller mesh size $N + 1$.

For unstable solution, Υ reads greater than 1. Hence, the error will be increased with decreasing the number of elements. The reason behind this behaviour is the large condition number of the matrix $[Z]$ of a system described by a matrix equation $[Z][I] = [V]$, where the very large condition number of a matrix indicates that it is ill conditioned.

The condition number of matrix $[Z]$ is given by the norm of the matrix as

$$\varsigma(Z) = \|Z\|\|Z^{-1}\|, \tag{3.9}$$

where $\|Z\|$ is the norm of the matrix $[Z]$ and can be written as

$$\|Z\| = \sqrt{\sum_{i=1}^{N}\sum_{j=1}^{N}|Z_{ij}|^2}. \tag{3.10}$$

The closer the condition number to 1, the better the stability of the solution. One can measure the sensitivity of the solution by making a small change $[\Delta V]$ in the matrix $[V]$ and notice the corresponding difference $[\Delta I]$ in the matrix $[I]$. This procedure will provide a good understanding about the role that the condition number plays in the solution stability. The matrix equation will become

$$[Z + \Delta Z][I + \Delta I] = [V + \Delta V]. \tag{3.11}$$

In this case, the change in $[V]$ or $[Z]$ will be amplified by the condition number. In other words, small changes in the algorithm of the system may result in a large impact in the final solution as given by the inequality concept below [37]

$$\frac{\|\Delta I\|}{\|I\|} \leq \varsigma(Z)\frac{\|\Delta Z\|}{\|Z\|}, \qquad \text{when } [\Delta V] = 0, \tag{3.12}$$

$$\frac{\|\Delta I\|}{\|I\|} \leq \varsigma(Z)\frac{\|\Delta V\|}{\|V\|}, \qquad \text{when } [\Delta Z] = 0. \tag{3.13}$$

Assume that $\varsigma(Z) = 10^4$ and V is used with relative error of 10^{-7} due to using short precision computer arithmetic, then the solution I will have an error of 10^{-3}. This will reduce the solution accuracy dramatically. The *accuracy*, therefore, is the measure of the difference between the final approximated solution and the exact solution. The error in the solution may arise from several sources such modelling errors, truncation errors and round-off errors [33].

Modelling error: This type of errors come from the approximated assumptions which are used to simplify the algorithms. Finer meshing can contribute in reducing such errors.

Truncation error: Truncation errors occur due to truncating infinite series into finite number of terms. This can be overcome by using large number of terms.

Round-off error: The round-off errors are related to the inadequate numerical precision in computer arithmetic unit. This type of errors can be reduced by using long or double precision, where the round-off error in MATLAB is 10^{-16} when double precision is used. Although this error is minor, increasing the number of mathematical operations will increase the round-off error.

High accuracy solution can be achieved by increasing the size of vectors and matrices. However, the relation between the accuracy of the solution and the available computer resources needs to be fully considered when using computational methods.

3.5 Method of Moments

The MoM is widely used for solving linear partial differential equations by formulating them as integral equations. The basic approach of MoM is to expand the unknown distribution into a series of known functions with unknown coefficients. The complex integral equation can be converted to the general linear system of (3.14), which can be solved numerically to find the unknown coefficients of g.

$$F(g) = h. \tag{3.14}$$

Let us now expand g into a set of N weighted basis functions, this yields

$$g \approx \sum_{n=1}^{N} a_n g_n, \tag{3.15}$$

where a_n are unknown weighting coefficients.

The residual, R, will therefore be [15]

$$R = g - \sum_{n=1}^{N} a_n g_n. \tag{3.16}$$

According to (3.15) we will have one equation with N unknown coefficients. This equation is not sufficient to find the unknowns a_n. We therefore need N equations to solve the problem which can be accomplished by enforcing the boundary conditions at every segment of the structure. For the case of calculating the current distribution over a conducting wire, we can observe the scattered field from each segment including the segment from which the observation is made. We will have N linearly independent equations for this case and the solution can be found numerically using computer codes.

The solution can be improved by using weighting (testing) functions as inner products $\langle \omega, g \rangle$ that should satisfy the following conditions [12]:

$$\langle \omega, g \rangle = \langle g, \omega \rangle, \tag{3.17}$$

$$\langle xf + yg, \omega \rangle = x\langle f, \omega \rangle + y\langle g, \omega \rangle, \tag{3.18}$$

$$\langle g^*, g \rangle > 0, \qquad \text{if} \quad g \neq 0, \tag{3.19}$$

$$\langle g^*, g\rangle = 0, \qquad \text{if} \quad g = 0. \tag{3.20}$$

where x and y are scalars, and ω's are the weighting functions. An example of a typical inner product is

$$\langle \omega, g\rangle = \int\int_S \omega^*.g \quad dS. \tag{3.21}$$

After expanding the unknown distribution by using basis functions and after using the weighting function, equation (3.1) can be given as

$$\sum_{n=1}^{N} a_n \langle \omega_m, F(g_n)\rangle = \langle \omega_m, h\rangle. \qquad m = 1, 2, \cdots, N \tag{3.22}$$

It should be noted that if the Dirac delta function is used as testing function, the method will be called *point matching* or *collocation* method. On the other hand, if the same basis function is used as testing function the method is called *Galerkin's* method.

Let us take an example of a thin wire placed along the z-axis with a constant applied potential of V=1 V as shown in Fig. 3.5. The length of the wire is $l = 1$ m and its diameter is $a = 0.001$ m. The aim is to apply MoM in order to find the charge distribution along the wire length. The charge density ($\rho(z')$) for this case can be given as

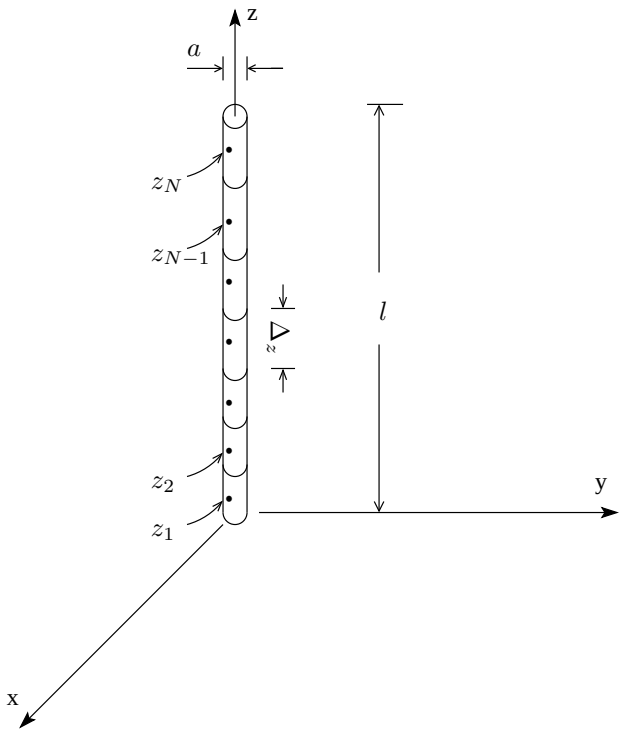

Figure 3.5: Segmentation of a straight wire with constant potential placed on z-axis.

$$\frac{1}{4\pi\varepsilon_0}\int_0^l \frac{\rho(z')}{R(z,z')}dz' = V, \tag{3.23}$$

where

$$R|_{x=y=0} = \sqrt{a^2 + (z-z')^2}. \tag{3.24}$$

It is clear from (3.23) and (3.24) that the observation is on z-axis. The integral equation of the charge density can be solved numerically using MoM for the unknown $\rho(z')$ and the known excitation source. The wire is discretised into N segments each of length $\Delta_z = \frac{l}{N}$ and the unknown charge density is expanded into a series of N terms of unknown coefficients as

$$\rho(z') = \sum_{n=1}^{N} a_n \rho_n(z'), \tag{3.25}$$

where $\rho_n(z')$ is a pulse basis function that has a constant value over the length of the segment and can be defined as

$$\rho_n(z') = \begin{cases} 0 & \text{if} \quad z' < (n-1)\Delta \\ 1 & \text{if} \quad (n-1)\Delta \leq z' \leq n\Delta \\ 0 & \text{if} \quad n\Delta < z'. \end{cases} \tag{3.26}$$

Thus, substituting (3.25) in (3.23) yields

$$\int_0^l \frac{1}{R(z,z')}\left[\sum_{n=1}^{N} a_n \rho_n(z')\right] dz' = 4\pi\varepsilon_0. \tag{3.27}$$

This will be simplified by taking the summation outside the integration and can be written as

$$\sum_{n=1}^{N} a_n \int_0^l \frac{\rho_n(z')}{\sqrt{a^2 + (z-z')^2}}dz' = 4\pi\varepsilon_0. \tag{3.28}$$

By expanding the summation and make the observation at fixed points, z, in the centre of each segment, equation (3.27) will be rearranged to be as

$$a_1 \int_0^{\Delta} \frac{\rho_1(z')}{\sqrt{a^2+(z_1-z')^2}} dz' + \cdots + a_N \int_{(N-1)\Delta}^{l} \frac{\rho_N(z')}{\sqrt{a^2+(z_1-z')^2}} dz' = 4\pi\varepsilon_0,$$

$$\vdots \qquad\qquad \vdots \qquad\qquad \vdots$$

$$a_1 \int_0^{\Delta} \frac{\rho_1(z')}{\sqrt{a^2+(z_N-z')^2}} dz' + \cdots + a_N \int_{(N-1)\Delta}^{l} \frac{\rho_N(z')}{\sqrt{a^2+(z_N-z')^2}} dz' = 4\pi\varepsilon_0. \tag{3.29}$$

Now, we have one equation for each segments with N unknowns. This can be written in matrix form as

$$[Z_{mn}][a_n] = [S_m], \tag{3.30}$$

where

$$Z_{mn} = \int_{(n-1)\Delta}^{n\Delta} \frac{\rho_n(z')}{\sqrt{a^2+(z_m-z')^2}} dz', \tag{3.31}$$

and

$$a_n = \begin{bmatrix} a_1 \\ a_2 \\ \vdots \\ a_N \end{bmatrix}, \tag{3.32}$$

$$S_m = \begin{bmatrix} 4\pi\varepsilon_0 \\ 4\pi\varepsilon_0 \\ \vdots \\ 4\pi\varepsilon_0 \end{bmatrix}. \tag{3.33}$$

Since the potential is fixed along the wire, all the values of $[S_m]$ equal to $(4\pi\varepsilon_0)$. A Matlab code is used to solve (3.30) and find the charge distribution over the thin wire. The unknowns a_n have been calculated by the inverting the matrix $[Z_{mn}]$ as

$$[a_n] = [Z_{mn}]^{-1}[S_m]. \tag{3.34}$$

The values of a_n are shown in Table 3.1 for the 7-segment solution, whereas, Fig. 3.6 shows the charge distribution over a thin wire for the 7-segment and 21-segment solutions.

It can be clearly seen that increasing the number of segments will increase the accuracy of the solution.

Table 3.1: Calculated unknown coefficient of the charge distribution for 7-segment discretisation.

Coefficient	Value (pC/m)
a_1	8.98
a_2	8.14
a_3	7.93
a_4	7.87
a_5	7.93
a_6	8.14
a_7	8.98

3.6 Finite Element Method

The origin of the FEM dated back to 1940s when it was used for structural analysis. However, the first use for FEM in solving electromagnetic problems was in late 1960s [38]. FEM is one of the most powerful and efficient computational methods in solving irregular and complex geometries and inhomogeneous dielectric.

The finite element solution of any problem involves the following basic steps:

- meshing the solution domain into finite number of subdivisions or elements,
- deriving of the element matrix,
- assembling all elements matrices,
- finding the solution of the system matrix.

The element size need to be small enough to achieve an acceptable solution accuracy. Thus, it is recommended that the element size should be less than 1/10 of the wavelength. This will ensure that the field across the element can be easily approximated by using one of the expansion functions. Several cell shapes can be used in the discretisation process. It is not necessary to subdivide the structure by using identical cells or elements throughout the whole structure. Fig. 3.7 illustrates the meshing of a cylinder cross section by using triangular cell with different sizes. Each node has a unique number within the cell called the local number, where x_i^e refers to the location of the ith node in the eth

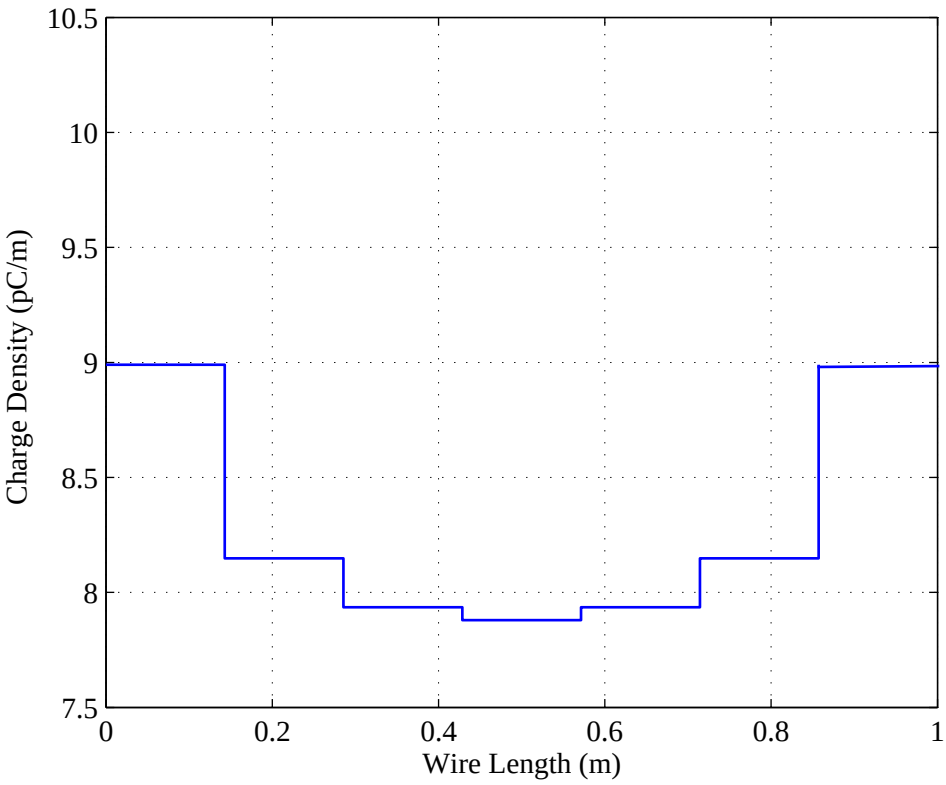

(a) 7 segments

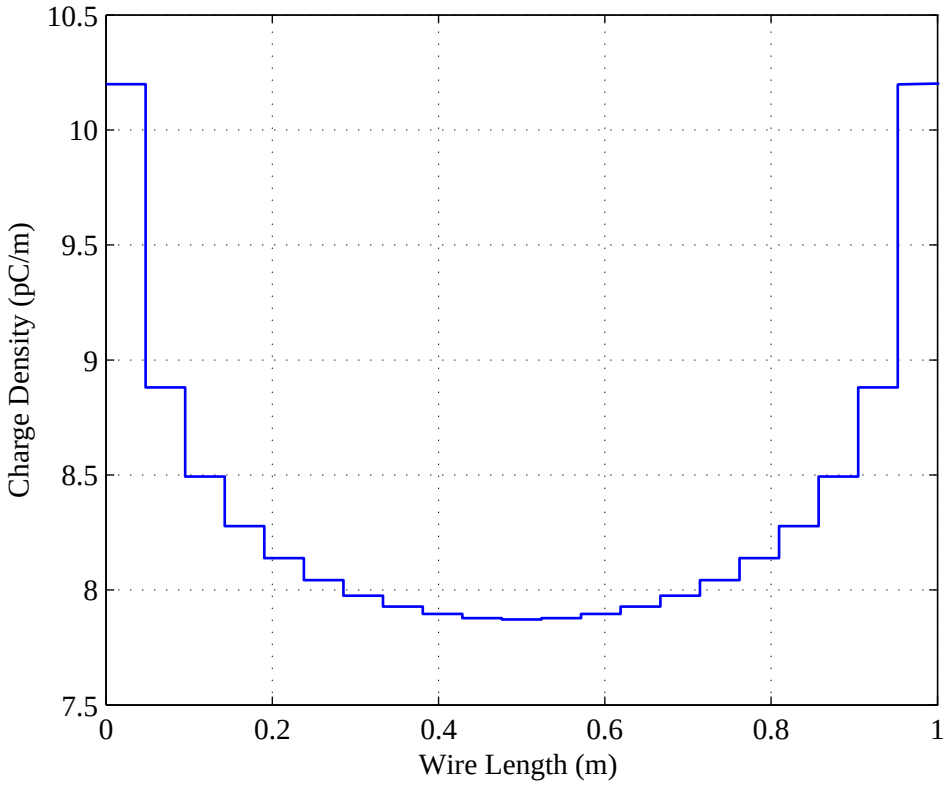

(b) 21 segments

Figure 3.6: Charge distribution over a thin wire.

element. In contrast, each node is assigned a number from 1 to N_e to represent the node in the whole domain which is so called the global number. The governing equation will be imposed over each element, and the element expansion functions will then be collected after applying the boundary conditions to form the matrix system equation. Solving the system equation leads to find the unknown coefficients which may represent the field at the nodes for *node-based* solution, or at the edges for *edge-based* solution.

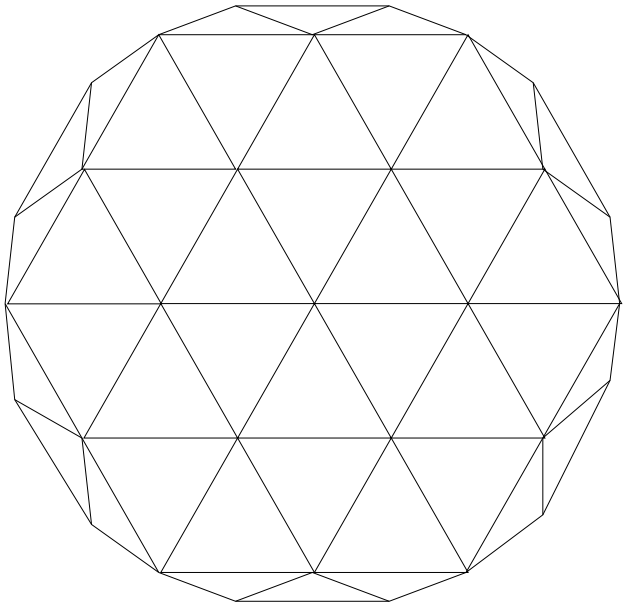

Figure 3.7: Discritisation of a cylinder cross section into 42 triangular cells which involves 31 nodes and 72 edges.

The element matrix equation for a two-node element can be represented by

$$[A_{ij}^e][U_j^e] = [b_i^e], \tag{3.35}$$

where U_j^e is the field at node i of the eth element and $[b_i^e]$ is the excitation vector. The entries of $[A_{ij}^e]$ depend on the governing equation and the boundary condition and can be given by

$$[A_{ij}^e] = \begin{bmatrix} A_{11}^e & A_{12}^e \\ A_{21}^e & A_{22}^e \end{bmatrix}. \tag{3.36}$$

In the following example, FEM will be applied to find the reflection coefficient, Γ_d, of a metal-backed dielectric slab when illuminated by a plane wave given by

$$E_z^i = e^{jk_0 x}. \tag{3.37}$$

The reflected field from this structure can be written as

$$E_z^{ref} = \Gamma_d e^{-jk_0 x}. \tag{3.38}$$

Assume that the dielectric slab shown in Fig. 3.8 has a thickness of $t = 0.3\lambda_0$, a dielectric constant $\varepsilon_r = 2 - j\beta$ and a permeability of $\mu_r = 1$. FEM will be employed to solve the differential form of the general wave equation [39]:

$$\frac{d^2 E_z}{dx^2} + k_0^2 \varepsilon_r E_z = 0. \tag{3.39}$$

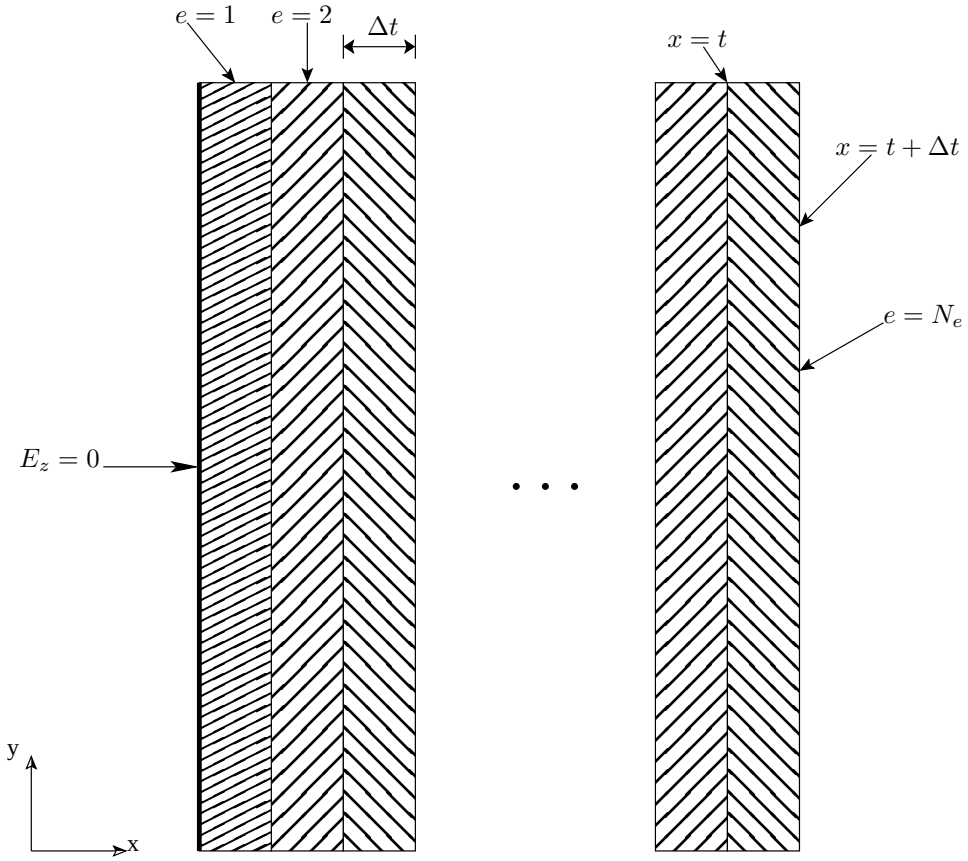

Figure 3.8: Subdividing the metal-backed dielectric slab into finite number of elements.

Using the following boundary conditions: $E_z(0) = 0$, and $\left(\frac{d^2 E_z}{dx^2} + jk_0^2 E_z\right)|_{x=x_a} = 2jk_0 e^{jk_0 x_a}$

The computed reflection coefficient, Γ_d^{FEM}, will then be compared with the exact value,Γ_d^{exact}, which can be given as

$$\Gamma_d = -\frac{Z_0 - jZ\tan(k_0\sqrt{\mu_r\varepsilon_r}t)}{Z_0 + jZ\tan(k_0\sqrt{\mu_r\varepsilon_r}t)}, \tag{3.40}$$

where $Z_0 = 120\pi$, and

$$Z = Z_0\sqrt{\frac{\mu_r}{\varepsilon_r}}. \tag{3.41}$$

The first step is to divide the geometry into N_e elements each of width Δt including one element representing the region $t < x < t + \Delta t$ which is air-filled region. The number of elements should be more than 10 elements per wavelength; or in other words, the element size should be less than $\lambda_d/10$, where λ_d is the wavelength in the dielectric. Based on 3.39, the entries of element equation will be [40]

$$A^e_{11} = A^e_{22} = \frac{1}{\Delta t} - \frac{k_0^2 \varepsilon_r \Delta t}{3}, \tag{3.42}$$

$$A^e_{12} = A^e_{21} = -\frac{1}{\Delta t} - \frac{k_0^2 \varepsilon_r \Delta t}{6}. \tag{3.43}$$

After forming an equation for each element, they will be assembled to obtain N_e equations. The entries of the first and last elements equation will be zero due to enforcing the boundary conditions, whereas, the equation of the other elements will be written in the form of

$$[0, 0, \cdots, A_{(m-1)m}, A_{mm}, A_{m(m+1)}, 0, \cdots, 0][U_z] = 0, \tag{3.44}$$

where $[U_z] = [U_{z1}, U_{z2}, U_{z3}, \cdots, U_{zN_e}]$ is the unknown coefficients of the node field, $A_{(m-1)m} = A^{m-1}_{21}$, $A_{mm} = A^m_{11} + A^{m-1}_{22}$ and $A_{m(m+1)} = A^m_{12}$. The excitation column will contain only one entry that is $b_{12} = 2k_0 e^{jk_0(t+\Delta t)}$.

After solving the assembled system, the reflection coefficient will be given as

$$\Gamma_d^{FEM} = \frac{U_{z11} - E^i_z(t + \Delta t)}{E^i_z(t + \Delta t)}. \tag{3.45}$$

Fig. 3.9 show the variation of Γ_d^{FEM} against the loss factor β for different number of elements and compared with the exact solution Γ_d^{exact}.

3.7 Finite Difference Time Domain Method

FDTD is one of the finite difference methods that approximate derivatives with finite differences. The FDTD method is a time domain implementation of Maxwell's curl equations firstly proposed by Yee in 1966 and is widely used for solving dynamic electromagnetic problems [35].

The solution procedure of finite difference methods involves subdividing the solution region into grids and nodes, approximating the derivatives of the differential equations

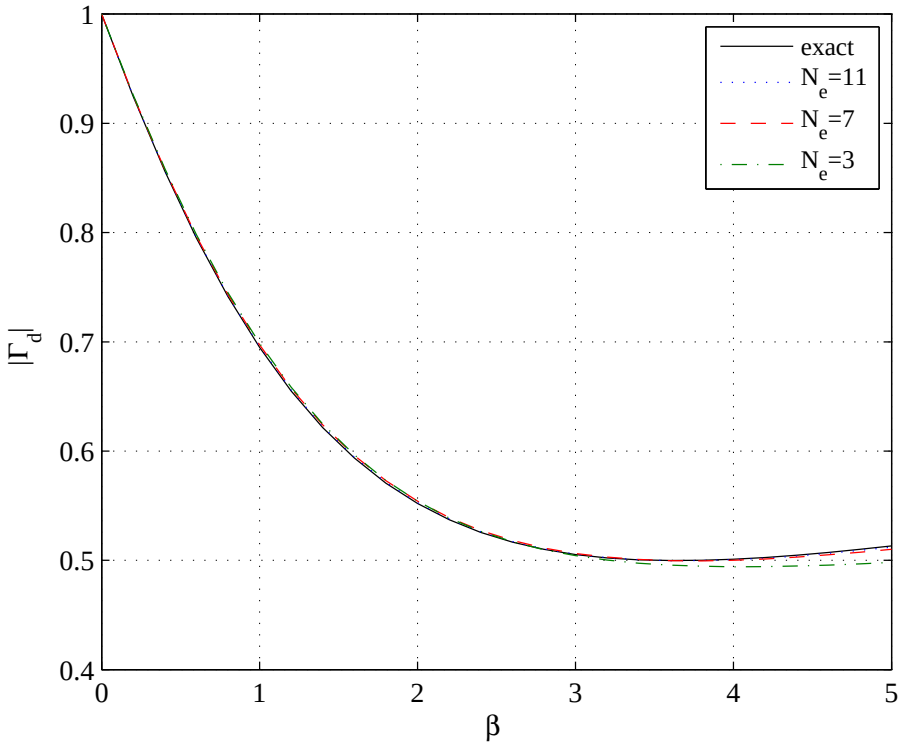

Figure 3.9: The numerically computed reflection coefficient versus loss parameter at normal incidence compared with analytical value Γ_d^{exact}.

using finite differences and solving the finite difference equations at each node after applying the boundary conditions. In these finite difference approximations, the value of the variable at a node will be related to the values at the neighbouring nodes.

Before describing the FDTD method in solving various electromagnetic problems, I will introduce the basic approach of the finite difference approximation of derivatives at discrete set of points. For the function shown in Fig. 3.10, the derivative at point Q can be approximated to find the slope of the arc QB by using the forward-difference formula [34],

$$f'(x_Q) \simeq \frac{f(x_Q + \Delta x) - f(x_Q)}{\Delta x}, \tag{3.46}$$

or by using the backward-difference formula to find slope of the arc AQ,

$$f'(x_Q) \simeq \frac{f(x_Q) - f(x_Q - \Delta x)}{\Delta x}, \tag{3.47}$$

or the central-difference formula to find the slope of the arc AB,

$$f'(x_Q) \simeq \frac{f(x_Q + \Delta x) - f(x_Q - \Delta x)}{2\Delta x}. \tag{3.48}$$

The second derivative can be given as

$$f''(x_Q) \simeq \frac{f'(x_Q + \Delta x/2) - f'(x_Q - \Delta x/2)}{2\Delta x}, \tag{3.49}$$

which can be simplified to

$$f''(x_Q) \simeq \frac{f(x_Q + \Delta x) - 2f(x_Q) + f(x_Q - \Delta x)}{(2\Delta x)^2}. \tag{3.50}$$

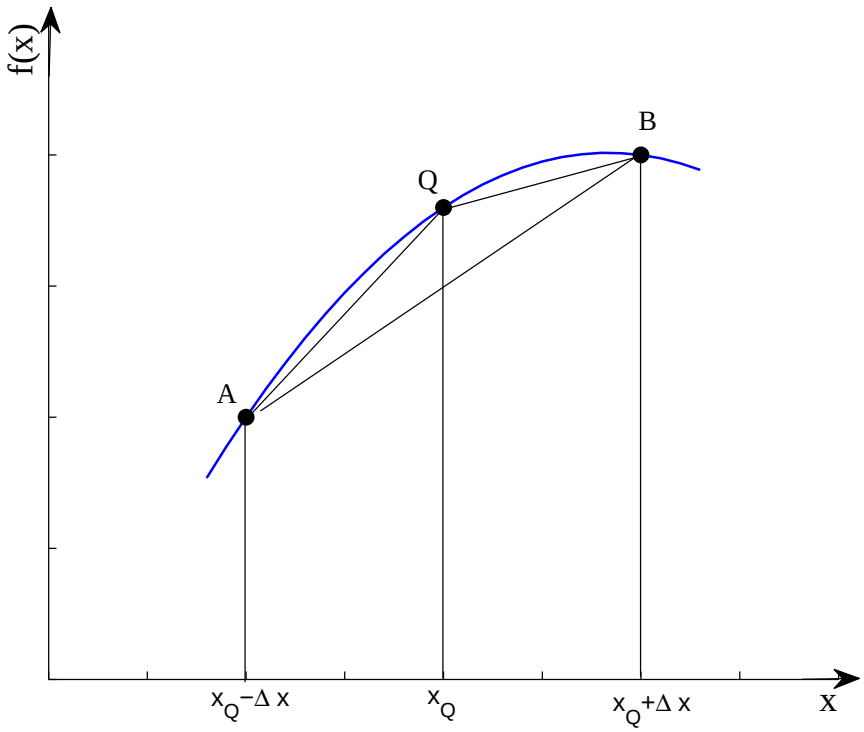

Figure 3.10: Approximating the derivative of $f(x)$ at point Q.

Taylor's series can be alternatively used to find the derivative of the above function. However, this will be accomplished by an error, $O(\Delta x)$, due to truncating the expansion. We can achieve higher order approximation from Taylor's series by taking more terms. The truncation error can be decreased also by reducing the mesh size and the time increment, Δt.

3.7.1 Yee's cell

Yee has proposed the finite difference algorithm and defined the grid point in the solution region as

$$(i, j, k) \equiv (i\Delta x, j\Delta y, k\Delta z), \tag{3.51}$$

where any function can be represented in space and time as

$$f^n(i, j, k) \equiv f(i\Delta s, j\Delta s, k\Delta s, n\Delta t), \tag{3.52}$$

where i,j,k and n are integers, $\Delta s = \Delta x = \Delta y = \Delta z$ is the space step and Δt is the time step.

The space and time derivative of (3.52) with respect to x and t using the central-difference formula can written as

$$\frac{\partial f^n(i, j, k)}{\partial x} = \frac{f^n(i + 1/2, j, k) - f^n(i - 1/2, j, k)}{\Delta s} + O(\Delta s^2), \tag{3.53}$$

$$\frac{\partial f^n(i, j, k)}{\partial t} = \frac{f^{n+1/2}(i, j, k) - f^{n-1/2}(i, j, k)}{\Delta t} + O(\Delta t^2). \tag{3.54}$$

The components of **E** and **H** can be positioned in Yee's cell by applying (3.53) to Maxwell's equations as shown in Fig. 3.11. The finite difference approximation of Maxwell's scalar equations for the components of electric and magnetic fields can be given by applying (3.54) as

$$\begin{aligned} H_x^{n+1/2}(i, j + 1/2, k + 1/2) = {} & H_x^{n-1/2}(i, j + 1/2, k + 1/2) \\ & + \frac{\Delta t}{\mu(i, j + 1/2, k + 1/2)\Delta s}[E_y^n(i, j + 1/2, k + 1) \\ & \qquad - E_y^n(i, j + 1/2, k) \\ & \qquad + E_z^n(i, j, k + 1/2) - E_z^n(i, j + 1, k + 1/2)], \end{aligned} \tag{3.55}$$

$$\begin{aligned} H_y^{n+1/2}(i + 1/2, j, k + 1/2) = {} & H_y^{n-1/2}(i + 1/2, j, k + 1/2) \\ & + \frac{\Delta t}{\mu(i + 1/2, j, k + 1/2)\Delta s}[E_z^n(i + 1, j, k + 1/2) \\ & \qquad - E_z^n(i, j, k + 1/2) \\ & \qquad + E_x^n(i + 1/2, j, k) - E_x^n(i + 1/2, j, k + 1)], \end{aligned} \tag{3.56}$$

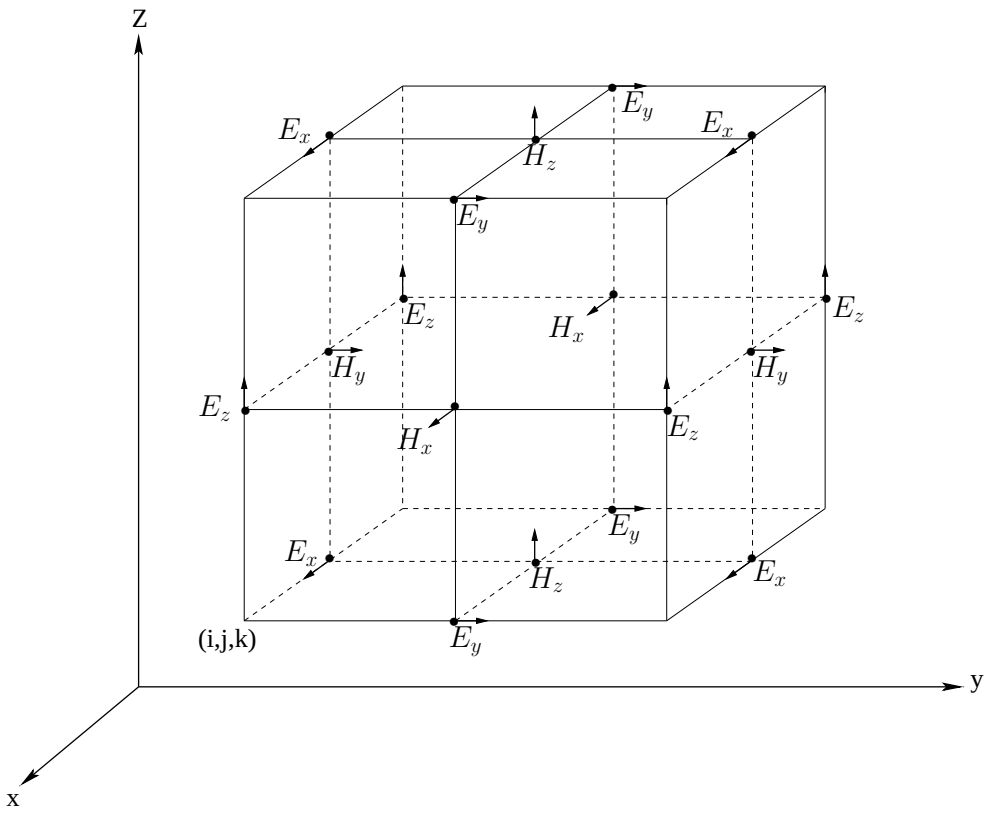

Figure 3.11: Positioning the fields components on Yee's cell.

$$H_z^{n+1/2}(i+1/2,j+1/2,k) = H_z^{n-1/2}(i+1/2,j+1/2,k) + \frac{\Delta t}{\mu(i+1/2,j+1/2,k)\Delta s}[E_x^n(i+1/2,j+1,k) - E_x^n(i+1/2,j,k) + E_y^n(i,j+1/2,k) - E_y^n(i+1,j+1/2,k)], \quad (3.57)$$

$$E_x^{n+1}(i+1/2,j,k) = (\frac{\sigma(i+1/2,j,k)\Delta t}{\varepsilon(i+1/2,j,k)})E_x^n(i+1/2,j,k) + \frac{\Delta t}{\varepsilon(i+1/2,j,k)\Delta s}[H_z^{n+1/2}(i+1/2,j+1/2,k) - H_z^{n+1/2}(i+1/2,j-1/2,k) + H_y^{n+1/2}(i+1/2,j,k-1/2) - H_y^{n+1/2}(i+1/2,j,k+1/2)], \quad (3.58)$$

$$E_y^{n+1}(i,j+1/2,k) = (\frac{\sigma(i,j+1/2,k)\Delta t}{\varepsilon(i,j+1/2,k)})E_x^n(i,j+1/2,k) + \frac{\Delta t}{\varepsilon(i,j+1/2,k)\Delta s}[H_x^{n+1/2}(i,j+1/2,k+1/2) - H_x^{n+1/2}(i,j+1/2,k-1/2) + H_z^{n+1/2}(i-1/2,j+1/2,k) - H_z^{n+1/2}(i+1/2,j+1/2,k)], \quad (3.59)$$

$$E_z^{n+1}(i,j,k+1/2) = (\frac{\sigma(i,j,k+1/2)\Delta t}{\varepsilon(i,j,k+1/2)})E_z^n(i,j,k+1/2) + \frac{\Delta t}{\varepsilon(i,j,k+1/2)\Delta s}[H_y^{n+1/2}(i+1/2,j,k+1/2) - H_y^{n+1/2}(i-1/2,j,k+1/2) + H_x^{n+1/2}(i,j-1/2,k+1/2) - H_x^{n+1/2}(i,j+1/2,k+1/2)]. \quad (3.60)$$

It can be noticed from Fig. 3.11 and (3.55)-(3.60) that the field components have been represented at half-time steps and occupy a quarter of a unit cell. When writing an FDTD computer code to implement (3.55)-(3.60), the user needs to use the results from one type of fields to calculate another type in the same time step.

3.7.2 FDTD solution stability

In order to achieve a high accuracy and stability, the space and time steps should satisfy particular condition. For the space step, the increment Δs need to be in the order of $\lambda/10$ as mentioned earlier in this chapter. In other words, we need at least ten cells per wavelength. In contrast, the time increment Δt is subject to the stability condition given by [34]

$$\nu_{max}\Delta t \leq \left[\frac{1}{\Delta x^2} + \frac{1}{\Delta y^2} + \frac{1}{\Delta z^2}\right]^{-1/2}, \quad (3.61)$$

where ν_{max} is the maximum wave velocity. As long as a cubic cell is used (i.e $\Delta x = \Delta y = \Delta z = \Delta s$), then (3.61) can be simplified as follows

$$\frac{\nu_{max}\Delta t}{\Delta s} \leq \frac{1}{\sqrt{n}}, \quad (3.62)$$

where n is the space dimensions number. Practically, the higher the $\frac{\nu_{max}\Delta t}{\Delta s}$ ratio, the more stable the solution.

3.8 Perfectly Matched Layer

We have learnt from the previous sections in this chapter that a stable and accurate solution can be achieved by using fine meshing. However, it is impossible to simulate an infinite or large solution domain when using small mesh size due to the limitations in the computational resources. This enforces us to terminate or truncate the solution domain into an area close to our structure in order to reduce the number of elements, and hence reduce the solution time. A specific boundary condition can be employed to truncate the computational domain which is so called *Absorbing Boundary Condition*. There are various types of the absorbing boundary condition, however, only the perfectly matched layers (PMLs) will be discussed as they are commonly used in the commercial full-wave simulators. PML is a layer of absorbing material surrounding the solution region that absorbs all incident waves at any angle without reflection as depicted in Fig.3.12. This is the same as the operation of anechoic chambers in practical measurements, where the accuracy of the results depends primarily on the absorbing properties of the material.

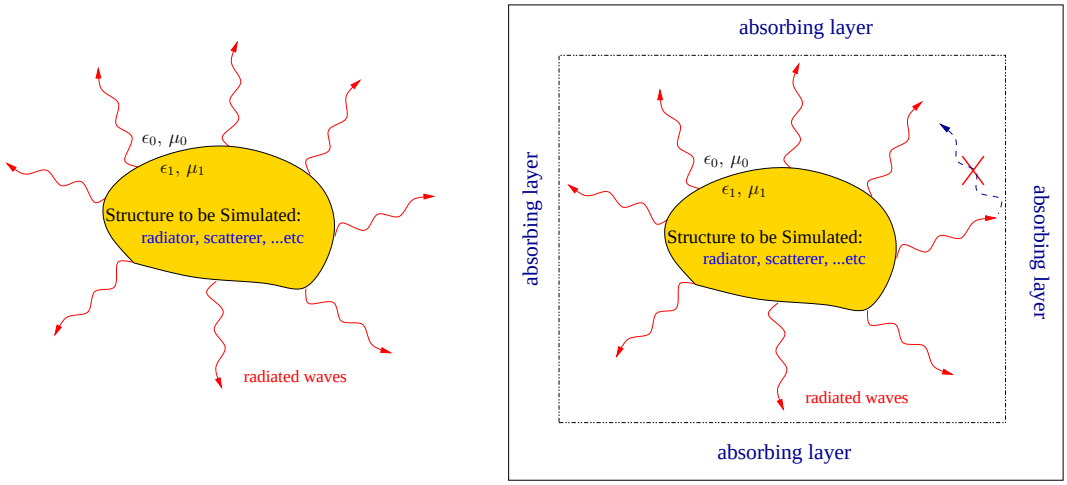

(a) (b)

Figure 3.12: Typical electromagnetic problem: (a) infinite solution region, and (b) the same problem with truncated computational domain using PMLs.

There are two formulations of PML: the first one is the split-field PML, which is proposed by Berenger [41]. In this formulation, for the case of TE mode with $E_z = 0 = \frac{\partial}{\partial z}$, the field components will be four rather than three (i.e E_x, E_y, H_{zx} and H_{zy}). The second formulation is called the uni-axial PML or UPML, where the PML is represented

by anisotropic absorbing materials. In all cases, the user needs to select the depth and conductivity of PML. In practical cases, the depth of PML could be the same as Δs and the conductivity should be very high ($\sigma \approx \infty$).

3.9 Hybrid Computational Methods

All the computational methods introduced in this chapter have their own merits and limitations. For instance, FEM fails to treat the highly conducting surfaces efficiently as it needs to mesh the area between the absorber and the radiator [35], whereas this can be implemented efficiently using MoM. Thus, the combination of FEM with MoM in a hybrid FEM-MoM method will be useful. Another example is exploiting the useful features in FDTD, such as the computational efficiency, and combine it with feature of body conforming meshing in FEM to form the hybrid FEM-FDTD [33]. In some cases, it is better to treat different parts of the electromagnetic problem with different methods to get benefit from the advantages of each method such as the hybridisation of FDTD-MoM [42]. In this hybrid method, the regions which will be solved using different methods need to be physically-unconnected.

3.10 Chapter Summary

This chapter provided an overview on the computational methods that are used to solve different electromagnetic problems. The first half of the chapter has highlighted some of the basis functions that have been used in numerical methods. In addition, the calculation of the stability and accuracy of the numerical solution has been presented. The second half described briefly the most popular computational methods in electromagnetics including MoM, FEM and FDTD methods. Two of these methods (i.e MoM and FEM) have been used throughout this thesis to analyse the designed nanoantennas.

Chapter 4

Design and Optimisation of Nanoantennas for Solar Energy Harvesting

The field of nanoantennas has received significant worldwide interest from researchers in the last few years due to the advances in nanoscience and nanotechnology. The research efforts primarily aimed to translate and scale down the microwave theories into optical region. The main attractive characteristic in nanoantennas is their ability to enhance and localise the fields in a small area, which has made them preferable in many different applications such as spectroscopy [43] [44], high-resolution microscopy [45] [46], sensing and detection [47] [48] [49] [26] [50], mixing [51], multiplexing [52] and photovoltaics [9] [53] [54] [55] [56]. It is worth mentioning here that the feed gap in optical regime plays a totally different role from that in radio frequencies. In RF antennas, the feed gap is matched to the excitation source to ensure that there is no discontinuity between antenna arms [16]. In contrast, the feed gap in optical regime is a high impedance region that holds a strong field intensity. Thus, the gap needs to be engineered to achieve the desired characteristics.

This chapter demonstrates the design and simulation of nanoantennas for solar energy harvesting and provides a performance comparison of different types of nanoantennas that fit with this application. Moreover, the chapter introduces the approach of coupling two or more elements in one structure in order to enhance the performance. The simulation results of this chapter have been published in [57], [58] and [59].

4.1 Design Considerations

Many approaches and designs have been previously studied that are dedicated to collect solar energy by using nanoantennas. This had been initially proposed by Bailey in 1972 [16]-[1]. The concept of collecting solar energy from sun and earth radiation using nanoantennas is based on the fact that when an electromagnetic wave is incident to a nanoantenna, a time-varying current will be induced on the antenna surface, and thus, a voltage will be generated at the feed gap of the antenna [60]. This induced current, or generated voltage, will oscillate at the frequency of the incident wave. Hence, in order to obtain DC power, a suitable rectifier should be embedded at the feed point of the antenna. Consequently, the performance of the investigated nanoantennas is measured in terms of the captured electric field at the feed gap.

In the last few years, numerous schemes and designs for collecting solar energy have been presented. In this chapter, we will present the design of four solar nanoantennas resonating around 13 μm including dipole, square spiral, logarithmic spiral and bowtie

nanoantenna, and investigate their performance.

Before getting started with the design procedure of a nanoantenna, the designer need to be concerned with several aspects. These include the material choice, configuration, frequency range, source excitation and boundary conditions. These aspects are described in details in the following subsections.

4.1.1 Material choice

There exists a significant difference between material properties at RF and optics, which necessitates careful consideration and special characterization of the optical properties of materials employed. In the RF region, metals are considered as perfect electrical conductors, however, in the case of nano-scale antennas operating at the optical and IR regimes, metals no longer behave as perfect conductors [61]. They exhibit lower conductivity (particularly at optical frequencies) and have frequency-dependent dielectric properties [26]. These dielectric properties, ε, and the refractive index, N, of metals have complex form and can be written as

$$\varepsilon = \varepsilon' + i\varepsilon'' = N^2 = (n + ik)^2, \tag{4.1}$$

where the real part is negative and higher than the imaginary part. The absorption properties are very high in noble metals at optical frequencies, however they tend to be lower within the IR regime and approximately disappear in radio frequencies. Ohmic absorption is determined by ε'' which is related directly to the metal conductivity $\sigma(\omega)$. Therefore, choosing a metal with low ε'' can keep the Ohmic losses low [45].

Since nanoantennas are usually supported by a dielectric substrate, thus, for the surface plasmon resonance occurrence condition, the real part of the dielectric function for the two materials (i.e metal and dielectric) need to have different signs. The negative real part of the dielectric properties has a crucial role in producing the surface palsmon resonance as it results in absorption and scattering at certain frequencies. According to Mie description, the condition for the resonance in two spheres occurs when $\varepsilon' = -2$ [62].

Classical models have been widely used to characterise the dielectric properties of metals at visible and IR regimes such as Debye, Drude and Lorentz models. Some of the classical models fail in describing the dielectric properties accurately within a certain frequency range [63]. Thus, these models can be modified by fitting with experimental data within the desired frequency range [64]. Another approach to address the inaccuracy problem is to develop a hybrid model such as the Drude-Lorentz model.

Several noble metals have been considered in recent nanoantenna designs such as gold [65] [66] [67] [68], silver [61] [69] [70], Nickel [71] [72] and Aluminium [73] [74] at both visible and IR wavelengths. The material choice for a given application has received significant interest recently in order to find the best optical material to be employed in nanoantenna design [75] [56].

It is demonstrated that gold is the best choice among various materials used in nanoantennas due to its chemical stability and the fact that it suffers from less oxidation compared with other materials [3]. In this work, gold will therefore be adopted in designing our nanoantennas. The dielectric properties of gold, which is used in simulations, is obtained from fitting the experimental data into Drude model [64], i.e.

$$\varepsilon(\omega) = \varepsilon_\infty - \frac{\omega_p^2}{\omega^2 - i\omega\omega_\tau}, \tag{4.2}$$

where ε_∞ represents the contribution of the bound electrons to the relative dielectric constant, ω_p is the plasma frequency (rapid oscillation of the electron density in conducting media such as metals) and ω_τ is the damping frequency. Fig. 4.1 shows the real and imaginary parts of the frequency-dependent dielectric properties of gold.

The dielectric parameters are frequency-dependent as shown in (4.1), however, it is commonly approved in the research literature [26] that the material parameters at a single frequency close to the resonance can be used instead of the frequency-dependent variable $\varepsilon(\omega)$. An acceptable agreement is maintained as long as the imaginary part of ε is included.

4.1.2 Configuration

The ability of nanoantennas for confining the electric field in a small hot area has been widely studied. The research on nanoatennas started with investigating the light scattering from single nanoparticles then developed and extended to couple two particles in an antenna form. Several types of structures have been recently used as nanoantennas, however, only simple structures have been considered in theoretical studies due to the simple scattering problem in these structures in both the visible and IR regimes. This include dipoles [52] [71] [73] [76], bowties [77] [78] [27] [79], square spirals [60] [1] [66], Archimedean spirals [80] [81], loops [82] and dimers or disks [83] [29]. In some cases, more than two elements have been coupled together in one single antenna to increase the localised field into the antenna feed gap such as the cross nanoantennas [45] [28] [84] and

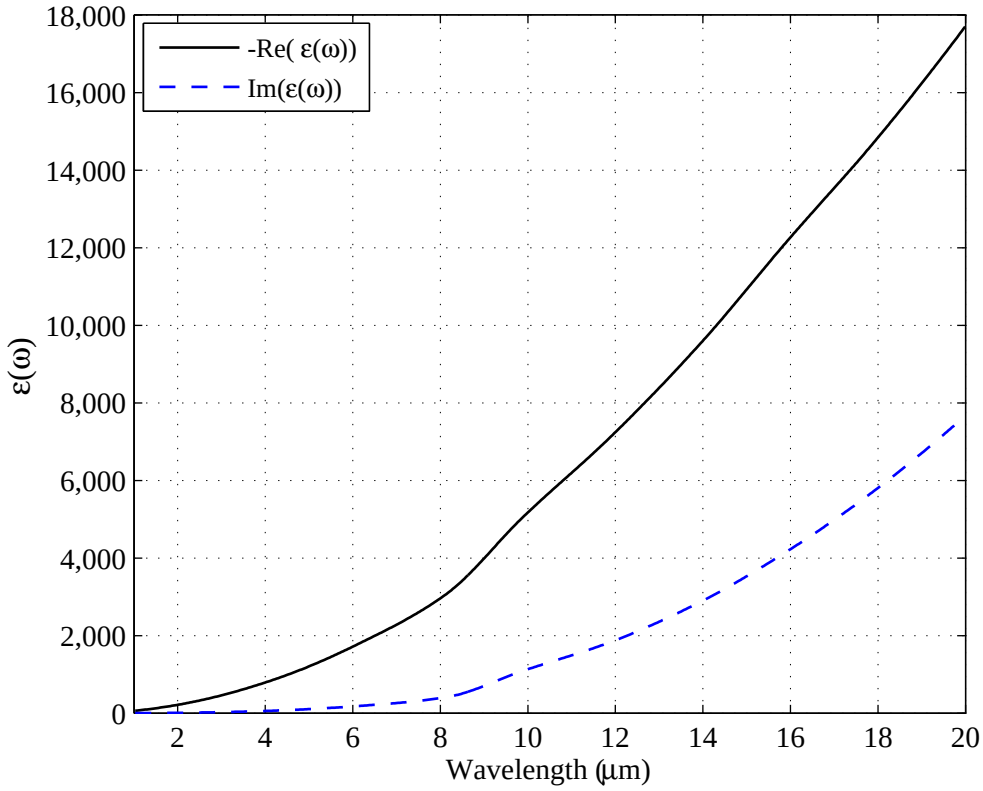

Figure 4.1: Dielectric constant of gold as a function of wavelength, real (solid line) and imaginary (dashed-dotted line).

the Yagi-Uda structure [85]. Numerous attempts have investigated the geometrical effect on the antenna response by comparing the performance of different configurations to find the optimum one for a particular application [53] [86] [87] .

In this work a study is conducted of the dipole, bowtie and spiral nanoantennas into their feasibility to capture the IR solar radiation for energy harvesting in single and array forms. These structures feature most of the radiation properties in their RF counterparts, however the feed gap role and the metal dispersion at these frequencies should be carefully considered.

4.1.3 Frequency range and source excitation

The power density of the solar radiation that reach the Earth's atmosphere is approximately 1370 W/m^2 over a wide spectrum. This spectrum can be classified into three main bands: ultraviolet (UV) radiation $(\lambda < 400$ nm$)$ of which the content is less than 9%; visible light $(400$ nm $< \lambda < 700$ nm$)$ where the content is approximately 39%; and the remaining 52% consisting of infra-red (IR) [2]. The collection of solar radiation can be either in the visible range of the electromagnetic spectrum or in the IR range. Designing

nanoatennas for photovoltaics in the visible range is quite challenging due to the fact that the metal conductivity at these wavelengths is very low (i.e high losses). The second reason is the difficulty in designing ultrafast diodes that will be able to rectify signals in this range of THz frequencies. This fact has motivated researchers to exploit the unused part of the solar spectrum and move up to the IR wavelengths. Some of the IR energy will be absorbed or reflected back by the atmosphere and the rest will be re-radiated to the earth's surface in the wavelength range of $4 - 25$ μm [88]. The wide range of reradiated IR energy gives the designer the freedom to move within this range in the design process. In our theoretical work, we have designed our antennas to be resonated within $7 - 14$ μm where most of the energy is expected [1].

4.1.4 Simulation method and boundary conditions

This subsection describes the main components and procedures in simulating the designed nanoantennas. The Finite Element Method (FEM) of COMSOL Multiphysics is used to simulate the gold nanoantennas, which are placed on a 20 μm silica glass substrate with ε_r=2.09. The nanoantenna is illuminated vertically (normal incidence) by a linearly polarised plane wave with a 1 $\mathrm{V/m}$ E-field magnitude, which has been launched from z-direction, followed by calculation of the electric field across the antennas' feed gap. The plane wave excitation has the form of $s_z = E_0 \exp(-jk_0 y)$ with polarisation parallel to antenna axis.

When designing a structure in COMSOL Multiphysics, the typical modeling steps include:

1- Creating the geometry using the CAD features

2- Discretising (Meshing) the structure

3- Defining the excitation and the boundary conditions on the domains

4- Solving the model

5- Postprocessing the solution

6- Performing parametric studies when needed.

Fig. 4.2 illustrates the simulation model and the boundary conditions, where perfectly matched layers (PMLs) of thickness 10 μm have been applied at the top and bottom of the

simulation model to reduce reflections from these boundaries. The incident plane wave is generated by an electric field source located on the xy-plane, 20 μm above the antenna (directly below the upper PML).

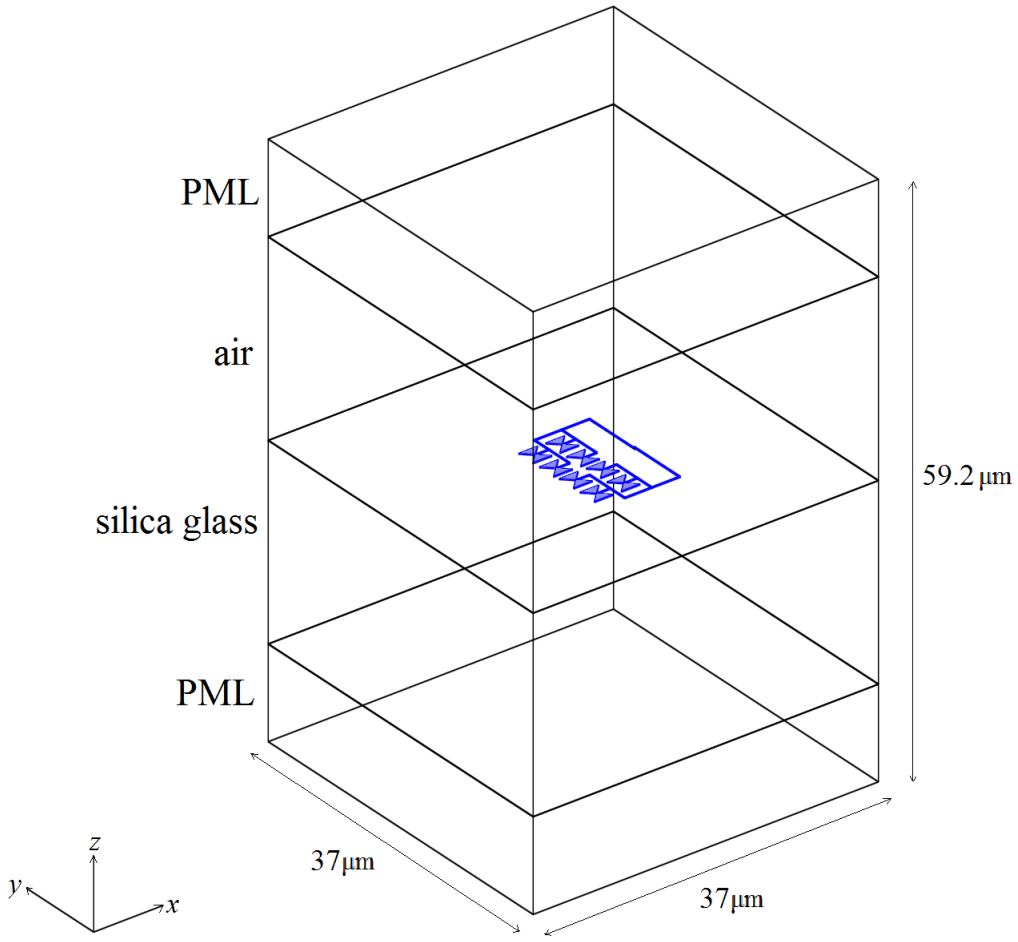

Figure 4.2: The illuminated nanoantenna with the simulation domain and the boundary conditions.

The performance of the bowtie nanoantenna is measured in terms of the captured electric field at the feed gap. The PMLs are included within the structure in order to eliminate or reduce the reflected waves [38].

COMSOL Multiphysics uses FEM techniques to solve Maxwell's equations for many problems in the field of electromagnetic waves, such as RF systems, photonics and optics. The mathematical equations utilised in the simulations can be derived from the first and second Maxwell's equations.

$$\nabla \times \mathbf{E} = -j\omega\mathbf{B}, \tag{4.3}$$

$$\nabla \times \mathbf{H} = -j\omega\mathbf{D} + \mathbf{J}, \tag{4.4}$$

Using the constitutive relations for linear materials $\mathbf{D} = \varepsilon\mathbf{E}$ and $\mathbf{B} = \mu\mathbf{H}$, as well as a current $\mathbf{J} = \sigma\mathbf{E}$, the above equations become

$$\nabla \times \mathbf{E} = -j\omega\mu\mathbf{H}, \tag{4.5}$$

$$\nabla \times \mathbf{H} = j\omega\varepsilon\mathbf{E} + \sigma\mathbf{E}. \tag{4.6}$$

The last two equations can be combined into either an equation for the electric field or one for the magnetic field, however, an equation is used for calculating the electric field by taking curl ($\nabla\times$) on both sides of (4.5), i.e.

$$\nabla \times (\nabla \times \mathbf{E}) = -j\omega\mu(\nabla \times \mathbf{H}), \tag{4.7}$$

Substituting (4.6) in (4.7) yields

$$\nabla \times (\nabla \times \mathbf{E}) = -j\omega\mu(j\omega\varepsilon\mathbf{E} + \sigma\mathbf{E}), \tag{4.8}$$

Equation (4.8) can be simplified as

$$\nabla \times (\mu^{-1}\nabla \times \mathbf{E}) - k_0^2\mathbf{E}(\varepsilon_r - j\frac{\sigma}{\omega}) = 0, \tag{4.9}$$

where $k_0 = \omega\sqrt{\varepsilon_0\mu_0}$, $\mu_0 = 4\pi \times 10^{-7}\,\mathrm{H\,m^{-1}}$ is the permeability and $\varepsilon_0 = 8.854 \times 10^{-12}\,\mathrm{F\,m^{-1}}$ is the permittivity in free space. This last equation is used in FEM-based software to calculate the electric field around the designed antennas.

The Area Under Curve (AUC) is used to measure the performance of the designed nanoantennas [89] [90], where its value has been calculated using the trapezoidal integration method using a uniform grid of K points (0.5 μm step increment) [91].

$$AUC \triangleq \int_a^b E(\lambda)\,d\lambda \approx \frac{1}{2}\sum_{k=1}^{K}(\lambda_k - \lambda_{k-1})\,[E(\lambda_k) + E(\lambda_{k-1})], \tag{4.10}$$

where a=10 μm, and b=200 μm.

COMSOL automatically meshes the geometry using an adaptive procedure, where the mesh generator generates a finer mesh when there are many fine geometrical details. In some cases, the problem does not converge, or the solution does not seem properly resolved. Therefore, the designer needs to re-solve the problem using a finer mesh by refining the existing mesh. Another approach is to mesh the structure manually by adjust-

ing the maximum allowed mesh element size for particular domains in the structure. The FEM approach approximates the solution within each element.

Small edges and details need a finer mesh to calculate the electromagnetic components properly, whereas, in wide and open regions a low resolution meshing can be implemented to avoid an excessive amount of mesh elements. It is important that the mesh size be smaller than the operation wavelength, where it is recommended by COMSOL to use 10 elements per wavelength in order to solve the problem properly. Fig. 4.3 shows the visualisation of the adaptive meshing for a bowtie nanoantenna where triangular elements are used. It can be seen that the denser meshing is around the fine geometrical details such as the tips of the bowtie. Finer meshing can be used to achieve more accurate results as shown in Fig. 4.4, however, the finer the meshing the more the computational resources needed.

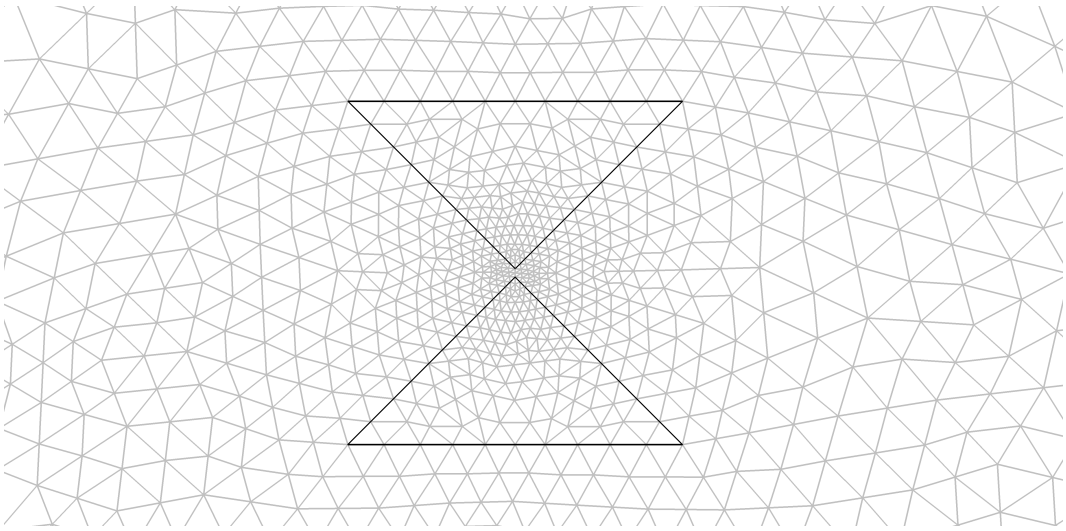

Figure 4.3: Adaptive meshing of a bowtie nanoantenna using triangular elements.

4.2 Simulation Results

FEM simulations have been carried out in this work to investigate the performance of nanoparticles and their utilisation as antennas at optical and IR frequencies, where gold has been used as a noble metal in all cases throughout this work. When a nanoparticle

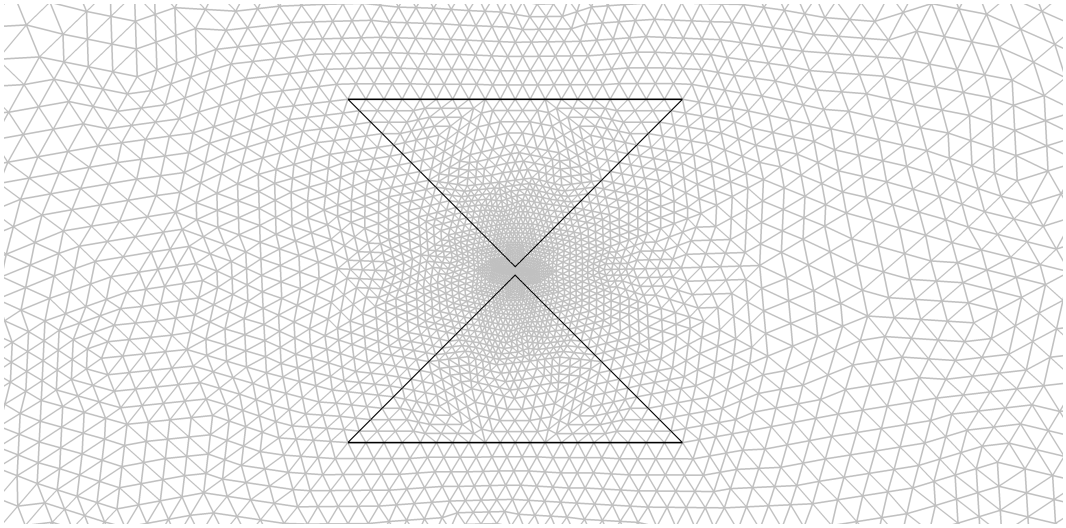

Figure 4.4: Denser discretisation using finer meshing for more accurate solution. The total number of elements in this domain is 27904 elements.

is illuminated by a plane wave, the free electrons on the surface will be induced and will oscillate at the same frequency of the incident wave. Such oscillation leads to a surface charge accumulation at the tips of the nanoparticle generating a concentrated electric field. When a proper length of the finite-length rod, L_R, is chosen, the surface charges will propagate towards the ends producing surface plasmon resonance. Due to the reactive characteristics of the ends, the propagation length will be extended outside the boundaries of the metallic rod resulting in enhanced near-field intensities [3]. Based on Fabry-Pérot model, the resonance occurs when the condition of $k_0 L_R = n\pi$ is satisfied, where ($n = 1, 2, 3, ...$).

A $1\,\mu\mathrm{m}$ long and $50\,n\mathrm{m}$ wide gold rod has been illuminated by an IR plane wave of magnitude 1 V/m and the electric field intensity around the structure is recorded as shown in Fig. 4.5. It is quite evident that most of the field is confined around the tips of the rod, which means that the rod is in resonance mode.

For the case of two-rod nanoantenna, the propagated surface charges towards the near tips of both arms will be confined and concentrated at the gap generating a highly enhanced near-field intensity due to the harmonic oscillation of the rods. The field enhancement inside the gap can be determined by engineering the gap size. In addition, the

resonance of the two-arm nanoantenna can be controlled by properly choosing the materials and the geometrical dimensions of the antenna. The ability of the gold nanoparticle to confine and enhance the electric field in the near-field region has led to their use as antennas for many applications by scaling down the classical electromagnetic theory. Fig. 4.6 shows the electric field intensity around the identical-rod nanoantenna, where it can be seen that most of the electric field has been concentrated in the $25\,nm$ feed gap region. It is worth mentioning that the configuration of Fig. 4.6 exhibits a dipolar radiation when illuminated by a plane wave polarised along the antenna axis.

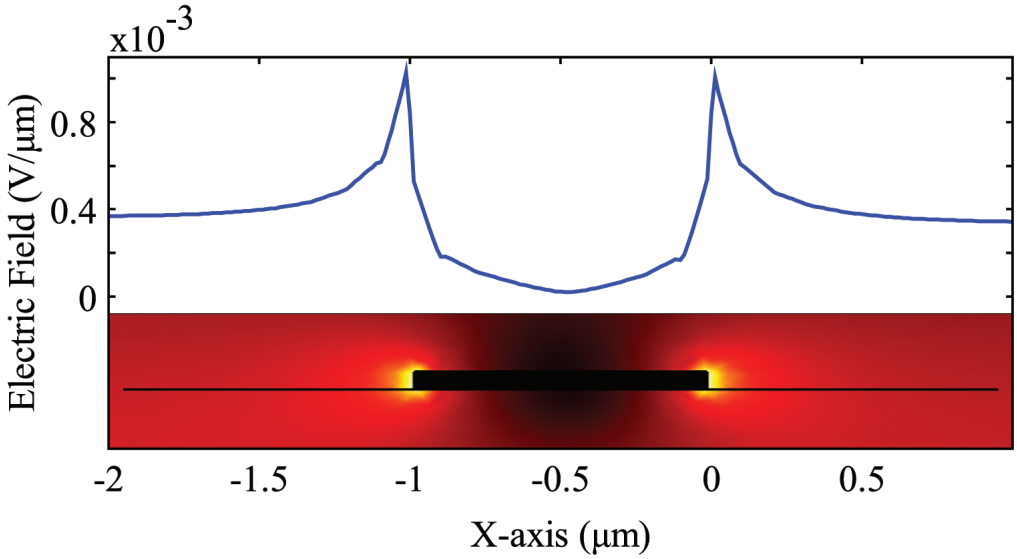

Figure 4.5: Near-field intensity around the $1\,\mu m$ single rod when vertically illuminated by a plane wave parallel to its axis at IR regime.

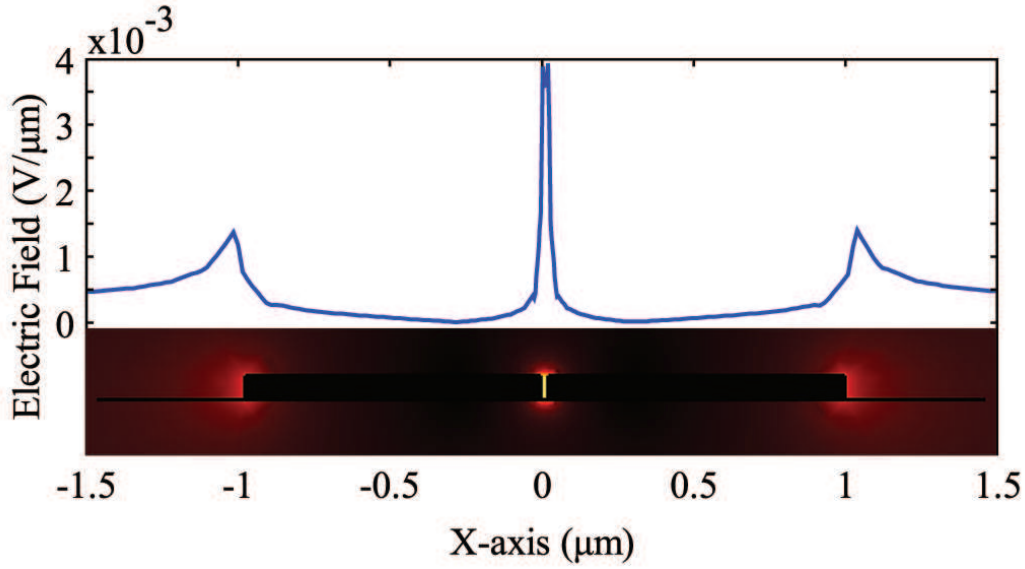

Figure 4.6: Electric field concentration in the gap of two-rod nanoantenna at resonance.

By comparing the spectra of the single rod with that of the two-rod structure, a larger electric near-field intensity can be observed for the two-arm nanoantenna due to the coupling between the two identical rods. In this configuration (i.e two-rod nanoantenna), the near-field intensity can be further enhanced by reducing the gap width, where it is shown that the smaller the gap size, the larger the electric field captured.

The current distribution on the surface of the single rod nanoparticle at resonance is shown in Fig. 4.7, where it is clearly shown that it exhibits approximately sinusoidal distribution which is quite similar to that of the half wavelength RF dipole antenna (as we will see in chapter 6). On the other hand, it is clearly noticed that there is a significant null in the surface current distribution for the two-rod nanoantenna within the gap region as shown in Fig. 4.8. This discontinuity in the current distribution is due to the mismatched air gap in nanoantennas, which represents one of the main differences between nanoantennas and their counterparts in RF regime. Figs. 4.7 and 4.8 illustrate the magnetic field on the surface of the single- and two-rod nanoantennas, where the current distribution can be found by integrating the magnetic field along the antenna surface.

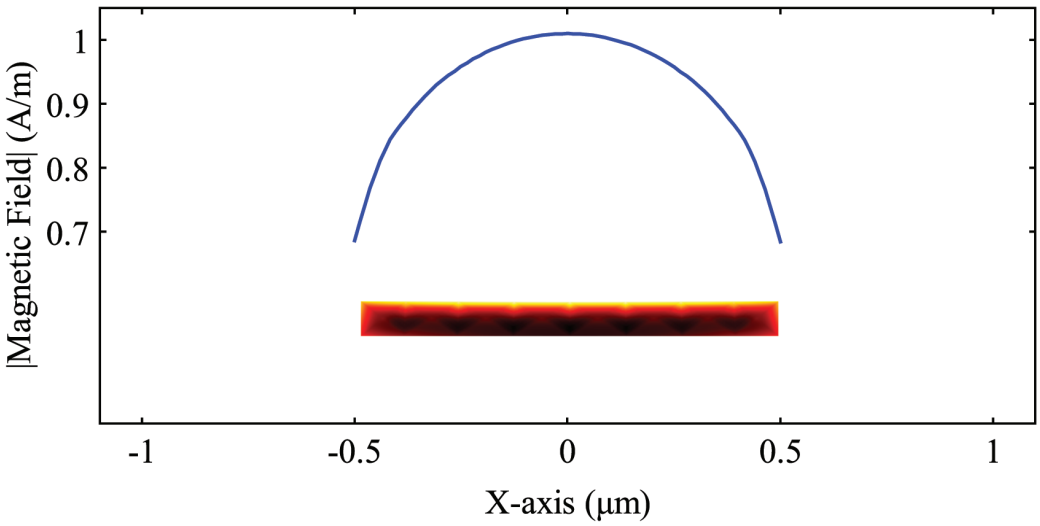

Figure 4.7: Magnetic field on the surface of the single rod nanoantenna.

4.2.1 Dipole nanoantenna

Two golden rods can be placed together to form a dipole antenna. This type of nanoantennas has been studied previously for different applications such as spectroscopy, biosensing, cancer treatment, and near-field probes [92]. The dipole nanoantenna in Fig. 4.9 with dimensions of $(2\mu m \times 100nm)$ and a gap of $50nm$ has been simulated and its cap-

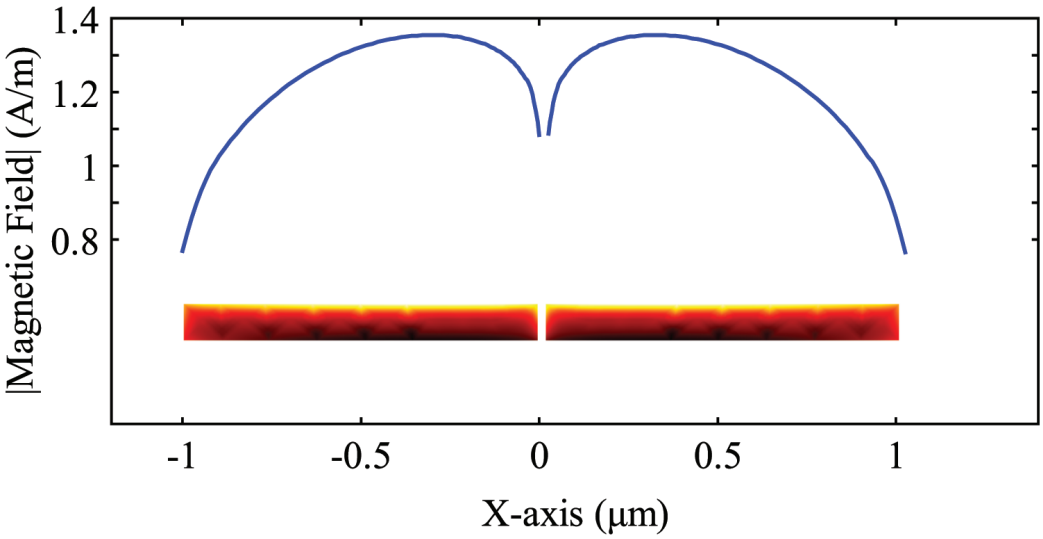

Figure 4.8: Magnetic field on the surface of the two-rod nanoantenna.

tured electric field has been recorded. Fig. 4.10 shows the electric field concentration at resonance in the gap of and around the dipole nanoantenna, wheres Fig. 4.11 illustrates the variation of the electric field inside the gap of the dipole nanoantenna versus the wavelength.

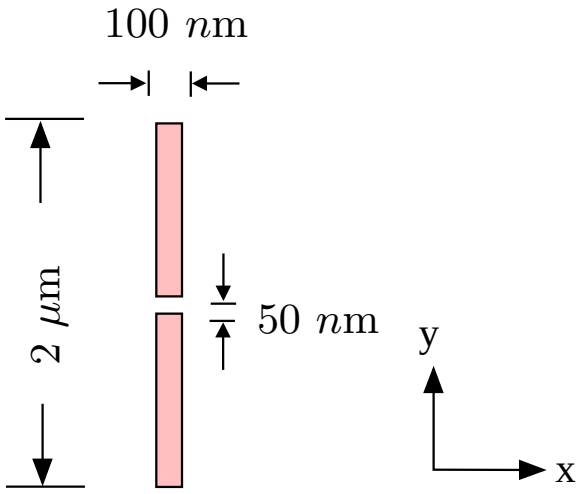

Figure 4.9: Configuration of the dipole nanoantenna.

It is clearly shown that most of the electric field has been captured in the gap region with a trivial field is concentrated around the antenna tips. In addition, it should be mentioned that there is no flexibility in this type of antennas to increase or optimise the electric field in the gap. The only approach is to vary the gap size or increase the rods width. There are other techniques to increase the captured electric field such as arrays, however the ability to build an array from this configuration is difficult if not impossible.

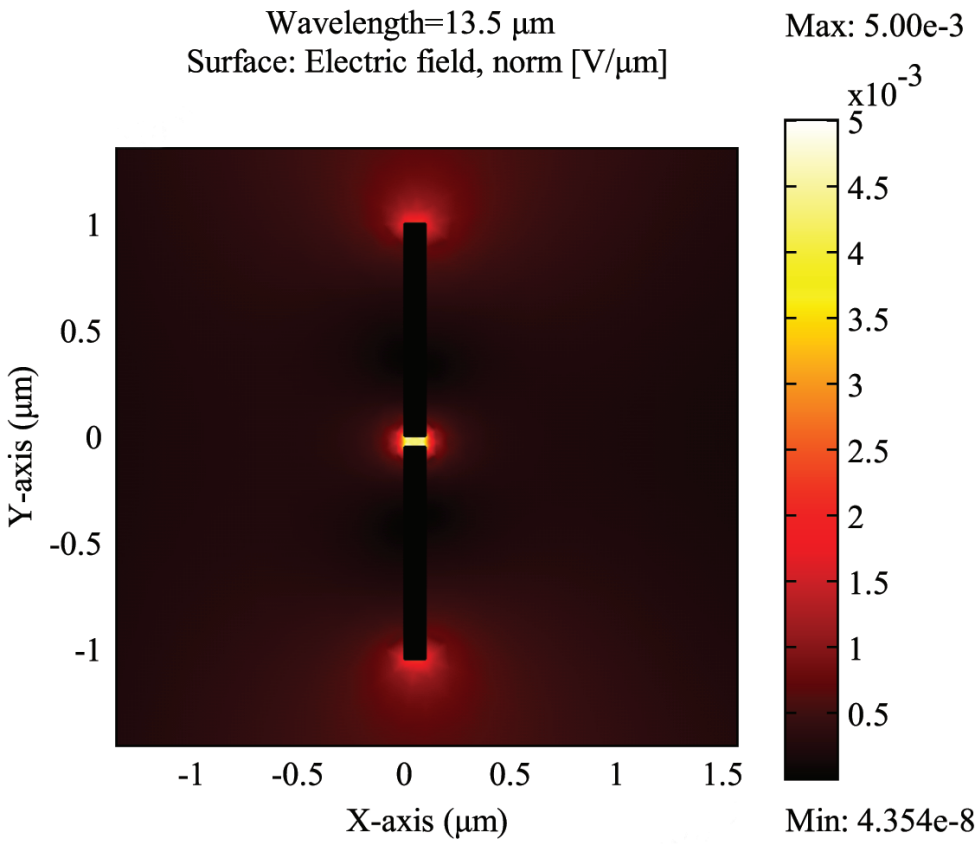

Figure 4.10: Electric field concentration in the gap of dipole antenna.

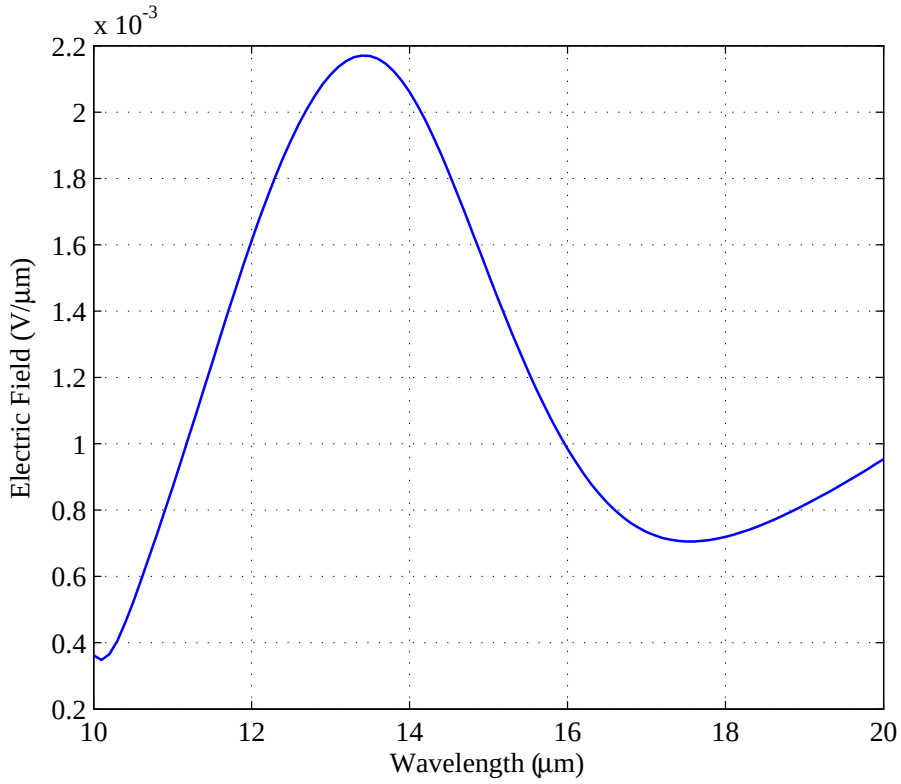

Figure 4.11: Electric field along the gap of the dipole nanoantenna versus the wavelength.

4.2.2 Square spiral nanoantenna

Spiral antennas are good resonators that can capture a large energy at resonance. The square spiral nanoantenna illustrated in Fig. 4.12 is designed for solar energy harvesting application. The square spiral nanoantenna in this study has 6 arms with an arm width of 50 nm and a gap of 50 nm, and overall dimensions of $(1.25\mu m \times 1.25\mu m)$. Fig. 4.13 shows the designed spiral nanoantenna at its resonance, where a large electric field is concentrated at the gap, whereas Fig. 4.14 shows the variation of the electric field against wavelength for the square spiral nanoantenna. The performance of this type of antennas can be enhanced by increasing the number of arms which in turn increases its aperture area that plays a significant role in the gain of the antenna. However, the problem with this type is the difficulty in configuring an array by connecting many elements by their feed gaps. The main aim of the array is to combine the captured electric field from each of its element, whereas in this case the arms will prevent embedding feeding lines due to overlapping.

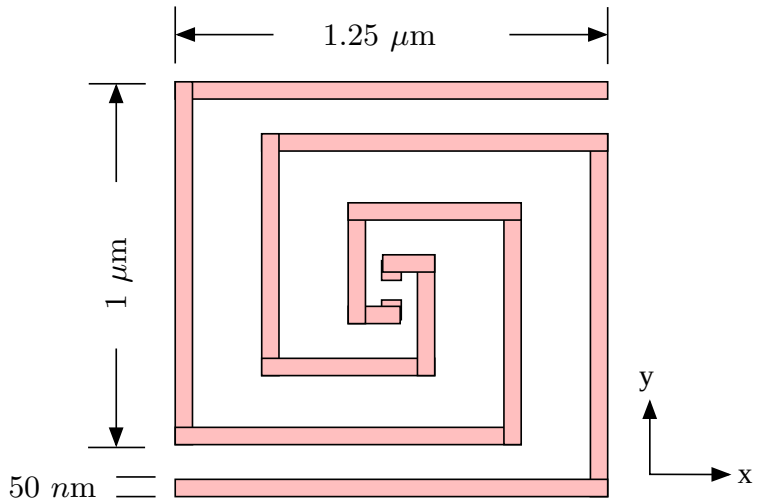

Figure 4.12: Configuration of the square spiral nanoantenna.

4.2.3 Logarithmic spiral nanoantennas

The logarithmic spiral nanoantenna consists of two identical arms with a shift of 180^o with respect to each other. The curves of its arms can be described by the following polar formula,

$$r = R_o e^{a\phi_s}, \tag{4.11}$$

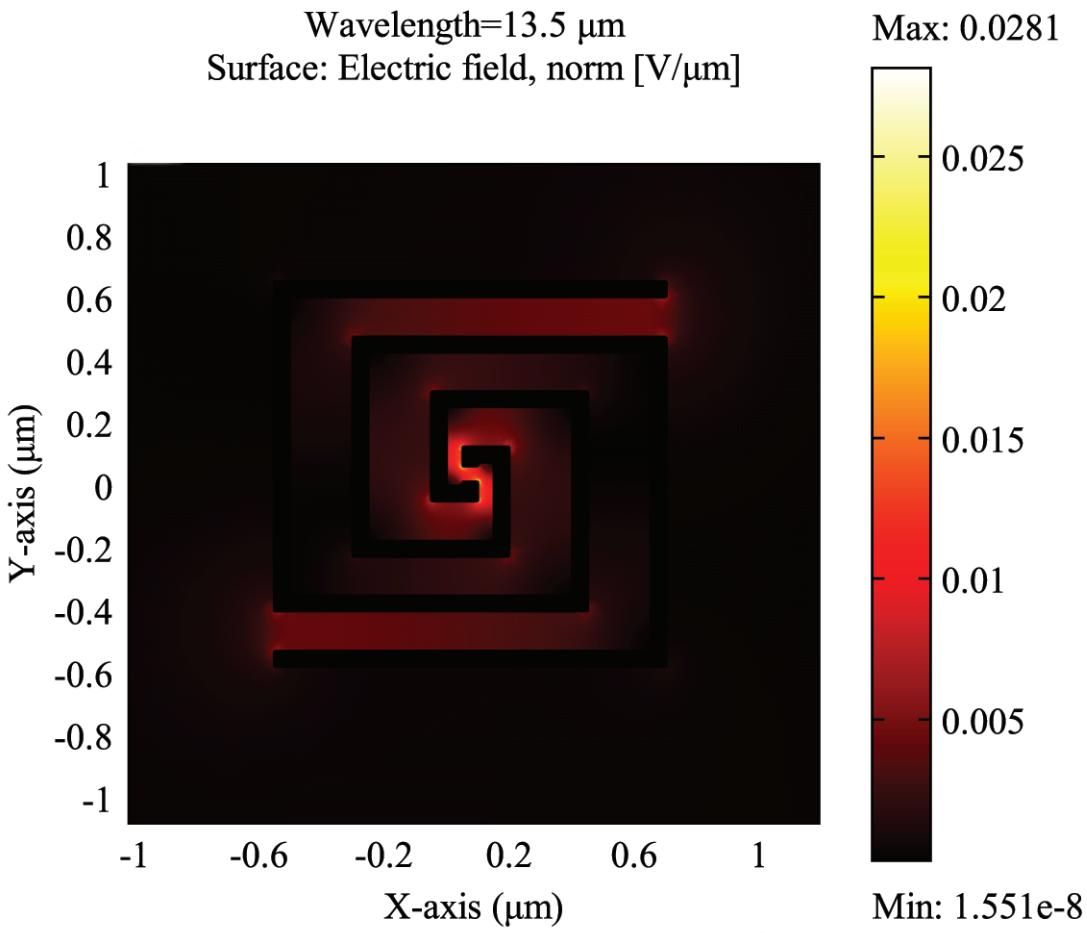

Figure 4.13: Square spiral nanoantenna at resonance with a concentrated electric field at its gap.

where R_o is a constant that controls the initial radius of the curve, a determines the increasing rate of r and ϕ_s is the angle in radians. Fig. 4.15 shows the configuration of the logarithmic spiral nanoantenna that is designed to resonate around 13 μm, whereas Fig. 4.16 illustrates the electric field intensity around the structure of the antenna. The captured electric field versus the wavelength for the logarithmic spiral nanoatenna is shown in Fig. 4.17.

4.2.4 Bowtie nanoantenna

A bowtie antenna consists of two triangles facing each other from their apices with a suitable gap to form a dipole configuration. The performance of nano-gap bowtie antennas depends on many geometrical parameters, including bowtie size, apex angle, and gap size [93]-[94]. The electric field is typically concentrated at the gap of the bowtie antenna due to the Coulomb field, and the gap will act as a capacitor [92]. Thus, for particles in the vicinity (i.e. a short gap) one can expect to obtain an electric field in the gap larger

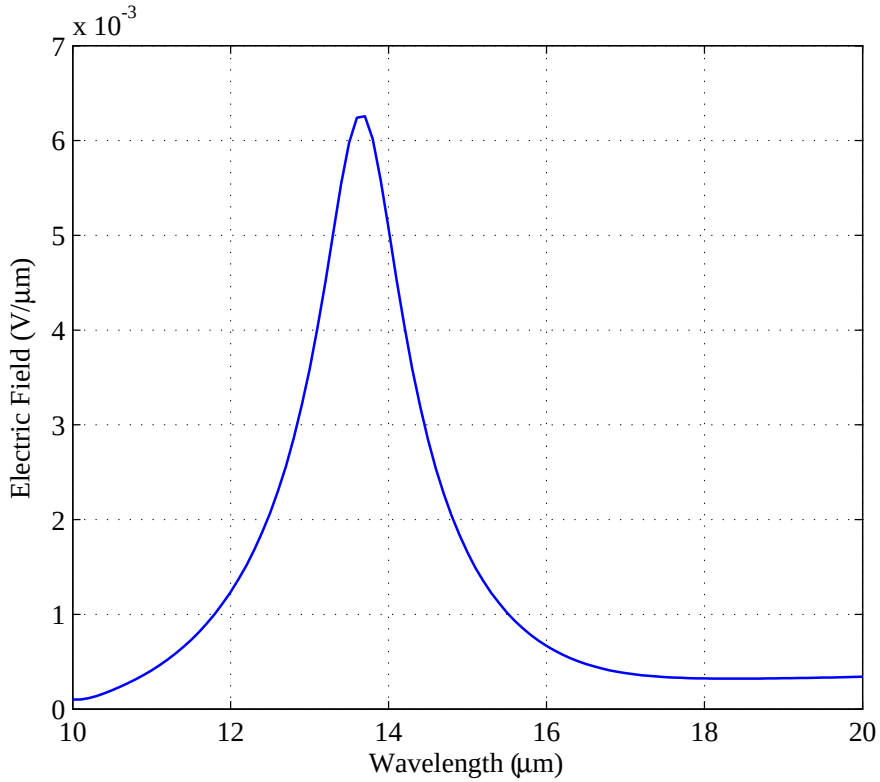

Figure 4.14: Variation of the electric field versus wavelength for the square spiral nanoantenna.

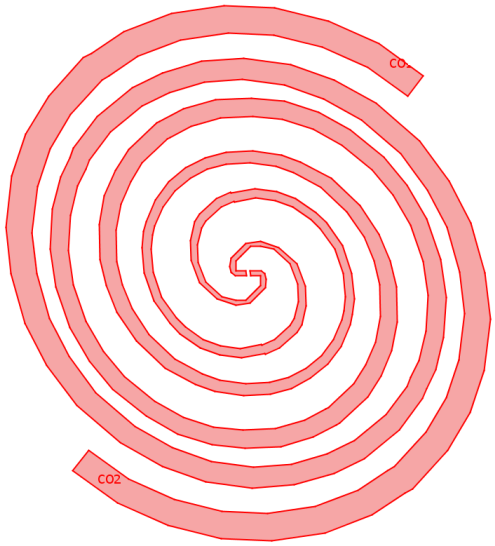

Figure 4.15: Configuration of the logarithmic spiral nanoantenna.

than that of isolated particles. The bowtie is a linearly polarised antenna and has broad beam perpendicular to the plane of radiation. The impedance of the bowtie antenna can be calculated theoretically using the transmission line theory as given by 4.12[21], and can be changed by varying the flare angle which may change the resonant wavelength slightly

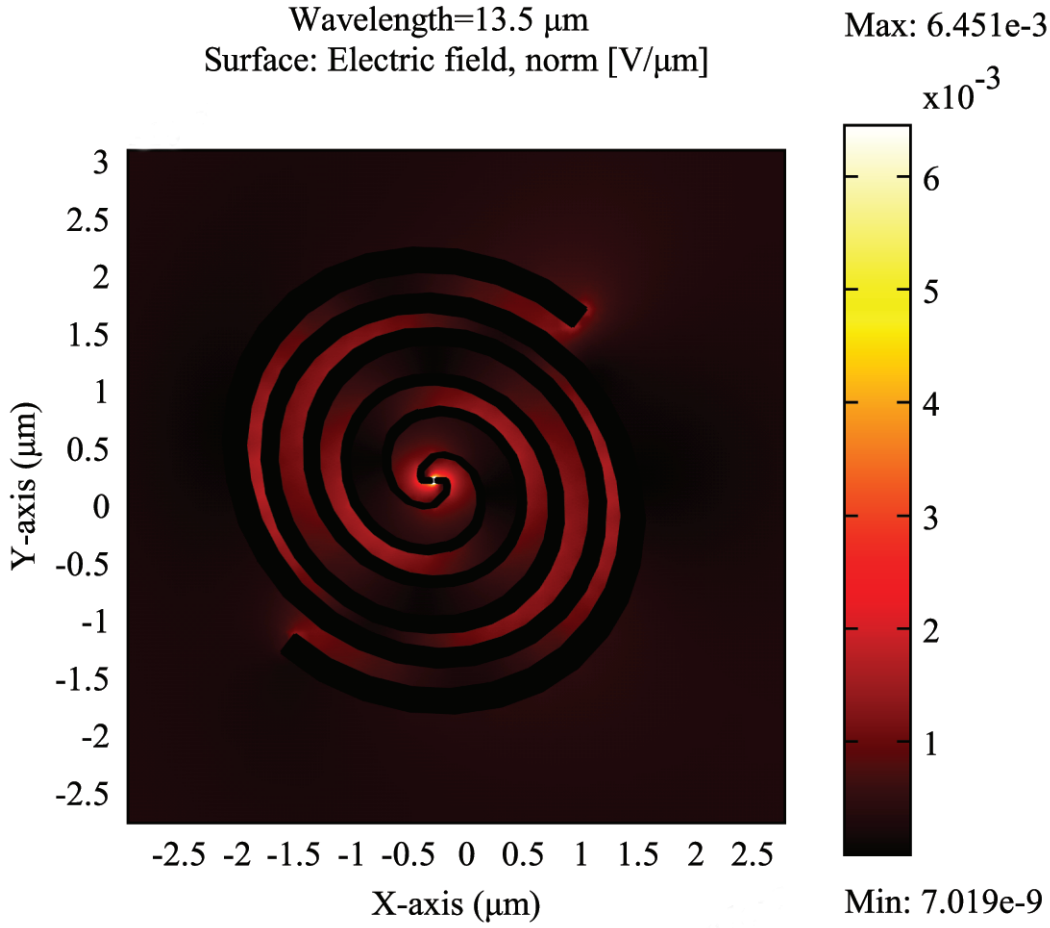

Figure 4.16: The captured Electric field at resonance for the logarithmic spiral nanoantenna.

[95].

$$Z = \frac{\eta_0}{2\sqrt{\varepsilon_{\text{eff}}}} \frac{K[\cos(\phi/2)]}{K[\sin(\phi/2)]}, \tag{4.12}$$

where

$$K(\alpha) = \int_0^1 \frac{dx}{\sqrt{(1-x^2)(1-\alpha^2 x^2)}}, \tag{4.13}$$

$K(\alpha)$ is the complete elliptic integral of the first kind, η_0 is the free-space intrinsic impedance and ε_{eff} is effective dielectric constant, which at infrared frequencies close to 30 THz, equals the dielectric constant of the substrate, and ϕ is the flare angle of the bowtie. In our case we have chosen a flare angle of 90^o that corresponds to bowtie impedance of approximately 50 Ω according to theory, however this value can be changed as required by the application. The dimensions of the designed bowtie nanoantenna are $2\,\mu\text{m} \times 2\,\mu\text{m}$ as shown in Fig. 4.18.

The bowtie nanoantenna shown in Fig. 4.18 is a suitable candidate to replace nano-

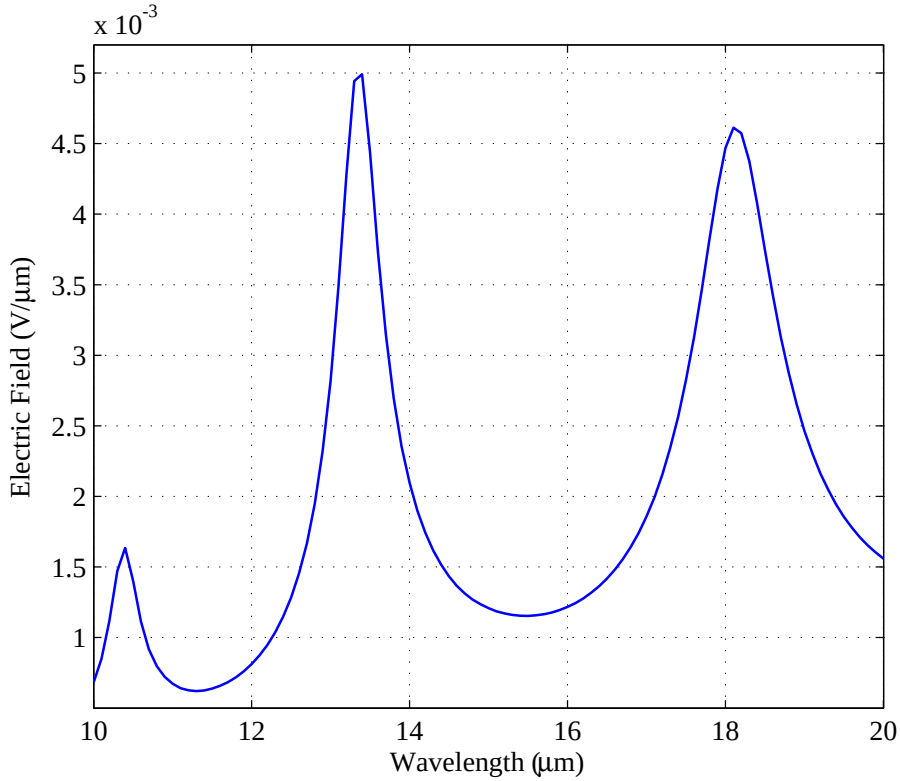

Figure 4.17: Variation of the electric field versus wavelength for the logarithmic spiral nanoantenna.

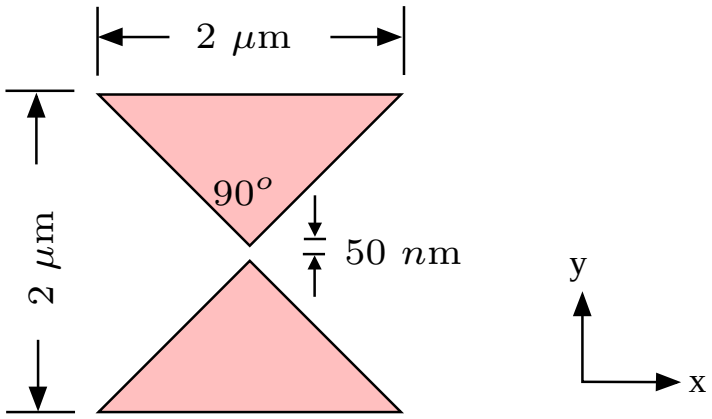

Figure 4.18: Structure of the bowtie nanoantenna.

dipole antennas as it produces a stronger electric field in the antenna's gap. In addition, this configuration gives the designer the freedom to vary several antenna parameters in order to increase the captured electric field in the gap, which is a key factor in this application. These parameters include the gap size, apex angle, and antenna dimensions. Another advantage of bowtie nanoantennas is the ability of building an array by coupling many bowtie elements in one configuration and combining the electric field from each element at the array feeding point, where a rectifier can be embedded as demonstrated in the following chapter. The electric field is concentrated in the gap of the bowtie nanoan-

tenna as shown in Fig. 4.19 for a $(2\mu m \times 2\mu m)$ structure with an apex angle of 90^o and a gap of 50 nm .

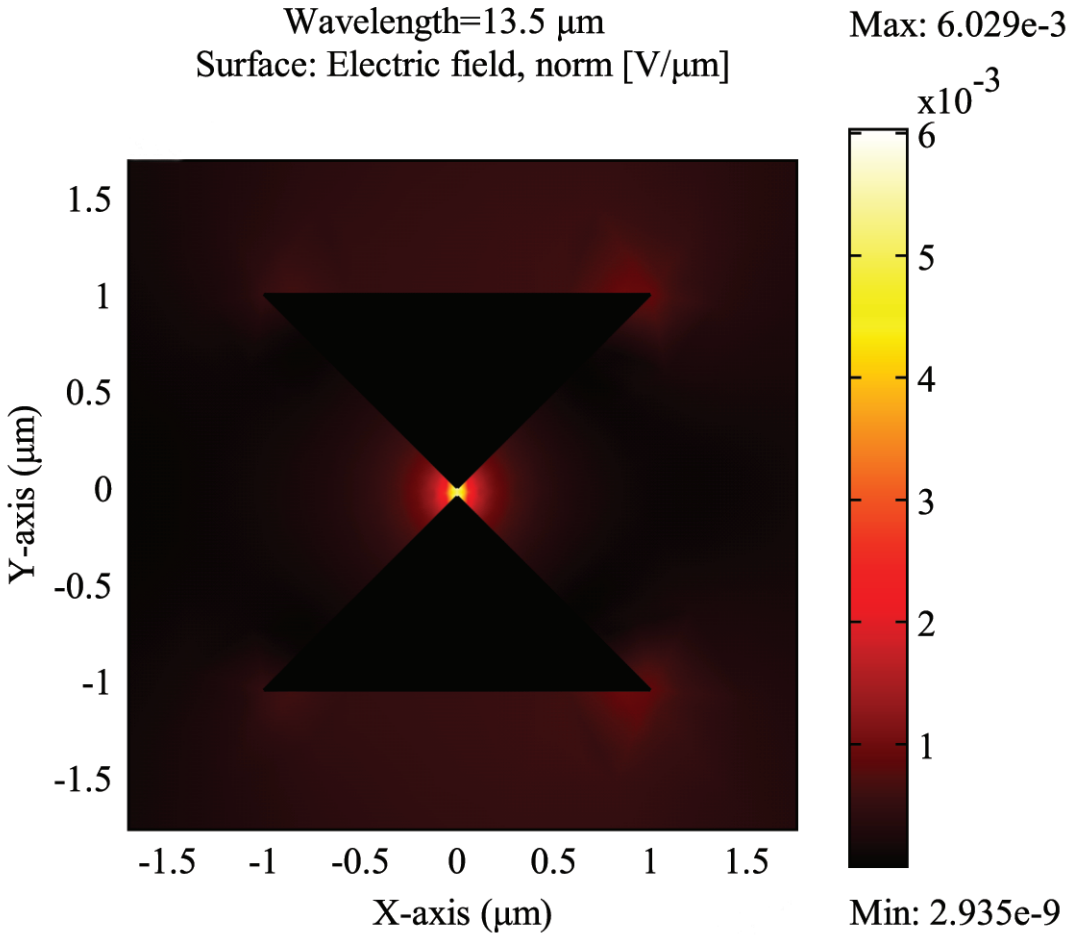

Figure 4.19: Electric field concentration in the gap of bowtie nanoantenna.

Fig. 4.20 shows the variation of the electric field as a function of the wavelength for the the bowtie nanoantennas. All the nanoantennas in this chapter exhibit a resonant wavelength around 13 μm, however, the magnitude of the captured electric field at resonance is different. It is clear that the spiral antenna has the largest value compared with the bowtie and the dipole nanoantennas, whereas the latter has the lowest value of electric field. The AUC is calculated for each type and the values are 0.012, 0.014, 0.0097 and 0.019 μV for the dipole, square spiral, logarithmic spiral and bowtie nanoantennas, respectively. It is thus demonstrated that the bowtie nanoantenna has larger AUC compared with the other types, which is more advantageous in this application.

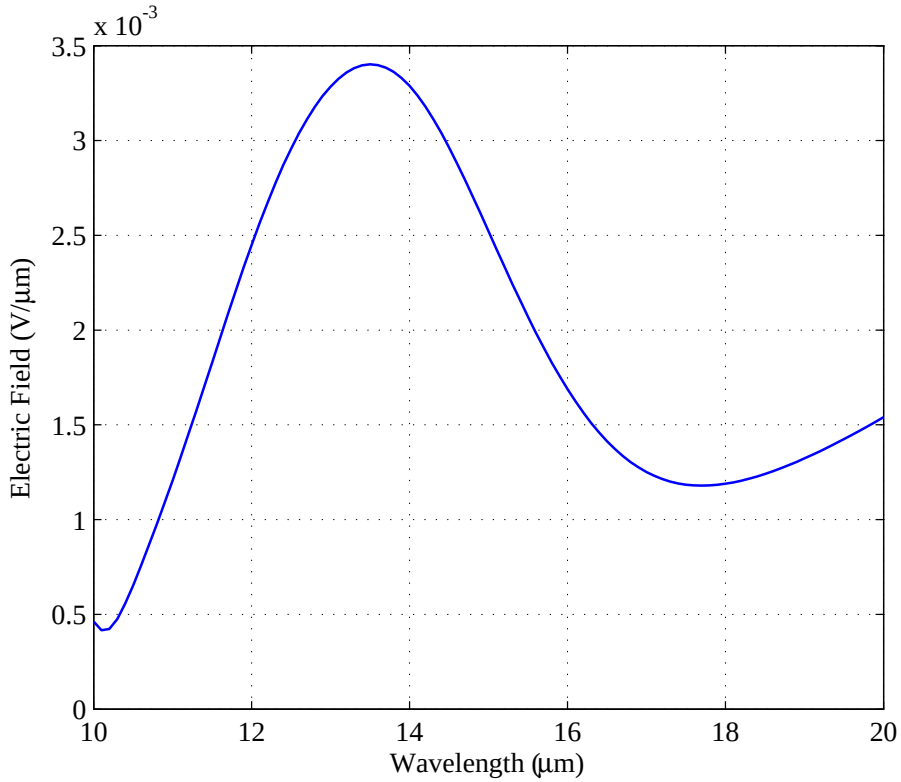

Figure 4.20: Variation of the electric field versus wavelength for the designed bowtie nanoantenna.

4.3 Polarisation Response

In polarisation division multiplexing (PDM) systems, it is possible to send/receive two carrier wavelengths with different polarisation by a single antenna, which should have a high polarisation discrimination ratio (i.e. sensitive to polarisation) [52]. However, in the solar energy harvesting application it is preferred that the nanoantenna exhibits lower polarisation discrimination ratio and responds well to both orthogonal polarisations (x- and y-polarisation). A simulation procedure was performed to calculate the polarisation ratio for the four nanoantennas at their resonance. Two orthogonal plane waves have been launched and the responses of the nanoantennas at the resonant wavelength were recorded. Subsequently, the polarisation discrimination ratio was calculated for each antenna. Figs. 4.21, 4.22, 4.23 and 4.24 show the response (in dB) to two orthogonal plane waves against the wavelength for the dipole, square spiral, logarithmic spiral and bowtie nanoantennas, respectively. It is shown from the figures that the logarithmic spiral nanoantenna has the lowest polarisation discrimination ratio of 4.1 dB , whereas the ratios of the square spiral, dipole and bowtie nanoantennas were 7.25 dB, 21.95 dB and 50.46 dB, respectively. Numerical simulations showed that although the logarithmic spi-

ral nanoantenna exhibits lower polarisation ratio, its geometry is not suited for antenna array configurations. Furthermore, the computed AUC was lower compared to the bowtie structure too.

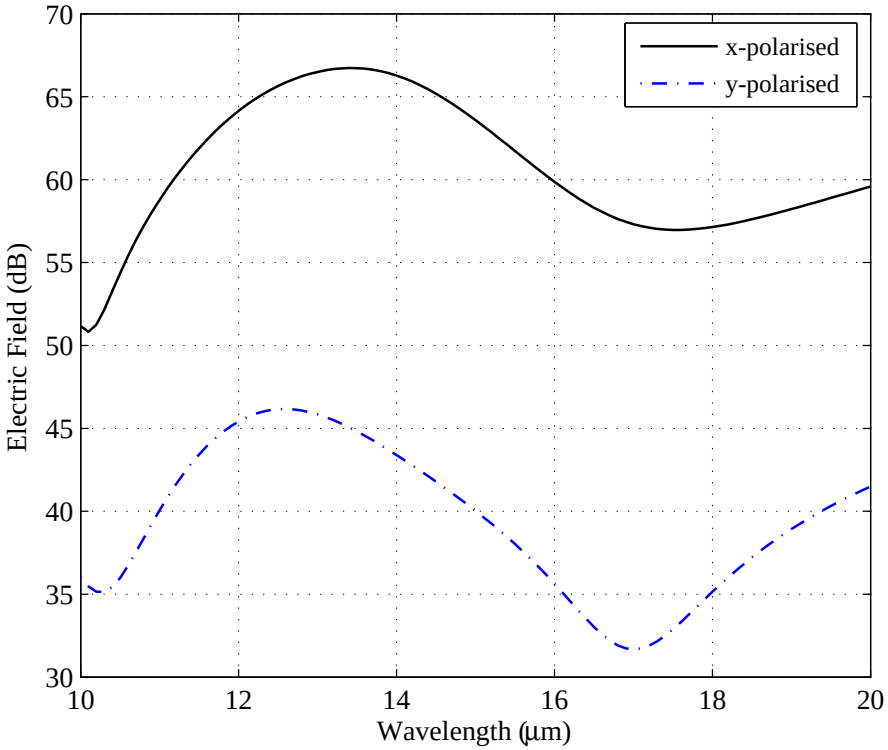

Figure 4.21: Response of the dipole nanoantennas to two orthogonal polarisations.

4.4 Increasing The Near-field Enhancement By Coupling More Antenna Elements

In the single-element case, the captured signal is often not sufficient to drive the rectifier. Thus, it is necessary to increase the gain of the receiving antenna by increasing its electrical size. This can be accomplished by assembling the single-element antennas in an electrical and geometrical configuration, which is referred to as an *array*. The total field captured by the array is determined by the vector addition of the fields captured by the individual elements. This assumes that the fields from the elements of the array interfere constructively.

The factors that control the overall performance of an array with identical elements are [13]:

- geometrical configuration.

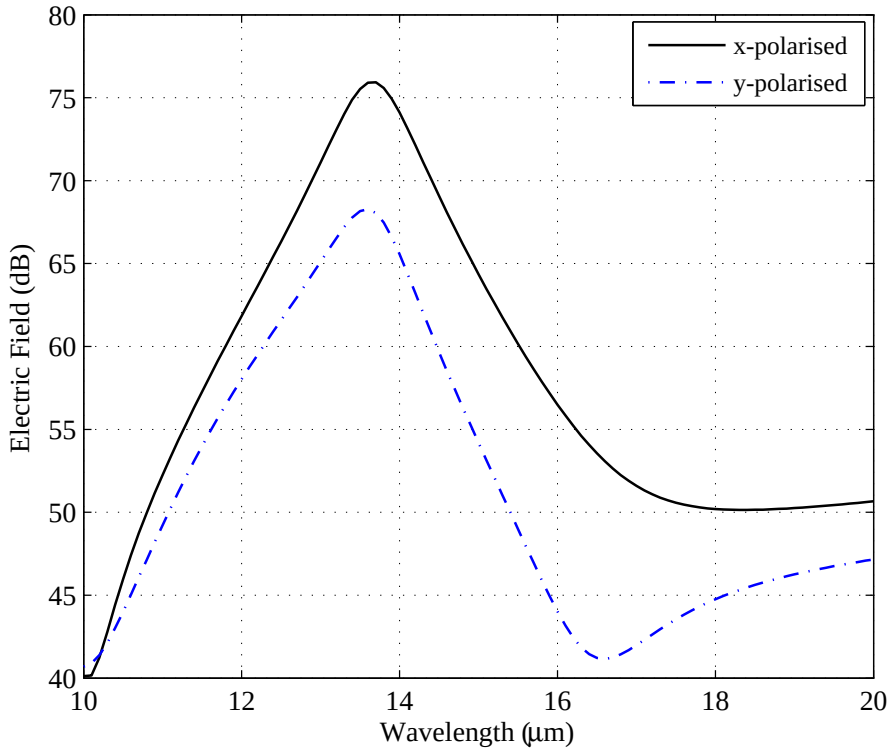

Figure 4.22: Response of the square spiral nanoantennas to two orthogonal polarisations.

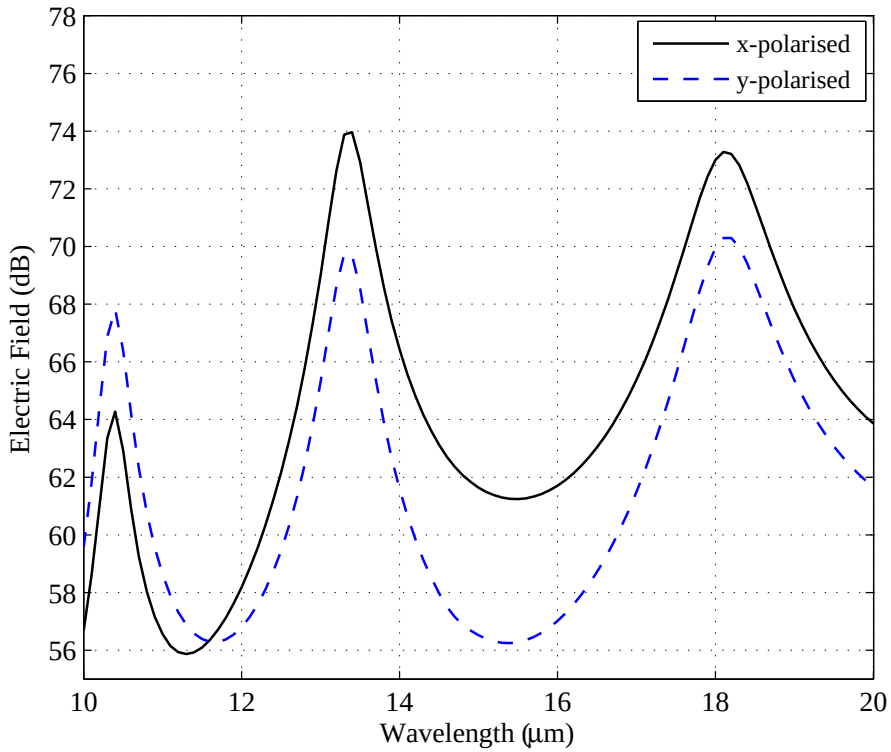

Figure 4.23: Response of the logarithmic spiral nanoantennas to two orthogonal polarisations.

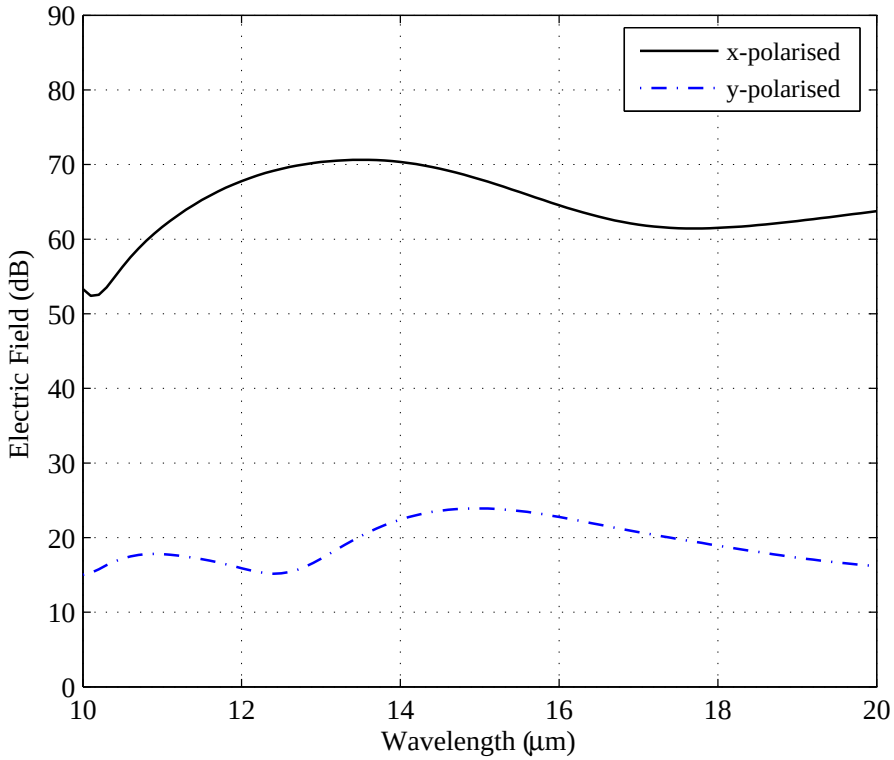

Figure 4.24: Response of the bowtie nanoantennas to two orthogonal polarisations.

- space between the elements.
- excitation amplitude and phase of the elements.
- relative pattern of the individual element.

The single-element antennas can be placed and positioned along a rectangular grid to form a planar array. Planar arrays can be used to control the pattern of the array, and they can also be used to scan the main lobe of the array toward any point in the space. The total field captured by the planar array is equal to the field of a single element in the array multiplied by the array factor ($AF(\phi, \theta)$). In order to find the array factor for a planar array, let us assume that we have K identical elements placed along the x-axis (linear array). The array factor of these elements can be written as [13]

$$AF(\phi, \theta) = \sum_{k=1}^{K} I_{k1} e^{j(k-1)\delta_x}, \tag{4.14}$$

where

$$\delta_x = \beta_o d_x \sin\theta \cos\phi + \beta_x, \tag{4.15}$$

and I_{k1} is the excitation coefficient of each individual element in the array, d_x is the

spacing between elements along the $x-axis$ and β_x is the phase shift. If L such arrays are placed along the $y-axis$ with a spacing d_y and phase shift β_y, a planar array will be formed. The array factor of the formed planar array can be written as

$$AF(\phi,\theta)=\sum_{l=1}^{L} I_{l1}\left(\sum_{k=1}^{K} I_{k1}e^{j(k-1)\delta_x}\right)e^{j(l-1)\delta_y}. \tag{4.16}$$

where

$$\delta_y=\beta_o d_y\sin\theta\cos\phi+\beta_y. \tag{4.17}$$

If the excitation amplitude of the entire array is uniform, (4.16) can be normalised to

$$AF(\theta,\phi)=\frac{1}{K}\frac{\sin(\frac{K}{2}\delta_x)}{\sin(\frac{\delta_x}{2})}\ \frac{1}{L}\frac{\sin(\frac{L}{2}\delta_y)}{\sin(\frac{\delta_y}{2})}. \tag{4.18}$$

In the following subsections we will demonstrate coupling two, or more, elements to form bowtie, square spiral and logarithmic nano-arrays.

4.4.1 Bowtie nano-array

A 2×2 bowtie nano-array is designed to increase the captured electric field. This array is constructed by four bowties with no gap between the bowtie's triangles, and 60 nm feeding lines are used to collect the electric field from the feed gap of the array elements. This design, although simple, offers a higher electric field than that of a single element antenna. The dimensions of this array are 3.6×3.6 μm with a feeding gap size of 60 nm and the metal area is 3.36 μm^2. Fig. 4.25 (a) and (b) shows respectively the configuration of the nano-array and the concentration of the captured electric field at its feeding point. Furthermore, the variation of the captured electric field versus the wavelength is shown in Fig. 4.26. It is seen that the nano-array resonates at 13.5 μm, which is the same resonant wavelength of the single elements, however, the array generates a higher electric field at the array gap. The AUC for the designed nano-array is 0.04 μV which is higher than that of single elements.

4.4.2 Square spiral nano-array

Three gold-based square spiral nano-antennas have been designed to resonate near 13 μm. The first design comprises a single spiral element while in the second design, two spiral elements have been coupled together in one structure that has one common gap by using

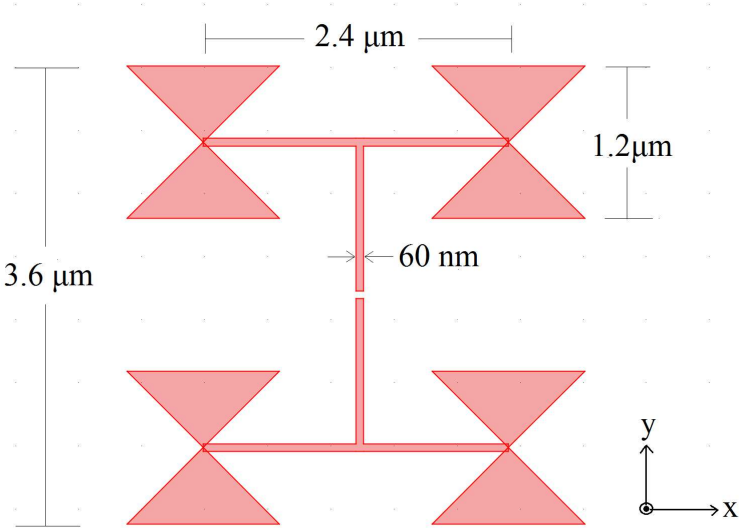

(a)

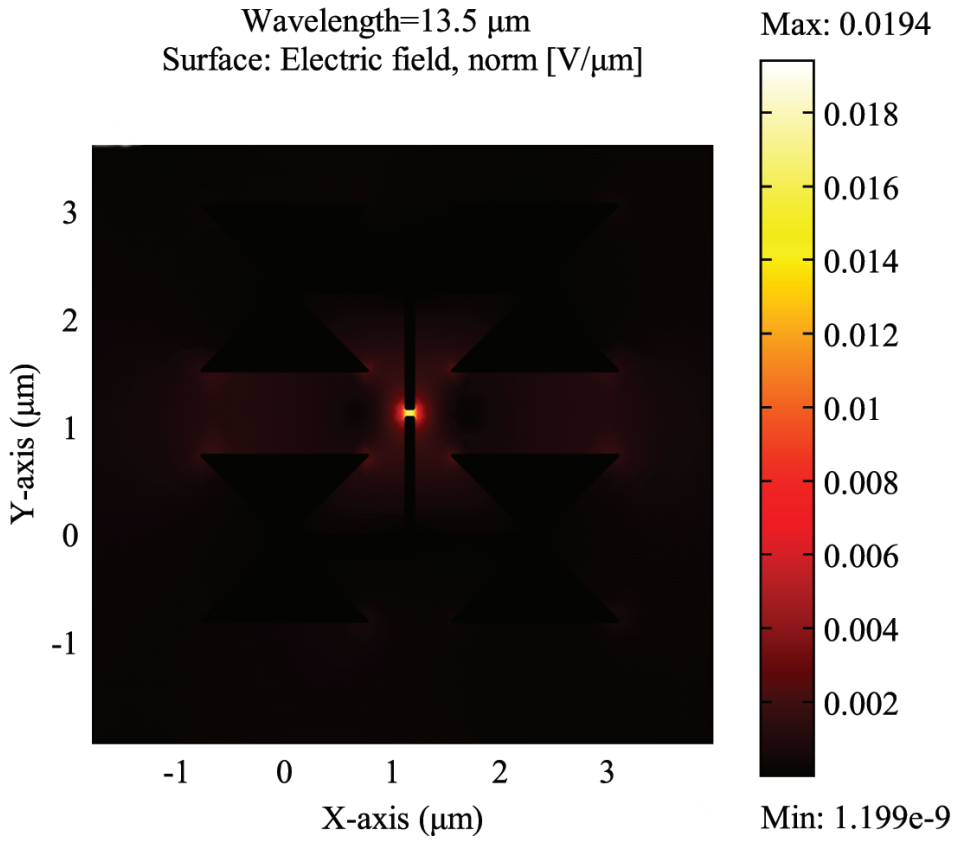

(b)

Figure 4.25: Bowtie nano-array: (a) Array configuration; (b) Concentration of the electric field at the feeding point of nano-array.

feeding line as shown in Fig. 4.27(b). In addition, Fig. 4.27(c) shows four spiral elements coupled together in one single array with one common gap. All the single elements in Fig. 4.27 have the same dimensions of the spiral in Fig. 4.27(a).

The captured electric fields inside the gap of the two and four element nanoantennas

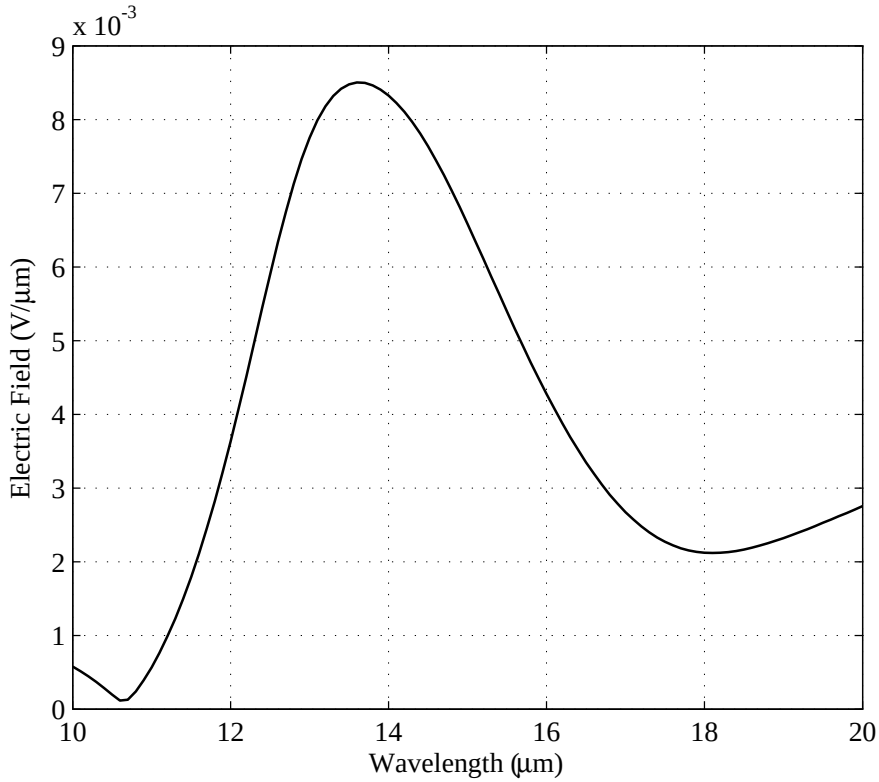

Figure 4.26: Variation of the electric field versus wavelength for the designed nano-array.

have been calculated and plotted versus the wavelength as shown in Figs. 4.29 and 4.30, respectively. It is evident that the four-element array has the largest value of the captured electric field compared with the two-element and the single spiral nano-antennas, whereas the latter has the lowest value. The AUC is calculated for each spiral antenna of Fig. 4.27 and their values are 0.0012, 0.0063, and 0.0132 μV for the single, two and four-element spiral nano-antennas, respectively. It is thus demonstrated that the four-element array exhibits the largest AUC compared with the other types. Table 4.1 summarises the simulation results of the designed spiral nano-antennas. In this application, a suitable rectifier (usually MIM diode) needs to be embedded in the feed gap (hot spot in Fig. 4.31) to rectify the captured signal, thus, in the four-element array design only one rectifier is required. This will reduce the rectifier related thermal losses, and hence, improve the efficiency of the overall system.

4.4.3 Logarithmic spiral Nano-array

In order to increase the captured electric field for the logarithmic spiral nanoantennas, two antenna elements have been combined together by using feeding lines as shown in Fig. 4.32(a). The new structure offers larger electric field in the gap region and larger

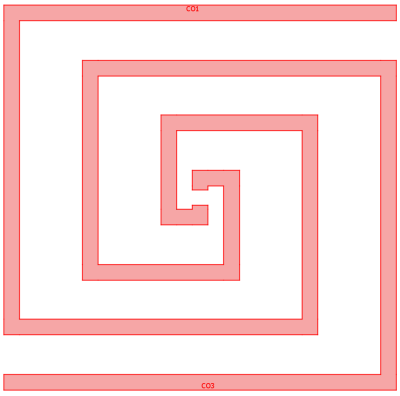

(a)

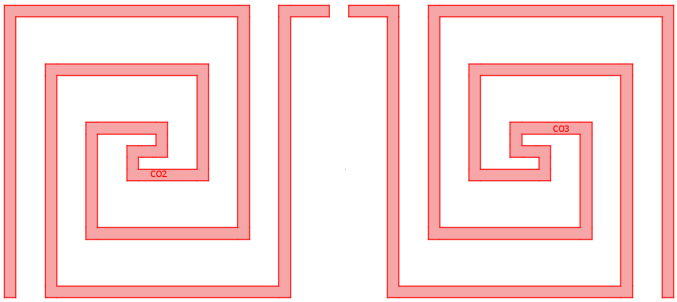

(b)

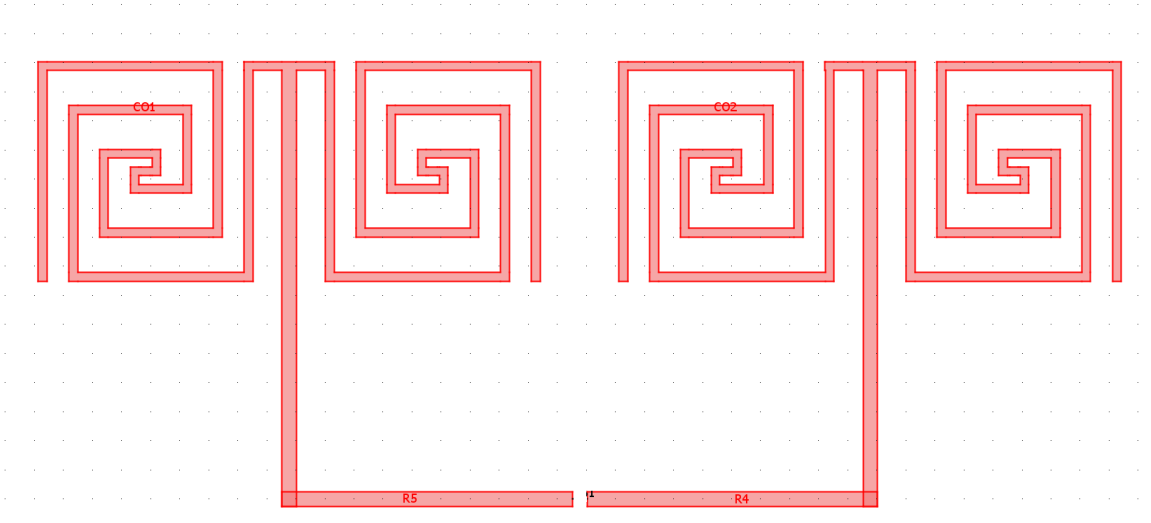

(c)

Figure 4.27: Square spiral nanoantennas: a)single-, b)two- and c) four-element configuration.

AUC as compared with all the spiral nano-antennas as demonstrated in Fig. 4.32(b). The calculated AUC for the single and the two-element logarithmic spiral nano-antennas are 0.0097 and 0.0533 μV, respectively. It is evident that the electric field has been concentrated in the gap region as shown in Fig. 4.33, where a MIM diode can be embedded

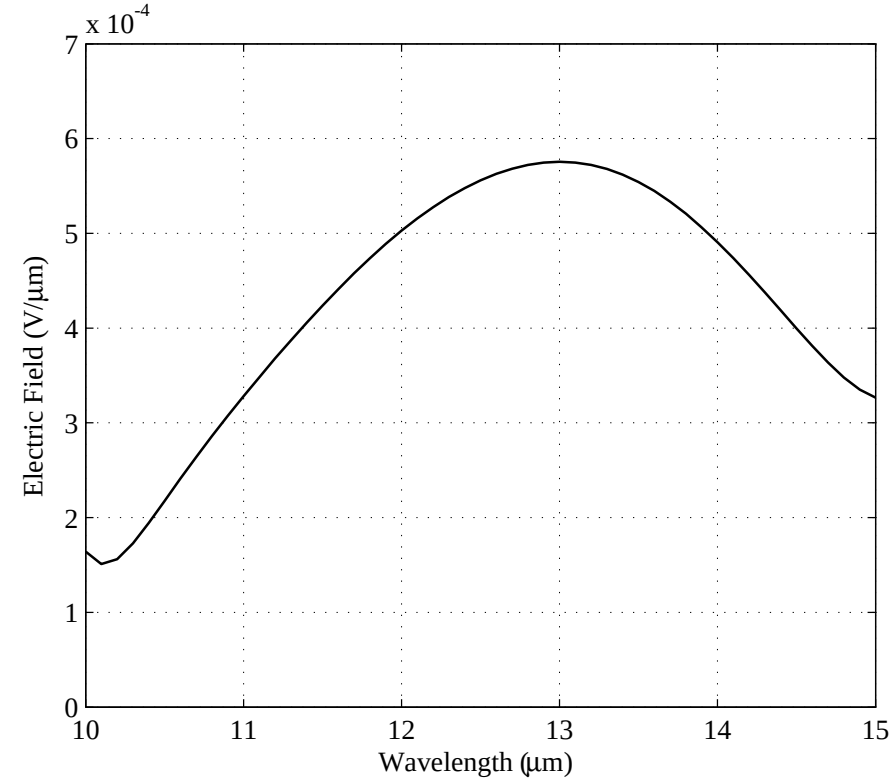

Figure 4.28: Variation of the electric field versus wavelength for the single spiral element

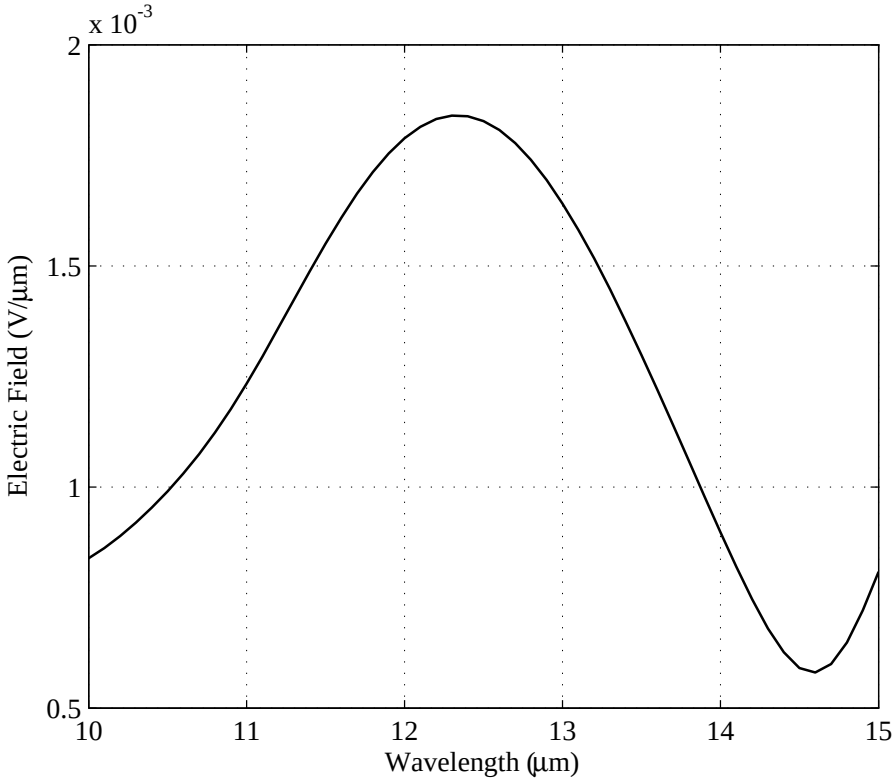

Figure 4.29: Variation of the electric field versus wavelength for the two-element spiral nano-array

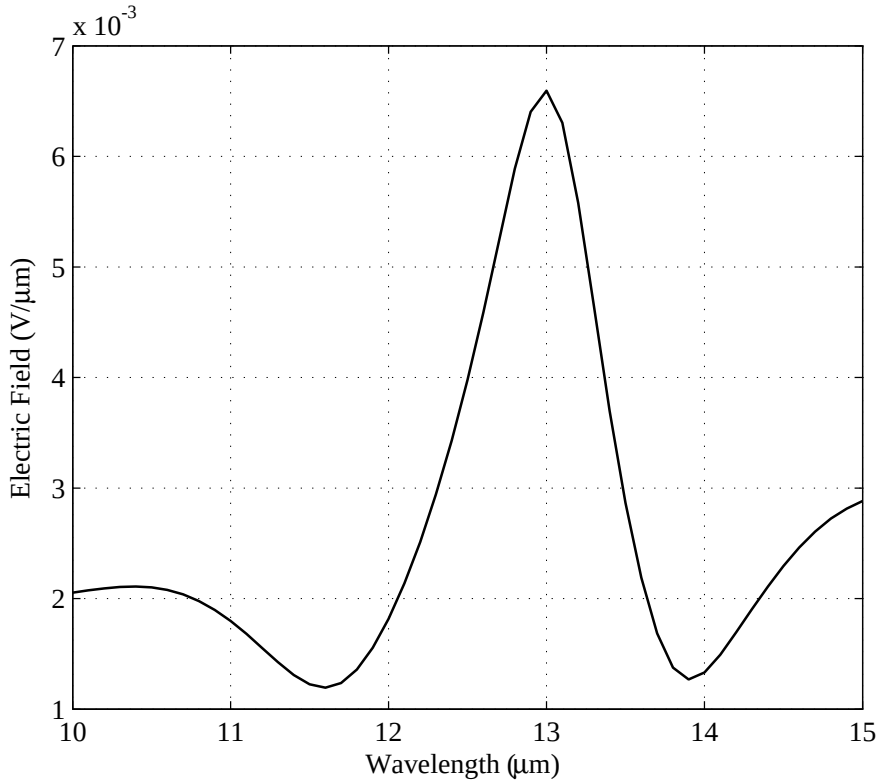

Figure 4.30: Variation of the electric field versus wavelength for the four-element spiral nano-array

Table 4.1: Comparison of the performance for three spiral configurations.

Array Elements	Resonant Wavelength (μm)	MAx E-field (V/μm)	A U C (μV)
Single	13	0.575×10^{-3}	0.0012
Two	12.3	1.84×10^{-3}	0.0063
Four	13	6.58×10^{-3}	0.0132

to rectify the captured signal. Assuming perfect rectification, an open circuit voltage per unit area of more than 400 V/m^2 can be achieved from the two-element logarithmic spiral nano-antenna compared to approximately 40 V/m^2 obtained from commercial photovoltaic panels [96].

4.5 Using Auxiliary Ring Resonator for Local Field Enhancement at The Feed Gap

Due to the geometrical convenience of dipole nanoantenna, it has been chosen in this work to be the main resonator that hosts the rectifier. However, the captured (confined) electric field at its gap is weak and needs to be further improved. To this end, an auxiliary

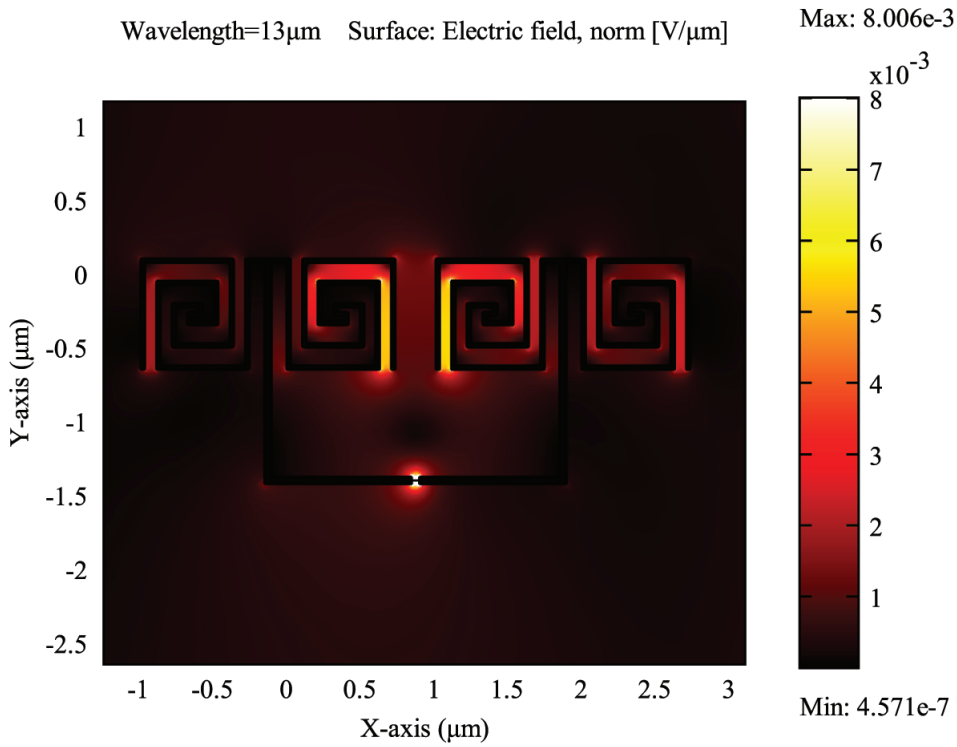

Figure 4.31: Electric field concentration in the gap of the four-element spiral array.

resonant element has been added to the structure in order to increase the captured field, and hence, improve the overall performance. Thus, in this approach, two elements will contribute in increasing the captured field at the antenna gap while only one rectifier is needed instead of two. That means we reduced the thermal losses in the rectifiers and increased the total efficiency of the rectenna.

Firstly, the dipole nanoantenna of Fig. 4.9 has been simulated and the captured field at the feed gap has been recorded as shown in Fig. 4.11. After that, a ring of 729 nm inner diameter and 40.5 nm width is also simulated separately on the same substrate and same boundary conditions, where the recorded electric field at the 40.5 nm feed gap is shown in Fig. 4.34.

It is clearly shown from results that the ring confines more energy at the feed gap than the dipole. If we put the ring in close proximity to the dipole (26 nm space), it is expected that the mutual coupling between the two elements will play a significant role in increasing the captured electric field of any of them. It is therefore expected that we might obtain a high electric field from this combination that overcome the captured field provided by single element, where the ring acts as a loop antenna.

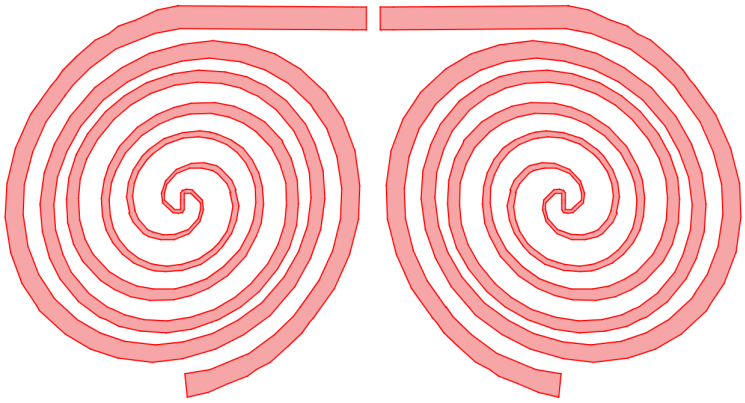

(a)

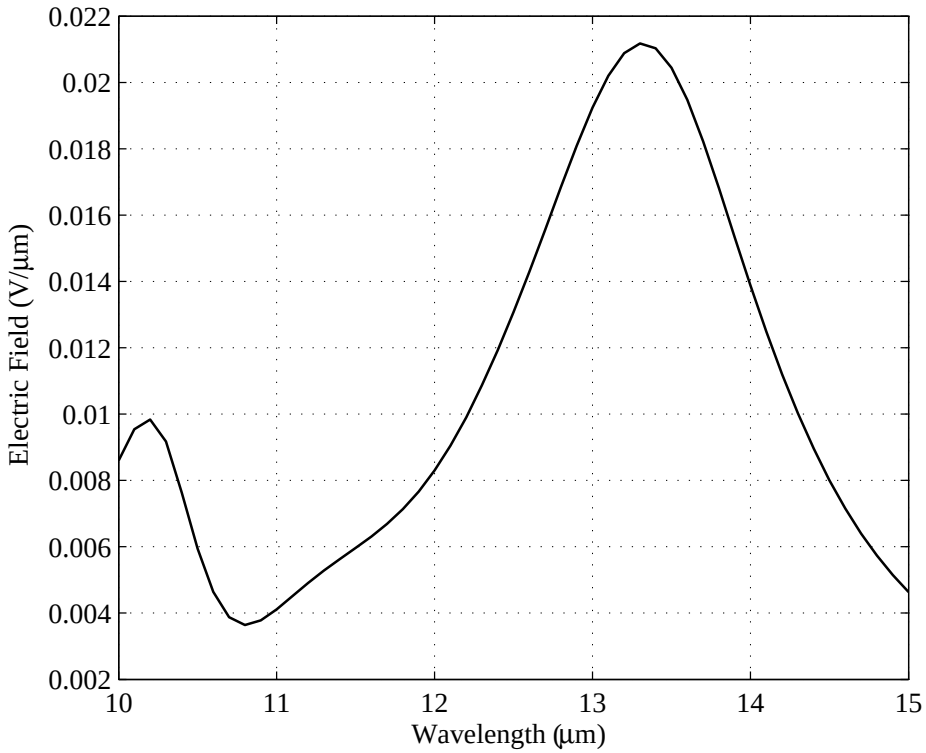

(b)

Figure 4.32: Two-element logarithmic spiral nanoantenna: a)antenna configuration, b)variation of the electric field versus the wavelength.

Fig. 4.35 illustrates the captured electric field at the feed gap of the dipole antenna, where it is obvious that the resulted field is higher than that given from single element. However, it can be seen that the resonant wavelength has been shifted from 12 μm to 13 μm due to the increased electrical length of the structure. However, this change in the resonant wavelength is trivial and the solar rectenna is still operating at the wavelength of interest. Fig. 4.36 depicts the highly localized electric field at the common gap of the

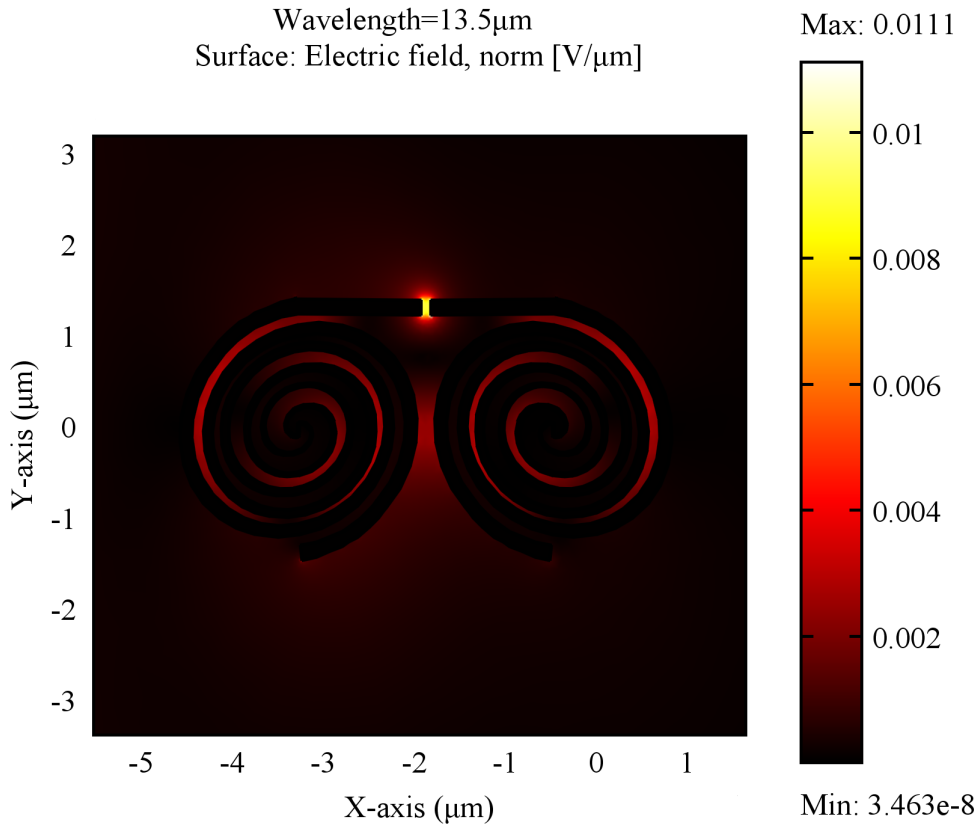

Figure 4.33: Electric field concentration in the gap of the two-element logarithmic spiral nano-antenna.

designed solar rectenna, where the rectifier is supposed to be embedded.

4.5.1 The effect of the distance between the ring and the dipole

The distance, d, between the ring and the dipole has been varied from 16 nm to 56 nm in steps of 10 nm to study its effect on the performance. It is expected that the distance has a direct impact on the mutual coupling between the elements, and hence, on the overall performance of the structure.

Fig. 4.37 illustrates the variation of the electric field versus the wavelength for different values of d. It is shown that the closer the distance the higher the electric field captured. It is also proved that the distance has trivial impact on the resonant wavelength. Thus, the distance should be adjusted carefully taking into account the shift in the resonant wavelength.

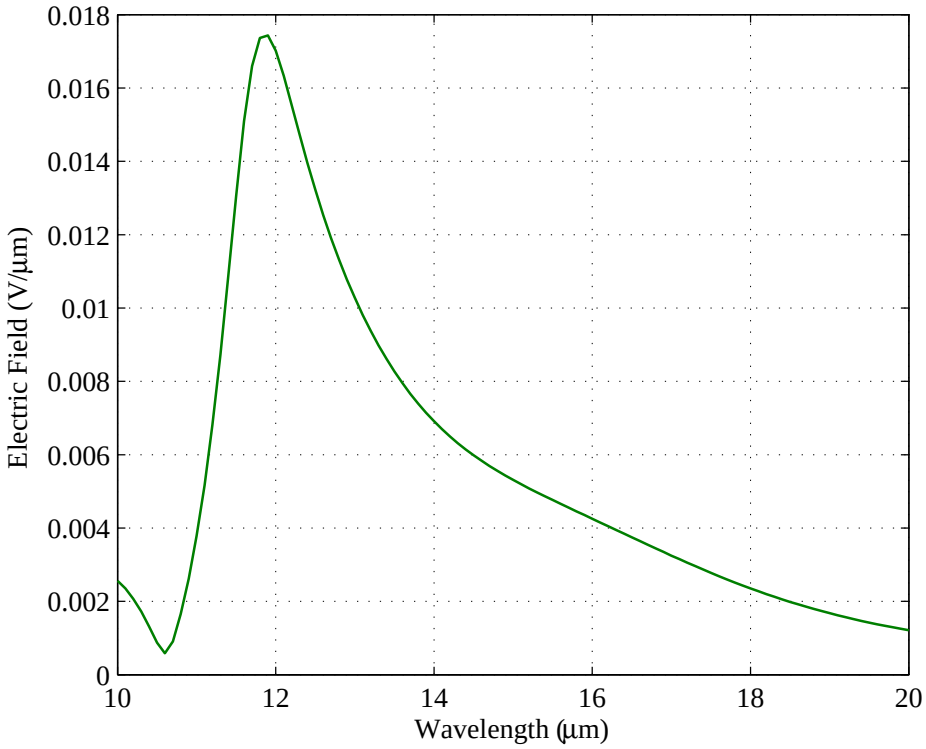

Figure 4.34: Variation of the captured electric field versus the wavelength of the circular ring.

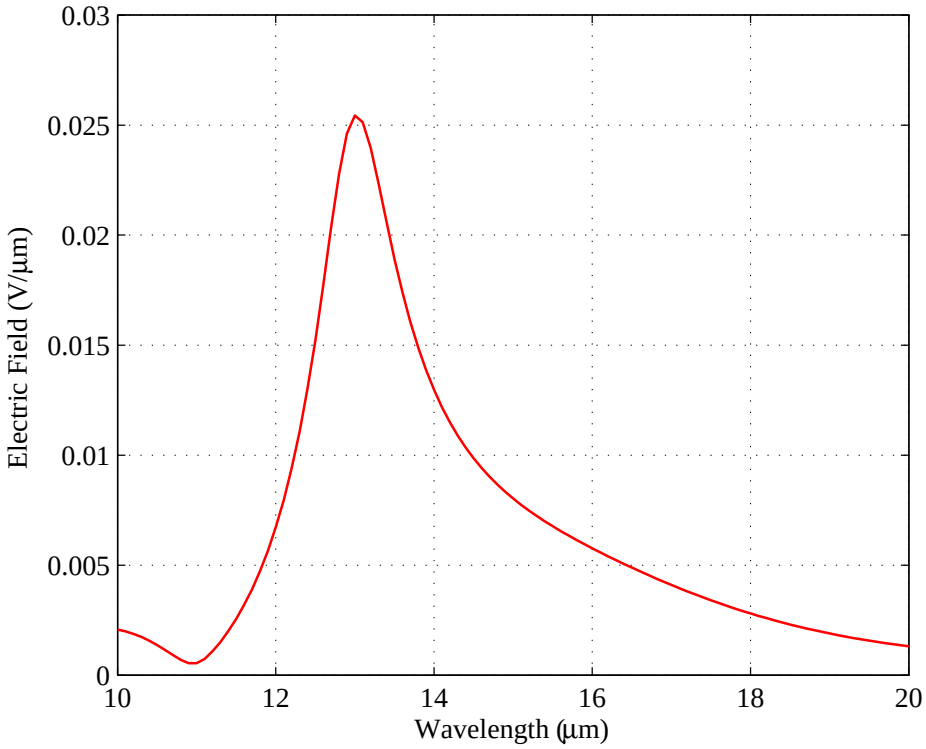

Figure 4.35: Variation of the captured electric field versus the wavelength of the designed solar rectenna.

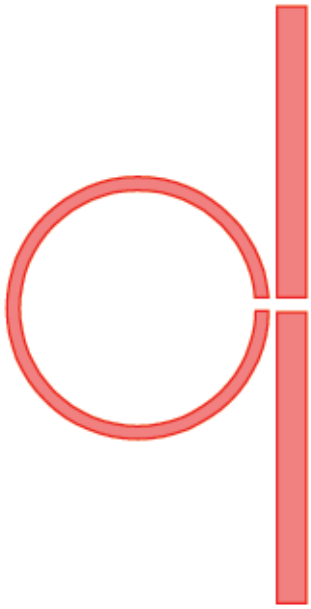

(a)

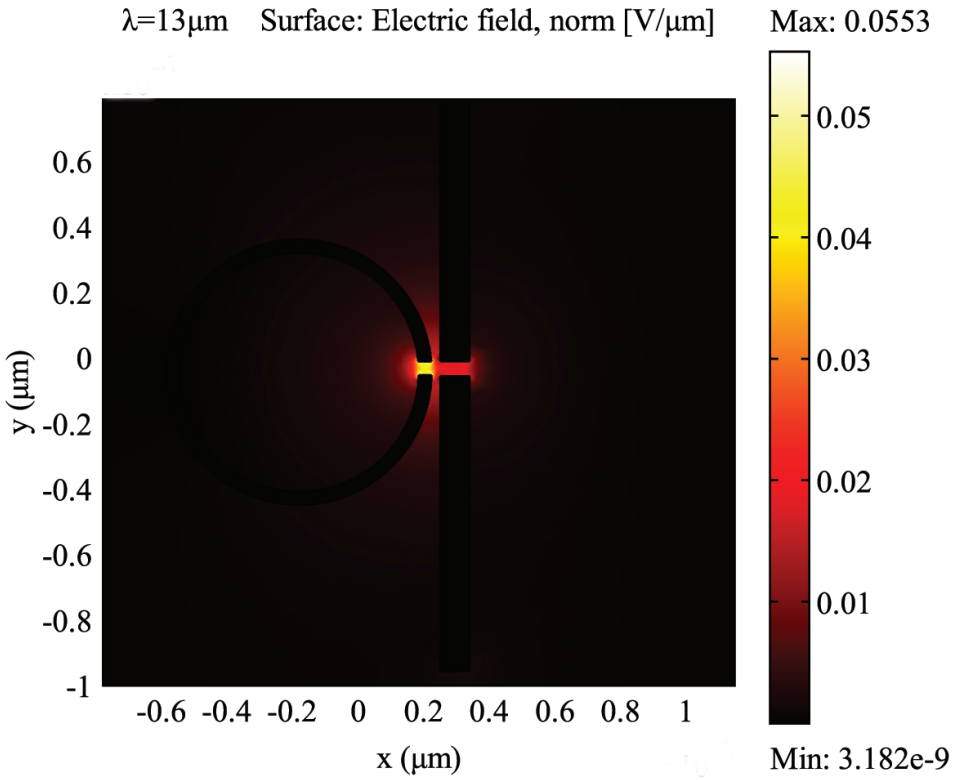

(b)

Figure 4.36: The designed solar rectenna with an auxiliary resonator ring: (a) rectenna configuration; (b) Concentration of the electric field at the common feed gap of the solar rectenna.

4.5.2 The effect of the geometrical shape of the ring

In the previous design a circular ring is used as an auxiliary resonator to boost the performance of the dipole. In this section, different geometries will be used to find their effect

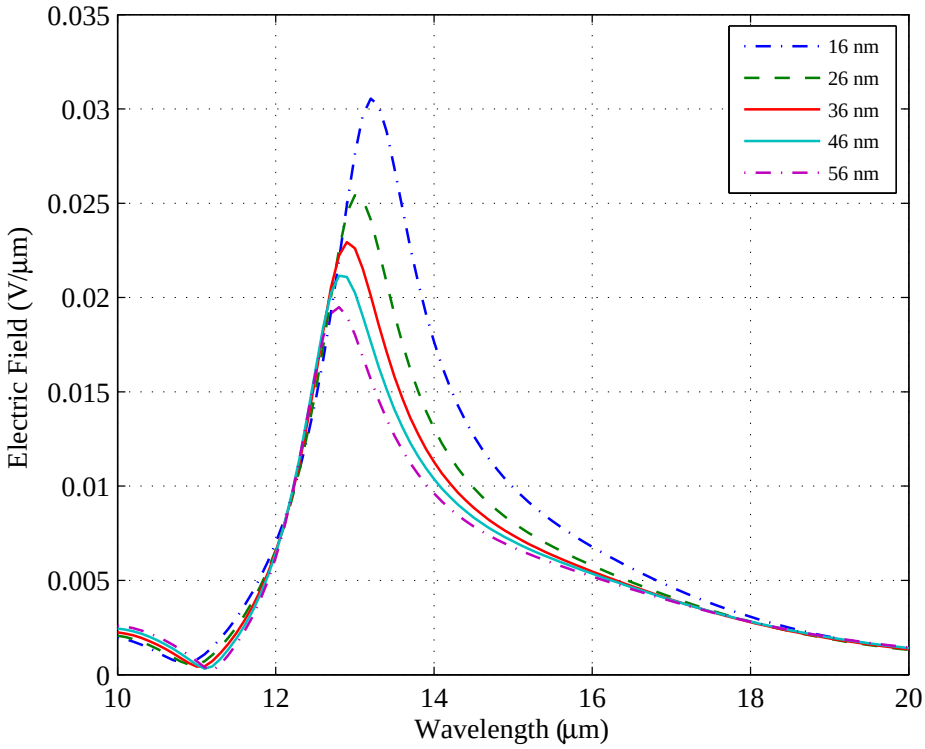

Figure 4.37: Variation of the captured electric field versus the wavelength for different values of the distance d.

on the performance. The circular ring has been replaced with an elliptical ring that has dimensions of $1.35\ \mu$m $\times$ 441 nm and a rectangular ring of dimensions $1.69\ \mu$m $\times$ 275 nm as shown in Figs. 4.38 and 4.39.

The performance of the three geometries (i.e circular, elliptical and rectangular rings) have been compared in Fig. 4.40. It can be seen that the circular ring has the best performance in terms of the captured electric field in the gap, whereas, the elliptical ring has the lowest field at the gap.

Although the difference in performance between the three geometries is trivial, the circular ring preferred due to its smaller footprint. The arms of the dipole antenna can be overlapped in a small area to form a metal/insulator/metal (MIM) diode in order to rectify the captured energy. Fig. 4.41 depicts the schematic view of the constructed solar rectenna, where the red area represents the thin insulator layer that sandwiched between the dipole's arms. In this design, the ring will contribute in increasing the electric field around the MIM diode which will convert the received signal from AC to DC. This structure is easy to manufacture and can be extended into large array by replication to produce efficient rectenna solar panels.

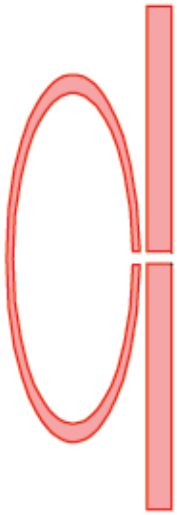

Figure 4.38: Elliptical ring as auxiliary element with the dipole antenna.

Figure 4.39: Rectangular ring as auxiliary element with the dipole antenna.

4.6 Chapter Summary

In this chapter, dipole, bowtie, and spiral nanoantennas have been investigated for solar energy collection and a comparison between their performances has been presented. The results showed that the spiral nanoantenna exhibited the largest captured electric field at resonance, whereas the bowtie nanoantenna demonstrated the widest bandwidth amongst them.

Starting from a single element, the design extended to an array in order to increase the captured electric field and to reduce the number of MIM diodes, which in turn leads to improved system efficiency. The results showed that the two-element logarithmic spiral

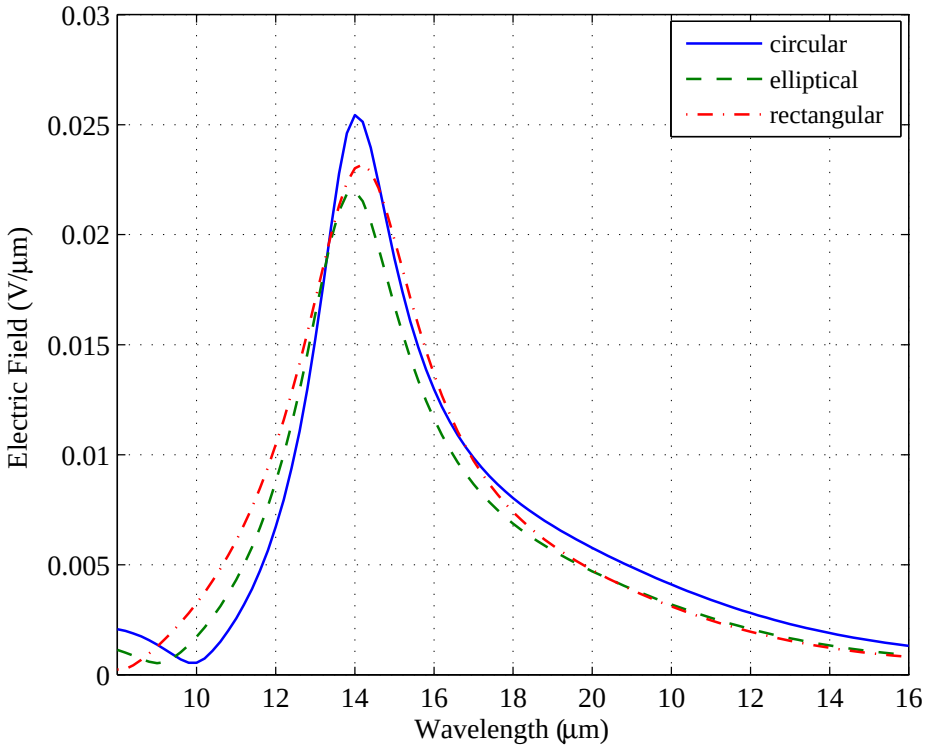

Figure 4.40: Comparison of the captured electric field versus the wavelength for the three types of rings.

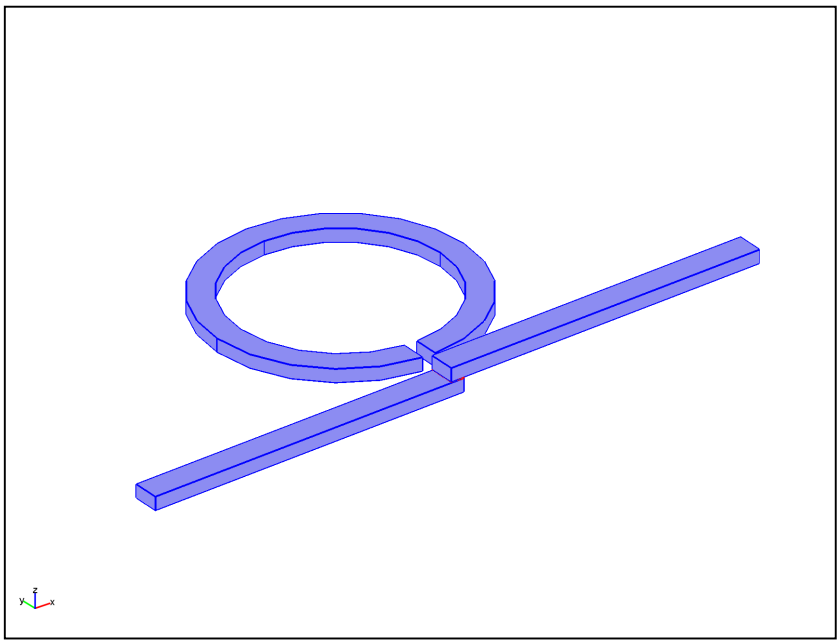

Figure 4.41: 3D schematic view of the solar rectenna showing the overlapping between the dipole arms to form the MIM diode. The red area represents the insulator layer.

nanoarray exhibited the largest captured electric field at resonance and the largest AUC. Additionally, the two-element logarithmic spiral nanoarray showed lower discrimination

ratio when illuminated with two orthogonal polarised waves. Furthermore, the spiral nanoarrays presented in this chapter are easy to fabricate compared with the structures presented in previous works.

The design of the bowtie nanoantenna was extended to an array due to the geometrical convenience of the bowtie structure. A 2×2 bowtie nano-array has been designed and the performance results showed that the captured electric field was more than twice the field captured by the single element at the same wavelength. Alternative complex structures need to be fabricated using electron-beam lithography, which is expensive and used for research purposes only. However, the bowtie nanoantenna element is a good candidate to be the focus of future works to design larger and more efficient arrays.

Finally, we introduced the use of an additional resonator element to boost the performance of the dipole nanoantenna for solar energy harvesting. The auxiliary element in this chapter is a ring that acts as a loop antenna. The main idea behind using auxiliary element is to increase the captured electric field inside the gap of the main resonator and to reduce the number of rectifiers, which in turn will help in reducing the losses and increasing the total conversion efficiency. The distance between the ring and the dipole has been varied and it is found that the captured electric field is higher when the ring is closer to the dipole. In addition, a study is conducted onto the geometrical parameters of the ring in order to increase the performance. Elliptical and rectangular rings are used and their performances have been compared with the circular one. It is found that the circular ring performs better than the other two and the elliptical ring has the lower field at the gap. Thus, the circular ring is the best choice in this application due to its smaller size and better response.

In the following chapter, we will study the coupling of more elements to form larger arrays in order to increase the power rectified by each individual array, and thus, reduce the number of rectifiers required per unit area.

Chapter 5

Parametric Study of Nanogap-based Planar Bowtie Nanoarrays

This chapter focuses on the design and optimisation of nanoarrays, where the characteristics of bowtie nanoarrays at infrared wavelengths ($10\,\mu\mathrm{m}$ - $200\,\mu\mathrm{m}$) will be investigated for utilisation in solar energy collection. The aim is to improve the performance and to increase the captured energy by coupling many elements in one structure has a common feed gap. This will therefore reduce the number of rectifying diodes, and hence, decrease the loses and increase the overall system efficiency as presented in [97] and [98]. The chapter is organised as follows. Section 5.1 describes the design considerations and the issues that need to be taken into account before starting the design process of nanoantennas. The simulation model, the boundary conditions and the source excitation are also discussed. The performance of the bowtie nanoantenna is investigated in Section 5.2, where a study is conducted into the feasibility of using feeding lines to transfer the captured electric field away from the center of the antenna. In addition, a parametric study of the bowtie nanoarray is presented and its performance as a function of the geometrical parameters is investigated. A bowtie nanoarray is realised in Section 5.3 based on the optimised parameters from Section 5.2 to obtain maximum performance. Moreover, the effect of the angle of incidence and the sharpness of edges on the array performance are demonstrated in Sections 5.4 and 5.5, respectively. Moreover, Section 5.6 introduces the integration of a rectifier with the designed bowtie nanoarray, whereas, Section 5.7 demonstrates the main characteristics of MIM diodes. Finally, Section 5.8 summarises the main conclusions of this chapter.

5.1 Bowtie Nanoantennas

A bowtie antenna consists of two triangles facing each other from their apices with a suitable gap to form a dipole antenna as mentioned in Chapter 4 of this thesis. The performance of nano-gap bowtie antennas depends on many geometrical parameters, including bowtie size, apex angle, and gap size [93]-[94]. In this section, we will investigate the effect of the gap on the performance of a bowtie nanoantenna and the feasibility of using feeding lines to transfer the captured electric field away from the center of the antenna. The electric field is typically concentrated at the gap of the bowtie antenna due to the Coulomb field, and the gap will act as a capacitor [92]. Thus, for particles in the vicinity (i.e. a short gap) one can expect to obtain a strong electric field in the gap larger than that of isolated particles. The bowtie is a linearly polarised antenna that exhibits a broad beam perpendicular to the plane of radiation. The impedance of the bowtie antenna can be

calculated theoretically by transmission line theory [21], and can be changed by varying the flare angle, which may change the resonant wavelength slightly [95].

The dimensions of the designed bowtie nanoantenna are (2μm $\times$ 2μm) as shown in Fig. 5.1.

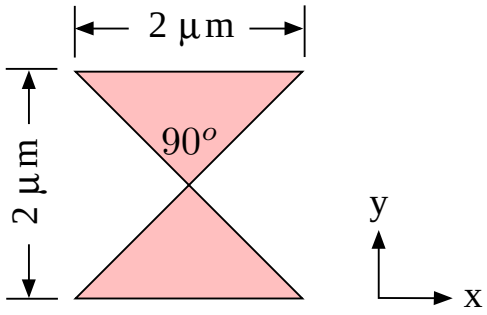

Figure 5.1: The structure of the bowtie nanoantenna.

Fig. 5.2 shows the effect of changing the gap size between the bowtie's triangles on the captured electric field where it is evident that the small the gap size, the higher the electric field captured. Fig. 5.3 illustrates the electric field concentration at the feed gap. It is seen that most of electric field concentrated at the feed gap whereas a very little field is found around the structure.

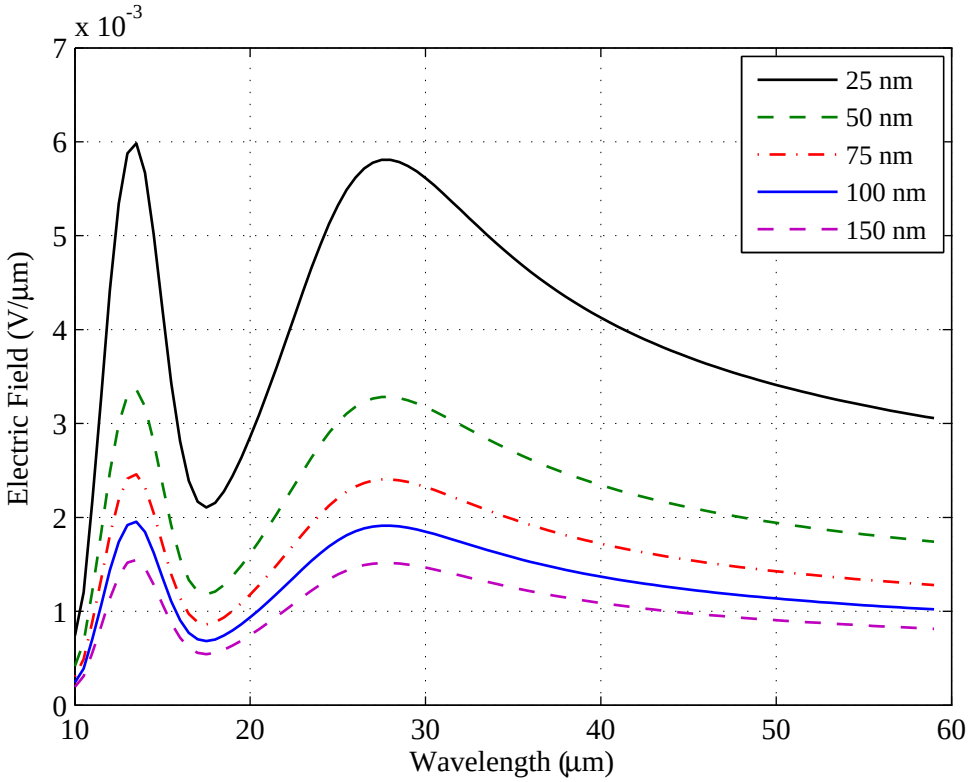

Figure 5.2: The variation of the electric field versus wavelength for different gap sizes.

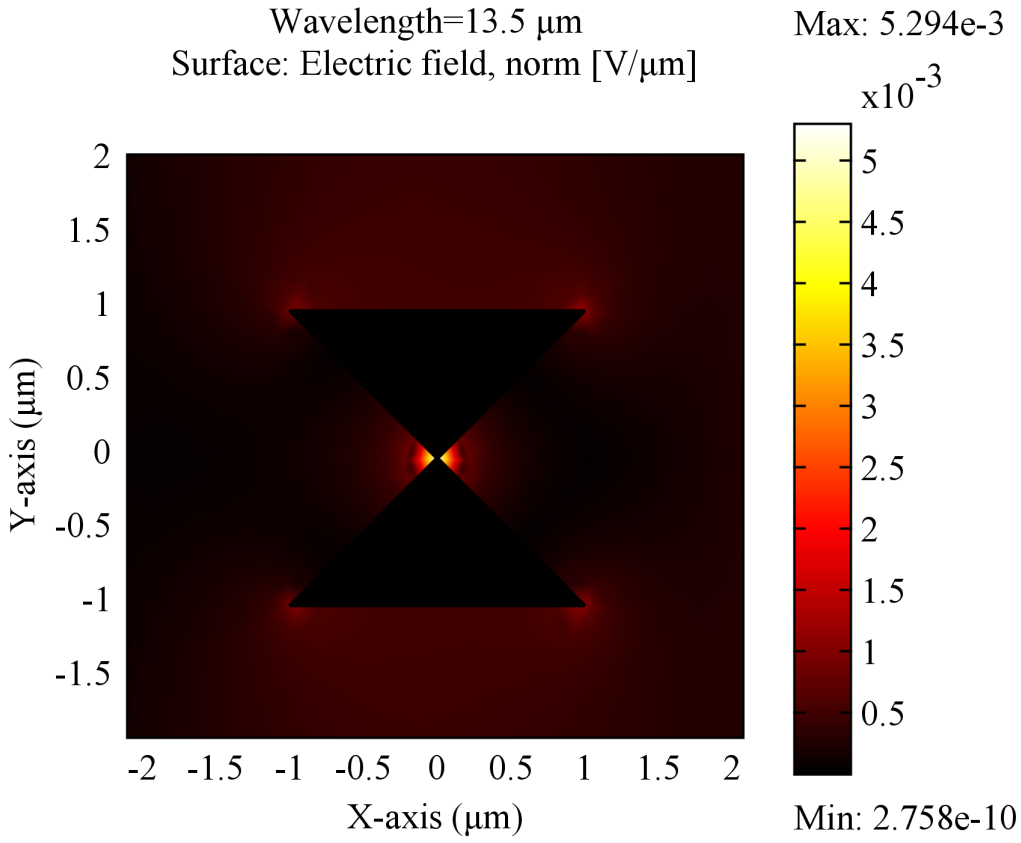

Figure 5.3: The concentration of the electric field at the contact point .

In this study, the bowtie's triangles have been designed to contact at their apices, i.e there is no gap between them, and the electric field at the bowtie's contact point has been calculated. Fig. 5.4 shows the captured electric field versus wavelength for this case.

It can be seen from Fig. 5.4 that the no-gap bowtie has less electric field than that of 25 nm gap, and a larger electric field than that with the 75 nm gap. Even the no-gap bowtie has fewer fields than that with the 25 nm gap, but it offers the possibility to combine it with a feeding line at the centre of the bowtie to collect the captured electric field away from the center, as shown in Fig. 5.5.

Although connecting the feeding line reduces the electric field, but nevertheless, it enables the use of array structures to recover for the loss and further improve performance. In the following section we will investigate coupling more elements connected by feeding lines to form an array in order to increase the captured electric field, which as far as we believe is the first attempt that deals with driving the captured field away from the nanoantennas towards a common feeding point. In such system, one rectifier is required for the whole array instead of one rectifier per single element. This approach will reduce the rectifier related thermal losses, and hence, improve the overall efficiency of the system.

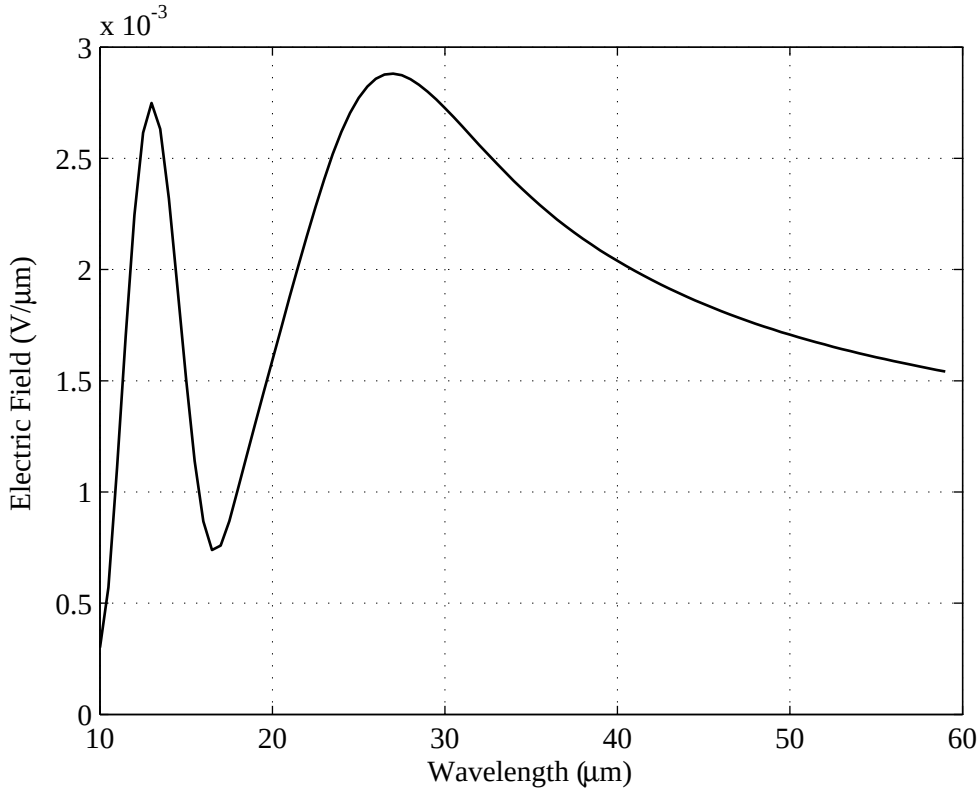

Figure 5.4: The variation of the captured electric field versus wavelength for the no-gap bowtie nano-aantenna.

5.2 Bowtie Nanoarray

Bowtie arrays have been utilised and studied due to their suitability for broadband operation, and due to the fact that they offer flexibility to optimise the radiation properties by adjusting their configuration [99]. In this work, a 2×4 bowtie planar nanoarray with a feeding network is designed to increase the captured electric field for solar energy collection applications. The elements in the array have an identical size of $2\,\mu\mathrm{m} \times 2\,\mu\mathrm{m}$ and an apex angle of 90^o. The array is placed on a dielectric substrate with dimensions of $37\,\mu\mathrm{m} \times 37\,\mu\mathrm{m}$. Furthermore, the feeding line width in all cases is $100\,\mathrm{nm}$.

By coupling many elements in an array form, the far-field characteristics will be improved and the amplitude will be increased [55]. The number of elements, N, and the spacing between elements, R, play a significant role in these improvements. The electric field is collected from each element by using feeding lines and subsequently concentrated in one *hot* spot. The following subsections will present a parametric study of this array and will investigate the performance as a function of the space between array elements, the width of feeding lines, w, and the gap size at the feeding point, g. The focus is now

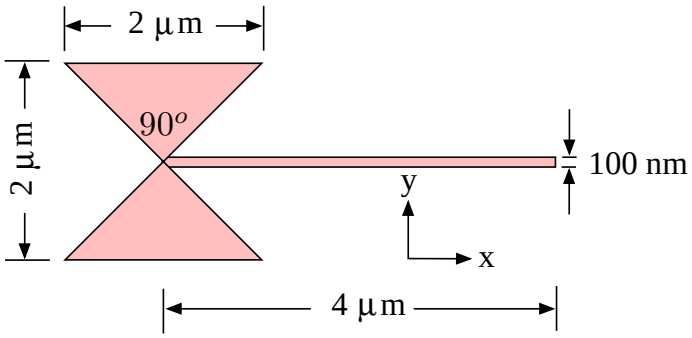

(a)

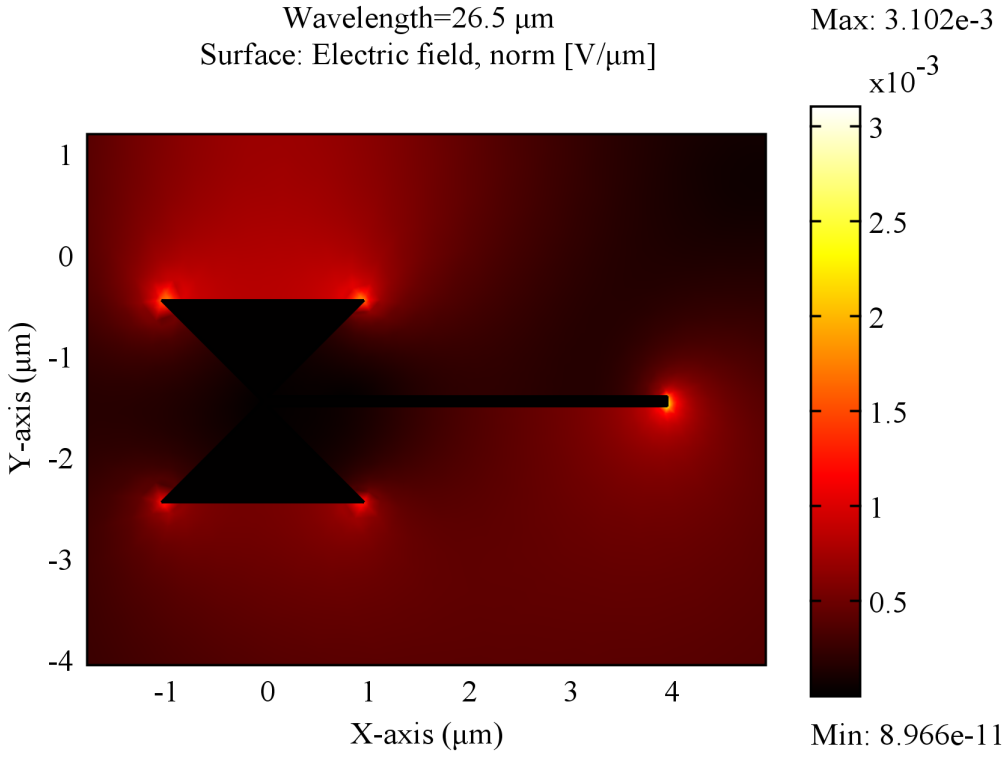

(b)

Figure 5.5: Connecting the bowtie to a feeding line: (a) Bowtie combined with feeding line; (b) Concentration of the captured electric field at the end of the feeding line.

concentrated on the design and optimisation of the bowtie nanoarray.

5.2.1 Effect of feeding lines configuration

The array elements can be connected using different approaches, however, each approach has its own effect on the overall performance [100]. In this work we will focus on three different configurations for connecting the elements of the array as shown in Fig. 5.6.

The elements in each configuration have the identical size (i.e. 2μm $\times$ 2μm), and have

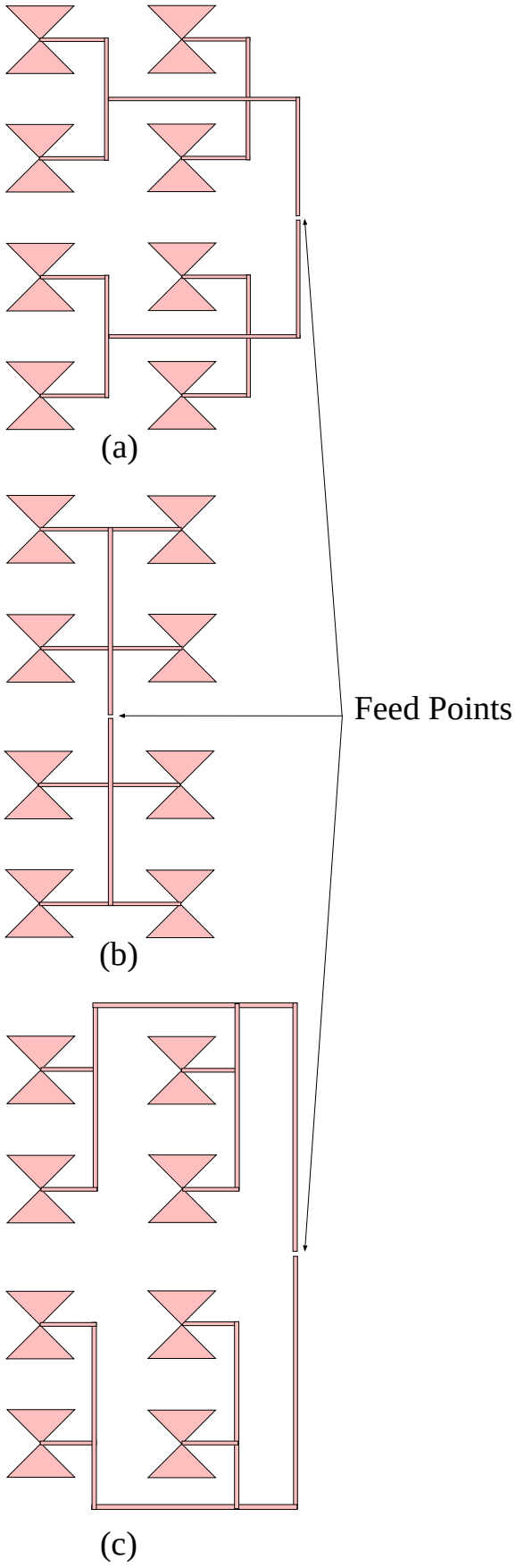

Figure 5.6: Three bowtie nano-array configurations: (a) configuration1, (b) configuration2, and (c) configuration3.

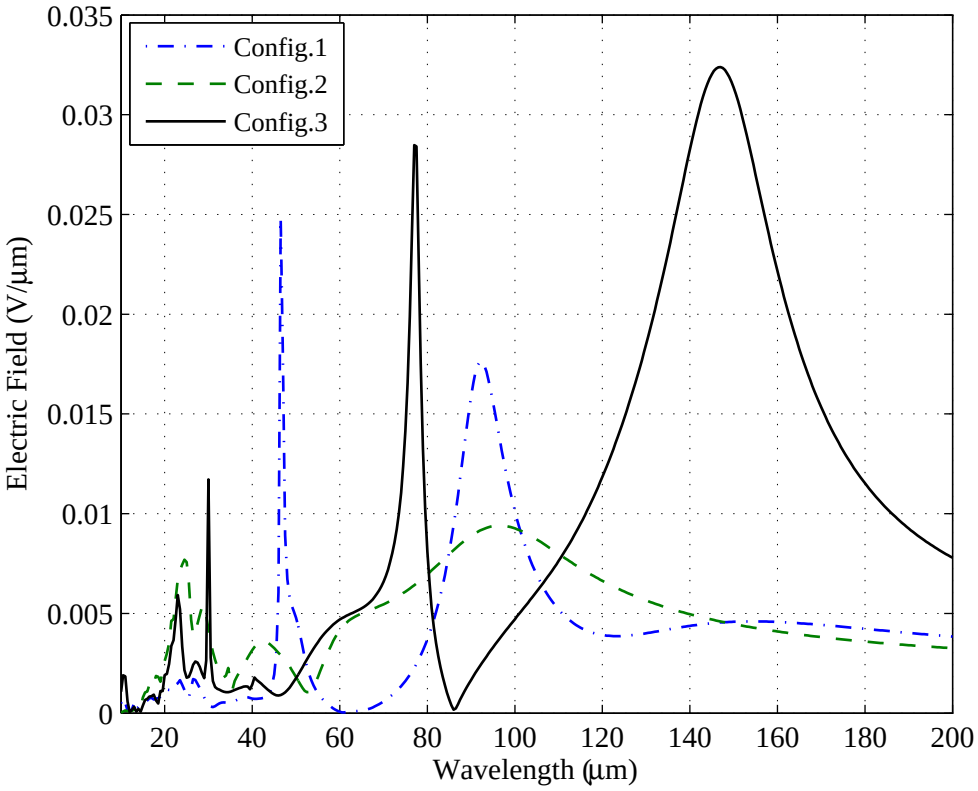

Figure 5.7: The variation of the electric field versus wavelength for different bowtie nano-array configurations.

Table 5.1: Comparison Between Different Nano-Array Configurations.

	Resonant Wavelength (μm)	A U C (μV)
Config.1	46 & 92	0.7984
Config.2	22.5 & 44 & 94	0.9284
Config.3	23 & 30 & 77 & 147	1.9743

an apex angle of 90^o. These arrays are placed on substrate with dimensions of (70μm $\times$ 70μm). The feeding line width in all cases is 100 nm. Fig. 5.7 shows a comparison between the captured electric fields at the feed point for these three configurations.

In Fig. 5.7, it can be seen that configuration3 has the maximum electric field at short-wavelengths and longer-wavelengths resonances, and has higher AUC, whereas configuration1 exhibits the lowest performance when compared with the other two configurations. It can also be observed that all configurations exhibit multiple resonances with higher electric field with different AUC values. Table 5.1 summarises the simulation results for the three configurations.

For comparison purposes at longer wavelengths, the performance of the array has been

compared with that of the single bowtie matching the area of the nanoarray and resonating at the same wavelength. The designed single bowtie is shown in Fig. 5.8, which has the same footprint area of the array (i.e. $9\,\mu\mathrm{m} \times 16\,\mu\mathrm{m}$).

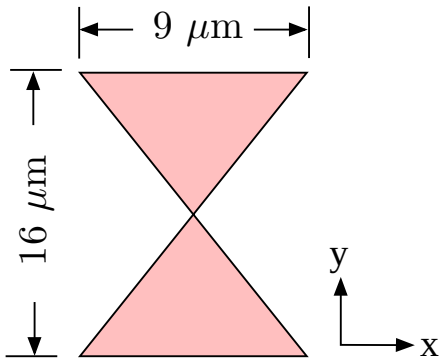

Figure 5.8: Structure of the bowtie nanoantenna.

In order to prove that the single bowtie with larger dimensions features the same characteristics of that with small dimensions, the gap size has been varied as shown in Fig. 5.9. It is clearly noticed that a higher electric field can be captured when small gap size is used. Fig. 5.10 illustrates the electric field concentration around the antenna, where it is seen that most of the field is confined at the feeding gap.

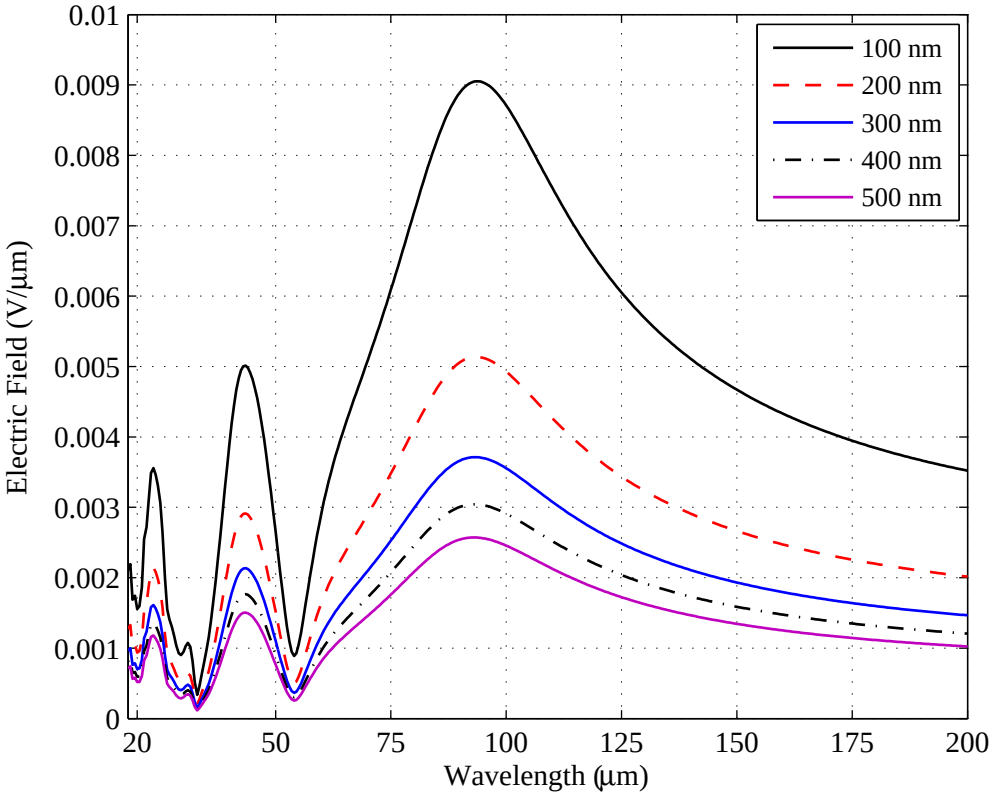

Figure 5.9: Variation of the electric field versus wavelength for different gap sizes.

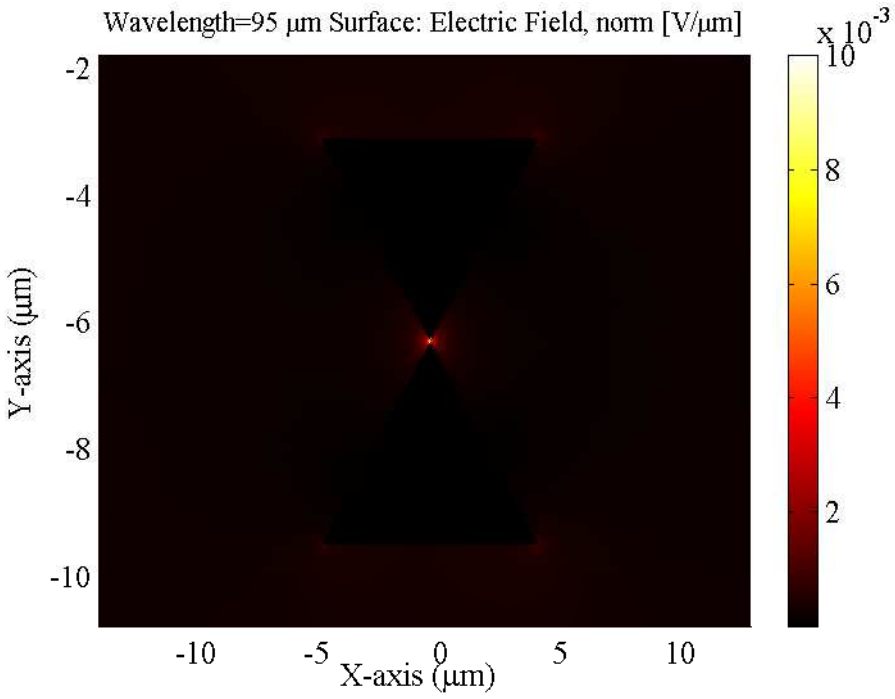

Figure 5.10: Concentration of the electric field at the contact point.

Fig. 5.11 shows a comparison between the captured electric fields at the feeding point of the bowtie nanoarray against that of the single bowtie of identical footprint and gap size of $100\,nm$. It can be observed that the designed array performs better and exhibits higher electric field and AUC than a single bowtie of the same footprint resonating at the same wavelength. It can be also seen that both antennas exhibit multiple resonances, which is advantageous in this application. The AUC for the bowtie array and the single bowtie is 1.974 and 0.902 μV, respectively. As seen from the results, the array is resonating at short-wavelength (at approx. $20\,\mu m$), however, there is also a resonance at longer wavelength. Thus, the resonance at the longer wavelength will further improve the efficiency as long as the array is already resonating in the shorter wavelength region. The detailed schematic of the designed bowtie nanoarray is shown in Fig. 5.12.

5.2.2 Effect of elements spacing

The array configuration in Fig. 5.12 will be adopted in the following subsections in order to optimise its performance. In this subsection, we will investigate the effect of varying the spacing between elements, R, on the nanoarray performance. The spacing is changed horizontally and vertically from 2 to $7\,\mu m$, and the captured electric field at resonance is calculated each time in the nanoarray gap. The spacing is calculated from center-to-center

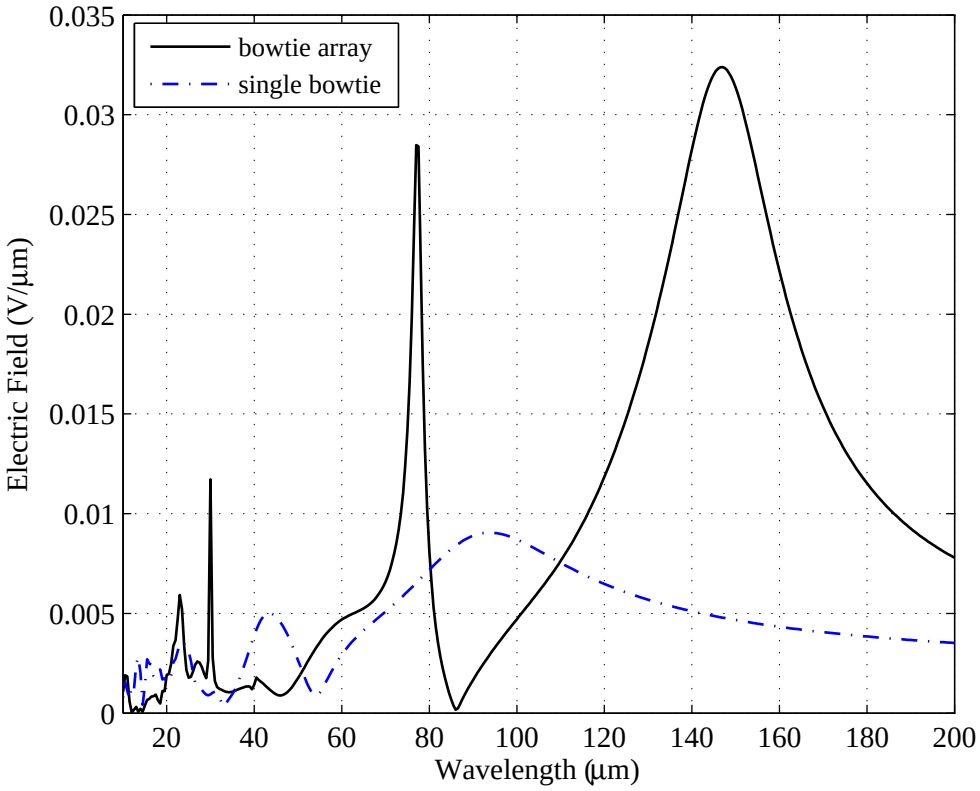

Figure 5.11: Variation of the electric field versus wavelength for the bowtie nanoarray and single bowtie of the same area.

of the bowties, hence, the minimum spacing distance is expected to be greater than $2\,\mu$m. Fig. 5.13 shows the effect of the distance between elements on AUC. It can be seen that, based on the largest AUC, the best performance is achieved with a spacing of $2.9\,\mu$m.

5.2.3 Feeding line width effect

The effect of feeding line width has also been studied in this work. The array configuration is investigated for different feeding line widths, i.e. w=50, 75, 100 and 125 nm. Fig. 5.14 shows the effect of the feeding line width on the captured electric field. A closer look reveals that varying the feeding line width can affect the captured electric field, albeit, with a minor difference in the resonant wavelength. Additionally, it is evident from Fig. 5.14 that the line width of $50\,\mathrm{nm}$ produces the strongest electric field. In contrast, $125\,\mathrm{nm}$ gives the lowest performance.

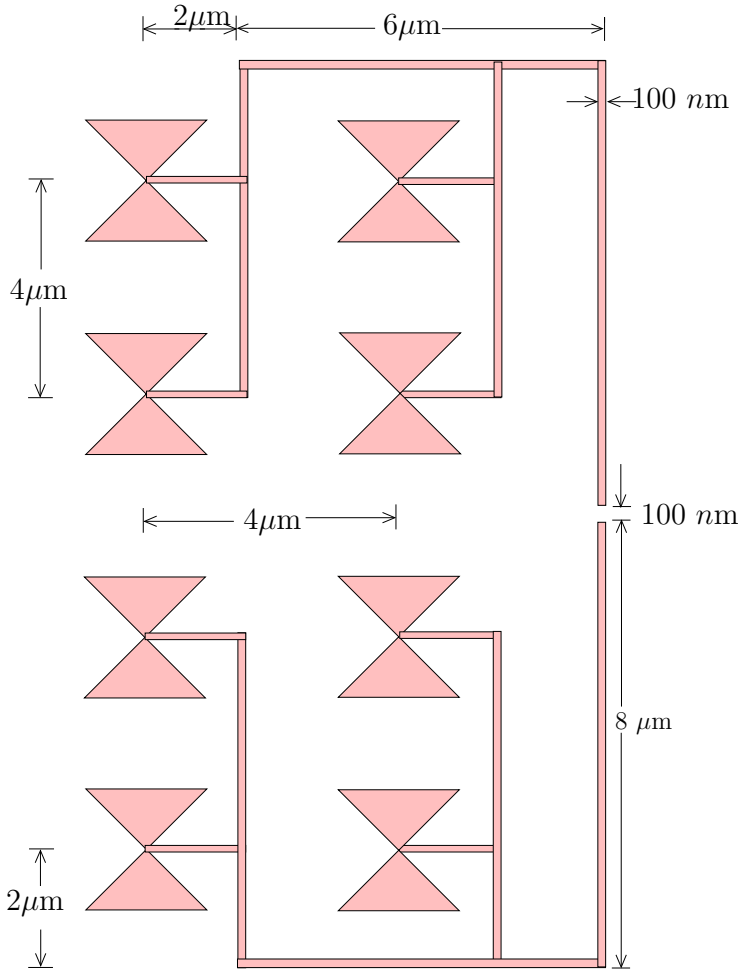

Figure 5.12: Bowtie nanoarray configuration.

5.2.4 Effect of gap size at the feeding point

The gap size effect for a single element has been investigated in the previous section. Here, we will study the role that the gap plays on the captured electric field for the whole bowtie nanoarray. Different gap sizes have been used to simulate the bowtie nanoarray using a feeding line width of $100\,\mathrm{nm}$ and $3\,\mu\mathrm{m}$ spacing between nanoarray elements. The range of the investigated gap sizes g is from 25 to $200\,\mathrm{nm}$ with $25\,\mathrm{nm}$ increments. Fig. 5.15 shows the changes in the captured electric field when the gap size at the feeding point is varied. It can be seen in this figure that the smaller the gap size, the higher the electric field generated. Additionally, it can be seen that there is a marginal shift in the resonant wavelength when the gap size is changed. The resonant wavelength is marginally longer for a nanoarray gap of $25\,\mathrm{nm}$ when compared with that of a $200\,\mathrm{nm}$ gap.

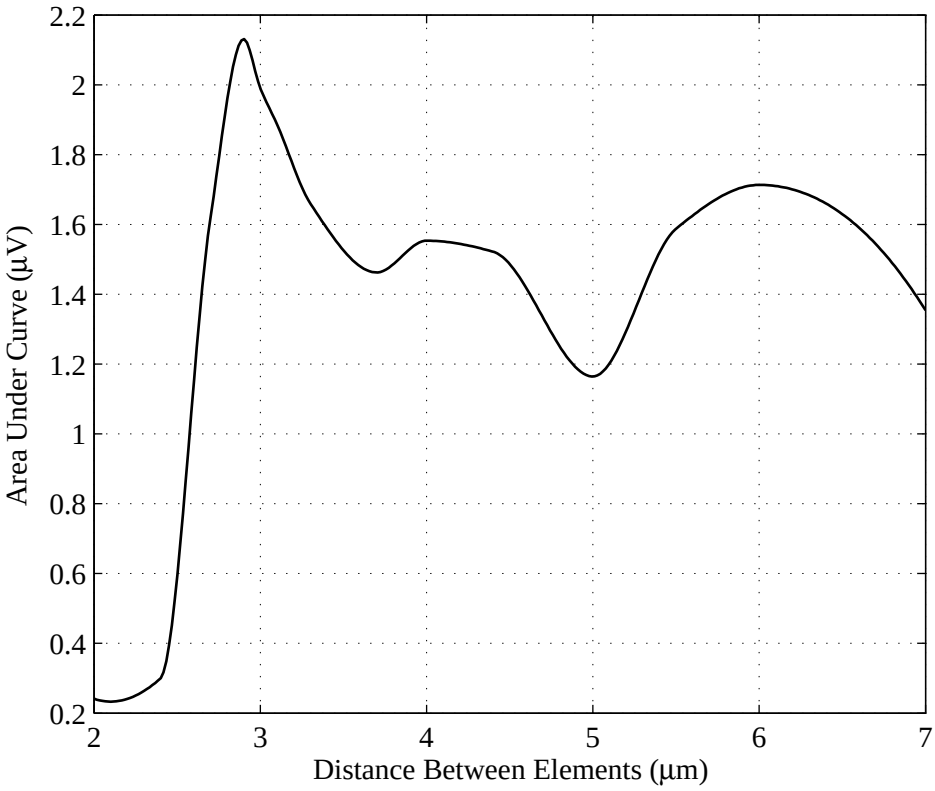

Figure 5.13: Area under curve versus spacing distance.

5.3 Optimised Bowtie Nanoarray

In the previous section, we discussed how we can capture the electric field by changing the geometrical parameters in the configuration of the bowtie nanoarray. From the simulated results in these investigations we have observed that the maximum electric field occurs for a $2.9\,\mu\mathrm{m}$ ($0.141\ \lambda$) element spacing. Furthermore, the captured electric field is enhanced when we reduce the feeding line width to $50\,\mathrm{nm}$ ($0.0024\ \lambda$) and the size of the gap at the feeding point to $25\,\mathrm{nm}$ ($0.0012\ \lambda$). Therefore, in this section we realize a bowtie nanoarray based on the optimised parameters from the previous section (shown in Table 5.2) to maximise performance. Fig. 5.16 presents the electric field captured by this optimised nanoarray configuration. The maximum electric field magnitude reaches $0.047\ \mathrm{V}/\mu\mathrm{m}$ at the first resonant wavelength of $20.5\,\mu\mathrm{m}$ (14.63 THz), and $0.258\ V/\mu$m at the second resonant wavelength of $158\,\mu\mathrm{m}$ (1.89 THz). The AUC value for the optimised nanoarray is $6.80\ \mu$V. This value of the converted voltage is higher than the AUC values in all previous cases. Fig. 5.17 shows the concentration of the electric field in the gap at the first and second resonant wavelengths. The dimensions of the optimised nanoarray are $8.35\,\mu\mathrm{m} \times 13.1\,\mu\mathrm{m}$.

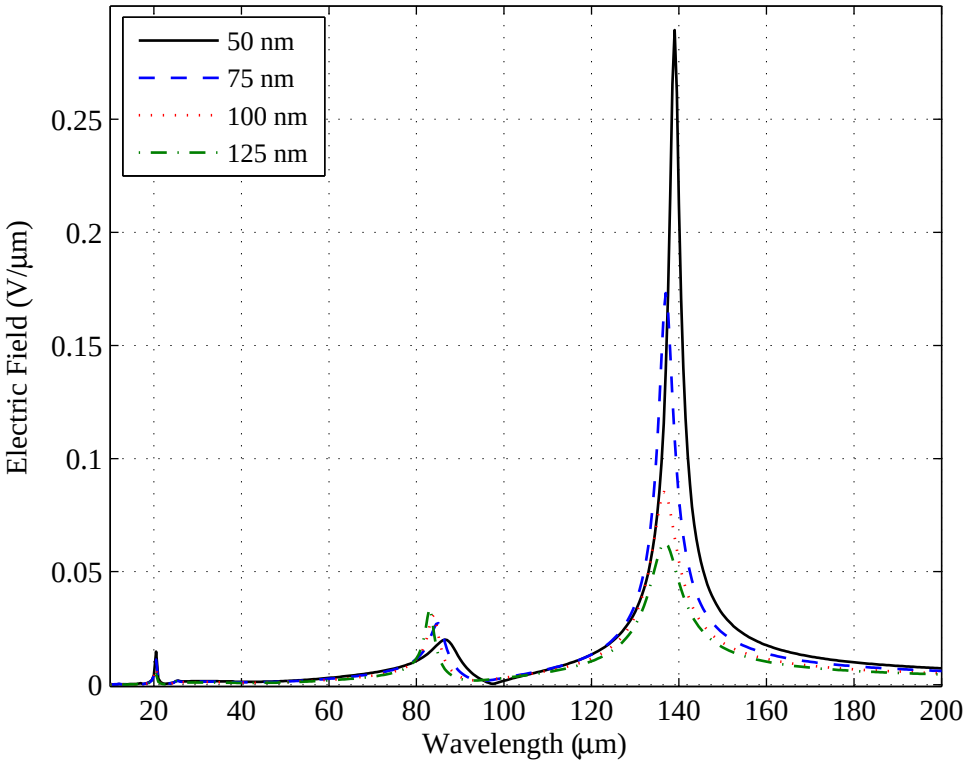

Figure 5.14: Variation of the captured electric field versus wavelength for different values of feeding line width.

Table 5.2: Optimised Parameters Used to Build The Optimised Nanoarray.

Parameter	Value
R	2.9 μm
w	50 nm
g	25 nm

5.4 Angle of Incidence Effect on The Nanoarray Response

In all the cases considered so far, linearly polarised radiation with the electric field parallel to the antenna axis has been assumed at normal incidence. This section describes the dependence of the response of the optimised nanoarray on the incident angle of the source plane wave. The angle ϕ between the antenna axis and the polarisation direction is rotated from -90^o to 90^o in increments of 1^o to investigate the effect of incident angle on the nanoarray performance.

Fig. 5.18(a) shows the captured electric field as a function of the incident angle. It is evident that the pattern is approximately omni-directional in the forward radiation. Additionally, it is demonstrated that the strongest fields are detected for the incident angles of

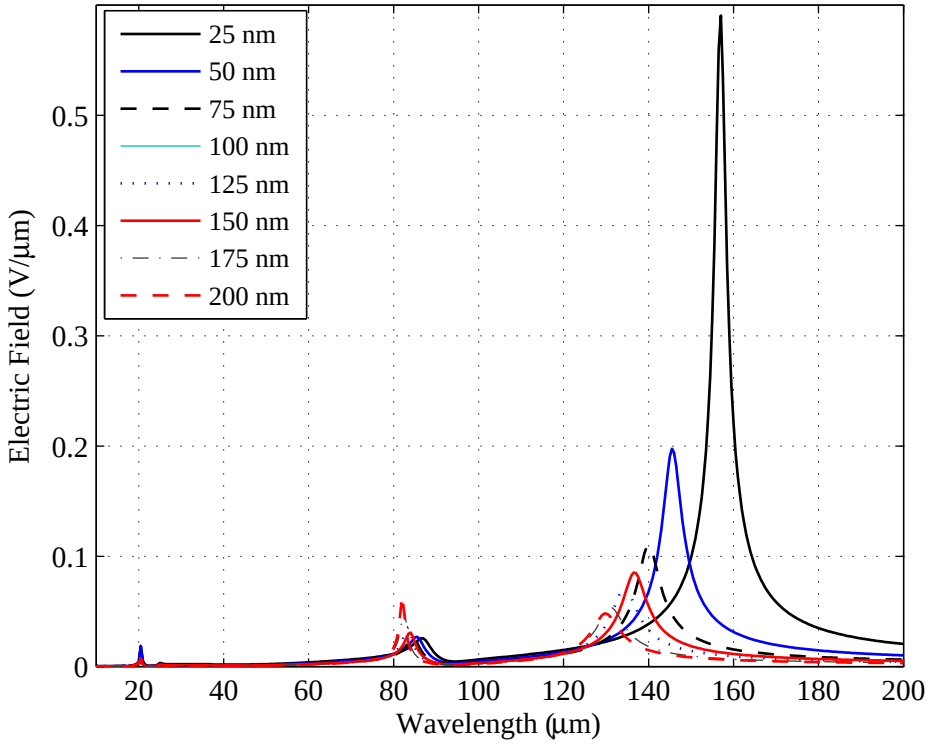

Figure 5.15: Variation of the captured electric field versus wavelength for different gap sizes.

0^o, 50^o and -50^o, whereas there are two nulls at 90^o and -90^o. The investigation into the effect of the incident angle leads to the estimation of the nanoarray's radiation pattern as shown in Fig. 5.18(b).

Two orthogonal polarisations (x and y-polarisation) have been launched and the response of the array at the resonant wavelength was recorded. Subsequently, the polarisation discrimination ratio was calculated, and it is found that the array has a resonant mode when the polarisation is rotated by 90^o. with a polarisation discrimination ratio of (7.77 dB) due to rotating the incident light polarisation.

5.5 Effect of Sharp Edges of Bowties and Feeding Lines

In the previous cases, all bowtie edges and feeding lines were perfectly sharp, however, in practice it is impossible to manufacture these nano-scale elements under this assumption. In this section, we investigate the effect of constructing the bowtie edges with different radii. The radius of curvature for the feeding lines is kept constant at 40 nm, while the radius is changed from 60 to $140\,\mathrm{nm}$ for the array bowtie's elements. Fig. 5.19 shows

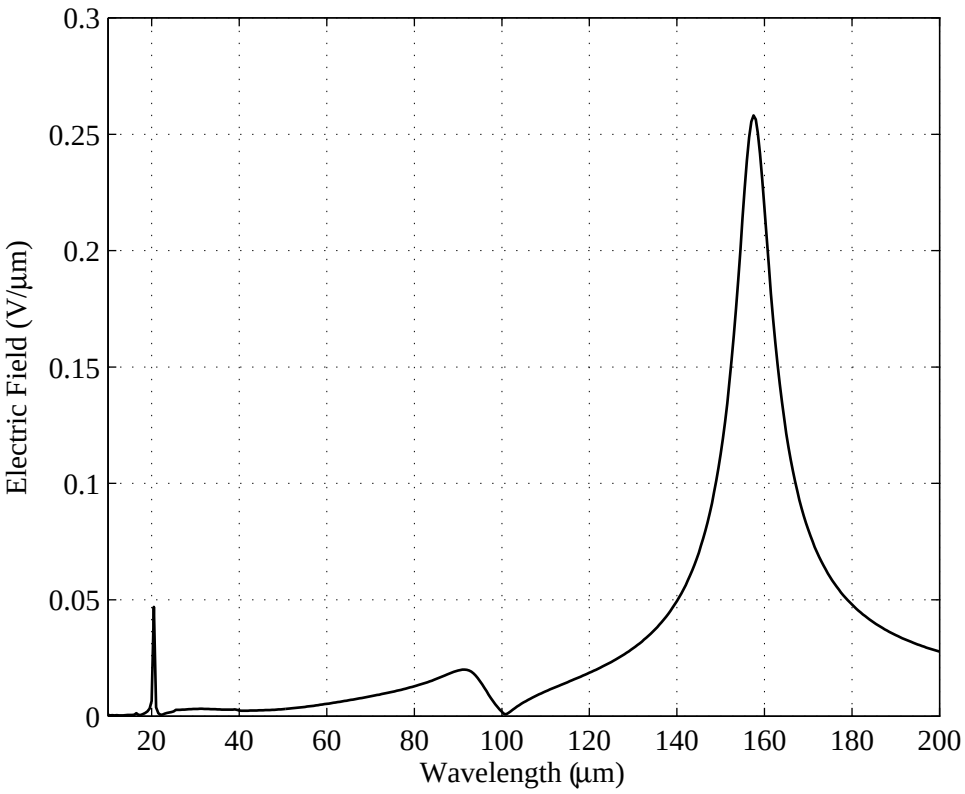

Figure 5.16: Variation of the captured electric field versus wavelength for the optimised bowtie nanoarray.

the optimised array with curved elements and feeding lines, whereas Fig. 5.20 shows the effect of curvature radius on the captured electric field at the array gap. It is clearly shown in Fig. 5.20 that the curvature radius has a small effect on the array performance (i.e. the value of the electric field and the resonant wavelength). Table 5.3 summarises the values of the captured electric field, resonant wavelength, and AUC for the optimised array when the radius of curvature varies from 60 to $140\,\mathrm{nm}$. The results in Fig. 5.20 show that there is a minor blue-shift in the resonant wavelength and an increment in the electric field magnitude due to the increase in the curvature radius.

5.6 Integrating the Rectifier into the Bowtie Nanoarray

The array arms are overlapping over a small area, which represents a metal/insulator/metal (MIM) diode to rectify the received signal. To build such diode, an insulator layer with a few nano-meters thickness is employed to fill the gap between the overlapping arms. To this end, a tunnel junction is hosted and the resulting MIM diode exhibits an area of 100×50 nm^2 as shown in Fig. 5.21.

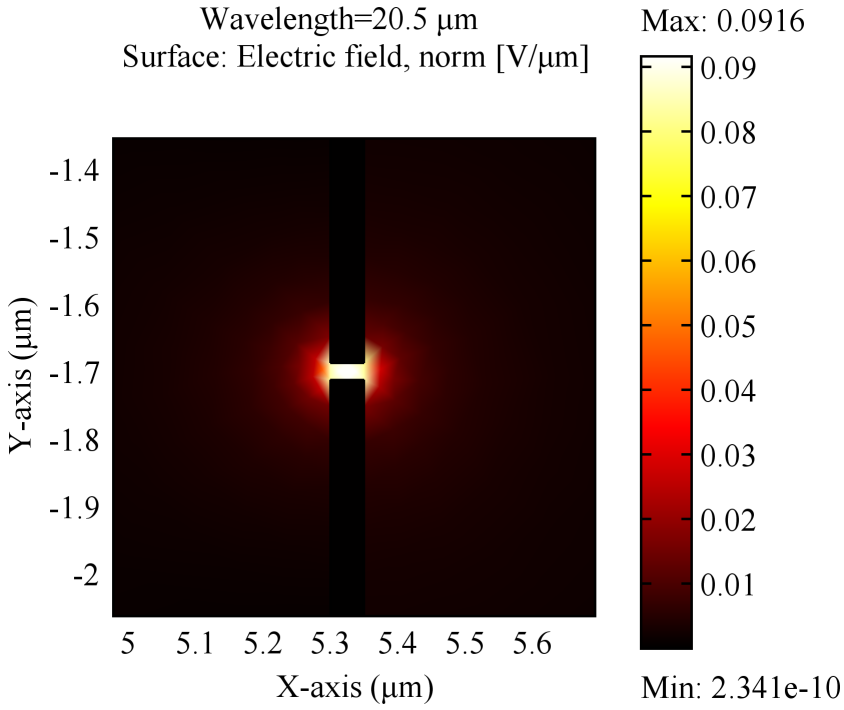

(a) 1st resonance

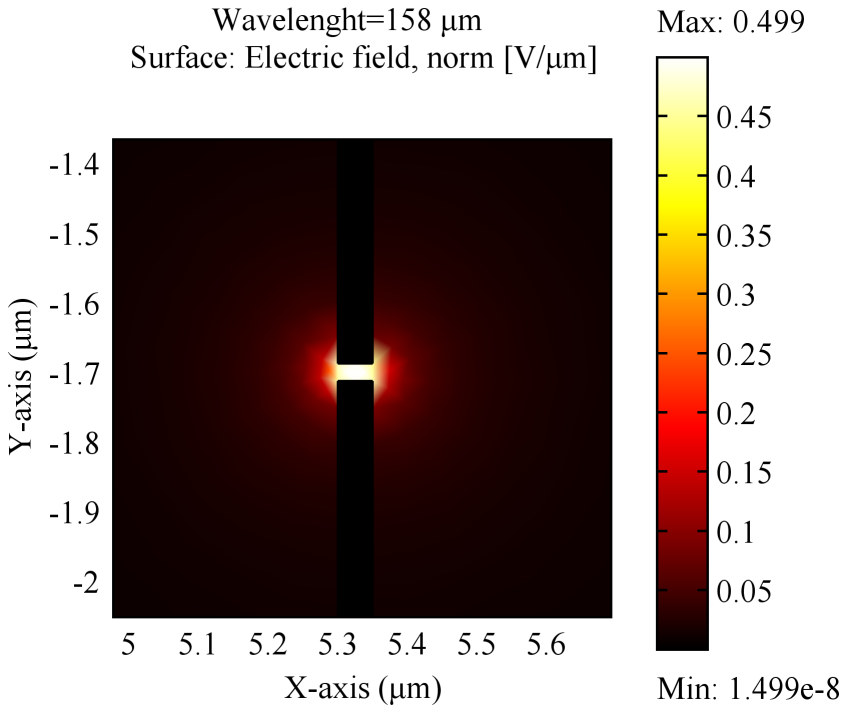

(b) 2nd resonance

Figure 5.17: Concentration of the captured electric field in the gap of the optimised bowtie nanoarray at resonant wavelengths.

In this section, we will optimise the performance of the bow-tie nano-array in terms of metal thickness, gap size (i.e insulator layer thickness) and the overlapping area. The metal thickness of the array has been varied from 50 to 120 nm, and it is seen that the

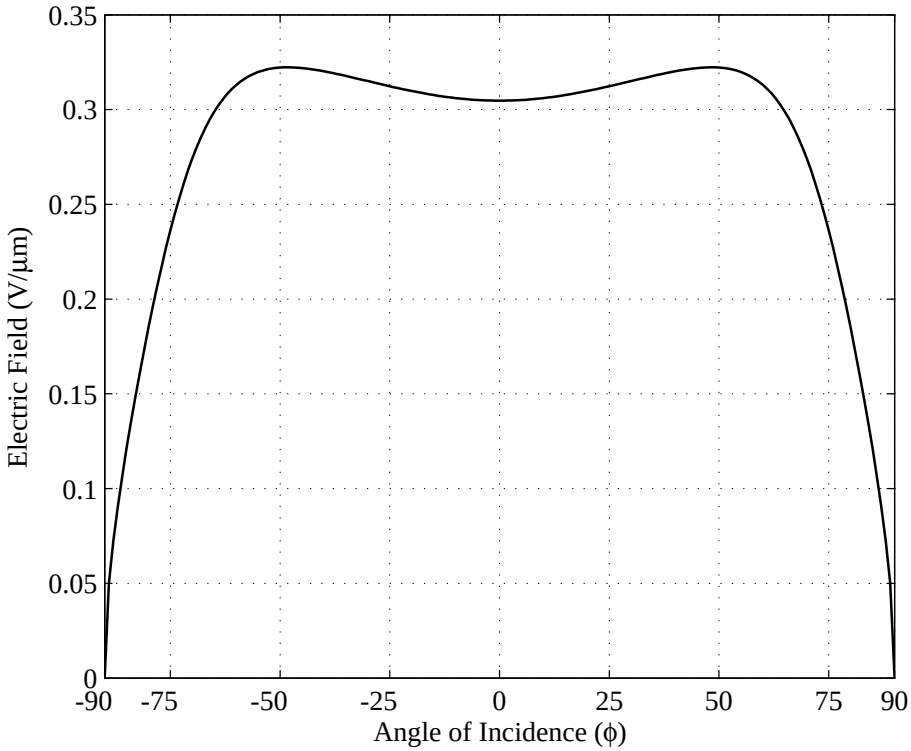

(a)

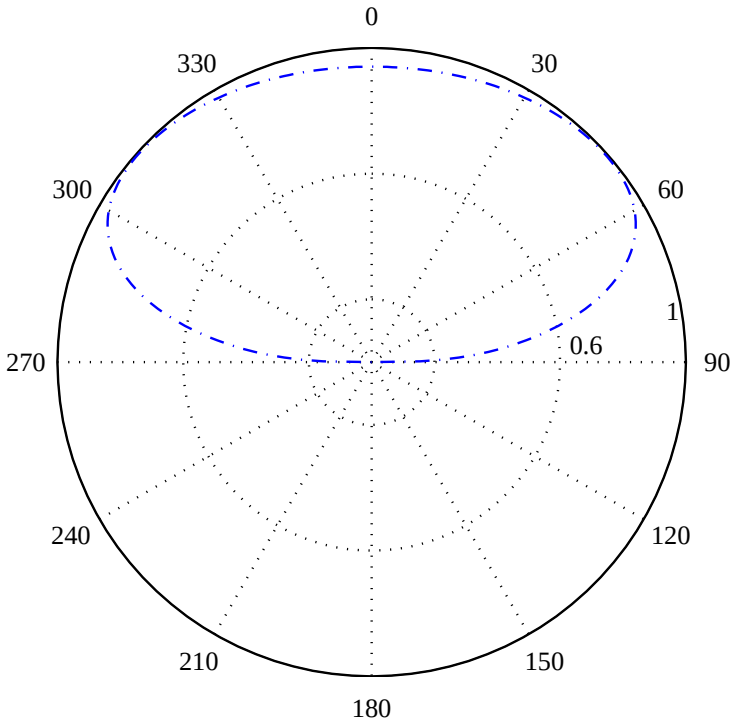

(b)

Figure 5.18: Variation of the captured electric field versus angle of incidence:(a) Cartesian Coordinate, (b) Polar plot for the values between -90^o and 90^o (normalised)

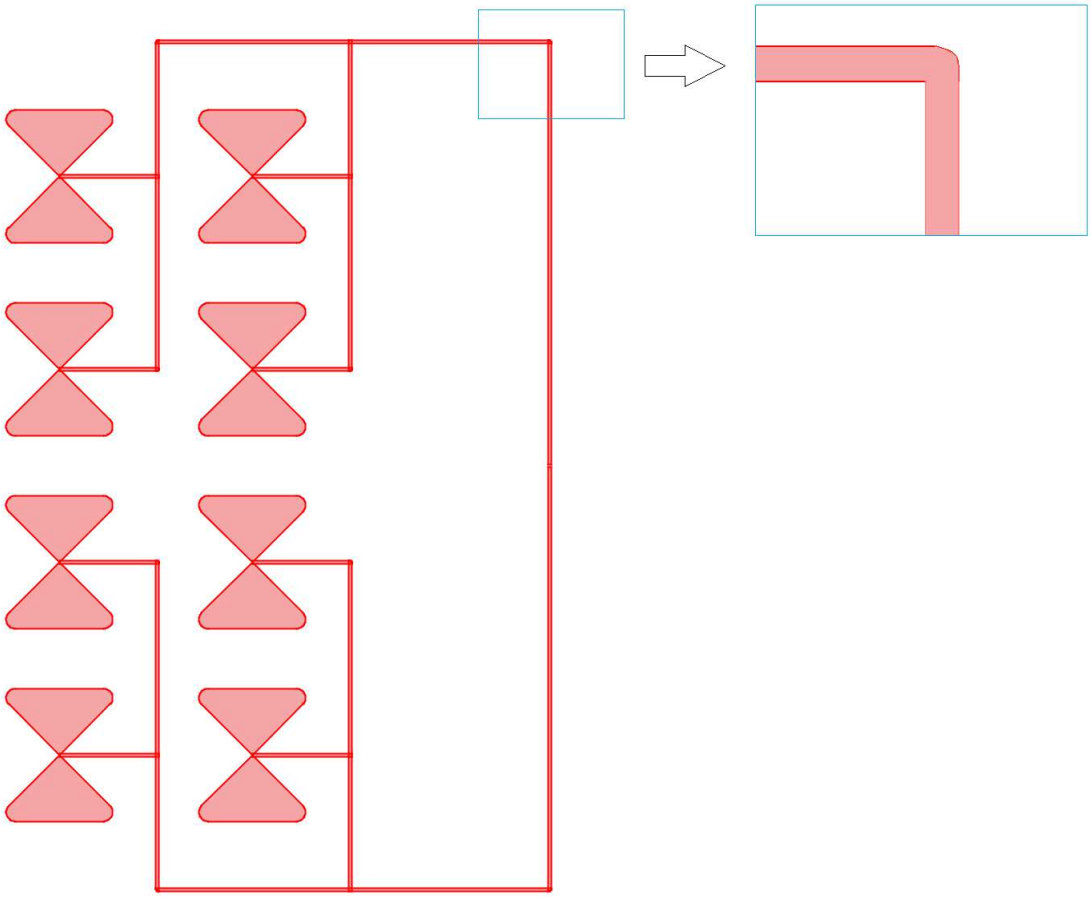

Figure 5.19: Optimised bowtie nanoarray with curved element edges and feeding lines (inset).

Table 5.3: Effect of curvature radius on the nanoarray performance.

Curvature Radius	E-field @1st Resonance (V/μm)	E-field @2nd Resonance (V/μm)	AUC (μV)
no-curvature	0.047	0.258	6.80
60 nm	0.015	0.289	6.93
80 nm	0.011	0.312	7.09
100 nm	0.014	0.336	7.20
120 nm	0.018	0.362	7.25
140 nm	0.024	0.400	7.46

highest electric field is obtained at a $95\,nm$ thickness as shown in Fig. 5.22. It is worth mentioning that this thickness does not represent a significant challenge from the manufacturing point of view.

The insulator layer thickness has been changed as following: 3, 5, 10, 15 and 20 nm. The values for the corresponding electric field in the gap at resonance were: 0.02, 0.025, 0.0275, 0.0833 and 0.0103 V/μm, respectively. It is clearly evident that the highest

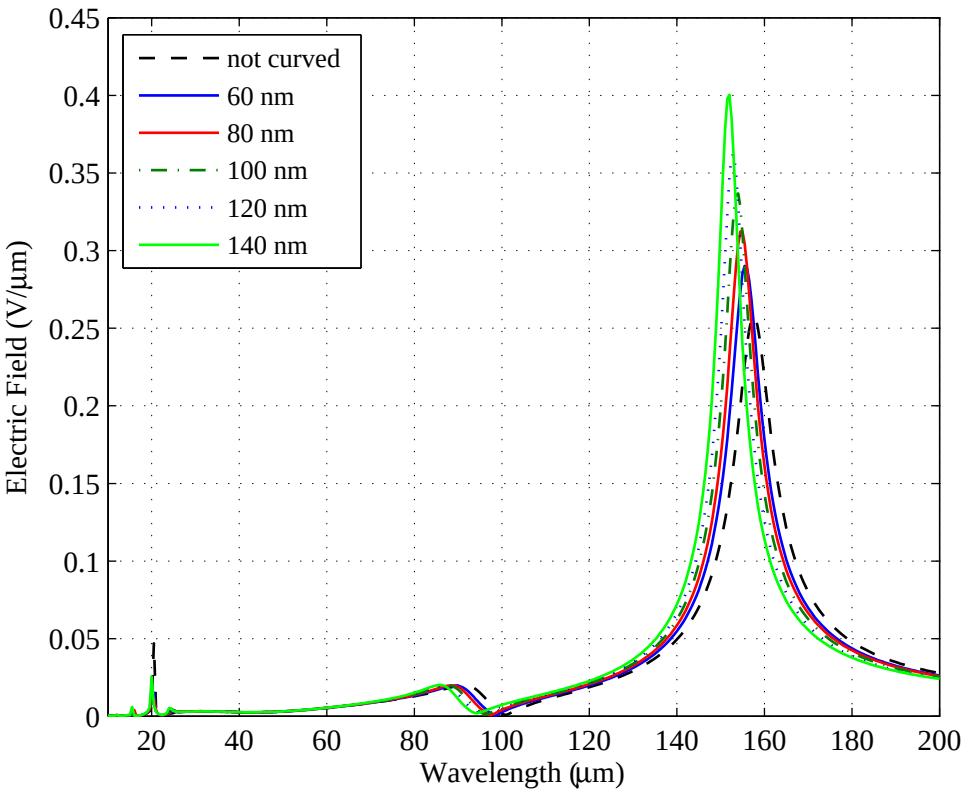

Figure 5.20: Effect of curvature radius on the captured electric field.

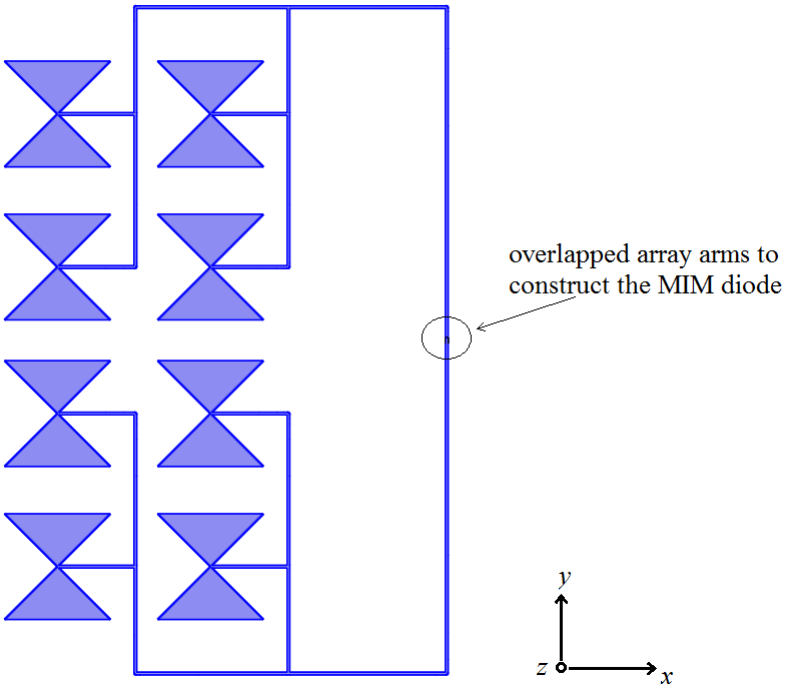

Figure 5.21: The designed bow-tie nano-array with the integrated MIM diode.

electric field has been obtained for the thickness of $15\,nm$. However, the insulator layer thickness plays a significant role in determining the cut-off frequency of the MIM diode

and affects directly the tunnelling process as will be discussed in the following Section. Regarding the effect of the overlapping area, the results have shown that the smaller the overlapping area the higher the electric field inside the gap obtained.

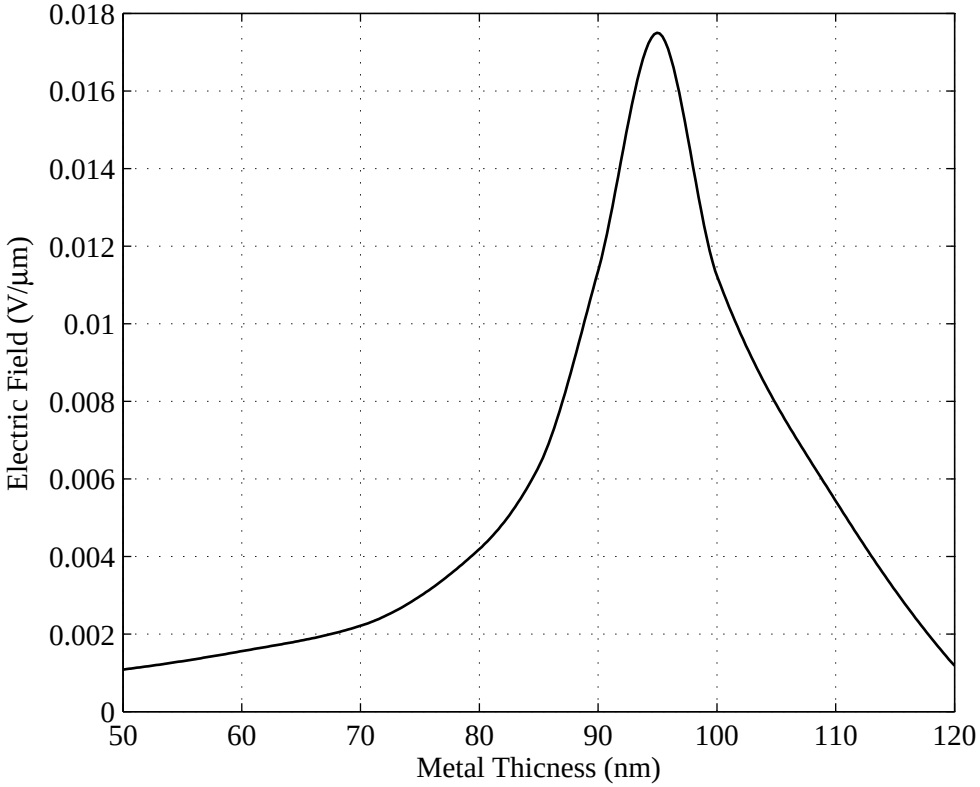

Figure 5.22: The variation of the captured electric field with the change of metal thickness.

5.7 Characteristics of the MIM Diode

MIM diode is a thin film device consists of a few nano-meters thin insulator layer sandwiched between two metal electrodes. The rectification process happens based on the concept of electron tunneling through a barrier (insulator layer) [101]. In designing MIM diodes, and in order to make them work properly, certain conditions need to be fulfilled [102]. These conditions are: 1) The insulator layer should be thin, in order of few nanometers, to ensure the occurrence of the tunneling effect. 2) The behavior of the I-V characteristics should be asymmetric. This can be obtained by using different metals on both sides of the insulator layer with large work function difference between them. 3) Low resistance to provide good impedance matching between the diode and the antenna.

The equivalent circuit of the antenna-coupled MIM diode can be described as a fixed resistance r connected in series with a non-linear resistance R_D and this combination is

in parallel with the diode capacitance C_D as shown in Fig. 5.23. The antenna can be represented by a voltage source V_{IR} with a series resistance R_a. The electric field has been integrated for different wavelengths along the overlapping area to find the extracted voltage that is supposed to be applied at the input of the MIM diode for rectification to DC power as shown in Fig. 5.24.

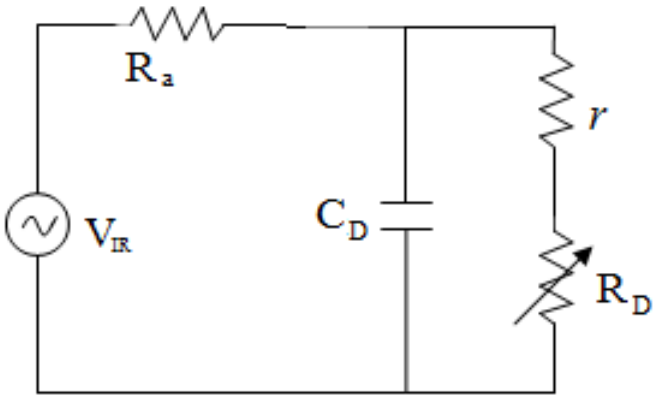

Figure 5.23: The equivalent circuit of the antenna-coupled MIM diode, where the bow-tie nano-array is represented by a voltage source in series with a resistor.

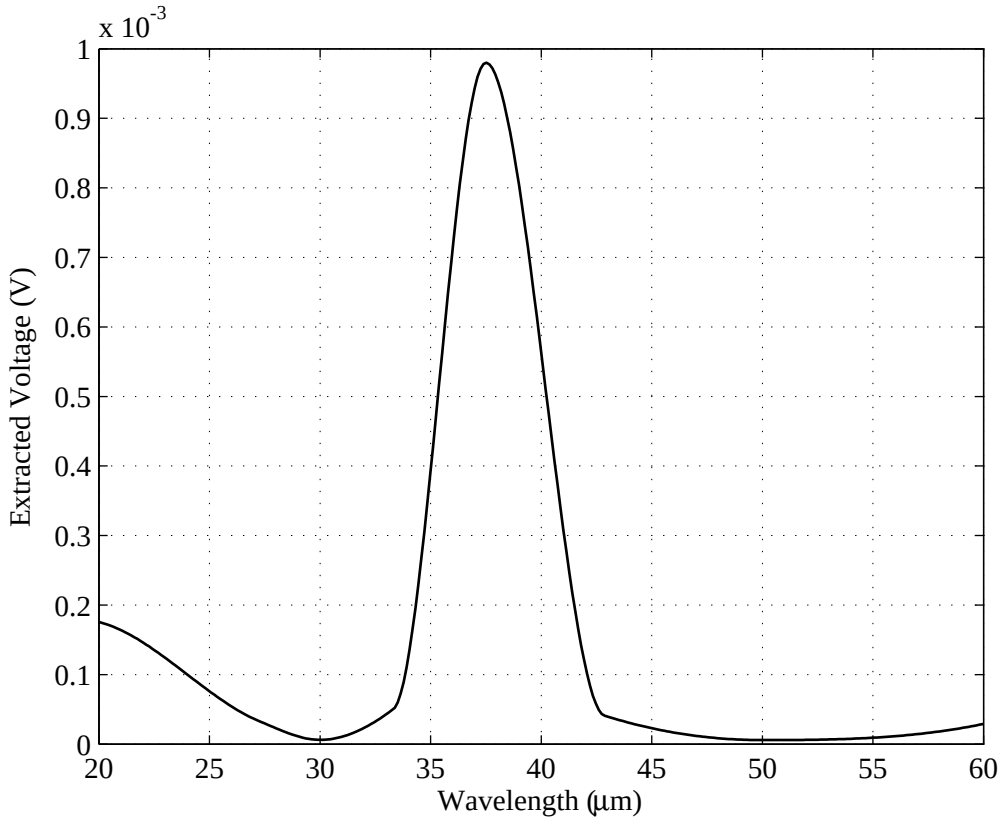

Figure 5.24: The voltage V_{IR} applied to the MIM diode verses the applied wavelength.

The cut-off frequency, f_c, for the MIM diode depends effectively on the equivalent

resistance, R, for the structure and the MIM diode capacitance, C_D, and can be described as follows [74].

$$f_c = \frac{1}{2\pi R C_D}. \tag{5.1}$$

The frequency response of the MIM diode is determined by the time constant (RC_D). The value of R depends heavily on the fabrication process and can be considered as a constant, so the diode capacitance C_D can be used to adjust the cut-off frequency of the MIM diode as it plays a significant role in controlling its value. The diode capacitance can be considered as a parallel-plate capacitor, and it is calculated as follows,

$$C_D = \frac{\varepsilon_{\text{ins}} \varepsilon_0 A}{g}, \tag{5.2}$$

where ε_{ins} represents the relative permittivity of the insulator layer of the MIM diode, ε_0 is the free space's permittivity, A is the diode junction area (overlapping area) and g is the thickness of the insulator layer. In order to achieve a high cut-off frequency for the MIM diode to be operating at infra-red regime, a very low diode capacitance is required. The lower capacitance is achievable by both minimising the overlapping area and/or increasing the insulator layer thickness. Actually, there is a trade off between these two factors. On one hand, increasing the thickness of the insulator layer will lower the diode capacitance and will decrease the tunneling probability, while decreasing this thickness would make the capacitance higher and at the same time this would short-circuit the THz frequencies [9]. On the other hand, minimising the overlapping area to attain a very high operating frequency (visible or infra-red regime) requires this area to be in terms of few nano-meters that makes the fabrication process extremely challenging [21].

In our case, the arms of the bow-tie nano-array are overlapping over an area of 100×50 nm^2 as shown in Fig. 5.25, and the thickness of the insulator layer is 20 nm. Additionally, the value of ε_{ins} has been chosen to be 8.5, and R has been assumed to be $100\ \Omega$. So, based on these characteristics, the cut-off frequency for the MIM diode will be 84.6 THz and this value is significantly higher than the resonant frequency of the array, i.e. the obtained cut-off frequency of the MIM diode is high enough to rectify the incident wave. In contrast, Fig. 5.26 illustrates the concentration of the electric field in the overlapping areas of the MIM diode.

As a final step in the design, all bowtie nanoarrays can be connected together using metal leads to collect the DC current from the diodes. Fig. 5.27 illustrates the proposed

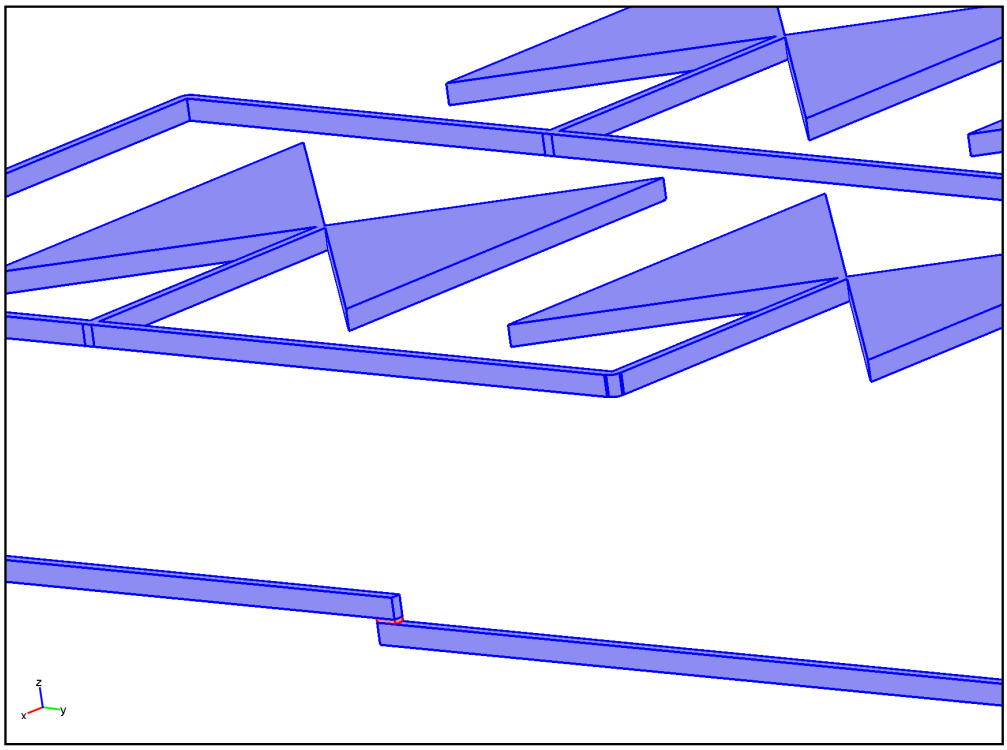

Figure 5.25: The MIM diode junction area (red area) made by the overlapped arms.

mask for collecting the bowtie nanoarrays, which can be repeated to cover the entire photovoltaic panel.

5.8 Chapter Summary

In this chapter, an investigation of bowtie based nanoarrays for solar energy collection has been presented. The simulation results have been obtained using FEM based software. The aim of this study has been to increase conversion efficiency of electric field to voltage in the gap of the array. A 2×4 bowtie planar nanoarray with feeding network has been designed to increase the captured electric field for energy harvesting applications. The performance of the designed bowtie nanoarray has been compared to that of a single bowtie with matching footprint and the results showed that the bowtie nanoarray can be designed and optimised to collect more energy than a single bowtie element using identical device areas. A parametric study of the distance between elements, feeding line width, and gap size has been carried out. The results have shown that the optimum space between elements is $2.9\,\mu\mathrm{m}$, and the best line width is $50\,n\mathrm{m}$. It has also been shown that a gap of $25\,n\mathrm{m}$ produces the strongest electric field.

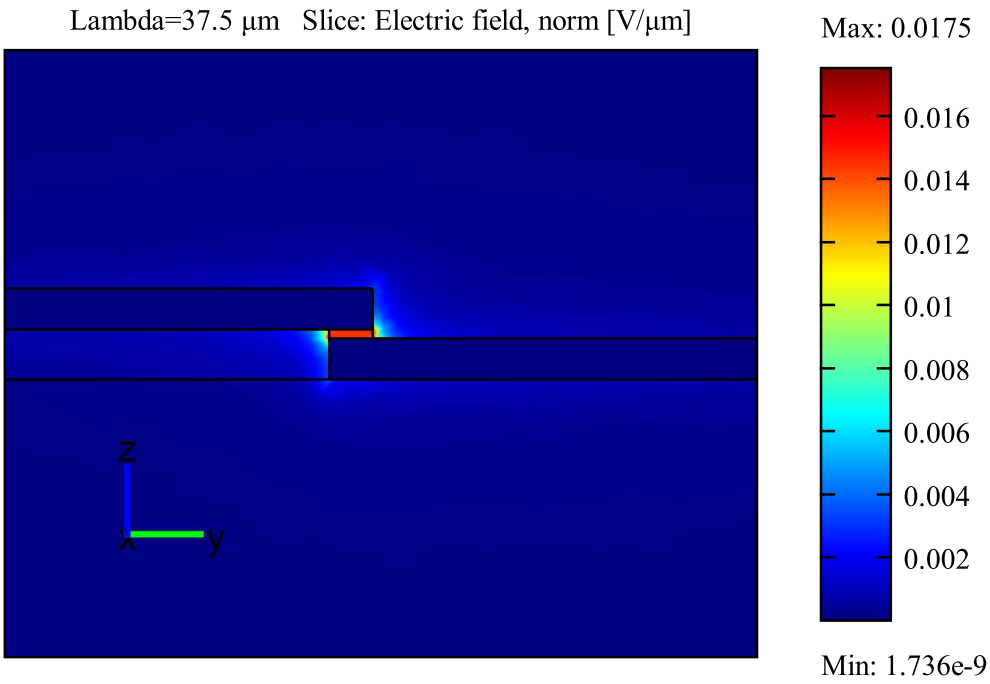

Figure 5.26: The concentration of the electric field around the antenna-coupled MIM diode.

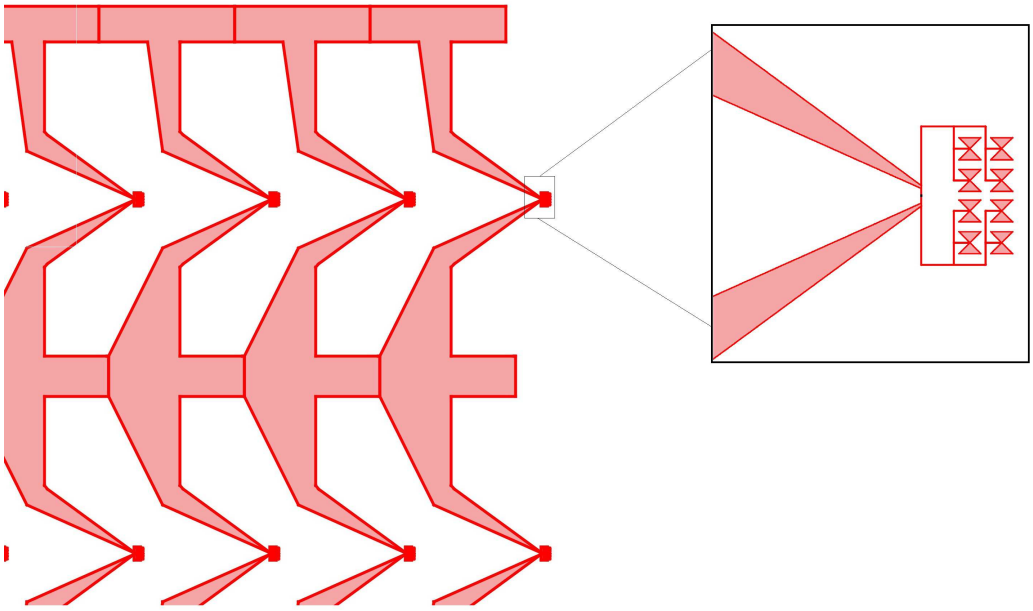

Figure 5.27: Connecting the bowtie nanoarrays via metallic leads to collect the DC power.

An optimised bowtie nanoarray has been designed based on the optimised parameters obtained in order to increase the captured electric field. A maximum electric field of $0.047\ V/\mu$m has been achieved at the first resonant wavelength of $20.5\ \mu\mathrm{m}$ (14.63 THz), and $0.258\ V/\mu$m at the second resonant wavelength of $158\ \mu\mathrm{m}$ (1.89 THz) corresponding to an AUC value of $6.80\ \mu$V. The effects of curving the edges of the array elements and feeding lines has also been studied and the results have shown that they have a clear impact on the values of the electric field and the resonant wavelengths. The nanoarray can be implemented using an electron-beam lithography technique and a suitable MIM diode can be embedded in the feeding gap to rectify the received signal. A low pass filter can be placed between the antenna and the MIM diode to prevent the re-radiation of higher harmonics generated from the rectification process by the non-linear diode, which can result in power losses. In addition, this filter can be designed to match the impedance between the antenna and the subsequent circuitry.

The designed array is integrated with a MIM diode by overlapping the array arms in an area of 100×50 nm^2 and a gap of 20 nm to host the tunnelling junction. Furthermore, a parametric study on the metal thickness has been conducted from $50\,n\mathrm{m}$ to $120\,n\mathrm{m}$, and the results showed that a $95\,n\mathrm{m}$ metal thickness exhibits the highest electric field. Additionally, it is found that the highest electric field has been obtained for the insulator layer thickness of $15\ n\mathrm{m}$, while its value has been changed from 3 to $20\,n\mathrm{m}$. Additionally, the results have shown that the smaller the overlapping area, the higher the electric field inside the gap.

Chapter 6

Analysis of Nanoantennas and the Efficiency of Solar Rectennas

In this chapter, an efficient and simple method to calculate the fundamental properties of finite-length center-fed wire nanoantennas, such as the current distribution and the input impedance, is presented. These properties have been calculated numerically using integral equation modeling with Matlab within the IR band (particularly 10 μm). Throughout this modeling, an imperfect conductivity of metal has been used within the optical and IR regimes, where an investigation into the gold conductivity within the IR spectrum has been conducted. Although two integral equations have been used, only Hallen's integral equation with delta-gap voltage source has been adopted throughout the chapter.

The chapter is organised as follows. Section 6.1 describes the utilising of Pocklington's and Hallen's integral equations in order to find the antenna input impedance with the aid of numerical methods, such as MoM, where a circuit model is presented based on these calculations. The parameters of MIM diodes are discussed in Section 6.2, where a design for an MIM diode has been presented by overlapping the antenna arms over a small area to construct an IR solar rectenna. The circuit model for the designed solar rectenna is found by combining the antenna circuit model with that of the MIM diode. Moreover, the influence of the various geometrical parameters of the MIM diode on the rectenna performance has been numerically investigated. Section 6.3 describes the terms of conversion efficiency of solar rectennas and shows the dependence of this efficiency on both antenna and diode characteristics. The section focuses on the important factors in calculating the MIM diode characteristics and the role that these characteristics play in improving the total conversion efficiency. Finally, Section 6.5 summarises the main conclusions of this paper. The analysis of the nanoantenna has been published in [103], whereas the analysis of the MIM diode has been published in [104].

6.1 Integral Equation Approach

When an incident electric field (E_z^i) impinges on the surface of a cylindrical wire antenna (shown in Fig. 6.1), the total tangential electric field (E_z^t) is given by

$$E_z^t = E_z^i + E_z^s, \tag{6.1}$$

where (E_z^s) is the scattered electric field.

According to the boundary conditions theory, the tangential electric field vanishes (i.e. $E_z^t = 0$) at the surface of the antenna. This is true for the conventional antennas at RF

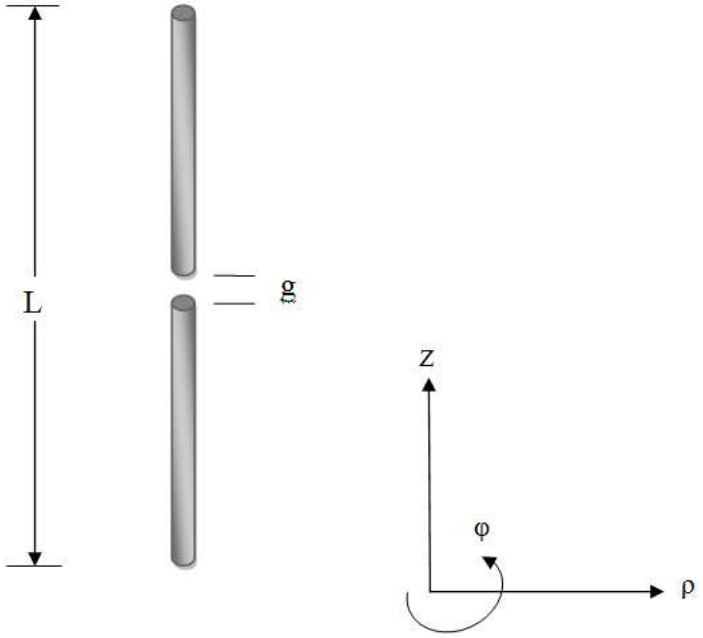

Figure 6.1: Geometry of a center-fed cylindrical dipole antenna; L: the length of the antenna; g: the gap distance.

frequencies, where the metals are considered to be perfect electric conductors (PEC), so that $E_z^s = -E_z^i$ [12]. However, in the case of nano-scale antennas operating at the optical and IR regimes, metals are no longer perfect conductors [61][26], as they exhibit lower conductivity (particularly at visible region) and have frequency-dependent dielectric properties. Consequently, the term E_z^t in (6.1) has to be taken into consideration, which can be represented by the surface impedance multiplied by the surface current ($I(z)Z_s$). The optical permittivity of the metal plays an important role in such cases, which is not the same as in RF systems and can be computed from Drude model as [105]

$$\varepsilon_r(f) = \varepsilon_\infty - \frac{f_p^2}{f^2 + if\Gamma}, \tag{6.2}$$

where ε_∞ represents the contribution of the bound electrons to the relative dielectric constant, f_p is the plasmon frequency and Γ is the damping frequency. Here, i denotes the imaginary operator.

The dielectric constant ε_r has a frequency-dependent complex form, from which the metal conductivity σ at optical frequencies can be calculated as [106]:

$$\sigma = i\omega\varepsilon_o(\varepsilon_r - 1). \tag{6.3}$$

Thus equation (6.1), in this case, can be written as

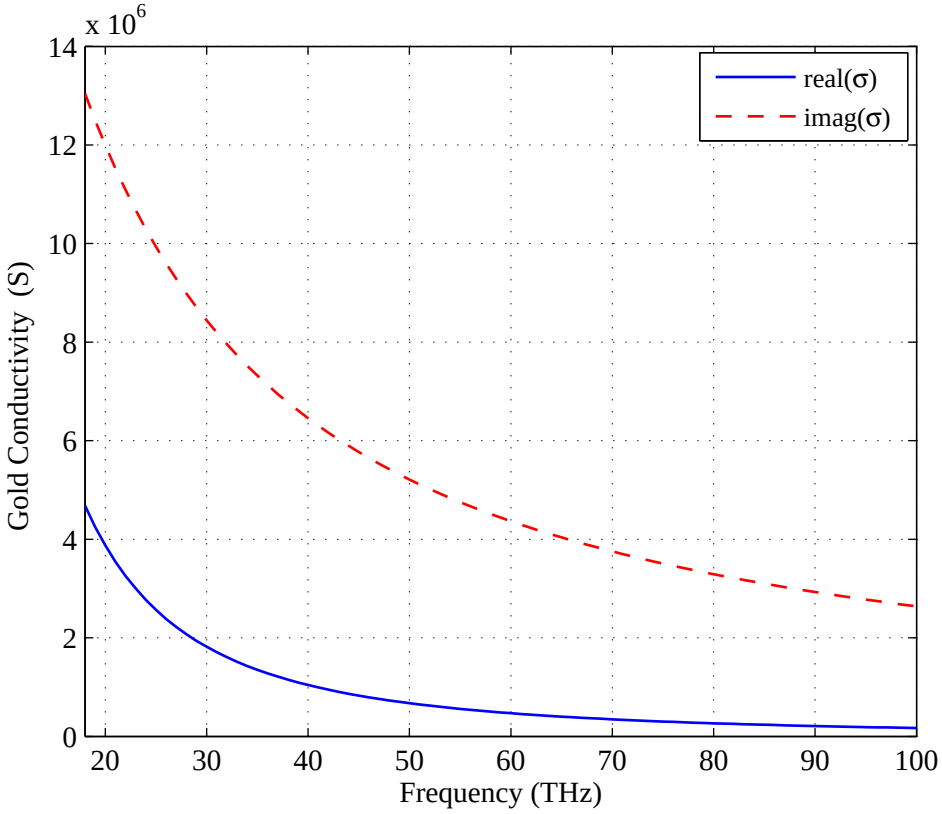

Figure 6.2: Real and imaginary parts of gold conductivity as a function of the frequency.

$$E_z^s = I(z)Z_s - E_z^i, \tag{6.4}$$

using Z_s as the surface impedance per unit length given by

$$Z_s = \frac{\xi J_o(\xi a)}{2\pi a \sigma J_1(\xi a)}, \tag{6.5}$$

where $J_0(\xi a)$ and $J_1(\xi a)$ are the first-kind Bessel functions, a is the radius of the cylindrical wire antenna, and

$$\xi = (1-i)\sqrt{\frac{\omega\mu\sigma}{2}}. \tag{6.6}$$

In order to observe the variation of gold conductivity within the IR frequency range, the conductivity of (6.3) is plotted at a frequency range of 18-100 THz for the gold parameters of: $\varepsilon_\infty = 1$, $f_p = 2.183$ PHz and $\Gamma = 6.46$ THz [107]. Fig. 6.2 shows how the conductivity of gold reduces as the frequency increases. It is clearly shown that at lower frequencies (around 18 THz) the conductivity is approximately the same as the DC bulk conductivity of gold (45×10^6 Sm^{-1}), whereas the conductivity tends to be lower

when the frequency is increased. The material can be classified as a good conductor when $|\psi| \gg 1$, where $\psi = \frac{\sigma}{\omega\varepsilon_o}$ [106]. Table 6.1 shows in details how the conductivity of the gold decreases with increasing frequency within the IR regime, in comparison to the visible region.

Table 6.1: Gold conductivity computed from (6.3) showing the range from far-IR to optical frequencies, indicating that the material has a high value of $|\psi|$ at the frequency of interest (30 THz).

Frequency	$\lvert\sigma\rvert$	$\lvert\psi\rvert$
1 THz	4.05×10^7	7.29×10^5
10 THz	2.2×10^7	4×10^4
30 THz	8.63×10^6	5.17×10^3
70 THz	3.77×10^6	968.4
100 THz	2.64×10^6	475.55
500 THz	5.3×10^5	19

When observing the electrical field at the surface of the antenna, only the z component is needed, hence E_z^s can be written as [13]

$$E_z^s = -i\frac{1}{\omega\mu\varepsilon}\left(\beta^2 A_z + \frac{\partial^2 A_z}{\partial z^2}\right), \tag{6.7}$$

and we can write the potential vector A_z as follows

$$A_z = \mu\int_{-\frac{L}{2}}^{\frac{L}{2}} I(z')K(z-z')dz', \tag{6.8}$$

where

$$K(z-z') = \frac{1}{2\pi}\int_0^{2\pi}\frac{e^{(-j\beta_o R)}}{R}d\phi' \qquad \text{(Exact kernel)} \tag{6.9}$$

and

$$R = \sqrt{a^2 + (z-z')^2}. \tag{6.10}$$

Assuming that the antenna is very thin, $a \ll \lambda$ or $\beta_o a \ll 1$, then the thin wire approximation can be used as follows [13]:

$$K(z-z') = \frac{e^{(-j\beta_o R)}}{R}. \qquad \text{(Approximate kernel)} \tag{6.11}$$

Substituting (6.8) into (6.7) and then into (6.4) leads the general integral equation of Pocklington (6.12) for a cylindrical wire antenna of an imperfectly conducting metal, which can then be used to determine the current distribution over the antenna surface by

knowing the incident electric field E_z^i, i.e.

$$(\partial_z^2 + \beta_o^2)\frac{\mu}{4\pi}\int_{-\frac{L}{2}}^{\frac{L}{2}} I(z')K(z-z')'dz' = i\omega\mu\varepsilon(I(z)Z_s - E_z^i(z)) \tag{6.12}$$

Pocklington's equation (6.12) can be converted into Hallen's integral equation [108] by writing

$$\int_{-\frac{L}{2}}^{\frac{L}{2}} I(z')(K(z-z') + \zeta(z-z'))dz' = C_1\text{sin}(\beta_o z) + C_2\text{cos}(\beta_o z) - \frac{i4\pi\varepsilon\omega}{2\beta_o}\text{sin}(\beta_o|z|), \tag{6.13}$$

where (C_1 and C_2) are the constants of Hallen's equation, and

$$\zeta(z-z') = \frac{\omega\mu}{a\sigma}\frac{e^{-i\beta_o|z-z'|}}{\beta_o}. \tag{6.14}$$

In order to solve (6.12) and (6.13) numerically for the unknown current $I(z')$, with a known excitation source of unity voltage at the center of the antenna, MoM [13][109] has been used by expanding the surface current distribution $I(z')$ into a series of N basis functions as follows

$$I(z') = \sum_{n=1}^{N} I_n G_n(z'), \qquad n = 1, 2, \cdots, N \tag{6.15}$$

$G_n(z')$ is piecewise constant function that can be defined as

$$G_n(z') = \begin{cases} 1, & \text{if} \quad z_n - \frac{D_z}{2} \leq z' \leq z_n + \frac{D_z}{2} \\ 0, & \text{otherwise} \end{cases} \tag{6.16}$$

where the antenna is divided into N segments of width $D_z = \frac{L}{N}$, and

$$Z_n = \left[D_z(n-1) + \frac{D_z}{2} - \frac{L}{2}\right]. \tag{6.17}$$

The integral equations are solved by matrix equation techniques as below

$$\sum_{n=1}^{N} I_n Z_{mn} = V_m, \qquad m = 1, 2, \cdots, N \tag{6.18}$$

We can write (6.18) more precisely by using the matrix notation as

$$[I_n]\,[Z_{mn}] = [V_m]\,. \tag{6.19}$$

Therefore, the current's coefficients can be determined as follows

$$[I_n] = [Z_{mn}]^{-1}\,[V_m]\,. \tag{6.20}$$

As an example, we will take the case of a center-fed cylindrical dipole antenna that is made of gold and has a total length of $L = 0.47\lambda$, $N = 51$, and a radius a=40 nm at λ=10 μm. In this case, Pocklington's equation (6.12) has been solved for both the delta-gap source and the magnetic frill generator. For comparison purposes, Hallen's integral equation (6.13) has also been solved by using the approximate kernel and the same MoM parameters, where a delta-gap source is employed. As mentioned in [110], an approximate kernel can only be used as long as the ratio $a/\lambda \leq 0.01$. In this example, a ratio of 0.004 is provided, which makes the approximation acceptable.

For the magnetic frill generator, the following expression has been used from [12]

$$E_z^i = -\frac{V_{in}}{2\ln(\frac{b}{a})}\left[\frac{e^{-j\beta R_1}}{R_1} - \frac{e^{-j\beta R_2}}{R_2}\right], \tag{6.21}$$

where

$$R_1 = \sqrt{a^2 + (z - z')}, \tag{6.22}$$

$$R_2 = \sqrt{b^2 + (z - z')}, \tag{6.23}$$

V_{in} is the excitation voltage at the feed gap, a is the inner radius of the current's annual aperture, which is identical to the antenna's radius and b is the outer radius.

The current distribution $I(z')$ over the antenna length L near the first resonance (λ=10 μm) is plotted and compared to a sinusoidal function as shown in Fig. 6.3. Additionally, a PEC based antenna has been simulated yielding identical results due to the fact that the conductivity of gold at the frequency of interest (30 THz) is high so that gold can be still considered as a good conductor. However, we expect different results at visible light as shown in Table 6.1 and Fig. 6.2. These results are consistent with the basic current distribution of a half-wavelength center-fed dipole antenna [13][111], which validates the results.

Since Pocklington's and Hallen's integral equations give similar results, it is expected that Hallen's equation provides more stable numerical results [112]. Equation (6.13) will

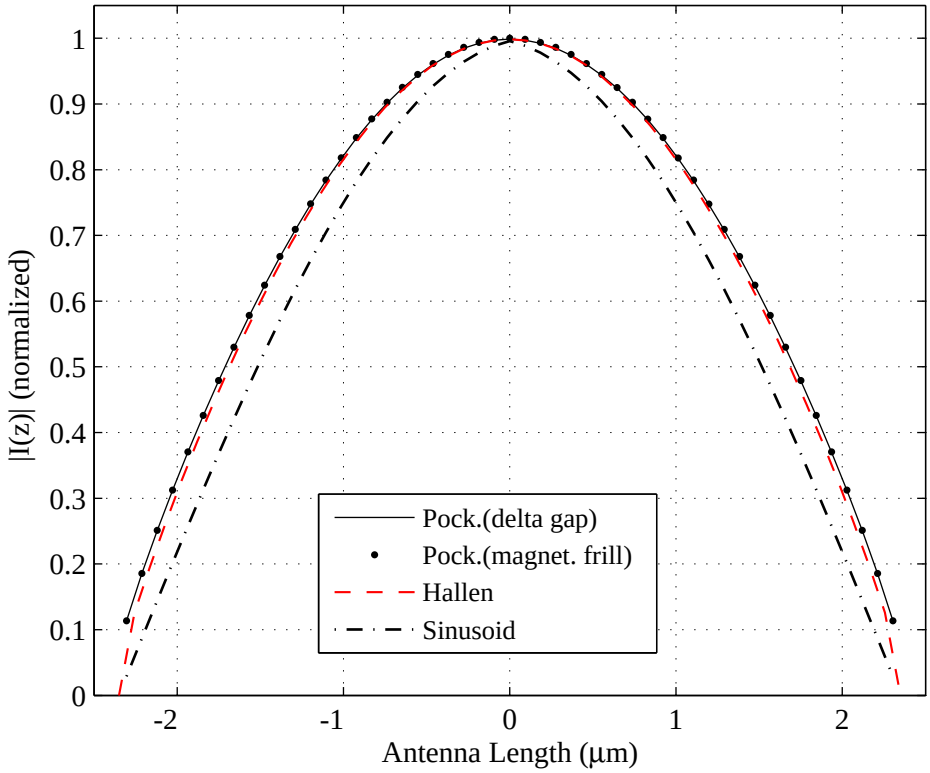

Figure 6.3: Current distribution on the surface of the IR wire dipole antenna at f=30 THz (λ=10 μm), computed using L=4.7 μm, a=40 nm, and $N = 51$.

thus be adopted henceforth. The solution is found by matching at points $z = z_m$, where both sides of (6.13) can be converted as follows

$$Z_{mn} = \int_{z_n-\frac{D_z}{2}}^{z_n+\frac{D_z}{2}} \frac{e^{(-j\beta_o\sqrt{a^2+(z_m-z')})}}{\sqrt{a^2+(z_m-z')}}dz' + \int_{z_n-\frac{D_z}{2}}^{z_n+\frac{D_z}{2}} \frac{\omega\mu}{a\sigma}\frac{e^{-i\beta_o|z_m-z'|}}{\beta_o}dz', \quad (6.24)$$

$$V_m = C_1\sin(\beta_0 z) + C_2\cos(\beta_0 z) - \frac{i4\pi\varepsilon\omega}{2\beta_o}\sin(\beta_o|z|) \quad (6.25)$$

and

$$I_n = \frac{V_m}{Z_{mn}} = C_1\frac{\sin(\beta_0 z)}{Z_{mn}} + C_2\frac{\cos(\beta_0 z)}{Z_{mn}} - \frac{\frac{i4\pi\varepsilon\omega}{2\beta_o}\sin(\beta_o|z|)}{Z_{mn}}. \quad (6.26)$$

Equation (6.26) can be simplified as follows:

$$I_n = C_1 s + C_2 c - k. \quad (6.27)$$

As the current distribution over the antenna length is approximately sinusoidal, equalling

zero at both ends, so the constants of Hallen's integral equation (C_1 and C_2) can be determined by applying the boundary conditions that imply $I(\pm L) = 0$ into (6.27) as follows:

$$I_1 = I_N = 0, \tag{6.28}$$

this yields

$$C_1 s^{-L} + C_2 c^{-L} - k^{-L} = 0 \quad \text{when } (z = -L) \tag{6.29}$$

and

$$C_1 s^{L} + C_2 c^{L} - k^{L} = 0, \qquad \text{when } (z = L) \tag{6.30}$$

where the term s^{-L} (s^L) refers to the value of s when $z = -L$ ($z = L$). This notation applies to c and k.

Solving equations (6.29) and (6.30) results in

$$C_2 = \frac{k^L}{\frac{-s^{-L}+k^{-L}}{c^{-L}} + s^L} \tag{6.31}$$

and

$$C_1 = -C_2 \frac{s^{-L} - k^{-L}}{c^{-L}}. \tag{6.32}$$

For verification of the results, the antenna in the previous example has been modeled and simulated using a finite element method (FEM) based simulation software. In the FEM simulations, the antenna is placed inside a 20 μm diameter sphere filled with air. The whole structure has been meshed into 4732 elements, and then appropriate boundary conditions have been applied. The antenna has been fed by employing a delta-gap electric field source that corresponds to an excitation voltage of 1 V at the center, and 2-D simulations have been performed. The results show that the current distribution over the antenna's surface correlate well with that obtained from MoM (6.13), as illustrated in Fig. 6.4. Through the FEM simulations, the air gap of the antenna has been excluded from the structure in order to decrease the simulation domain and hence decrease the computational requirements. Therefore, in order to calculate the input impedance ($Z_{in} = R_{in} - iX_{in}$) of the antenna, we have taken the air gap impedance into account which is in parallel with the antenna impedance ($Z_a = R_a - iX_a$), as shown in Fig. 6.5 [113]. The antenna resistance R_a and the antenna reactance X_a have been found from the FEM simulations.

Fig. 6.6 shows the variation of the input impedance when increasing the frequency

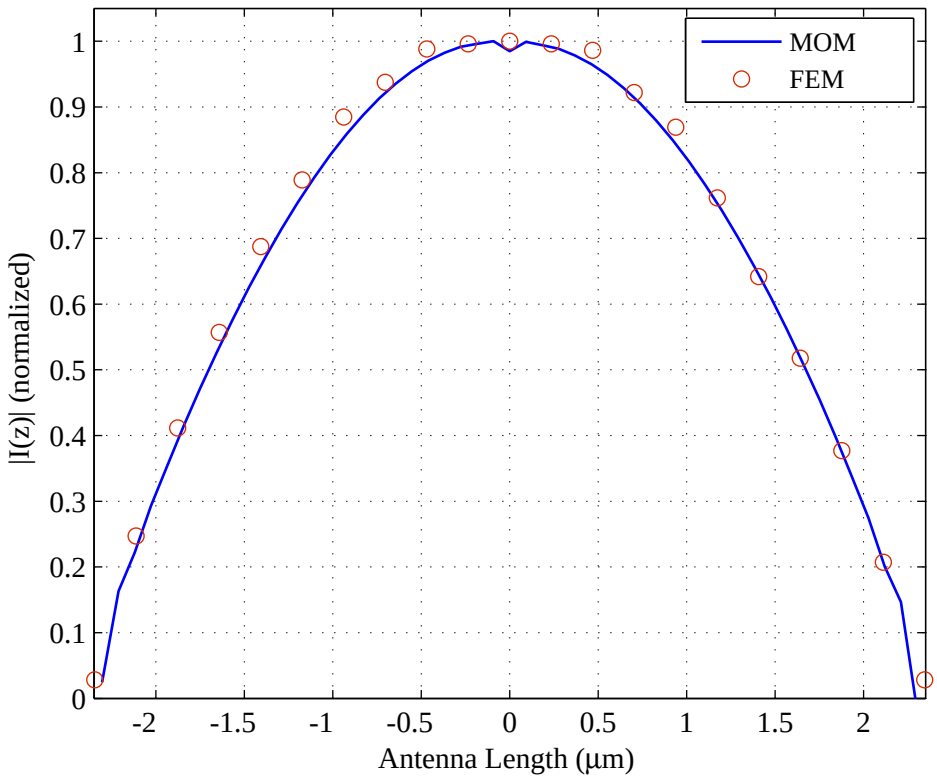

Figure 6.4: Magnitude of the current distribution over the antenna length, comparing results from MoM (6.13) with those obtained from the FEM simulations.

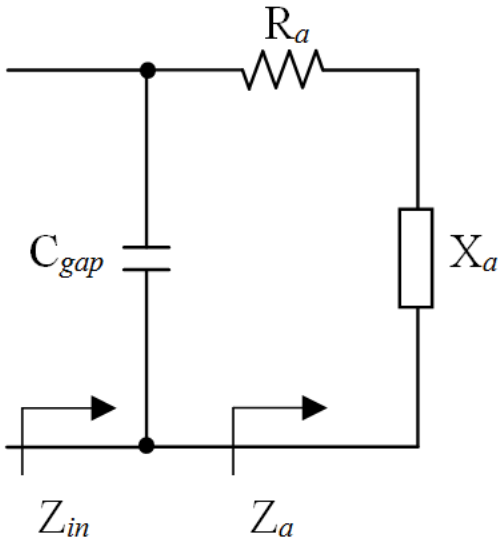

Figure 6.5: Circuit model of the IR dipole antenna showing the input impedance Z_{in} at the antenna's feed gap, where: C_{gap} is the capacitance generated by the air gap, R_a is the antenna resistance which is a combination of connecting the radiation resistance R_{rad} in series with the loss resistance R_{loss}, and X_a is the antenna reactance.

for the IR dipole antenna, and compares the results calculated from MoM with the corresponding values calculated from the FEM simulations. However, it can be shown in Fig.

6.6 that the two impedances are not identical. The reason for this may be due to the fact that in the MoM calculations, the approximate kernel has been used. However, the results are close enough so that the model can be used to analyze the IR dipole antennas using Hallen's integral equation for imperfectly conducting metals. The modeled IR antenna hits its first resonance at $X_{in} = 0$, which is approximately 30 THz, as shown in Fig. 6.6. This is consistent with the theoretical resonance of the center-fed half-wavelength dipole. Based on the classical antenna theory, the resonance can be determined from the reactance, X_{in}, when its value passes from negative to positive values. This approach can give a clear indication of resonance and can be used for high-Q systems [114]. In [108], [113], the authors employed this approach to define the resonant frequency of the dipole antenna.

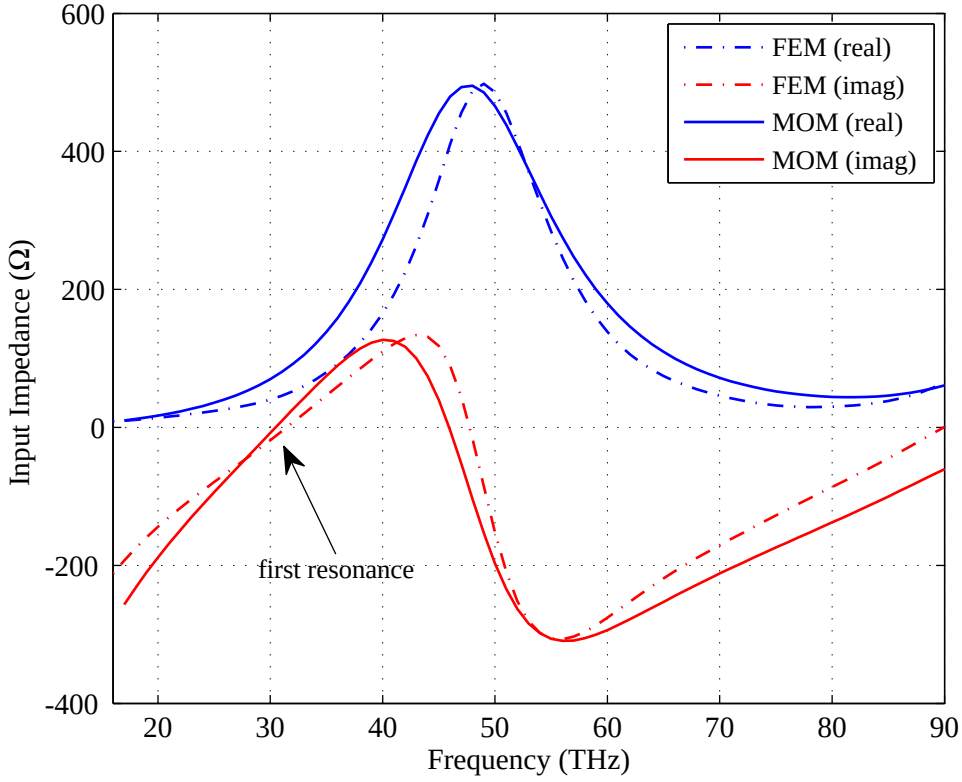

Figure 6.6: Real (blue line) and imaginary (red line) parts of the input impedance calculated from MoM (6.13) (solid line) compared with that computed from FEM simulations (dashed-dotted line).

6.2 Coupling The IR Wire Antenna to the MIM Diode

As mentioned earlier in this chapter, a suitable rectifier need to be attached to the antenna in order to obtain DC power. However, there is no solid-state type of diodes currently

available working at very-high frequencies (i.e. 30 THz) and have very small size (nano-scale). The Schottky diode is used for rectification and detection at the lower frequency range up to 5 THz. Thus, the solution is to integrate the rectifier in the body of the antenna in the manufacturing process. The most popular rectifier in solar rectennas is the MIM diode, which can be used as an alternative to Schottky diode for frequencies in the far-IR to visible range due to the femtosecond tunneling times of an electron through a thin barrier. The MIM diode is a thin film device consisting of an insulator layer that is a few nano-meters in thickness sandwiched between two metal electrodes. MIM diodes showed acceptable functionality in converting the THz signals into DC output [101]-[21].

The rectification occurs based on the electron tunnelling process through the insulator layer. In order to ensure a successful rectification, certain conditions need to be fulfilled. These conditions are: 1) The insulator layer should be very thin, in order of few nano-meters, to allow sufficiently large electrical current and ensure the occurrence of the tunneling effect. 2) The behaviour of the I-V characteristics should be asymmetric. This can be obtained by using different metals on both sides of the insulator layer with large work function difference between them. 3) The area must be very small in order to increase the cut-off frequency, which in turn allows the diode to rectify the THz frequencies. Additionally, the antenna resistance has to be close to the diode's resistance to provide good impedance matching between them, which therefore increases the system efficiency [102].

To build such a diode, one end of the dipole's arm has been pared, as depicted in Fig. 6.27(a), to provide a room for the diode. The two arms of the dipole are then overlapped over an area of 50×50 nm^2, where an insulator layer consisting of a dielectric constant of ϵ_r=7 and a thickness of 8.5 nm has been inserted within the gap region (the shaded red area) as illustrated in Fig. 6.7(a); this represents a solar rectenna that consists of an IR dipole nanoantenna coupled to a MIM diode. It is expected that the stacked antenna in Fig. 6.7(b) features all the desired characteristics of the standard antennas [76], while enabling the designer to implement and integrate the MIM diode to the antenna.

The equivalent circuit of the MIM diode, biased at zero voltage, can be described as a non-linear resistance R_D in parallel with the diode capacitance C_D as shown in Fig. 6.8. The cut-off frequency f_c of the MIM diode effectively depends on the diode resistance, R_D and the MIM capacitance, C_D; both of which can be described as [74]

$$f_c = \frac{1}{2\pi R_D C_D}. \tag{6.33}$$

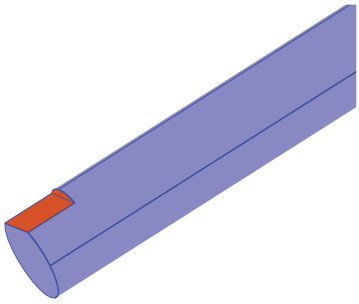

(a) Removing a block from the arm's end to provide room for the diode.

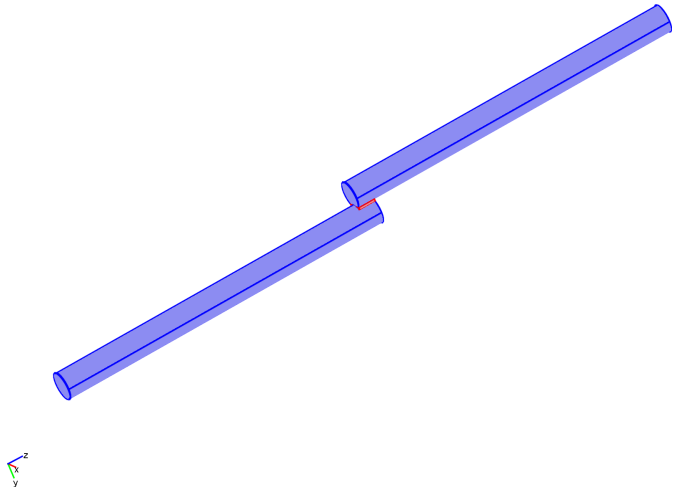

(b) Stacked IR dipole antenna integrated to the established MIM diode.

Figure 6.7: Schematic view of the IR solar rectenna.

The frequency response of the MIM diode is determined by the time constant ($R_D C_D$). The value of R_D depends mainly on the fabrication process, thus, the diode capacitance C_D can be used to adjust the cut-off frequency of the MIM diode, as it plays a significant role in controlling its value. The diode capacitance can be considered as a parallel-plate capacitor and is given by

$$C_D = \frac{\varepsilon_{\mathrm{r}} \varepsilon_0 A}{s}, \tag{6.34}$$

where ε_{r} represents the relative permittivity of the insulator layer of the MIM diode, ε_0 is the free space's permittivity, A is the diode junction area (overlapping area), and s is the thickness of the insulator layer.

In order to achieve a high cut-off frequency for the MIM diode to be operating within the IR regime, a very low diode capacitance is required. The low capacitance can be

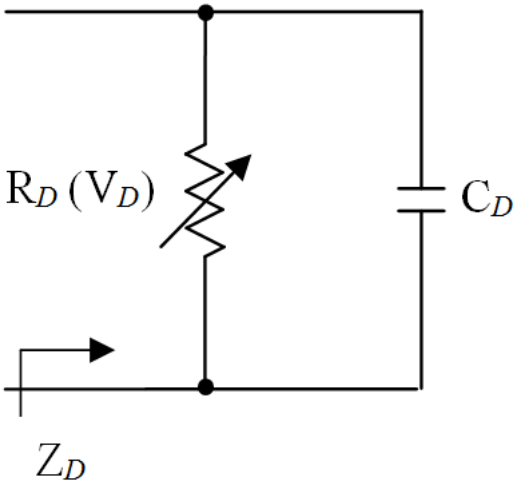

Figure 6.8: The equivalent circuit of the MIM diode which is a combination of the diode capacitance C_D connected in parallel with the variable diode resistance R_D, where V_D is the voltage that applied to the diode terminals provided by the antenna.

achieved by either minimising the overlapping area and/or increasing the insulator layer thickness. There is a trade-off between these two factors. On one hand, increasing the thickness of the insulator layer will lower the diode capacitance and will decrease the tunneling probability, while decreasing this thickness would make the capacitance higher, which in turn short-circuits THz frequencies [9]. On the other hand, minimizing the overlapping area to attain a very high operating frequency (visible or IR regime) requires this area to be no more than few nano-meters, which makes the fabrication process extremely challenging [21].

For the case of the antenna shown in Fig. 6.7, the diode resistance R_D has been assumed to be $100\ \Omega$. Based on these characteristics, the cut-off frequency for the MIM diode is 76.43 THz, which is higher than the resonant frequency of the rectenna (approximately 30 THz); i.e., the obtained cut-off frequency of this diode is high enough to rectify the 10 μm incident wave. The equivalent circuit of the solar rectenna consists of the MIM diode circuit connected in parallel with the antenna circuit. Hence, the overall system model can be assembled as demonstrated in Fig. 6.9, and the input impedance of the rectenna ($Z_{Rec} = R_{Rec} - iX_{Rec}$) becomes

$$Z_{Rec} = Z_D // Z_a = \frac{(R_D R_a - X_D X_a) - i(R_D X_a + R_a X_D)}{(R_D + R_a) - i(X_D + X_a)}, \tag{6.35}$$

where

$$R_{Rec} = \frac{(R_D R_a - X_D X_a)(R_D + R_a) + (R_D X_a + R_a X_D)(X_D + X_a)}{(R_D + R_a)^2 + (X_D + X_a)^2}, \tag{6.36}$$

and

$$X_{Rec} = \frac{(R_D X_a + R_a X_D)(R_D + R_a) + (R_D R_a - X_D X_a)(X_D + X_a)}{(R_D + R_a)^2 + (X_D + X_a)^2}. \tag{6.37}$$

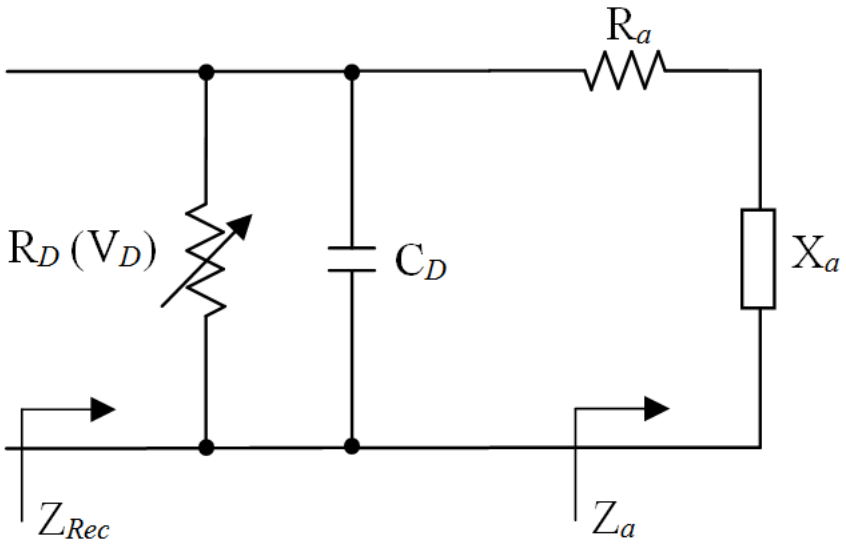

Figure 6.9: Circuit model of the IR solar rectenna, which is the parallel combination of the antenna circuit and the diode circuit

The rectenna input impedance Z_{Rec} has been calculated by solving (6.13) using MoM to attain the antenna impedance $Z_a = R_a - iX_a$, and then applying equations (6.35)-(6.37), where X_D can be calculated from (6.34). Fig. 6.10 shows the plot of Z_{Rec} versus frequency for different values of the diode resistance R_D=100 to 1000 Ω. This circuit model gives the designer a close physical insight on how the IR solar rectenna works, including the parameters that affect its performance

The results shown in Fig. 6.10 demonstrate the impact of the diode resistance R_D on the overall system input impedance, where it is clearly evident that both the input resistance and the input reactance increase as R_D increases. The increment in the input resistance is due to the parallel combination of the diode with the antenna, where the input resistance of the unloaded antenna reaches approx. 500 Ω at its maximum. Loading the antenna with a high impedance diode will therefore result in a rectenna with a total impedance close to that of the antenna.

The applied voltage (V_D) at the diode's terminals can be computed by integrating the electric field along the overlapping area. The extracted voltage is then rectified by the MIM diode into DC power, where the maximum received voltage is achieved at the resonance of the antenna (approximately 10 μm) as shown in Fig. 6.11.

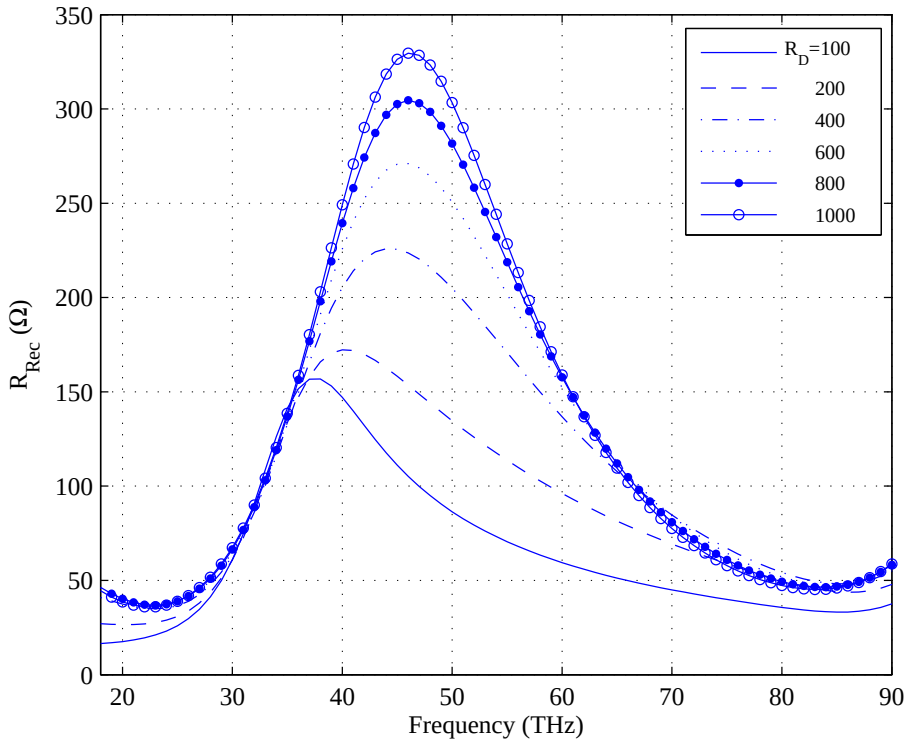

(a)

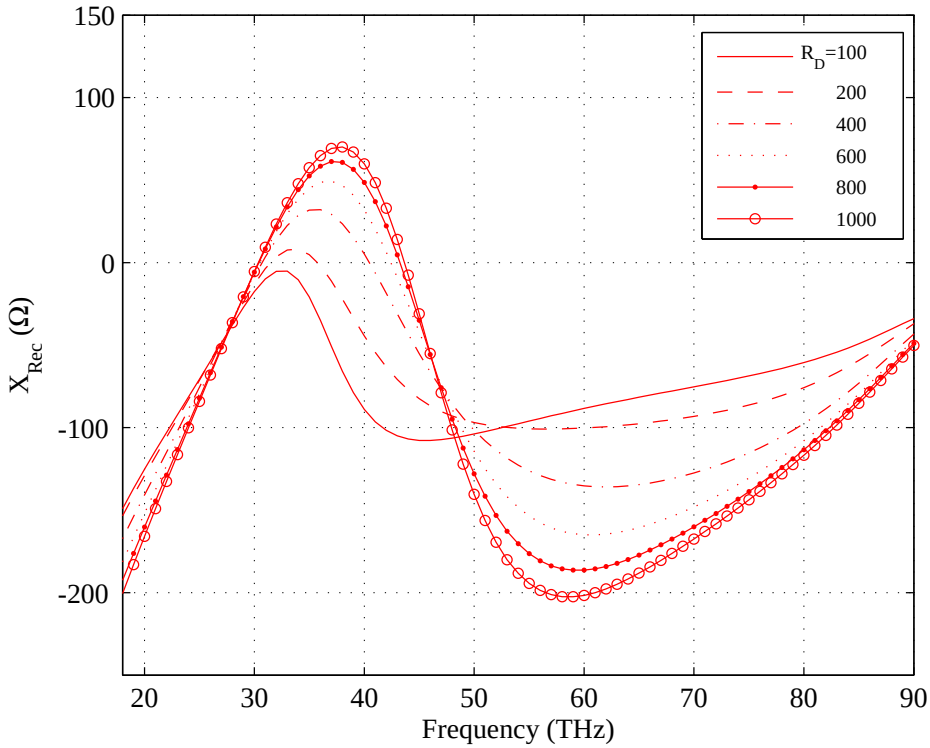

(b)

Figure 6.10: Input impedance of the solar IR rectenna of Fig. 6.7 with: L=4.7 μm, a=40 nm, overlapping area A=50×50 nm^2, with insulator layer thickness of 8.5 nm and varying the diode resistance R_D from 100 Ω to 1000 Ω: a) Input resistance, b) Input reactance.

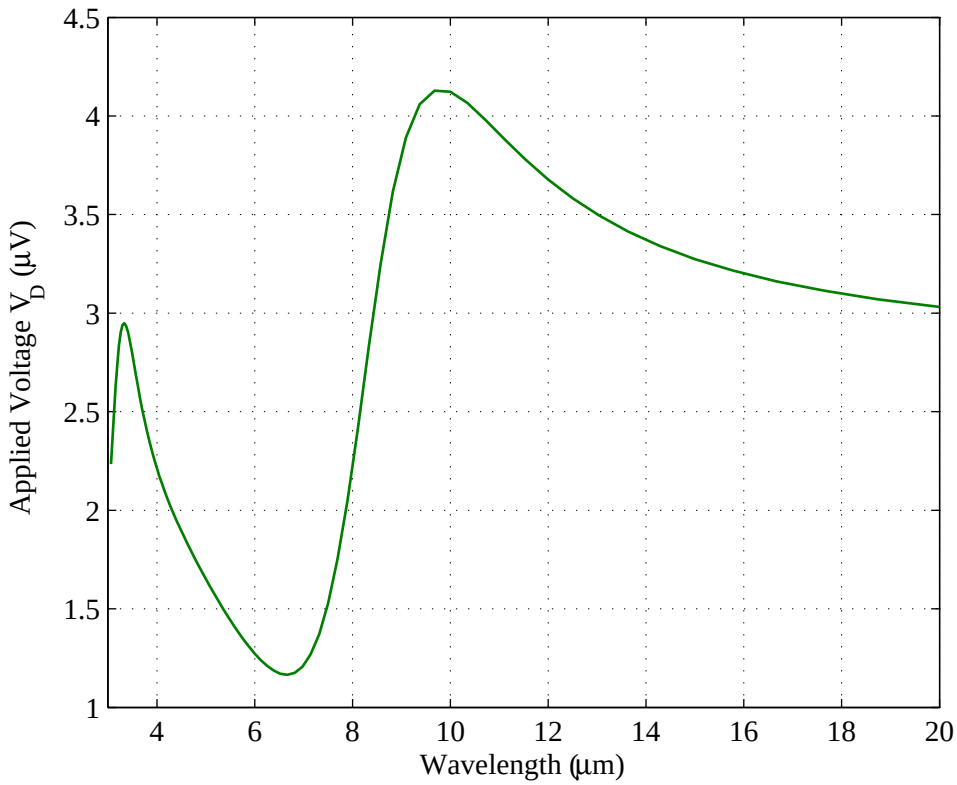

Figure 6.11: The voltage received by the antenna which is applied to the input of the MIM diode

Finally, a parametric analysis of the MIM diode parameters is presented to study the effect of the diode's area, including the gap between the diode's electrodes on the captured voltage, by adjusting the values of these parameters and holding the other parameters (kept constant). The performance of the IR solar rectenna is measured in terms of the captured AC voltage, which is applied at the diode's terminals. The area that was developed by overlapping the antenna arms has been changed to observe its impact on the solar rectenna performance. Fig. 6.12 shows the variation of the captured voltage versus wavelength for different values of the diode area, where it is evident that the voltage decreases and the resonant wavelength is shifted up with increasing wavelength. The gap between the diode's terminals is then varied from 5 to 10 nm as shown in Fig. 6.13, where it is clear that changing the gap value will result in a minor increase in the voltage, albeit with negligible effect on the resonant wavelength. This slight impact of the diode parameters on the rectenna performance gives the designer a certain amount of freedom in choosing the diode characteristics.

All previous analysis was for a single antenna element, which can only generated insignificant amount of power. Thus, in order to increase the output power, more elements

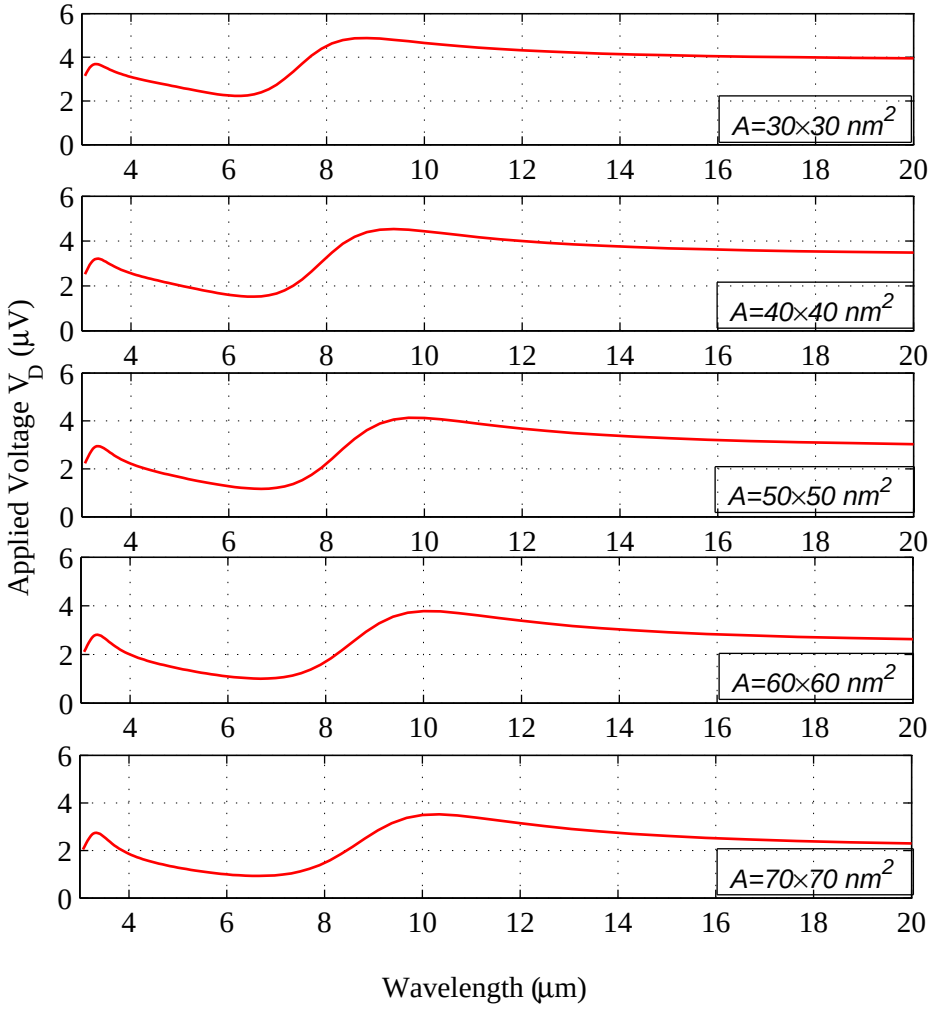

Figure 6.12: Variation of the diode voltage with the wavelength for different values of the diode area.

can be coupled together by feeding lines to form an array. In this case, mutual coupling effects will be introduced, which can be controlled by adjusting the separation between elements. However, such effect cannot be analysed easily [13]. However, the output from each element is a DC signal, which can be easily collected from elements by a simple feeding network.

6.3 Solar Rectenna Conversion Efficiency

The figure of merit in solar rectennas is the conversion efficiency, which depends on several factors related to both the antenna and the MIM diode. The conversion efficiency, η_t, of a solar rectenna can be described as [115] [116]

$$\eta_t = \eta_r \eta_s \eta_q \eta_c, \tag{6.38}$$

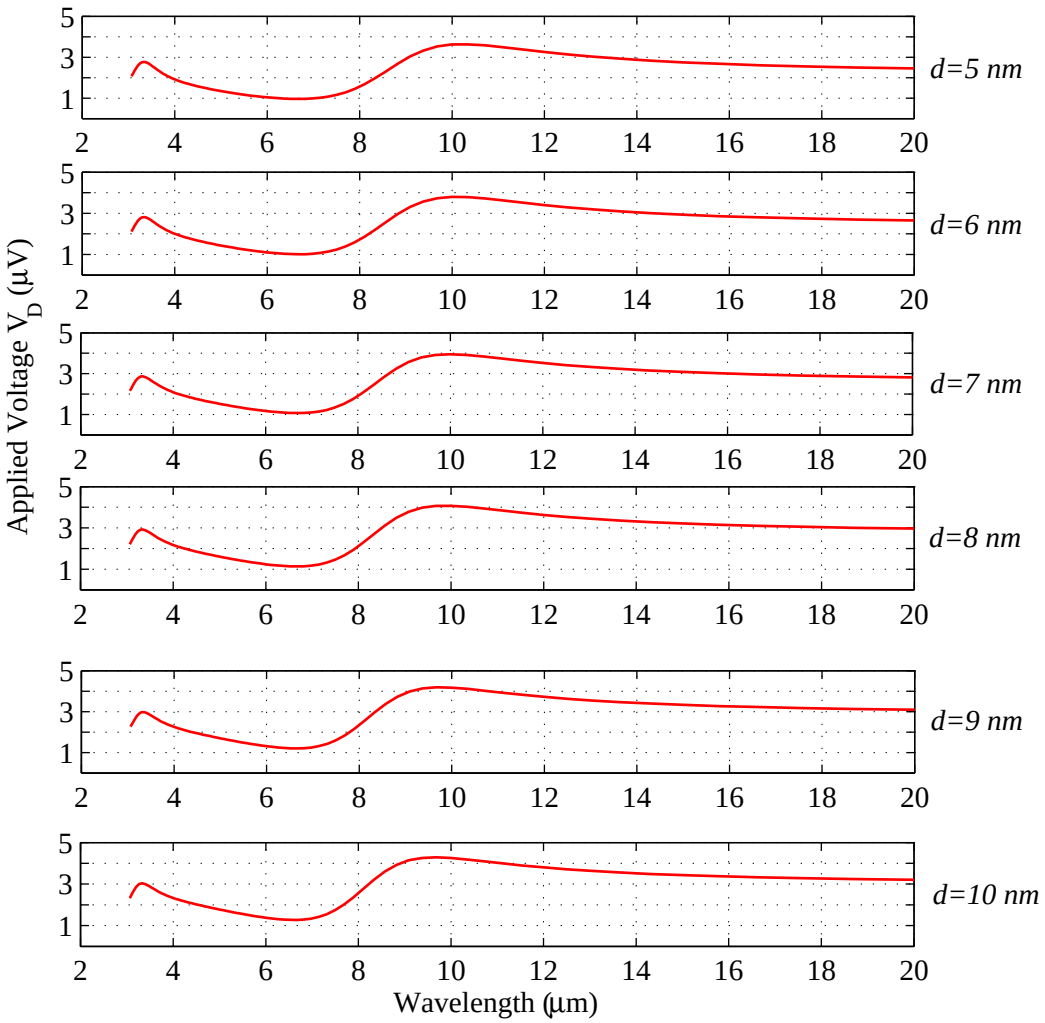

Figure 6.13: Variation of the diode voltage versus the wavelength for different gap distances between the diode terminals.

where η_r is the antenna radiation efficiency, η_s is the efficiency that related to the losses inside the antenna, η_q is the quantum efficiency that is responsible for the rectification of the received power, and η_c is the coupling efficiency between the antenna and the diode. It is worth noting that the term, $\eta_r\eta_s$, in (6.38) depends on the antenna type and its characteristics and is referred to, in this thesis, as the *antenna-dependent efficiency* of the solar rectenna. On the other hand, the term $\eta_q\eta_c$ relates strongly to the diode parameters and is referred to as the *diode-dependent efficiency*.

For solar energy conversion, each efficiency factor is required to be optimised and maximised. Recent works have focused on improving only the quantum efficiency [115], or the diode-dependent efficiency by assuming a perfect antenna (i.e without including antenna efficiency limits) [117]. This work, to the knowledge of the author, is the first attempt that take into account both the antenna and the diode efficiencies of solar recten-

nas analytically. The analysis of the complete conversion efficiency in one single work provides the reader with a clear understanding into the concept and performance of the IR solar rectenna, including the parameters that affect its performance.

In the following subsections, the efficiency terms in (6.38) will be investigated individually, their optimum values will be computed, and hence the overall conversion efficiency will be calculated and plotted .

6.3.1 Antenna-dependent efficiency

As mentioned earlier in Section 6.3, the antenna-dependent efficiency is represented by the term $\eta_r \eta_s$. This subsection will demonstrate how to numerically determine this efficiency which depends entirely on antenna parameters. The calculation of antenna efficiency should take into account the losses that relate to reflection, conduction and the dielectric inside the antenna. The reflection losses will be represented by the coupling efficiency, η_c, and will be discussed in details in the following subsection. Thus, this subsection will be dedicated to the calculation of the conduction and dielectric losses inside the antenna structure. Since it is very difficult to compute and separate these losses individually, they will therefore be lumped together to form the conduction-dielectric efficiency, η_{cd}, which can be defined as [13]

$$\eta_{cd} = \frac{R_r}{R_r + R_l}, \tag{6.39}$$

where R_r is the radiation resistance of the antenna and the resistance R_l represents the conduction-dielectric resistance, which can be written as [13]

$$R_l = 2\frac{L}{P} R_s, \tag{6.40}$$

where L is the antenna length, P is the cross-section perimeter of the wire antenna of radius a, and R_s is the conductor surface resistance that can be calculated as

$$R_s = \sqrt{\frac{\omega \mu_0}{2\sigma}}, \tag{6.41}$$

where ω is the angular frequency, μ_0 is the free-space permeability, and σ is the metal conductivity. It is worth mentioning here that equation (6.40) is valid for the case of a uniform current distribution.

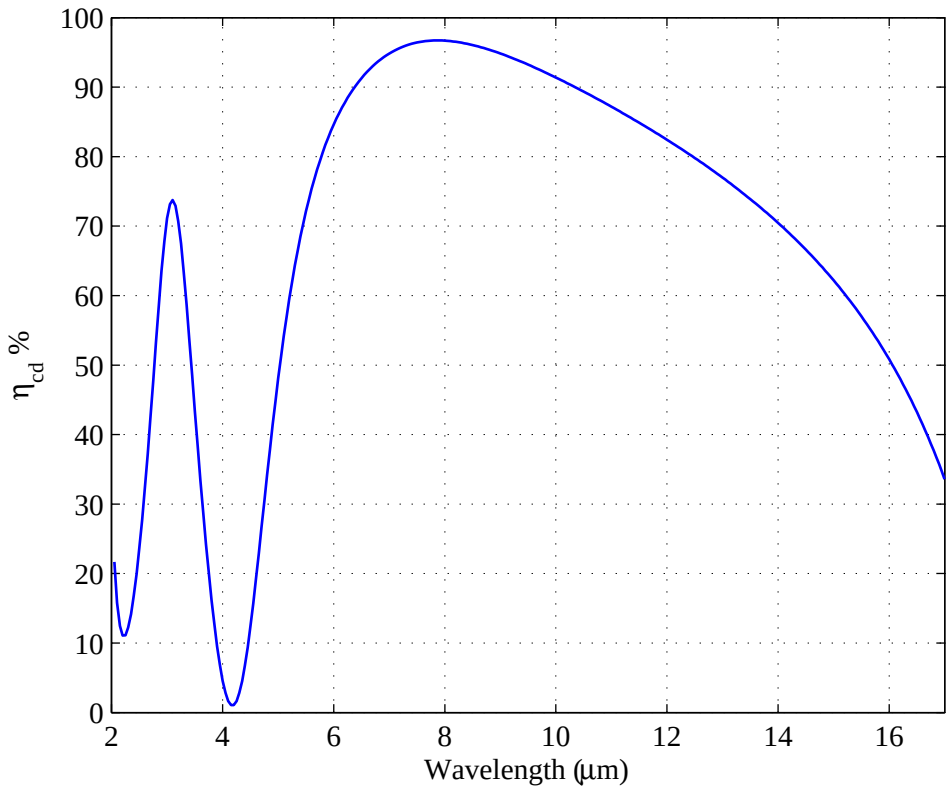

Figure 6.14: Conductor-dielectric efficiency versus wavelength for the Aluminium optical antenna.

Since the real part of the input impedance, which represents the radiation resistance, and the conductivity are already calculated, then we can easily calculate the conductor-dielectric efficiency, η_{cd}. Fig. 6.14 shows the conductor-dielectric efficiency of the optical antenna considered in this chapter.

It can be seen from Fig. 6.14 that the conductor-dielectric efficiency of this antenna is very high and reaches 94.39 % at resonance. In the following subsection, the diode-dependent part will be calculated and discussed in details.

6.3.2 Diode-dependent efficiency

The two terms of the diode-dependent efficiency are the coupling efficiency, η_c, and the quantum efficiency, η_q. In this work, the quantum efficiency is set to $\eta_q = S$, where S is the MIM diode responsivity, which will be explained more explicitly later in this section. On the other hand, the coupling efficiency can be written as [102]

$$\eta_c = \frac{4R_a R_D/(R_a + R_D)^2}{1 + (\omega(R_a R_D/(R_a + R_D)C_D))^2}, \tag{6.42}$$

where R_a is the antenna resistance, ω is the angular frequency, R_D is the diode resistance and C_D is the diode capacitance. The value of R_D depends on the I-V characteristics of the MIM diode, whereas, C_D can be given from (6.34).

It is clearly evident that the MIM diode parameters play a significant role in determining the entire conversion efficiency of solar rectennas. Therefore, in this subsection, we will investigate the effect of diode responsivity and resistance on the diode-dependent part of conversion efficiency.

In order to construct the solar rectenna, an MIM diode needs to be integrated with the optical antenna for rectifying the received signal. To build such rectenna, one end of antenna arms has been tapered to provide space to build the MIM diode. The two arms of the dipole are then overlapped over an area of 120×120 nm^2, where an insulator layer of a dielectric constant ϵ_r=7 is employed as shown in the red area of Fig. 6.15. This design, which is illustrated in Fig. 6.15, features all the desired characteristics of standard antennas [76], while it enables the designer to implement and integrate the MIM diode to the antenna. MIM diodes are the most popular rectifiers utilised in solar rectennas which can be used as an alternative to Schottky diodes for visible and IR frequencies due to the lower frequency range of the latter. This type of diodes has shown acceptable functionality in converting the THz signals into DC output. The rectification properties of MIM diodes made them very popular in detecting and mixing high frequency waves [101]-[21].

After designing the solar rectenna, we can now investigate the characteristics of the antenna-coupled MIM diode. The most important characteristics in determining the solar rectenna conversion efficiency are the responsivity, which is a measure of the rectified dc current as a function of input power, and the resistance of the MIM diode. These two features can be calculated directly from the I-V curve of the MIM diode. The current density (J) of MIM diodes can be determined using the approximate expression of Simmons' formula for the tunneling current across a thin barrier, which is described by quantum mechanics as follows [118]

$$J = \frac{e}{\hbar(2\pi\beta\Delta s)^2}(\bar{\varphi}exp(-A_t\bar{\varphi}^{\frac{1}{2}}) - (\bar{\varphi} + eV_b)exp(-A_t(\bar{\varphi} + eV_b)^{\frac{1}{2}})), \quad (6.43)$$

where e is the electron charge, $\bar{\varphi}$ is the mean barrier height of the metal/insulator junction, V_b represents the applied bias, and A_t is

$$A_t = \frac{2\beta\Delta s}{\hbar}(2m)^{\frac{1}{2}}, \quad (6.44)$$

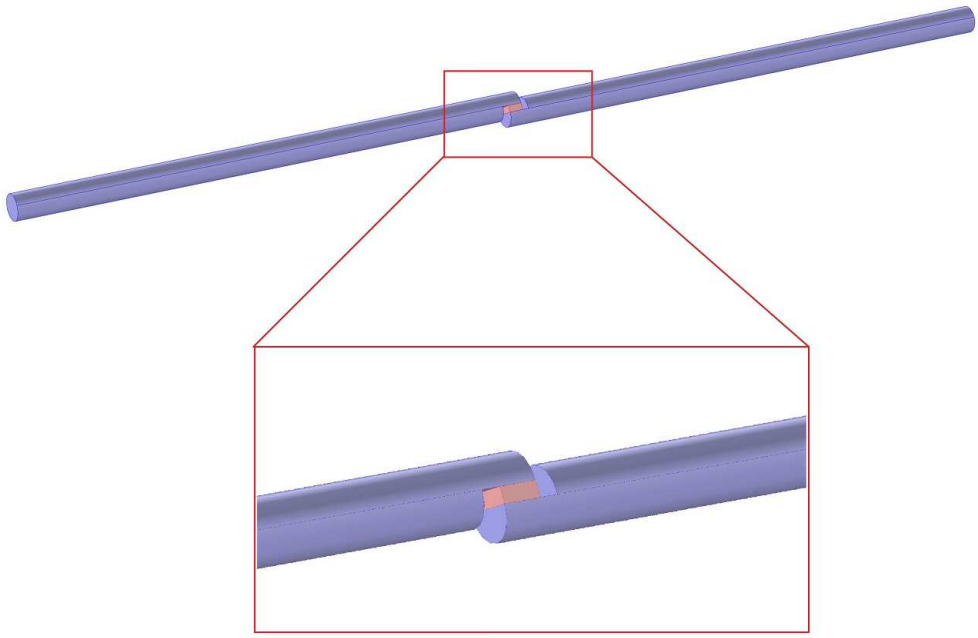

Figure 6.15: Schematic view of the stacked optical dipole antenna integrated to the MIM diode. The red area represents the insulator layer.

where $\hbar$ is the reduced Plank's constant, Δs is the tunneling distance, which is determined by Fermi level of the negatively biased electrode, m is the electron mass and β is a correction factor (set to 1 in this work).

It is worth mentioning that the barrier heights are critical in determining the tunneling current through the insulator layer. Consequently, the barrier heights should be calculated accurately. To this end, the effect of image potential between the electrodes, which depends on the high-frequency dielectric constant of the insulator, have been taken into account when calculating the barrier heights. The total barrier height, φ_t, including the effect of image potential, can be written as [119]

$$\varphi_t(x) = \varphi_1 + (\Delta\Phi - eV_b)(x/s) - \frac{0.288s}{Kx(s-x)}, \tag{6.45}$$

where φ_1 is the barrier height of the left metal, $\Delta\Phi$ is the work function difference between the metals on both sides of the diode, and K is the high-frequency dielectric constant of insulator layer. Fig. 6.16 shows the barrier potential energy of the symmetric $Al/Al_2O_3/Al$ diode at 1-V biasing, φ_1=φ_2=2.9 eV, s=5 nm and K=7.

The mean barrier height, $\bar{\varphi}$, in (6.43) is calculated by integrating the total barrier

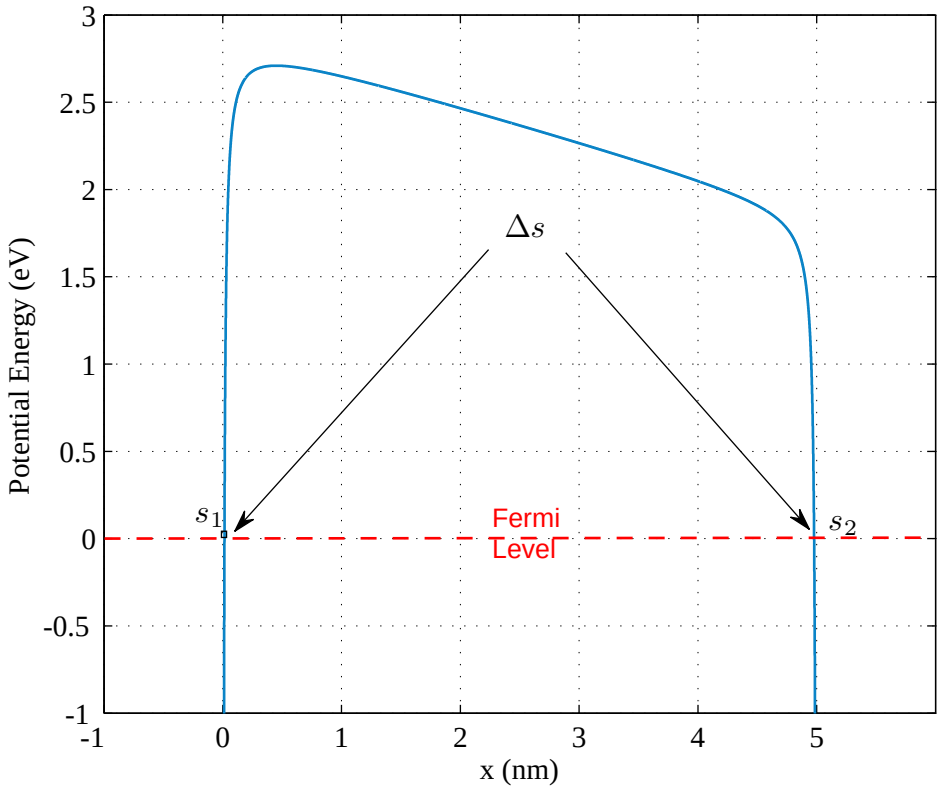

Figure 6.16: Barrier potential energy of the symmetric $Al/Al_2O_3/Al$ MIM diode with 1-V biasing, φ_1=2.9 eV, s=5 nm and K=7.

height over the tunneling distance as follows

$$\bar{\varphi} = \frac{1}{\Delta s} \int_{s_1}^{s_2} \varphi_t(x) dx, \tag{6.46}$$

where s_1 and s_2 can be determined from the intersection of the barrier height with Fermi level of the negatively biased electrode and $\Delta s = s_2 - s_1$ as shown in Fig. 6.16.

Let us assume that the antenna is made of Aluminium (Al). Equation (6.43) can now be used to plot the current density against the bias voltage, V_b, for the symmetric MIM diode of similar electrodes (i.e both are made of Al). However, asymmetric and non-linear characteristics are required for the MIM structure in order to act as a rectifier and be able to rectify the THz signals [120][121]. This can be achieved by replacing one side of the diode by another metal other than Al, giving unequal barrier heights. Hence, the left side of the MIM diode will be kept fixed to Al (i.e φ_1=2.9 eV), whereas the right side will be changed to Platinum (Pt). The work functions of Al and Pt are $\Psi_1 = 3.9$ eV and $\Psi_2 = 5.65$ eV, respectively, and the electron affinity of the insulator Al_2O_3 is $\chi = 1$ eV.

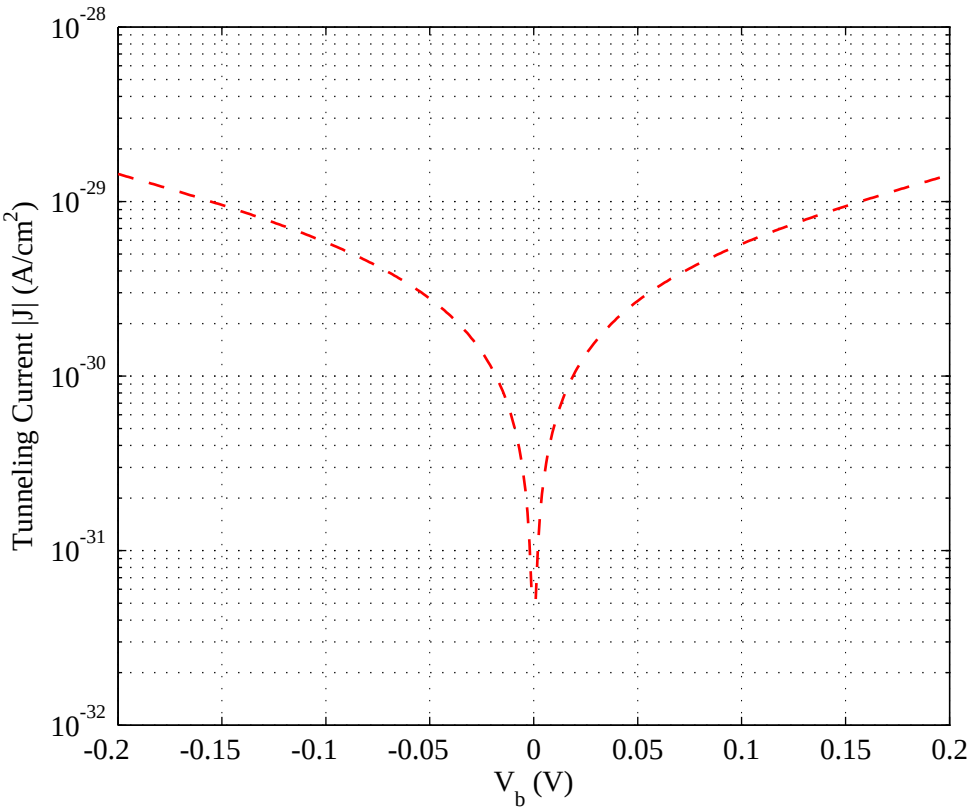

Figure 6.17: Current density versus biasing voltage for the asymmetric MIM diode with $\Delta\varphi$=1.37 eV and s=5 nm.

Based on these values the barrier height at both sides of the diode will be $\varphi_1 = 2.9$ eV and $\varphi_2 = 4.65$ eV. Barrier heights are calculated directly from the difference between metal work function and the electron affinity of insulator. The work function difference of the new asymmetric $Al/Al_2O_3/Pt$ diode is 1.37 eV [122].
Simmons' formula (6.43) is used to plot the current density versus bias voltage for the $Al/Al_2O_3/Pt$ diode with an insulator thickness of 5 nm as shown in Fig. 6.17.

The resistance, R_D, the non-linearity, N, and the responsivity, S, of the diode can be found directly from the I-V characteristics shown in Fig. 6.18. The I-V curve is fitted with a seventh-order polynomial and the other parameters are then calculated, where $R_D = \frac{1}{dI/dV}$, $N = d^2I/dV^2$, and $S = \frac{d^2I/dV^2}{dI/dV}$. The nonlinear I-V characteristics, which depend on the shape of the barrier, lead to the tunneling of current through the potential barrier [118]. It can be seen from Fig. 6.18 that the resistance is very high due to the fact that a very low current has been tunneled through the insulator. The high barrier height in the left metal (i.e φ_1) and the thick insulator, 5 nm, have contributed in producing this marginal current. Since the coupling efficiency depends on R_D, a very low value is expected for this efficiency. Thus, in the following subsection we will optimise the diode resistance to

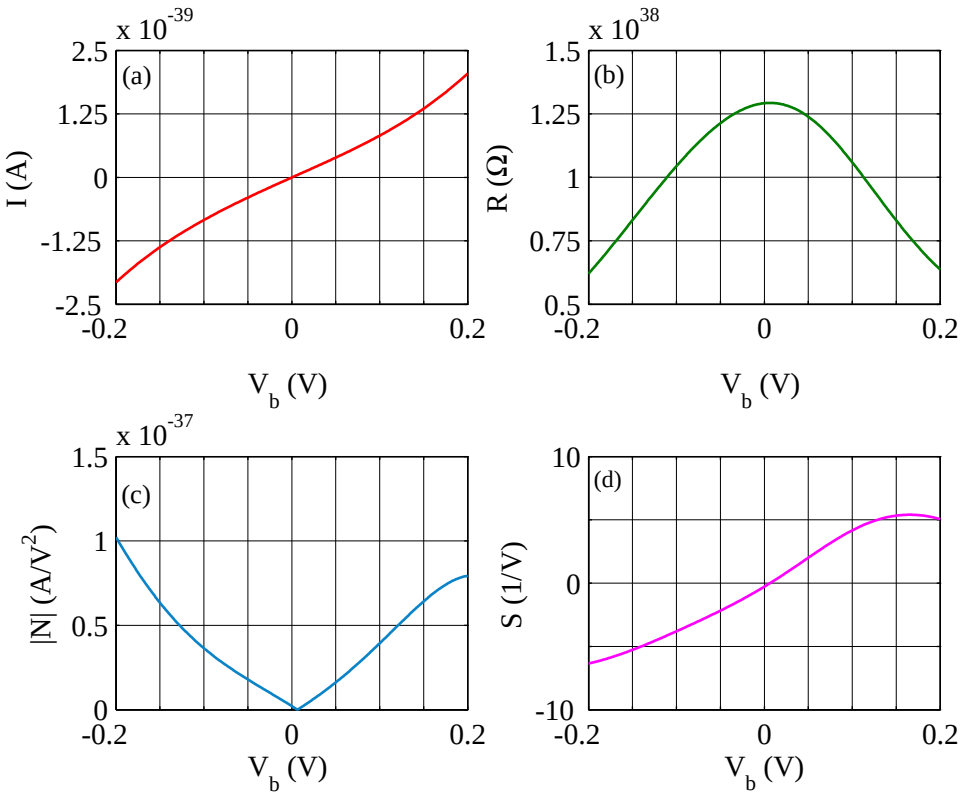

Figure 6.18: Characteristics of the asymmetric MIM diode with insulator thickness s=5 nm and barrier heights $\Delta\varphi = 1.37$ eV: (a) I-V, (b) diode resistance, (c) non-linearity, and (d) responsivity.

enhance the coupling efficiency.

6.3.3 Optimisation of the diode-dependent efficiency

In this subsection, we will characterise and optimise the diode-dependent part of efficiency, where the effect of the insulator layer thickness and the metal work function difference will be investigated. The quantum efficiency depends directly on the diode responsivity as mentioned earlier in this section. Hence, this part of the efficiency can be increased by only improving the diode responsivity. Unlike the quantum efficiency, the coupling efficiency relates to the diode resistance that should be matched with antenna resistance in order to achieve higher conversion efficiency.

It was evident from Section 6.3 that very low values of quantum and coupling efficiencies are expected due to the low diode responsivity and the poor antenna-diode matching, which will reduce the total conversion efficiency. Thus, the diode parameters will be optimised to enhance the diode-dependent efficiency. It is clearly shown in (6.42) that reducing the diode resistance leads to increasing the coupling efficiency. Additionally, it

is also shown that increasing the diode responsivity will increase the quantum efficiency. In order to improve the diode efficiency, a parametric study on the effect of insulator thickness and work function difference on the diode performance will be presented. Firstly, the effect of insulator thickness on the diode resistance and responsivity will be studied by varying the thickness from 2 to 5 nm. Fig. 6.19 demonstrates the effect of varying the insulator thickness on the diode resistance (Fig. 6.19-a) and on the diode responsivity (Fig. 6.19-b). It is shown that decreasing the thickness from 5 nm to 2 nm reduces the value of the diode resistance significantly from 1.3×10^{38} Ω to 3.35×10^{12} Ω at zero-biasing. Thus, the smaller the insulator thickness the lower the diode resistance. Furthermore, it is noted that the changes in responsivity versus insulator thickness is trivial at zero-biasing due to the high barrier height in the left metal (i.e φ_1), whereas, the responsivity increases when increasing the thickness for higher biasing values. The results show that in order to increase the efficiency at zero-biasing it is highly recommended to use a thinner insulator layer. Therefore, a 2 nm insulator thickness will be adopted for the remainder of this subsection.

The effect of metal work function difference is also studied by utilising different metals in the right side of the MIM diode while keeping the left side as Al. The proposed metals are: Platinum (Pt), Gold (Au) and Tungsten (W), where the difference in work functions for each case is: 1.37 eV, 0.82 eV and 0.27 eV, respectively [122] [123]. The diode resistance and responsivity are then calculated at $s = 2$ nm as shown in Fig. 6.20.

It can be seen in Fig. 6.20(b) that varying the work function difference has a negligible impact on the responsivity due to the high value of barrier heights on both sides of the MIM diode with respect to applied bias. At these levels of barrier heights, a constant value of tunneling distance results in, and hence varying the work function difference will have no significant impact. As a result, this will diminish the role that the work function difference plays on responsivity, and therefore the focus will be on its effect on the resistance. In addition, it is shown that there is a clear impact of the work function difference on diode resistance as it increases by increasing this difference as shown in Fig. 6.20(a). In conclusion, it is evident that the diode-dependent efficiency can be improved by choosing metals on both sides of MIM diode with a small difference in their work function values to reduce the diode resistance. After this parametric study, the efficiency can be maximised by choosing the optimised values of insulator thickness, $s = 2$ nm, and metals work function difference, $\triangle\varphi = 0.27$ eV.

Based on the above results, it is quite evident that the diode $Al/Al_2O_3/W$ shows the

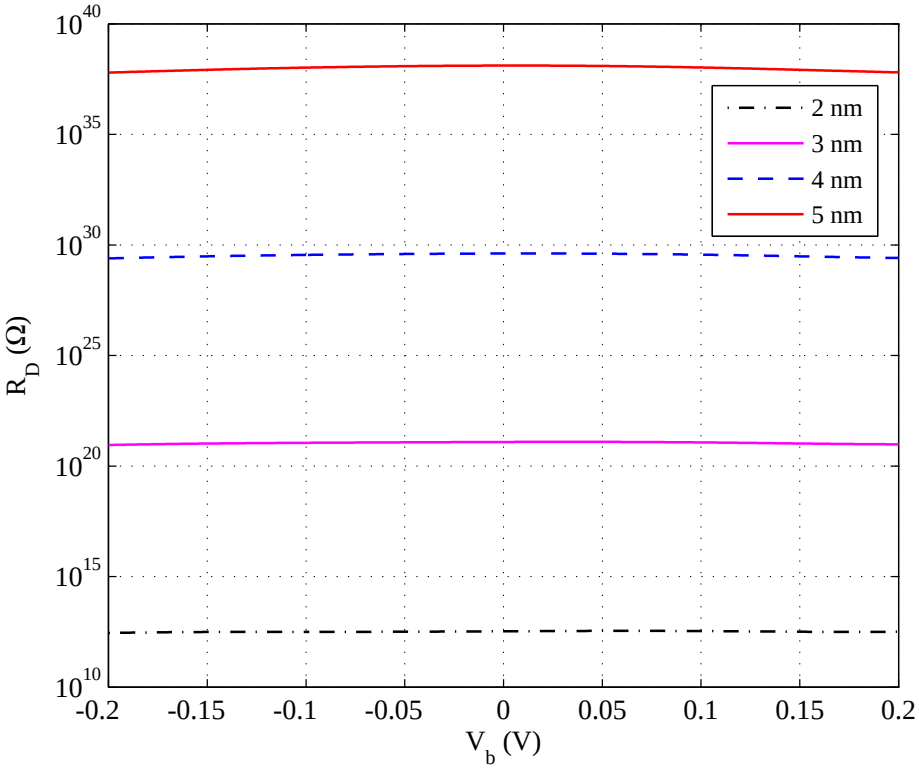

(a)

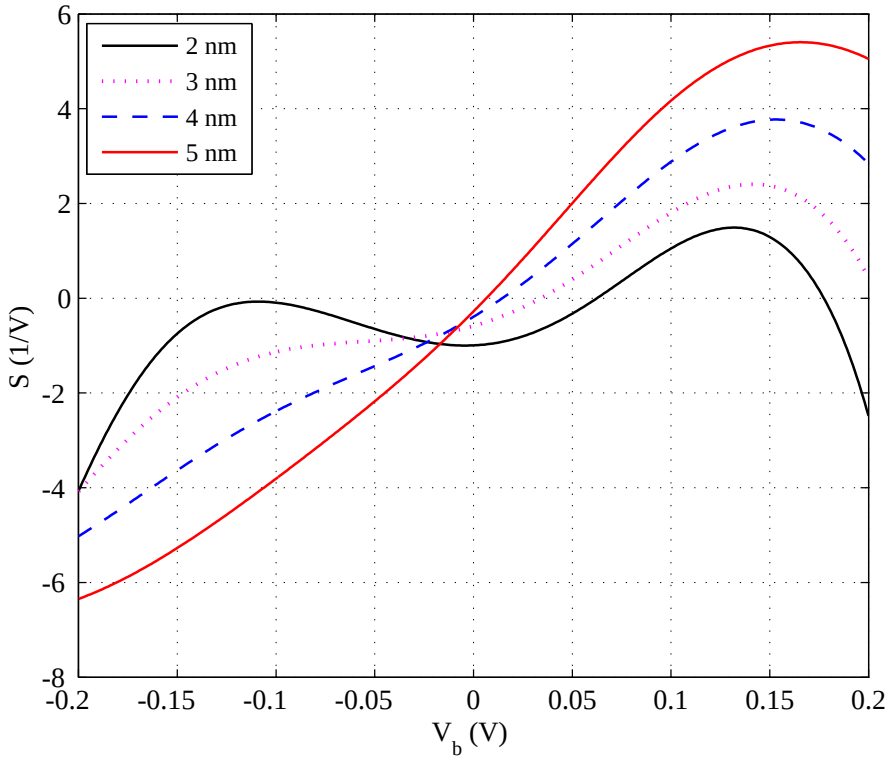

(b)

Figure 6.19: Effect of changing the insulator thickness on: (a) The diode resistance, (b) The diode responsivity. The metal work function difference is fixed to $\triangle\varphi = 1.37$ eV.

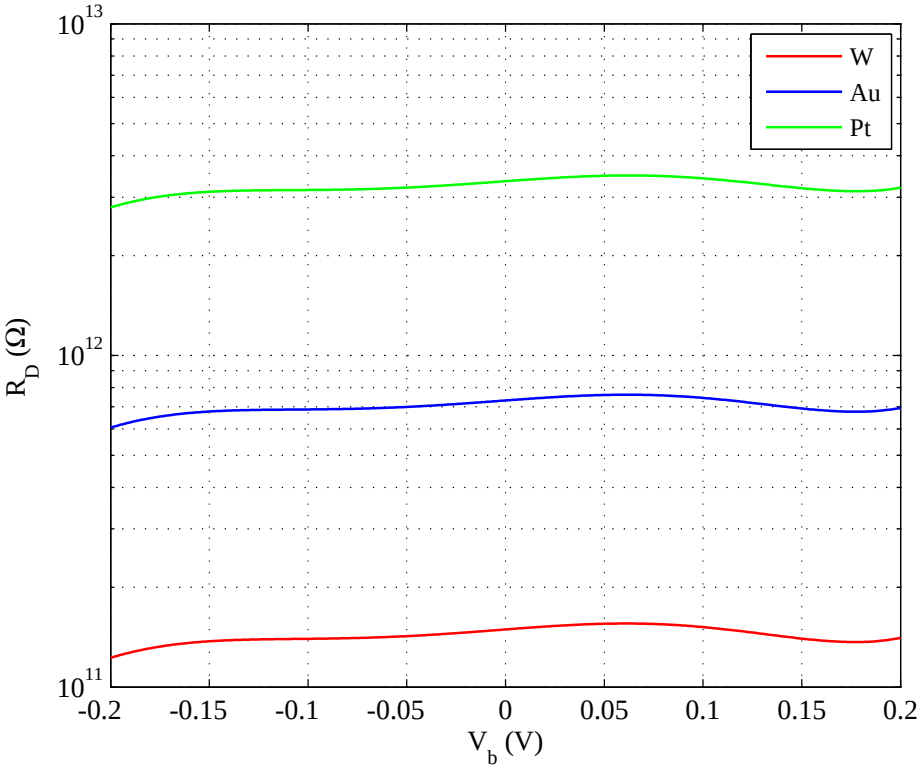

(a)

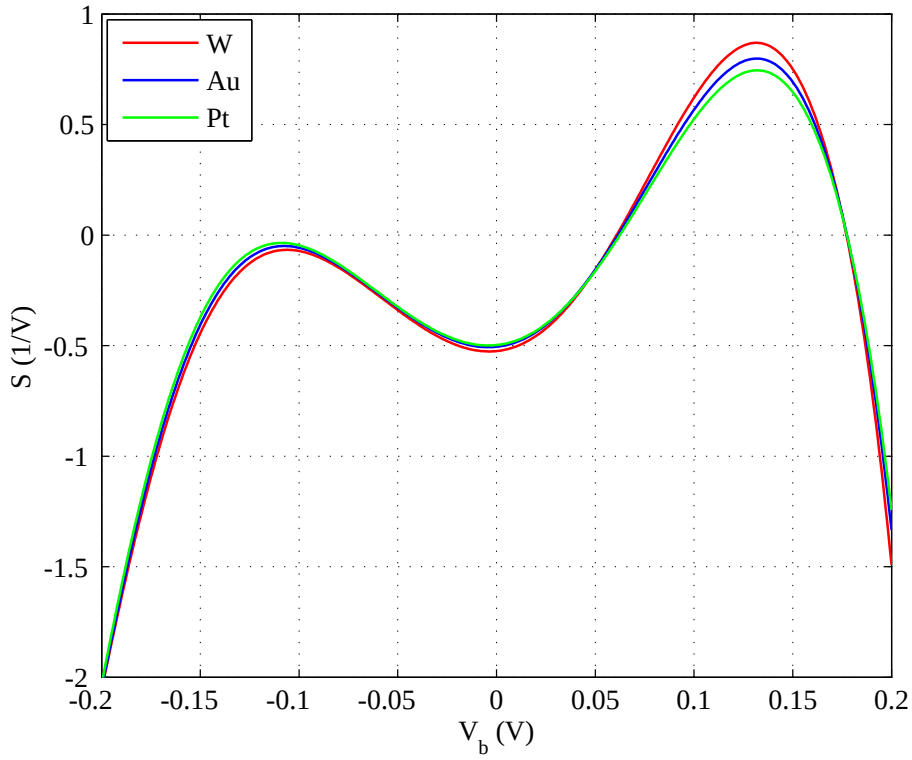

(b)

Figure 6.20: Effect of changing the work function difference on: (a) The diode resistance, (b) The diode responsivity. Insulator thickness is set to $s = 2$ nm in all cases.

best characteristics in terms of resistance and responsivity and will be adopted to calculate the diode-dependent efficiency. The optimised parameters of this diode are: insulator thickness $s = 2$ nm, and metals work function difference $\triangle\varphi = 0.27$ eV. The resistance of this optimised diode is $R_d = 1.5 \times 10^{11}\ \Omega$ and the responsivity is $|S| = 0.52\ \frac{1}{V}$.
As mentioned before, the quantum efficiency will be set to the value of the responsivity. We only need to calculate the coupling efficiency from (6.42), where R_a can be found from (6.13) which represents the real part of input impedance shown in Fig. 6.6. In addition, the diode capacitance, C_D, can be calculated using (6.34).

Fig. 6.21 shows the total conversion efficiency (solid line) for the designed IR solar rectenna versus the wavelength. Moreover, we have added the diode-dependent efficiency (dashed line) to the same graph to show the role that the antenna plays in shaping the conversion efficiency. The total conversion efficiency has been calculated based on the terms of (6.38), where each single term is calculated individually and all the terms are then combined. A closer look at Fig. 6.21 reveals that a very poor conversion efficiency is achieved . The main reason behind this low efficiency is the mismatch between the resistance of the designed MIM diode, R_d, and the antenna resistance, R_a. This mismatch has led to a lower coupling efficiency in (6.42), where one of the conditions to achieve unity efficiency is to let $R_d = R_a$.

It is worth mentioning here that Simmons' formula was developed based on WKB approximation, which neglects the reflection at the interface of the layers. Therefore, other techniques are required for more accurate results such as the transfer-matrix method (TMM), the non-equilibrium Green's function (NEGF) and the quantum transmitting boundary method (QTBM) [120] [121].

6.4 The effect of using different metals on the left side of the diode

In order to observe the role of the materials in the performance of MIM diodes, the Al side of the previous diode has been replaced with different metal (Nb). Equation (6.43) is used to plot the current density against the bias voltage, V_b, for the symmetric MIM diode of similar electrodes (i.e both made of Nb) as shown in Fig. 6.22. As seen from this figure that the J-V characteristics are symmetrical for both the positive and negative biasing. These symmetrical characteristics lead to zero non-linearity and zero respon-

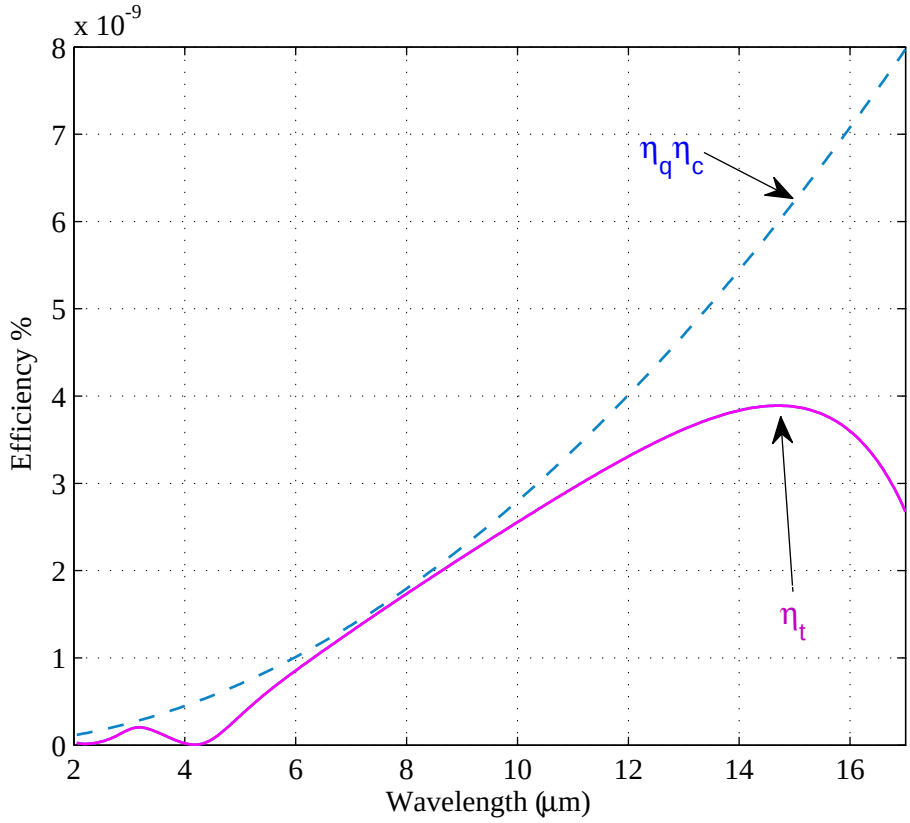

Figure 6.21: Total conversion efficiency, η_t, and the diode-dependent efficiency, $\eta_q\eta_c$, of the designed solar rectenna.

sivity at the zero biasing case, and hence, no rectification will occur. To achieve higher responsivity, different metals need to be chosen at both sides of the diode with different work functions. Thus, one arm of the antenna has been replaced with Platinum (Pt) to form a $Nb/Nb_2O_5/Pt$ diode. The work functions of Nb and Pt are $\Psi_1 = 4.3$ eV and $\Psi_2 = 5.65$ eV, respectively, and the electron affinity of the insulator Nb_2O_5 is $\chi = 3.9$ eV. Based on these values the barrier height at both sides of the diode will be $\varphi_1 = 0.4$ eV and $\varphi_2 = 1.75$ eV. The energy-band diagram for both the symmetric and asymmetric MIM diodes is shown in Fig. 6.23. The current density against bias voltage for the asymmetric $Nb/Nb_2O_5/Pt$ diode is shown in Fig. 6.24, where the non-linear and asymmetric characteristics of this diode are clearly shown.

The asymmetric current density of Fig. 6.24 is obtained due to the metal work function difference on both sides. The resistance, R_D, the non-linearity, N, and the responsivity, S, of the diode can be found from the I-V characteristics shown in Fig. 6.25, where $S = 0.88\ \frac{1}{\mathrm{V}}$, $R_D = 3.9 \times 10^{11}\ \Omega$ and $N = 2.13 \times 10^{-12}\ \frac{\mathrm{A}}{\mathrm{V}^2}$ at zero-biasing. These parameters lead to a coupling efficiency of $1.22\ \times 10^{-21}\ \%$ at $10\ \mu$m.

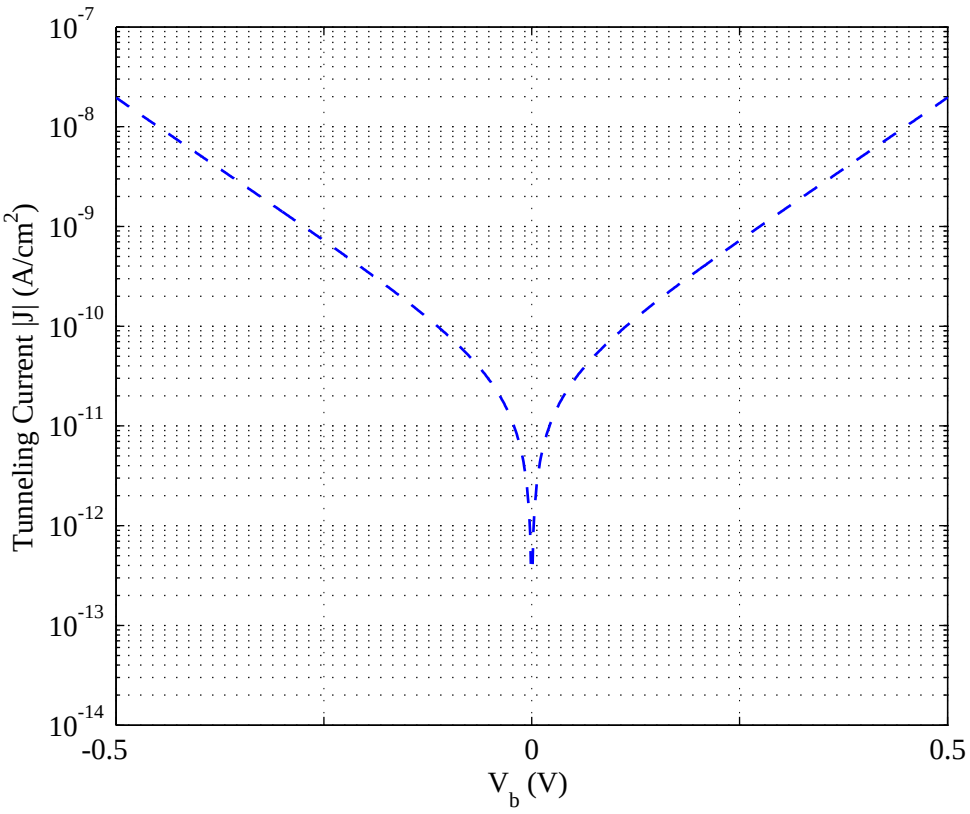

Figure 6.22: The current density versus biasing voltage for the symmetric MIM diode with insulator thickness $s = 5$ nm.

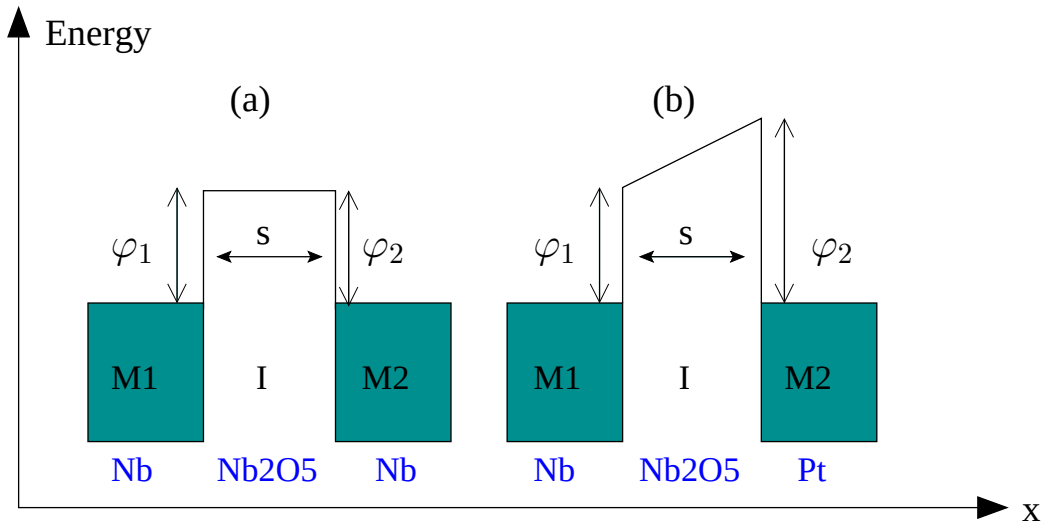

Figure 6.23: Equilibrium band diagram of: (a)symmetric $Nb/Nb_2O_5/Nb$ diode and (b)asymmetric $Nb/Nb_2O_5/Pt$ diode. s indicates the insulator thickness, and φ_1 and φ_2 represent the barrier heights of metal electrodes.

The diode parameters can be optimised to enhance the diode-dependent efficiency. It is clearly shown that reducing the diode resistance could lead to increasing the coupling efficiency. Additionally, it is also shown that increasing the diode responsivity will increase the quantum efficiency.

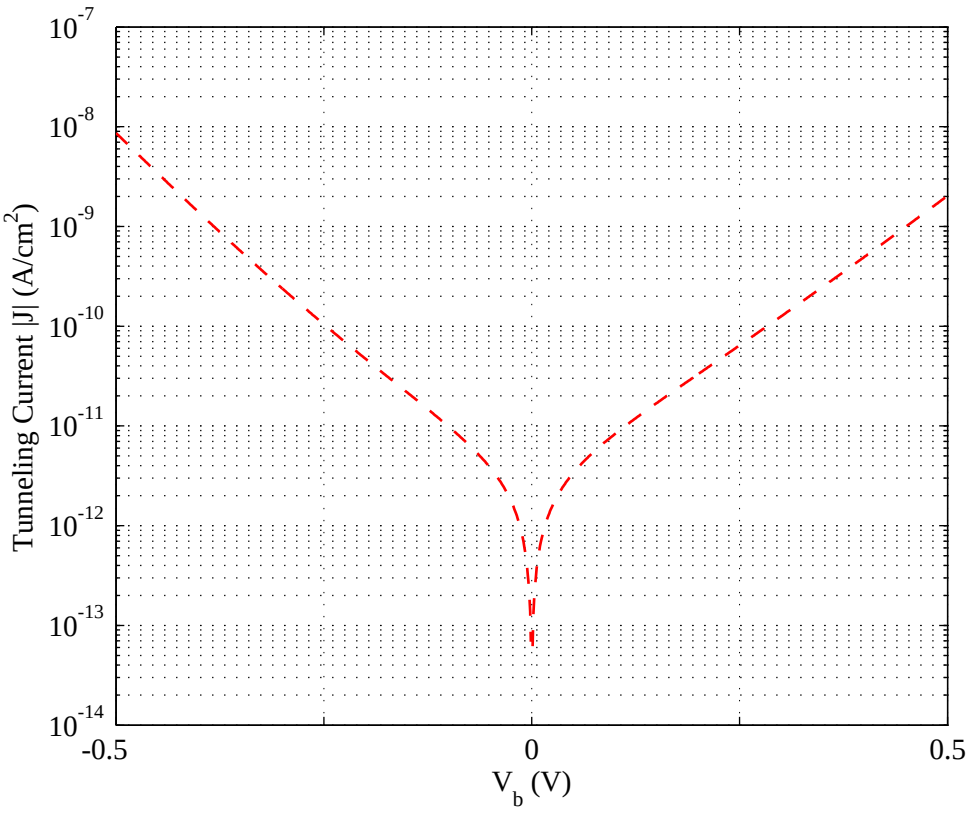

Figure 6.24: The current density versus biasing voltage for the asymmetric MIM diode with insulator thickness $s = 5$ nm and barrier heights $\varphi_1 = 0.4$ eV and $\varphi_2 = 1.7$ eV.

In order to improve the diode efficiency, another parametric study on the effect of insulator thickness and work function difference on the diode performance will be presented. Firstly, the effect of insulator thickness on the diode resistance and responsivity will be studied by varying the thickness from 2 to 5 nm. Fig. 6.26 demonstrates the effect of changing the insulator thickness on the diode resistance (Fig. 6.26-a) and on the diode responsivity (Fig. 6.26-b). It is shown that increasing the thickness has a significant impact on the value of the diode resistance, where the smaller the insulator thickness the lower diode resistance can be achieved. Furthermore, it is noted that the changes in responsivity versus insulator thickness is trivial at zero biasing, whereas, the responsivity increases when increasing the thickness for higher biasing values. The results show that in order to increase the efficiency at zero-biasing condition it is highly recommended to use a thinner insulator layer.

Consequently, the effect of metal work function difference is also studied by changing different metals other than P_t with different work functions. The difference in work function has been varied from 0.6 eV to 1.4 eV, this may include different metals such as: Mo (4.95 eV), Ni (5.04 eV), Au (5.3 eV), Pt (5.65 eV) [123]. The diode resistivity and

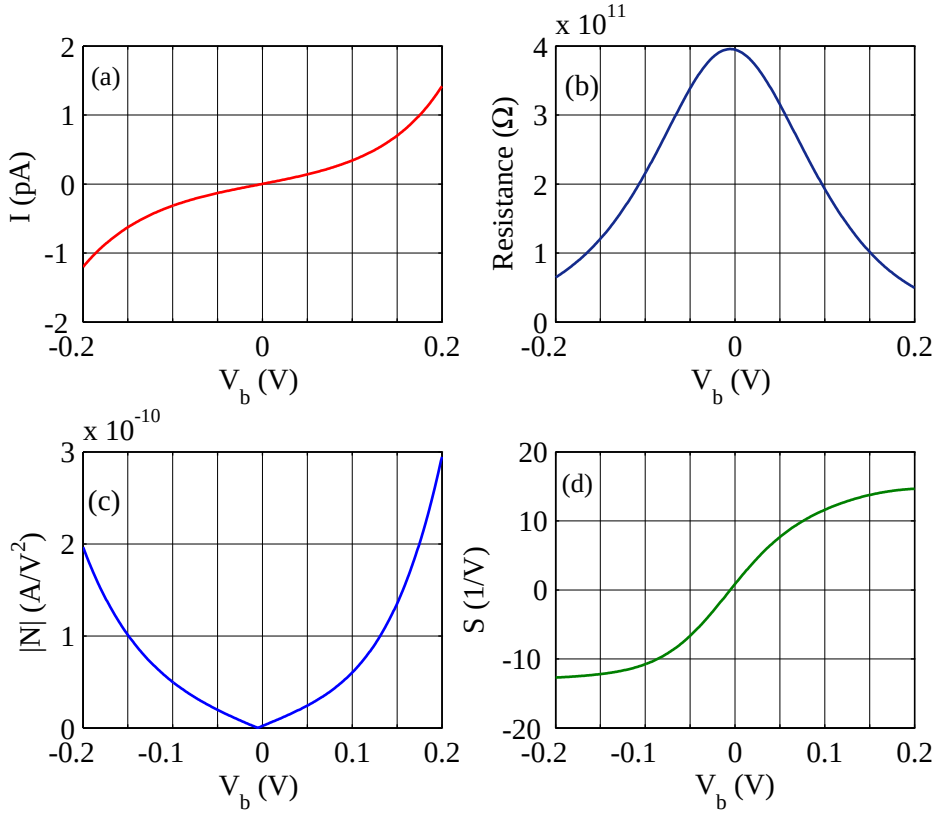

Figure 6.25: The current vs. biasing voltage for the asymmetric MIM diode with insulator thickness s=5 nm and barrier heights $\varphi_1 = 0.4$ eV and $\varphi_2 = 1.75$ eV.

responsivity are then calculated at $s = 2$ nm as shown in Fig. 6.27.

It can be seen in Fig. 6.27 that the diode performance can be enhanced by choosing small values of work function difference. In addition, it can be seen that there is an impact of the work function difference on the diode resistance as it increases by increasing the difference as shown in Fig. 6.27(b). Hence, it is evident that the diode-dependent efficiency can be improved by choosing metals on both sides of MIM diode with small difference in their work functions. After this parametric study, the efficiency can be maximised by choosing the optimised values of the insulator thickness, $s = 2$ nm, and metals work function difference $\triangle\varphi = 0.6$ eV. The coupling efficiency, after optimisation, will be 1.01×10^{-5} % at 10 μm for the zero-biasing condition.

6.5 Chapter Summary

In this chapter, the integral equation method has been utilised to model IR wire antennas for the application of solar energy collection at 10 μm wavelength, taking into account the imperfect conductivity of metals within this frequency band. Pocklington's integral

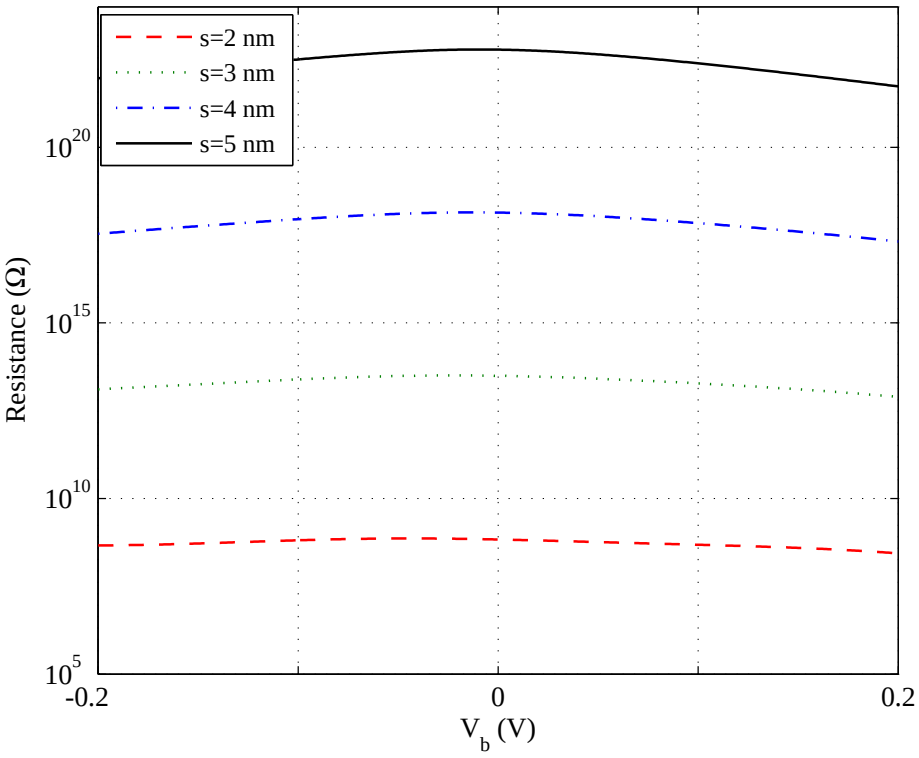

(a)

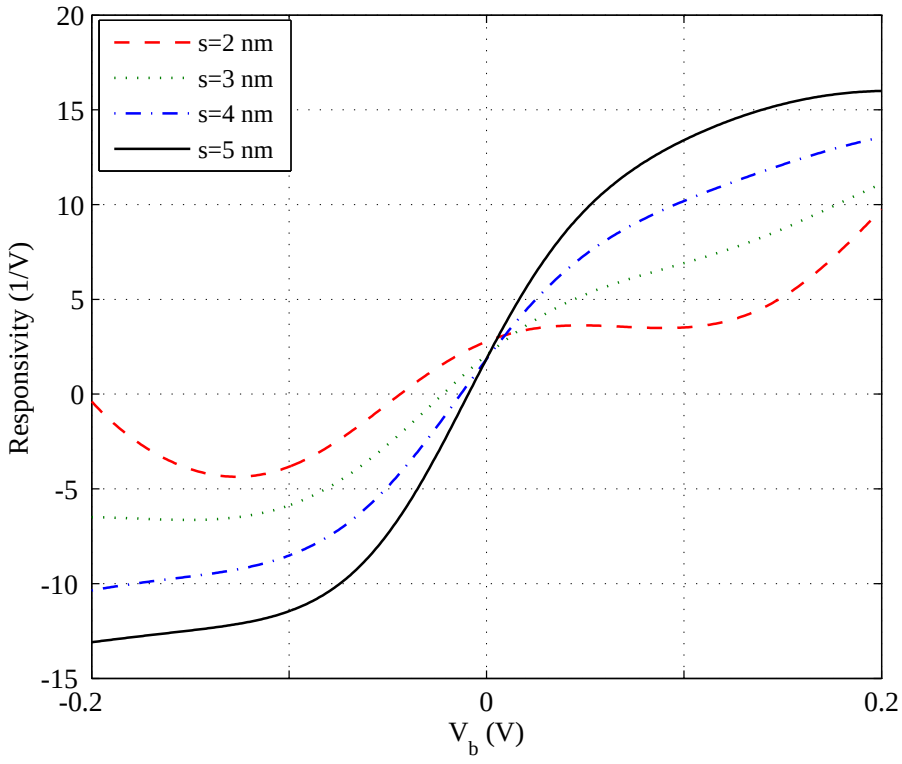

(b)

Figure 6.26: The effect of changing the insulator thickness on: (a) The diode resistance, (b) The diode responsivity. Metal work function difference fixed to $\triangle\varphi = 1.35$ eV.

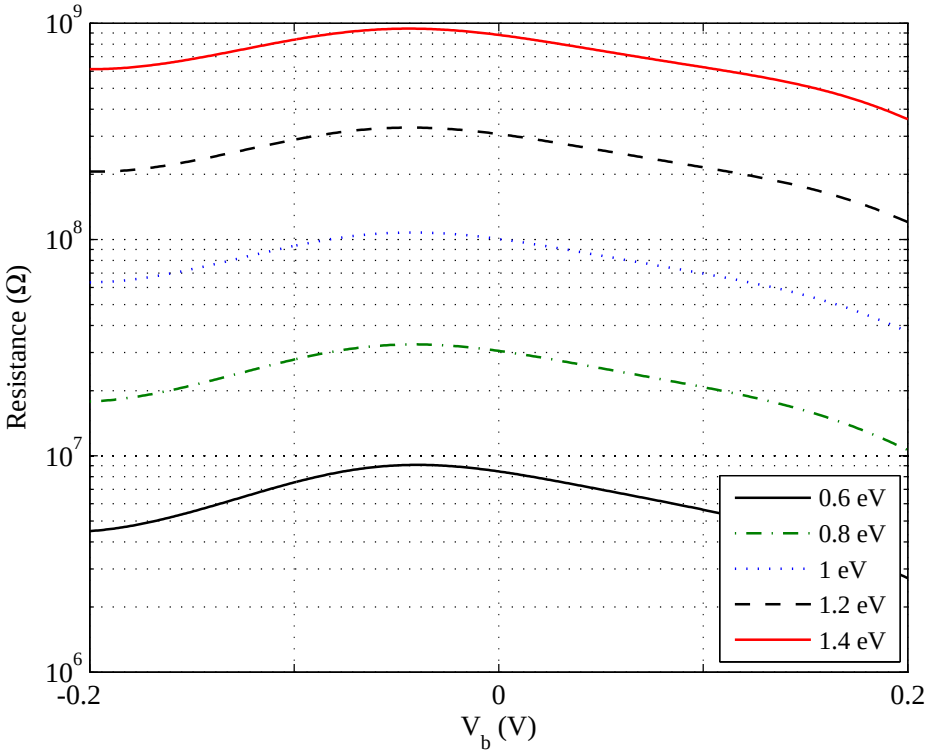

(a)

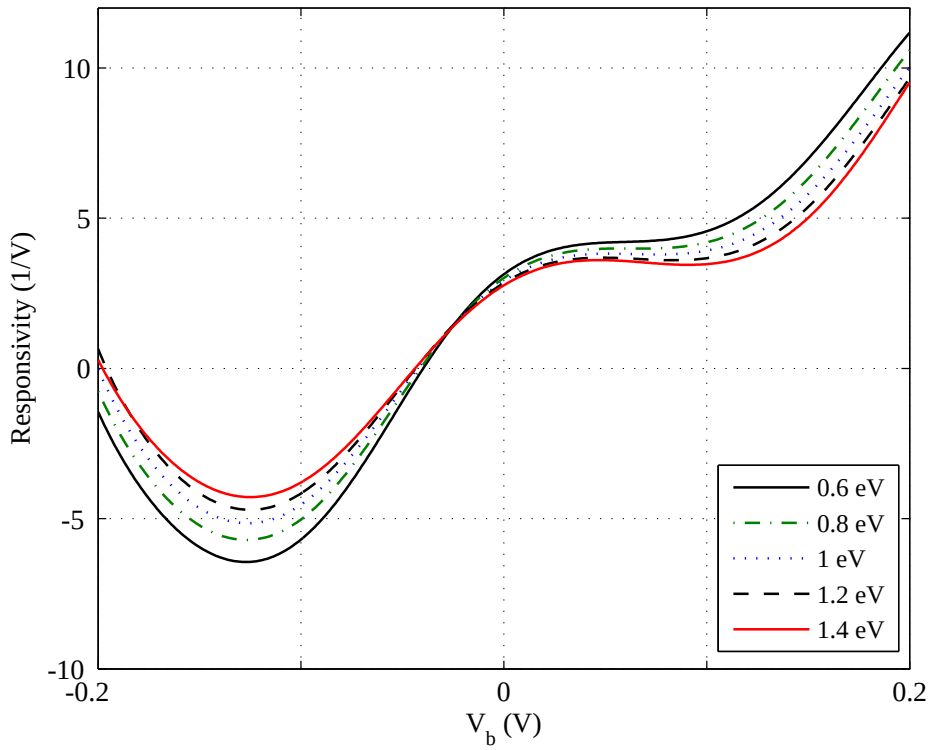

(b)

Figure 6.27: The effect of changing the work function difference on: (a) The diode resistance, (b) The diode responsivity. Insulator thickness is set to $s = 2$ nm in all cases.

equation and Hallen's integral equation have been used to find the current distribution over the antenna surface, where they showed similar results by employing MoM numerical method with a piecewise function. However, the Hallen's integral equation has been adopted throughout the chapter, since it provides more stable results. A circuit model for the IR dipole antenna has been presented by finding the antenna parameters from the results of the integral equation modelling. Moreover, the obtained results have been verified using an FEM-based full-wave electromagnetic simulator and strong correlation was found. Additionally, the design of the MIM diode, with its equivalent circuit, has been demonstrated. This diode has then been integrated into the IR dipole antenna at its feed gap, constructing a solar rectenna that works at IR frequencies in order to rectify the received signal and convert it to DC power. The circuit model for the whole system and the appropriate equations for finding its elements have been presented. Furthermore, a parametric study into the effect of the MIM diode parameters on the captured voltage has been investigated. This modelling approach can be used to find the IR dipole antenna properties easily, without the need for full-wave simulations that may otherwise require high computational resources, and in parallel, provide significant insight into the operation of the IR nanoantennas.

Solar rectennas have been proposed as an alternative to conventional semiconductor photovoltaics due to their ability to directly rectify solar and thermal radiation. Since the rectifiers can convert a wide range of frequencies, it is expected from solar rectennas to efficiently harvest the entire solar spectrum with an efficiency that approaches 100 % theoretically. However, there are many factors that limit the total conversion efficiency of solar rectennas. Some of these factors are related to the optical antenna whilst others are related to the MIM diode itself. This chapter highlighted the most important factors that influence the conversion efficiency of solar rectennas with the main objective of their improvement and optimisation. Firstly, the integral equation method has been utilised to model optical wire antennas at 10 μm wavelength, taking into account the imperfect conductivity of metals within this frequency band. The conductor-dielectric efficiency, which represent the antenna-dependent efficiency, is then calculated and plotted based on the results from MoM numerical analysis. An antenna efficiency of 94.39 % is achieved at the frequency of interest, which is quite high and promising. On the other hand, the MIM diode has been analysed and its parameters have been found by using Simmons' formula for tunnelling currents. The diode-dependent part of conversion efficiency has then been calculated and plotted with the total conversion efficiency. The results showed

that, even when optical antennas couple thermal radiation efficiently, the total conversion efficiency, after optimisation, is still very low ($\eta_t \sim 10^{-5}$). This is due to the poor matching between the diode and the antenna, where a very high diode resistance is obtained compared to the low antenna resistance. Although the diode characteristics have been optimised, the coupling efficiency is still low. However, this value of efficiency demonstrates an enhancement to a recently reported conversion efficiency of ($\eta_t \sim 10^{-9} - 10^{-12}$) [54].

As a summary, optical antennas are attractive option to replace PV cells in coupling solar energy, however this technique requires further developments in rectification process. Rectification and coupling efficiencies can be improved by utilising multi-insulator barriers which produce high responsivity with lower diode resistance, and hence a better matching can be achieved.

Chapter 7

Conclusion and Future Work

Although the use of commercial solar panels are widespread around the world, researchers are paying efforts to reduce their cost and increase their low efficiency. They have used new materials and different approaches, such as multi-junction solar cells, to meet these requirements. However, there is no pragmatic change in their efficiency that is still low. With the advances in nanotechnology, and with the breakthroughs in designing efficient optical detectors, it is now possible to consider designing solar rectenna for receiving the solar radiation and converting it into electricity. This can be achieved by designing an efficient nanoantenna for receiving the solar radiation and coupling it to an integrated rectifier for AC to DC conversion.

The focus of this research was to design and optimise different types of nanoantennas and to choose the most appropriate one for this application by performing FEM simulations. For this purpose, four types of nanoantennas have been designed and simulated and a comparison is made to find the best candidate for this application. The figure of merit in choosing the best design was the captured electric field in the feed gap of the nanoantenna and the area under curve, which is essential in calculating the harvested energy. By comparing the performance of dipole, square spiral, logarithmic spiral and bowtie nanoantennas, it was found that the square spiral nanoantenna exhibited the largest captured electric field in the feed gap at resonance, whereas, the bowtie nanoantenna showed higher AUC and widest bandwidth. Moreover, it was found that coupling two elements in one structure will increase the captured electric field at the feed gap. The two-element logarithmic spiral nanoarray showed the largest captured electric field and the largest AUC. Furthermore, the discrimination ratio has been calculated for the designed antennas by illuminating the antenna with two orthogonal polarised waves, where the two-element logarithmic spiral nanoarray showed lower discrimination ratio.

Due to the wideband performance of bowtie nanoatennas and the geometrical convenience of this structure, the design was extended into 2×4 bowtie planar nanoarray with feeding network. The electric field from each single bowtie has been collected using feed lines and driven to a common feed gap. The reason behind establishing one common gap is to reduce the number of MIM diodes, and hence increase the total efficiency. The performance of the designed bowtie nanoarray was compared with that of a single bowtie with matching footprint and the results showed that the bowtie nanoarray collect more energy than a single bowtie element using identical device areas.

In order to enhance the array performance, a geometrical parametric study of the distance between elements, feeding line width, and gap size was carried out. The results

showed that the optimum space between elements is $2.9\,\mu$m, and the best line width is $50\,n$m. It also showed that a gap of $25\,n$m provides the highest captured electric field. Based on the optimised parameters, a maximum electric field of $0.047\ V/\mu$m was achieved at the first resonant wavelength of $20.5\,\mu$m (14.63 THz), and $0.258\ V/\mu$m at the second resonant wavelength of $158\,\mu$m (1.89 THz) corresponding to an AUC value of $6.80\ \mu$V.

Furthermore, a new approach is presented by overlapping the arms of the designed array at the feed gap to establish an MIM diode. The characteristics of this diode were calculated and optimised by using a $95\,n$m metal thickness, which exhibits the highest electric field. Additionally, it is found that the highest electric field can be obtained for the insulator layer thickness of $15\,n$m. Furthermore, the results showed that the smaller the overlapping area, the higher the electric field inside the gap is provided.

All the above results have been found using commercial FEM simulator(i.e COMSOL), which is user-friendly software. However, when using such software the user might find difficulties and lack of information in understanding how the system works. Thus, a simple analysis on dipole nanoantenna using MoM is presented in this research. The results obtained from this method is compared with those found from FEM simulations and an acceptable agreement is achieved. Hallen's integral equation was used to find the input impedance of thin wire nano-dipoles with imperfect conductors. The radiation efficiency was then calculated based on the input impedance. To calculate the total conversion efficiency of solar rectennas, it is important to compute the rectification efficiency of the MIM diode along with the coupling efficiency between the antenna and the diode. To this end, Simmon's formula for tunnelling currents has been used to calculate the characteristics of the MIM diode.

It is expected from solar rectennas to efficiently harvest the entire solar spectrum with an efficiency approaches 100 % theoretically. However, the results showed that the total conversion efficiency was very low. The radiation efficiency was found to be high (approaching more than 90 %) and the factor that reduced the total efficiency was the coupling efficiency due to the poor antenna-diode matching. It is generally accepted that the dipole antenna has low resistance (less than 100 Ω), however it is found that the MIM diode showed very high resistance. Although some optimisation techniques were applied to decrease the resistance of the diode, the efficiency was still low and more efforts need to be paid to enhance the total efficiency.

In summary, this research project concentrated primarily on the antenna part of solar

rectennas. The results presented in this research showed that the designed nanoatnenna fulfil the requirements for the use in solar energy harvesting as they exhibited high captured electric field in the feed gap. In addition they showed applicability to connect more than two elements in an array form using feeding network. However, to design an efficient rectenna that can overcome the limitations of solar cells, the MIM diode needs to be efficiently coupled to the antenna, which is still an issue in this project. In the following section, suggestions for future work will be highlighted in order to achieve higher conversion efficiency.

Future Work

The results of this research project are promising towards replacing the traditional PVs and/or exploiting the unused infrared energy of the solar radiation. Solar rectenna system is a quite new technology and needs years of research to be available commercially to the users. Hence, it is difficult to cover all the aspects of this system and address all of its challenges in one thesis. Following are some of the proposed ideas to be considered in future work:

- Employ different materials to optimise the performance of nanoantennas.
- Use different types of antennas and compare the results with the current geometries to find the optimum solution for this application.
- Increase the number of elements in each single array to maximise the captured energy.
- Replicate the designed arrays to cover millions of elements in one single panel and calculate the total power provided.
- Fabricate the designed array in this thesis and perform the necessary measurements to calculate the output power and the conversion efficiency.
- Apply various computational methods such FDTD to obtain more accurate results for the antenna part, and apply efficient quantum mechanics techniques for the accuracy of the I-V characteristics of the MIM diode. These techniques include the transfer-matrix method (TMM), the non-equilibrium Green's function (NEGF) and the quantum transmitting boundary method (QTBM).

References

[1] D. Kotter, S. Novack, W. Slafer, and P. Pinhero, "Theory and manufacturing processes of solar nanoantenna electromagnetic collectors," *Journal of Solar Energy Engineering*, vol. 132, no. 1, p. 011014, 2010.

[2] T. A. Report, "An assessment of solar energy conversion technologies and research opportunities," GCEP Energy Assessment Analysis, Tech. Rep., 2006.

[3] P. Biagioni, J.-S. Huang, and B. Hecht, "Nanoantennas for visible and infrared radiation," *Reports on Progress in Physics*, vol. 75, no. 2, p. 024402, 2012.

[4] W. C. Brown, "The history of power transmission by radio waves," *Microwave Theory and Techniques, IEEE Transactions on*, vol. 32, no. 9, pp. 1230–1242, 1984.

[5] R. Corkish, M. Green, and T. Puzzer, "Solar energy collection by antennas," *Solar Energy*, vol. 73, no. 6, pp. 395–401, 2002.

[6] A. M. Marks, "Device for conversion of light power to electric power," Apr. 24 1984, uS Patent 4,445,050.

[7] G. H. Lin, R. Abdu, and J. O. M. Bockris, "Investigation of resonance light absorption and rectification by sub nanostructures," vol. 80, p. 565, 1996.

[8] B. Berland, "Photovoltaic technologies beyond the horizon: Optical rectenna solar cell," 2003.

[9] M. Midrio, M. Romagnoli, S. Boscolo, C. De Angelis, A. Locatelli, D. Modotto, and A. Capobianco, "Flared monopole antennas for 10-μm radiation," *Quantum Electronics, IEEE Journal of*, vol. 47, no. 1, pp. 84–91, 2011.

[10] N. H. Karam, R. R. King, B. T. Cavicchi, D. D. Krut, J. H. Ermer, M. Haddad, L. Cai, D. E. Joslin, M. Takahashi, J. W. Eldredge *et al.*, "Development and characterization of high-efficiency $ga_{0.5}in_{0.5}p$/gaas/ge dual- and triple-junction solar cells," *Electron Devices, IEEE Transactions on*, vol. 46, no. 10, pp. 2116–2125, 1999.

[11] J. Nahas, "Modeling and computer simulation of a microwave-to-dc energy conversion element," *Microwave Theory and Techniques, IEEE Transactions on*, vol. 23, no. 12, pp. 1030–1035, Dec 1975.

[12] C. A. Balanis, *Advanced engineering electromagnetics*. Wiley New York, 1989, vol. 205.

[13] ——, *Antenna theory: analysis and design*. John Wiley & Sons, 2005.

[14] W. L. Stutzman and G. A. Thiele, *Antenna theory and design*. John Wiley & SonsInc., NY, 1998.

[15] W. C. Gibson, *The method of moments in electromagnetics*. CRC press, 2007.

[16] P. Bharadwaj, B. Deutsch, and L. Novotny, "Optical antennas," *Advances in Optics and Photonics*, vol. 1, no. 3, pp. 438–483, 2009.

[17] M. Bareiß, D. Kälblein, P. M. Krenz, U. Zschieschang, H. Klauk, G. Scarpa, B. Fabel, W. Porod, and P. Lugli, "Large-area fabrication of antennas and nanodiodes," in *Rectenna Solar Cells*. Springer, 2013, pp. 297–311.

[18] L. Novotny, "The history of near-field optics," *Progress in optics*, vol. 50, pp. 137–184, 2007.

[19] J. Wessel, "Surface-enhanced optical microscopy," *JOSA B*, vol. 2, no. 9, pp. 1538–1541, 1985.

[20] U. C. Fischer and D. Pohl, "Observation of single-particle plasmons by near-field optical microscopy," *Physical Review Letters*, vol. 62, no. 4, p. 458, 1989.

[21] C. Fumeaux, W. Herrmann, F. Kneubühl, and H. Rothuizen, "Nanometer thin-film ni–nio–ni diodes for detection and mixing of 30 thz radiation," *Infrared physics & technology*, vol. 39, no. 3, pp. 123–183, 1998.

[22] L. Novotny and N. van Hulst, "Antennas for light," *Nature Photonics*, vol. 5, no. 2, pp. 83–90, 2011.

[23] J.-J. Greffet, "Introduction to surface plasmon theory," in *Plasmonics*. Springer, 2012, pp. 105–148.

[24] A. Alu and N. Engheta, "Theory, modeling and features of optical nanoantennas," *Antennas and Propagation, IEEE Transactions on*, vol. 61, no. 4, pp. 1508–1517, April 2013.

[25] P. Chen, C. Argyropoulos, and A. Alù, "Optical antennas and enhanced nonlinear effects," in *Rectenna Solar Cells*. Springer New York, 2013, pp. 277–294.

[26] F. J. González, J. Alda, J. Simón, J. Ginn, and G. Boreman, "The effect of metal dispersion on the resonance of antennas at infrared frequencies," *Infrared Physics & Technology*, vol. 52, no. 1, pp. 48–51, 2009.

[27] J. Chen, K. He, and Z. Zhang, "Triangle defects in bowtie nanoantennas," *Applied Physics A*, pp. 1–6, 2013.

[28] Z. Gao, L. Shen, E. Li, L. Xu, and Z. Wang, "Cross-diabolo nanoantenna for localizing and enhancing magnetic field with arbitrary polarization," *Journal of Lightwave Technology*, vol. 30, no. 6, pp. 829–833, 2012.

[29] H. Nouri and T. Pakizeh, "Spectrally-tunable directionality of compact optical nanoantennas," *Plasmonics*, pp. 1–9, 2013.

[30] G. Vandenbosch and Z. Ma, "Study of the radiation efficiency of nano-dipoles," in *Electromagnetics in Advanced Applications (ICEAA), 2012 International Conference on*. IEEE, 2012, pp. 916–919.

[31] J.-W. Liaw, "Simulation of surface plasmon resonance of metallic nanoparticles by the boundary-element method," *JOSA A*, vol. 23, no. 1, pp. 108–116, 2006.

[32] J. Dorfmuller, R. Vogelgesang, W. Khunsin, C. Rockstuhl, C. Etrich, and K. Kern, "Plasmonic nanowire antennas: experiment, simulation, and theory," *Nano letters*, vol. 10, no. 9, pp. 3596–3603, 2010.

[33] R. Garg, *Analytical and computational methods in electromagnetics*. Artech House, 2008.

[34] M. N. Sadiku, *Numerical techniques in electromagnetics*. CRC press, 2010.

[35] D. B. Davidson, *Computational electromagnetics for RF and microwave engineering*. Cambridge University Press, 2005.

[36] J. M. Jarem and P. P. Banerjee, *Computational methods for electromagnetic and optical systems*. Taylor & Francis US, 2000.

[37] K. E. Atkinson, *An introduction to numerical analysis*. John Wiley & Sons, 1989.

[38] J.-M. Jin, *The finite element method in electromagnetics*. Wiley New York, 2002.

[39] A. F. Peterson, S. L. Ray, and R. Mittra, *Computational methods for electromagnetics*. IEEE press New York, 1998, vol. 24.

[40] J. L. Volakis, A. Chatterjee, and L. C. Kempel, *Finite element methods for electromagnetics: antennas, microwave circuits and scattering applications*. IEEE press New York, 1998.

[41] S. G. Johnson, "Notes on perfectly matched layers (pmls)," *Lecture notes, Massachusetts Institute of Technology, Massachusetts*, 2010.

[42] R. A. Abd-Alhameed, P. S. Excell, and M. A. Mangoud, "A hybrid computational electromagnetics formulation for simulation of antennas coupled to lossy and dielectric volumes," *Broadcasting, IEEE Transactions on*, vol. 50, no. 3, pp. 253–259, 2004.

[43] S. V. Boriskina and L. Dal Negro, "Multiple-wavelength plasmonic nanoantennas," *Optics letters*, vol. 35, no. 4, pp. 538–540, 2010.

[44] L. Razzari, A. Toma, M. Clerici, M. Shalaby, G. Das, C. Liberale, M. Chirumamilla, R. P. Zaccaria, F. De Angelis, M. Peccianti *et al.*, "Terahertz dipole nanoantenna arrays: Resonance characteristics," *Plasmonics*, pp. 1–6, 2013.

[45] P. Biagioni, J. Huang, L. Duò, M. Finazzi, and B. Hecht, "Cross resonant optical antenna," *Physical review letters*, vol. 102, no. 25, p. 256801, 2009.

[46] B. Rosner, J. Peck, and D. van der Weide, "Near-field antennas integrated with scanning probes for thz to visible microscopy: Scale modeling and limitations on performance," *Antennas and Propagation, IEEE Transactions on*, vol. 50, no. 5, pp. 670–675, 2002.

[47] J. Alda, J. M. Rico-García, J. M. López-Alonso, and G. Boreman, "Micro-and nano-antennas for light detection," *Egypt. J. Solids*, vol. 28, no. 1, pp. 1–13, 2005.

[48] S. S. Acimovic, M. P. Kreuzer, M. U. González, and R. Quidant, "Plasmon near-field coupling in metal dimers as a step toward single-molecule sensing," *ACS nano*, vol. 3, no. 5, pp. 1231–1237, 2009.

[49] J. A. Bean, B. Tiwari, G. H. Bernstein, P. Fay, and W. Porod, "Thermal infrared detection using dipole antenna-coupled metal-oxide-metal diodes," *Journal of Vacuum Science & Technology B: Microelectronics and Nanometer Structures*, vol. 27, no. 1, pp. 11–14, 2009.

[50] S. Liu, X. Shou, and A. Nahata, "Coherent detection of multiband terahertz radiation using a surface plasmon-polariton based photoconductive antenna," *Terahertz Science and Technology, IEEE Transactions on*, vol. 1, no. 2, pp. 412–415, 2011.

[51] F. M. Boussaha, J. H. Kawamura, J. A. Stern, A. Skalare, and V. White, "A low noise 2.7 thz waveguide-based superconducting mixer," *Terahertz Science and Technology, IEEE Transactions on*, vol. 2, no. 3, pp. 284–289, 2012.

[52] J. Simon and F. González, "Nanoantennas for polarisation division multiplexing," *Electronics Letters*, vol. 47, no. 2, pp. 120–121, 2011.

[53] I. Kocakarin and K. Yegin, "Glass superstrate nanoantennas for infrared energy harvesting applications," *International Journal of Antennas and Propagation*, vol. 2013, 2013.

[54] E. Briones, J. Alda, and F. J. González, "Conversion efficiency of broad-band rectennas for solar energy harvesting applications," *Optics Express*, vol. 21, no. 103, pp. A412–A418, 2013.

[55] M. Aldrigo, D. Masotti, A. Costanzo, and V. Rizzoli, "Numerical analysis of an innovative energy-harvesting system in the infrared region," in *Wireless Power Transfer (WPT)*. IEEE, 2013, pp. 123–126.

[56] Z. Ma and G. A. Vandenbosch, "Optimal solar energy harvesting efficiency of nano-rectenna systems," *Solar Energy*, vol. 88, pp. 163–174, 2013.

[57] A. M. A. Sabaawi, C. C. Tsimenidis, and B. S. Sharif, "Infra-red nano-antennas for solar energy collection," in *Antennas and Propagation Conference (LAPC), 2011 Loughborough*. IEEE, 2011, pp. 1–4.

[58] ——, "Infra-red spiral nano-antennas," in *Antennas and Propagation Conference (LAPC), 2012 Loughborough*. IEEE, 2012, pp. 1–4.

[59] ——, "Auxiliary ring resonator for local field enhancement in solar rectennas," in *Antennas and Propagation Conference (LAPC), 2014 Loughborough*. IEEE, 2014, pp. 1–4.

[60] M. Bozzetti, G. de Candia, M. Gallo, O. Losito, L. Mescia, and F. Prudenzano, "Analysis and design of a solar rectenna," in *Industrial Electronics (ISIE), 2010 IEEE International Symposium on*. IEEE, 2010, pp. 2001–2004.

[61] C. De Angelis, A. Locatelli, D. Modotto, S. Boscolo, M. Midrio, F. Sacchetto, A.-D. Capobianco, F. Pigozzo, and C. Someda, "Extending antenna theory to the optical domain," in *Microwave Conference, 2009. EuMC 2009. European*. IEEE, 2009, pp. 810–813.

[62] Q. Fu and W. Sun, "Mie theory for light scattering by a spherical particle in an absorbing medium," *Applied Optics*, vol. 40, no. 9, pp. 1354–1361, 2001.

[63] M. Yu-Ming, "Analysis and design of nanoantennas," Ph.D. dissertation, National University of Singapore, 2010.

[64] M. A. Ordal, L. L. Long, R. J. Bell, S. E. Bell, R. R. Bell, R. W. Alexander, Jr., and C. A. Ward, "Optical properties of the metals al, co, cu, au, fe, pb, ni, pd, pt, ag, ti, and w in the infrared and far infrared," *Applied Optics*, vol. 22, no. 7, pp. 1099–1120, 1983.

[65] C. Fumeaux, M. A. Gritz, I. Codreanu, W. L. Schaich, F. J. González, and G. D. Boreman, "Measurement of the resonant lengths of infrared dipole antennas," *Infrared physics & technology*, vol. 41, no. 5, pp. 271–281, 2000.

[66] F. J. González, B. Ilic, J. Alda, and G. D. Boreman, "Antenna-coupled infrared detectors for imaging applications," *Selected Topics in Quantum Electronics, IEEE Journal of*, vol. 11, no. 1, pp. 117–120, 2005.

[67] H. Li and X. Cheng, "Optical antennas: A boost for infrared detection," *Journal of Vacuum Science & Technology B: Microelectronics and Nanometer Structures*, vol. 26, no. 6, pp. 2156–2159, 2008.

[68] P. M. Krenz, B. A. Lail, and G. D. Boreman, "Calibration of lead-line response contribution in measured radiation patterns of ir dipole arrays," *Selected Topics in Quantum Electronics, IEEE Journal of*, vol. 17, no. 1, pp. 218–221, 2011.

[69] W. Ding, R. Bachelot, S. Kostcheev, P. Royer, and R. Espiau de Lamaestre, "Surface plasmon resonances in silver bowtie nanoantennas with varied bow angles," *Journal of Applied Physics*, vol. 108, no. 12, pp. 124 314–124 314, 2010.

[70] Z. Fang, L. Fan, C. Lin, D. Zhang, A. J. Meixner, and X. Zhu, "Plasmonic coupling of bow tie antennas with ag nanowire," *Nano letters*, vol. 11, no. 4, pp. 1676–1680, 2011.

[71] M. Abdel-Rahman, F. Gonzalez, and G. Boreman, "Antenna-coupled metal-oxide-metal diodes for dual-band detection at 92.5 ghz and 28 thz," *Electronics Letters*, vol. 40, no. 2, pp. 116–118, 2004.

[72] P. Esfandiari, G. Bernstein, P. Fay, W. Porod, B. Rakos, A. Zarandy, B. Berland, L. Boloni, G. Boreman, B. Lail *et al.*, "Tunable antenna-coupled metal-oxide-metal (mom) uncooled ir detector," in *Defense and Security*. International Society for Optics and Photonics, 2005, pp. 470–482.

[73] M. Bareiß, B. N. Tiwari, A. Hochmeister, G. Jegert, U. Zschieschang, H. Klauk, B. Fabel, G. Scarpa, G. Koblmuller, G. H. Bernstein *et al.*, "Nano antenna array for terahertz detection," *Microwave Theory and Techniques, IEEE Transactions on*, vol. 59, no. 10, pp. 2751–2757, 2011.

[74] J. A. Bean, A. Weeks, and G. D. Boreman, "Performance optimization of antenna-coupled al/alox/pt tunnel diode infrared detectors," *IEEE J. Quantum Electron*, vol. 47, no. 1, pp. 126–135, 2011.

[75] F. G. de Arquer, V. Volski, N. Verellen, G. A. Vandenbosch, and V. V. Moshchalkov, "Engineering the input impedance of optical nano dipole antennas: materials, geometry and excitation effect," *Antennas and Propagation, IEEE Transactions on*, vol. 59, no. 9, pp. 3144–3153, 2011.

[76] D. W. Pohl, S. G. Rodrigo, and L. Novotny, "Stacked optical antennas," *Applied Physics Letters*, vol. 98, no. 2, pp. 023 111–023 111, 2011.

[77] K. Q. Da Costa and V. A. Dmitriev, "Bowtie nanoantennas with polynomial sides in the excitation and emission regimes," *Progress In Electromagnetics Research B*, vol. 32, pp. 57–73, 2011.

[78] J.-W. Liaw, "Analysis of a bowtie nanoantenna for the enhancement of spontaneous emission," *Selected Topics in Quantum Electronics, IEEE Journal of*, vol. 14, no. 6, pp. 1441–1447, 2008.

[79] K. Choi, F. Yesilkoy, A. Chryssis, M. Dagenais, and M. Peckerar, "New process development for planar-type cic tunneling diodes," *Electron Device Letters, IEEE*, vol. 31, no. 8, pp. 809–811, 2010.

[80] F. J. González and J. Alda, "Fresnel spiral antenna for detection at visible and far-infrared bands," in *Antennas and Propagation (EuCAP), 2010 Proceedings of the Fourth European Conference on*. IEEE, 2010, pp. 1–4.

[81] A. Shurakov, S. Seliverstov, N. Kaurova, M. Finkel, B. Voronov, and G. Goltsman, "Input bandwidth of hot electron bolometer with spiral antenna," *Terahertz Science and Technology, IEEE Transactions on*, vol. 2, no. 4, pp. 400–405, 2012.

[82] A. Locatelli, "Peculiar properties of loop nanoantennas," *Photonics Journal, IEEE*, vol. 3, no. 5, pp. 845–853, 2011.

[83] Z. Liu, A. Boltasseva, R. H. Pedersen, R. Bakker, A. V. Kildishev, V. P. Drachev, and V. M. Shalaev, "Plasmonic nanoantenna arrays for the visible," *Metamaterials*, vol. 2, no. 1, pp. 45–51, 2008.

[84] E. S. Ünlü, R. U. Tok, and K. Sendur, "Broadband plasmonic nanoantenna with an adjustable spectral response," *Opt. Express*, vol. 19, pp. 1000–1006, 2011.

[85] D. Dregely, R. Taubert, J. Dorfmüller, R. Vogelgesang, K. Kern, and H. Giessen, "3d optical yagi-uda nanoantenna array," *Nature communications*, vol. 2, p. 267, 2011.

[86] F. González and G. Boreman, "Comparison of dipole, bowtie, spiral and log-periodic ir antennas," *Infrared physics & technology*, vol. 46, no. 5, pp. 418–428, 2005.

[87] V. Mishra, T. Singh, A. Alam, V. Kumar, A. Choudhary, and V. D. Kumar, "Design and simulation of broadband nanoantennae at optical frequencies," *Micro & Nano Letters*, vol. 7, no. 1, pp. 24–28, 2012.

[88] M. Gallo, L. Mescia, O. Losito, M. Bozzetti, and F. Prudenzano, "Design of optical antenna for solar energy collection," *Energy*, vol. 39, no. 1, pp. 27–32, 2012.

[89] J. Hanely and B. McNeil, "The meaning and use of the area under a receiver operating characteristic (roc) curve," *Radiology*, vol. 143, no. 1, pp. 29–36, 1982.

[90] S. Atapattu, C. Tellambura, and H. Jiang, "Analysis of area under the roc curve of energy detection," *Wireless Communications, IEEE Transactions on*, vol. 9, no. 3, pp. 1216–1225, 2010.

[91] MATLAB, *version 7.10.0 (R2010a)*. Natick, Massachusetts: The MathWorks Inc., 2010.

[92] E. Cubukcu, N. Yu, E. J. Smythe, L. Diehl, K. B. Crozier, and F. Capasso, "Plasmonic laser antennas and related devices," *Selected Topics in Quantum Electronics, IEEE Journal of*, vol. 14, no. 6, pp. 1448–1461, 2008.

[93] W. Yu-Ming, L. Le-Wei, and L. Bo, "Geometric effects in designing bow-tie nanoantenna for optical resonance investigation," in *Electromagnetic Compatibility (APEMC), 2010 Asia-Pacific Symposium on*. IEEE, 2010, pp. 1108–1111.

[94] Y.-M. Wu, L.-W. Li, and B. Liu, "Gold bow-tie shaped aperture nanoantenna: Wide band near-field resonance and far-field radiation," *Magnetics, IEEE Transactions on*, vol. 46, no. 6, pp. 1918–1921, 2010.

[95] W. Ding, R. Bachelot, S. Kostcheev, P. Royer, and R. Espiau de Lamaestre, "Surface plasmon resonances in silver bowtie nanoantennas with varied bow angles," *Journal of Applied Physics*, vol. 108, no. 12, pp. 124 314–124 314, 2010.

[96] *E20/327 Solar panel datasheet*. Sunpower Corporation, 2011.

[97] A. M. A. Sabaawi, C. C. Tsimenidis, and B. S. Sharif, "Planar bowtie nanoarray for thz energy detection," *IEEE Transactions on Terahertz Science and Technology*, vol. 3, no. 5, pp. 1–8, 2013.

[98] A. M. A. Sabaawi, C. Tsimenidis, and B. Sharif, "Bow-tie nano-array rectenna: Design and optimization," in *Antennas and Propagation (EUCAP), 2012 6th European Conference on*. IEEE, 2012, pp. 1975–1978.

[99] S. Uysal, M.-S. Leong, and C. H. Ng, "Bowtie patch antennas and simple arrays for wireless indoor communications," *Microwave Theory and Techniques, IEEE Transactions on*, vol. 47, no. 6, pp. 738–745, 1999.

[100] M. Silva-López, A. Cuadrado, N. Llombart, and J. Alda, "Antenna array connections for efficient performance of distributed microbolometers in the IR," *Optics express*, vol. 21, no. 9, pp. 10 867–10 877, 2013.

[101] C. Fumeaux, W. Herrmann, H. Rothuizen, P. De Natale, and F. Kneubühl, "Mixing of 30 thz laser radiation with nanometer thin-film ni-nio-ni diodes and integrated bow-tie antennas," *Applied Physics B*, vol. 63, no. 2, pp. 135–140, 1996.

[102] S. Grover and G. Moddel, "Applicability of metal/insulator/metal (mim) diodes to solar rectennas," *Photovoltaics, IEEE Journal of*, vol. 1, no. 1, pp. 78–83, 2011.

[103] A. M. A. Sabaawi, C. C. Tsimenidis, and B. S. Sharif, "Analysis and modeling of infrared solar rectennas," 2013.

[104] ——, "Characterization of coupling and quantum efficiencies in solar rectennas," in *Antennas and Propagation Conference (LAPC), 2013 Loughborough*. IEEE, 2013, pp. 363–368.

[105] P. B. Johnson and R.-W. Christy, "Optical constants of the noble metals," *Physical Review B*, vol. 6, no. 12, p. 4370, 1972.

[106] G. W. Hanson, "On the applicability of the surface impedance integral equation for optical and near infrared copper dipole antennas," *Antennas and Propagation, IEEE Transactions on*, vol. 54, no. 12, pp. 3677–3685, 2006.

[107] M. A. Ordal, R. J. Bell, R. Alexander Jr, L. Long, M. Querry *et al.*, "Optical properties of fourteen metals in the infrared and far infrared: Al, co, cu, au, fe, pb, mo, ni, pd, pt, ag, ti, v, and w." *Applied Optics*, vol. 24, no. 24, pp. 4493–4499, 1985.

[108] G. W. Hanson, "Fundamental transmitting properties of carbon nanotube antennas," *Antennas and Propagation, IEEE Transactions on*, vol. 53, no. 11, pp. 3426–3435, 2005.

[109] S. J. Orfanidis, *Electromagnetic waves and antennas*. Rutgers University, 2002.

[110] G. Fikioris and T. T. Wu, "On the application of numerical methods to hallen's equation," *Antennas and Propagation, IEEE Transactions on*, vol. 49, no. 3, pp. 383–392, 2001.

[111] P. J. Burke, S. Li, and Z. Yu, "Quantitative theory of nanowire and nanotube antenna performance," *Nanotechnology, IEEE Transactions on*, vol. 5, no. 4, pp. 314–334, 2006.

[112] J. Hao and G. W. Hanson, "Infrared and optical properties of carbon nanotube dipole antennas," *Nanotechnology, IEEE Transactions on*, vol. 5, no. 6, pp. 766–775, 2006.

[113] A. Alù and N. Engheta, "Input impedance, nanocircuit loading, and radiation tuning of optical nanoantennas," *Physical review letters*, vol. 101, no. 4, p. 043901, 2008.

[114] J. D. Dudley and W. J. Strong, "Why are resonant frequencies sometimes defined in terms of zero reactance?" *American Journal of Physics*, vol. 55, pp. 610–613, 1987.

[115] M. Dagenais, K. Choi, F. Yesilkoy, A. N. Chryssis, and M. C. Peckerar, "Solar spectrum rectification using nano-antennas and tunneling diodes," in *OPTO*. International Society for Optics and Photonics, 2010, pp. 76 050E–76 050E.

[116] S. Grover, O. Dmitriyeva, M. J. Estes, and G. Moddel, "Traveling-wave metal/insulator/metal diodes for improved infrared bandwidth and efficiency of antenna-coupled rectifiers," *Nanotechnology, IEEE Transactions on*, vol. 9, no. 6, pp. 716–722, 2010.

[117] S. Joshi and G. Moddel, "Efficiency limits of rectenna solar cells: Theory of broadband photon-assisted tunneling," *Applied Physics Letters*, vol. 102, p. 083901, 2013.

[118] J. G. Simmons, "Generalized formula for the electric tunnel effect between similar electrodes separated by a thin insulating film," *Journal of Applied Physics*, vol. 34, p. 1793, 1963.

[119] T. O'Regan, M. Chin, C. Tan, and A. Birdwell, "Modeling, fabrication, and electrical testing of metal-insulator-metal diode," ARMY RESEARCH LAB ADELPHI MD SENSORS AND ELECTRON DEVICES DIRECTORATE, Tech. Rep., 2011.

[120] S. Grover and G. Moddel, "Engineering the current–voltage characteristics of metal–insulator–metal diodes using double-insulator tunnel barriers," *Solid-State Electronics*, vol. 67, no. 1, pp. 94–99, 2012.

[121] I. E. Hashem, N. H. Rafat, and E. A. Soliman, "A theoretical study of metal insulator metal tunneling diode figures of merit," *IEEE J. Quantum Electron*, vol. 49, no. 1, pp. 72–79, 2013.

[122] P. Periasamy, J. J. Berry, A. A. Dameron, J. D. Bergeson, D. S. Ginley, R. P. O'Hayre, and P. A. Parilla, "Fabrication and characterization of mim diodes based on nb/nb2o5 via a rapid screening technique," *Advanced Materials*, vol. 23, no. 27, pp. 3080–3085, 2011.

[123] Y.-C. Yeo, T.-J. King, and C. Hu, "Metal-dielectric band alignment and its implications for metal gate complementary metal-oxide-semiconductor technology," *Journal of Applied Physics*, vol. 92, no. 12, pp. 7266–7271, 2002.